Illuminating Molecular Spin Relaxation Mechanisms through Ligand Field Theory and Physical Inorganic Spectroscopy

Thesis by

Nathanael Parker Kazmierczak

In Partial Fulfillment of the Requirements for the
Degree of
Doctor of Philosophy in Chemistry

Caltech

CALIFORNIA INSTITUTE OF TECHNOLOGY
Pasadena, California

2025
Defended April 18, 2025

ACKNOWLEDGEMENTS

I have been blessed to have excellent teachers my entire life, without whom this thesis would not have been possible. I will mention those who have been closest to me, but there has been an entire community of scholars, friends, and mentors who have influenced my academic formation, too numerous to list here. To all who have played a role in my journey, I wish to express my heartfelt gratitude.

First, I would like to acknowledge my truly exceptional high school teachers. Dr. Kristen Fulfer (now a faculty member at Centre College) tutored me throughout AP chemistry, and was probably the single biggest influence leading me to pursue a career in chemistry. Her enthusiasm for the subject was contagious, and her stories of graduate school adventures with lasers first sparked my own interest in physical chemistry. Brian Daigle and Kevin Lindholm were superlative humanities and arts instructors at my high school classical education program, Sequitur Classical Academy. They taught me the value of a liberal arts education for the pursuit of the good life.

When I attended Calvin College for undergraduate studies, the streak of excellent instructors continued. My research advisor, Prof. Douglas A. Vander Griend, taught me how to execute a research project for the first time. He always knew how to strike the perfect balance between guidance and freedom, and I became confident as an independent scientist under his mentorship. I greatly respect him as a scientist, educator, and person, and his support and advocacy for my subsequent career means a lot to me. Prof. Herb Fynewever opened many doors for me as my academic advisor and was an excellent quantum mechanics instructor. Prof. Mark Muyskens taught me kinetics, which has proven extremely valuable in my graduate research. Prof. Carolyn Anderson, Prof. Chad Tatko, Prof. Michael Barbachyn, and Prof. Karl Seper taught me organic chemistry, which ignited my love for the adventures of laboratory work. Prof. Barbachyn also kindly allowed me to conduct organic synthesis research in his laboratory during a January term, which proved key for increasing my confidence in the wet lab. Prof. Kumar Sinniah taught me analytical chemistry, and has continued to offer valuable and perceptive advice beyond the confines of the classroom. Prof. Rachael Baker, Prof. Larry Louters, and Prof. Laura Westrate taught me biochemistry, which has been a valuable foundation of knowledge. Prof. Dave Benson taught me inorganic chemistry and instrumentation with great depth, breadth, and humor. In retrospect, I realize how well his classes prepared me for graduate education, and he first suggested spectroscopy as a research specialization that might fit my particular aptitudes and interests. This group of liberal arts professors constitutes some of the best educators I have ever met. When I arrived at Caltech for graduate school, I found myself equally well prepared as other students who had graduated from the top-ranked research universities in the world.

I also have great gratitude towards Prof. Kwabena Bediako for taking me on as an summer undergraduate student when he was just starting his lab at UC Berkeley. Kwabena took a chance on me as an unknown liberal arts student, and that opportunity helped propel me into a career in graduate research. Samra Husremović and Maddie Van Winkle, my two graduate student mentors in the Bediako Lab, first modeled for me how to be a successful graduate student. I greatly appreciate their teaching and friendship.

My time at Caltech has been a joy, and I will miss being a graduate student here. My advisor, Prof. Ryan Hadt, has been a fantastic research mentor and a wonderful person to work with. He is intellectually fearless, willing to venture into multiple research subdisciplines to solve interesting problems. His group has contained spectroscopists, synthetic chemists, and pure computational chemists alike. As his graduate student, I was afforded the opportunity to learn new skills in all these areas, which is a rather unusual experience. Ryan is also incredibly kind, and I have learned much from him about the type of mentor I want to be in my future career.

My coworkers and friends in the Hadt Lab have provided continual comradery and support along the journey, and I will miss each of them. Their enthusiasm for science and diversity of perspectives have produced an intellectually stimulating environment key to my education. Ruben Mirzoyan mentored me when I joined the group and provided a perfect balance of guidance and freedom that enabled me to take ownership of productive projects early in my graduate career. Ryan Ribson provided early training in lab equipment and procedures. Chris Totoiu and Katie Luedecke stuck it out alongside me from the beginning to the end, and have been great friends throughout. David Cagan was a role model to me at every step of the process, and I have the greatest respect for his dedication and determination. Dr. Daniel Bím taught me much about computational chemistry and was a fearsome opponent over the chessboard. Dr. Brendon McNicholas played a critical role in bringing the magnetic circular dichroism setup to fruition. Outside of this thesis work, I also assisted David, Daniel, and Brendon on projects related to nickel photoredox catalysis, and it was a great pleasure to learn from their expertise. Dr. Erica Sutcliffe was a fantastic teacher for all things related to laser spectroscopy. Dr. Thais Scott was a valuable collaborator on computational chemistry simulations of X-ray spectra. Dr. Kay Xia provided critical synthetic expertise to facilitate projects towards the end of my Ph.D. Dr. Stefan Lohaus has been a valuable collaborator on phonon projects and has set an example as a great scientific communicator. I would like to download Dr. Stephen DiLuzio's knowledge of photochemistry – he has provided many insights that I will take into my future career. Dr. Jake Rothbaum brings great energy to the lab. I have greatly enjoyed working with each of the newer graduate students in the lab – Maria Blankemeyer, Keon Ha Hwang, Arshiyan Alam Laaj, Jonathan Aalto, and Juliette Whiteside – and I am excited about the talent they bring to the table. The Hadt Lab has a bright future because of them. Additionally, several scientists outside of the Hadt Lab have played key roles in fruitful research collaborations, some of which are included in this thesis and some of which are not. These collaborators include Dr. Matt Espinosa, Fernando Guerrero, Yong-Rui Poh, Kacie Nelson, Joseph Zsombor-Pindera, Phil Kocheril, Jax Dallas, Dr. Thomas Kroll, Dr. Amy Cordones-Hahn, Prof. Pierre Kennepohl, Prof. Victor Nemykin, Prof. Joel Yuen-Zhou, and Prof. Theo Agapie.

I would also like to thank the Caltech faculty and staff who have played an essential role in my education. I profited from Prof. Theo Agapie's great passion and diligence in teaching graduate inorganic chemistry. Prof. Nick Hutzler was kind enough to teach atomic, molecular, and optical physics to a curious chemist, and his clear exposition of key concepts in quantum mechanics was critical for the success of my thesis research. Prof. Harry Gray taught me in one traditional lecture class on advanced inorganic chemistry and three nontraditional problem set classes on advanced ligand field theory, which are not for the faint of heart! The skills I gained from them played an essential role in my thesis research. Harry's support of young scientists is remarkable for a researcher of his stature, and I count myself truly fortunate to have known him and received his mentorship. Prof. Geoff Blake, Prof. Jonas Peters, and Prof. Garnet Chan served on my thesis committee, providing ever-helpful suggestions and critiques that challenged me to reach my highest scientific potential. Dr. Paul Oyala taught me everything I know about pulse EPR spectroscopy. His expertise and diligence in keeping the instrument in good operational condition was one of the most important factors enabling my productivity in graduate school. Dr. Jay Winkler played a critical role in maintaining the resonance Raman setup, as well as providing a wealth of wisdom regarding spectroscopy. Dr. Mike Takase was ever-helpful in performing crystallography on very short notice and also taught me in a crystallography class. The facilities and administrative staff – Joe Drew, Alison Ross, Elisha Okawa, and many others – were absolutely stellar in producing the environment needed to do this research.

My scientific education would not have been possible without the financial support of a number of private foundations and federal agencies. The Arnold and Mabel Beckman Foundation supported me as a Beckman Scholar during my undergraduate work, and the Barry Goldwater Foundation supported me as a Goldwater Scholar. These early votes of confidence in my potential gave me critical confidence needed to pursue the next steps. The National Science Foundation supported the majority of my first three years of graduate school via an NSF Graduate Research Fellowship. The Fannie and John Hertz Foundation supported me in part or in full for the final four years of graduate school on a Hertz Fellowship. Beyond the financial benefit, the Hertz Foundation has provided me access to a truly exceptional community of scholars and entrepreneurs, and I count myself very lucky to have received their support. I am grateful to Cheri Ackerman for making me aware of the Hertz Fellowship and giving advice on the path to a successful application. The research projects themselves were funded by multiple organizations, including the Department of Energy, the National Science Foundation, and the Research Corporation for Science Advancement.

As always, my family provided the essential nurturing, support, and wisdom to launch me into the world, but I owe my parents a special debt of gratitude for my academic path. Mom and Dad homeschooled me from an early age until I reached high school, and their passion and deep knowledge across so many subjects was undoubtedly the single most important thing for forming my love of learning. My parents never pushed me to succeed, but rather equipped me with the tools for success and gave me space to grow into them at my own pace. I am truly grateful for the sacrifices they have made for me, and I cherish the love we share.

Finally, I would like to thank my beautiful and beloved wife, Joyce, who has unfailingly supported me through graduate school and beyond. Joyce and I married during my second year of graduate school, and we have both noticed a major increase in my happiness level since that time! As a brilliant mathematician about to receive her own Ph.D., Joyce understands what the academic life is like. She is ever patient, always kind, very funny, a joyful companion, and wise in counsel. I am so blessed to spend my days with her, and I eagerly look forward to our future lives together.

ABSTRACT

Electron spin relaxation is a fundamental process in paramagnetic molecules, and successful development of molecular quantum bits (qubits) for quantum information science hinges on suppressing the rate of spin relaxation. While the relaxation process has been studied since the early 20th century, no consensus has been reached regarding the physical relaxation mechanism in S = 1/2 transition metal molecules. Practical guidelines for designing molecules with slow spin relaxation have likewise remained obscure. This thesis describes the use of ligand field theory and physical inorganic spectroscopy techniques to shed new light on molecular spin relaxation mechanisms, connecting relaxation rates to chemical bonding and transition metal electronic structure. Part 1 (Chapters 1-4) details the use of electron paramagnetic resonance (EPR), magnetic circular dichroism (MCD), and resonance Raman (rR) to interrogate the origins of spin relaxation. Experimental spectroscopic results are analyzed within the context of a model based on group theory, yielding a paradigm referred to as ligand field spin dynamics. Part 2 (Chapters 5-7) describes the development of a new experimental observable, T_1 anisotropy, as a novel approach for distinguishing between competing theoretical spin relaxation models. Part 3 (Chapters 8-10) shows how the insights of ligand field spin dynamics and T_1 anisotropy have been leveraged to rationally design molecules with slow spin relaxation and other desirable spin dynamics properties. This thesis establishes a framework for controlling the physical process of spin relaxation through distinctly chemical molecular design principles.

PUBLISHED CONTENT AND CONTRIBUTIONS

[1] Mirzoyan, R.; Kazmierczak, N. P.; Hadt, R. G. Deconvolving Contributions to Decoherence in Molecular Electron Spin Qubits: A Dynamic Ligand Field Approach. *Chemistry – A European Journal* **2021**, *27*, 9482–9494.
DOI: 10.1002/chem.202100845.

- As second author, I assisted with the literature review and conceptualization, as well as conducting writing, editing, and figure preparation for the manuscript.

[2] Kazmierczak, N. P.; Mirzoyan, R.; Hadt, R. G. The Impact of Ligand Field Symmetry on Molecular Qubit Coherence. *Journal of the American Chemical Society* **2021**, *143*, 17305–17315. DOI: 10.1021/jacs.1c04605.

- As first author, I conceptualized the project, performed the derivations and computational analysis, and performed the main writing on the manuscript.

[3] Kazmierczak, N. P.; Hadt, R. G. Illuminating Ligand Field Contributions to Molecular Qubit Spin Relaxation via T_1 Anisotropy. *Journal of the American Chemical Society* **2022**, *144*, 20804–20814. DOI: 10.1021/jacs.2c08729.

- As first author, I conceptualized the project, performed the spectroscopic experiments, computations, theoretical derivations, synthesized chemical samples, and wrote the manuscript.

[4] Kazmierczak, N. P.*; Luedecke, K. M.*; Gallmeier, E. T.; Hadt, R. G. T_1 Anisotropy Elucidates Spin Relaxation Mechanisms in an $S = 1$ Cr(IV) Optically Addressable Molecular Qubit. *The Journal of Physical Chemistry Letters* **2023**, *14*, 7658–7664. DOI: 10.1021/acs.jpclett.3c01964.

- As co-first author with K. M. Luedecke, I performed project conceptualization, spectroscopic experiments, analysis, theoretical derivations, and wrote the manuscript.

[5] Kazmierczak, N. P.; Lopez, N. E.; Luedecke, K. M.; Hadt, R. G. Determining the Key Vibrations for Spin Relaxation in Ruffled Cu(II) Porphyrins via Resonance Raman Spectroscopy. *Chemical Science* **2024**, *15*, 2380–2390. DOI: 10.1039/D3SC05774G.

- As first author, I performed project conceptualization, spectroscopic experiments, computations, analysis, and wrote the manuscript.

[6] Lohaus, S. H.; Kazmierczak, N. P.; Luedecke, K. M.; Marx, B.; Nemykin, V. N.; Hadt, R. G. Quantifying the Effects of Peripheral Substituents on the Spin-Lattice Relaxation of a Vanadyl Molecular Quantum Bit. *Journal of Porphyrins and Phthalocyanines* **2024**, *28*, 383-389. DOI: 10.1142/S1088424624500329.

- As second author, I assisted in project conceptualization, data interpretation, experiments, and editing the manuscript.

[7] Sutcliffe, E.; Kazmierczak, N. P.; Hadt, R. G. Ultrafast All-Optical Coherence of Molecular Electron Spins in Room-Temperature Water Solution. *Science* **2024**, *386*, 888-892. DOI: 10.1126/science.ads0512.

- As second author, I assisted in project conceptualization, performed experiments and data analysis, and co-wrote the manuscript.

[8] Kazmierczak, N. P.; Oyala, P. H.; Hadt, R. G. Spectroscopic Signatures of Phonon Character in Molecular Electron Spin Relaxation. *ACS Central Science* **2024**, *10*, 2353–2362. DOI: 10.1021/acscentsci.4c01177.

- As first author, I conceptualized the project, performed the experiments and data analysis, and wrote the manuscript.

[9] Kazmierczak, N. P.*; Xia, K. T.*; Sutcliffe, E.; Aalto, J. P.; Hadt, R. G. A Spectrochemical Series for Electron Spin Relaxation. *Journal of the American Chemical Society* **2025**, *147*, 2849–2859. DOI: 10.1021/jacs.4c16571.

- As co-first author with K. T. Xia, I conceptualized the project, performed spectroscopic measurements and data analysis, and wrote the manuscript.

[10] Espinosa, M. R.*; Guerrero, F.*; Kazmierczak, N. P.*; Oyala, P. H.; Hong, A.; Hadt, R. G.; Agapie, T. Slow Electron Spin Relaxation at Ambient Temperatures with Copper Coordinated by a Rigid Macrocyclic Ligand. *Journal of the American Chemical Society* **2025**, *147*, 14036–14042. DOI: 10.1021/jacs.5c00803.

- As co-first author with M. R. Espinosa and F. Guerrero, I conducted the computational investigations, analyzed the CW and pulse EPR data, and co-wrote the initial manuscript. M.R.E., F.G., and A.H. conducted chemical synthesis, characterization, and crystallography. M.R.E., F.G., A.H., and P.H.O. conducted experimental pulse and CW EPR data acquisition. N.P.K. conducted DFT calculations. N.P.K., M.R.E., and F.G. conducted analysis of CW and pulse EPR data. M.R.E., F.G., and N.P.K. co-wrote the initial manuscript. R.G.H. and T.A. conceptualized the study and provided guidance and resources.

TABLE OF CONTENTS

Acknowledgements . . . iii
Abstract . . . vii
Published Content and Contributions . . . viii
Table of Contents . . . x
List of Illustrations . . . xiv
List of Tables . . . xvii
Nomenclature . . . xviii
Chapter I: Introduction: Deconvolving Contributions to Decoherence in Molecular Electron Spin Qubits—A Dynamic Ligand Field Approach . . . 1
  1.1 Abstract . . . 1
  1.2 Introduction . . . 2
  1.3 Spin-Spin and Motional Contributions to Decoherence . . . 7
  1.4 Phonon Contributions to Decoherence . . . 10
  1.5 Dynamic Ligand Fields in Electron Spin Qubits . . . 14
  1.6 Summary and Outlook . . . 21
Bibliography . . . 23
Chapter II: The Impact of Ligand Field Symmetry on Molecular Qubit Coherence . . . 33
  2.1 Abstract . . . 33
  2.2 Introduction . . . 34
  2.3 Ligand Field Paradigm for Electron Spin Relaxation . . . 36
  2.4 Discussion . . . 48
Bibliography . . . 52
Chapter III: Determining the Key Vibrations for Spin Relaxation in Ruffled Copper(II) Porphyrins via Resonance Raman Spectroscopy . . . 57
  3.1 Abstract . . . 57
  3.2 Introduction . . . 58
  3.3 Results . . . 62
  3.4 Discussion . . . 72
  3.5 Conclusions . . . 73
Bibliography . . . 74
Chapter IV: A Spectrochemical Series for Electron Spin Relaxation . . . 78
  4.1 Abstract . . . 78
  4.2 Introduction . . . 79
  4.3 Results . . . 82
  4.4 Discussion . . . 91
  4.5 Conclusions . . . 95
Bibliography . . . 96

Chapter V: Illuminating Ligand Field Contributions to Molecular Qubit Spin Relaxation via T_1 Anisotropy . . . 102
- 5.1 Abstract . . . 102
- 5.2 Introduction . . . 103
- 5.3 Results . . . 105
- 5.4 Discussion . . . 111
- 5.5 Conclusions . . . 123

Bibliography . . . 125

Chapter VI: T_1 Anisotropy Elucidates Spin Relaxation Mechanisms in an S = 1 Chromium(IV) Optically Addressable Molecular Qubit . . . 130
- 6.1 Abstract . . . 130
- 6.2 Introduction . . . 131
- 6.3 Results and Discussion . . . 132

Bibliography . . . 140

Chapter VII: Spectroscopic Signatures of Phonon Character in Molecular Electron Spin Relaxation . . . 144
- 7.1 Abstract . . . 144
- 7.2 Introduction . . . 145
- 7.3 Results . . . 147
- 7.4 Discussion . . . 155
- 7.5 Conclusion . . . 160

Bibliography . . . 160

Chapter VIII: Slow Electron Spin Relaxation at Ambient Temperatures with Copper Coordinated by a Rigid Macrocyclic Ligand . . . 165
- 8.1 Abstract . . . 166
- 8.2 Introduction . . . 166
- 8.3 Results and Discussion . . . 168

Bibliography . . . 175

Chapter IX: Quantifying the Effects of Peripheral Substituents on the Spin-Lattice Relaxation of a Vanadyl Molecular Quantum Bit . . . 179
- 9.1 Abstract . . . 179
- 9.2 Introduction . . . 180
- 9.3 Materials and Methods . . . 181
- 9.4 Results and Discussion . . . 183
- 9.5 Conclusions . . . 191

Bibliography . . . 192

Chapter X: Ultrafast, All-Optical Coherence of Molecular Electron Spins in Room-Temperature Aqueous Solution . . . 195
- 10.1 Abstract . . . 195
- 10.2 Introduction . . . 195
- 10.3 Design Criteria for All-Optical Molecular Qubits . . . 197
- 10.4 Ultrafast Detection of Free Induction Decay . . . 199
- 10.5 Sensing Viscosity with T_2^* . . . 201
- 10.6 Comparison with EPR . . . 202
- 10.7 Discussion . . . 204

Bibliography 205
Chapter XI: Conclusion 209
Bibliography 214
Appendix A: Supporting Information for Chapter II: The Impact of Ligand Field Symmetry on Molecular Qubit Coherence 217
Appendix B: Supporting Information for Chapter III: Determining the Key Vibrations for Spin Relaxation in Ruffled Copper(II) Porphyrins via Resonance Raman Spectroscopy 218
Appendix C: Supporting Information for Chapter IV: A Spectrochemical Series for Electron Spin Relaxation 219
Appendix D: Supporting Information for Chapter V: Illuminating Ligand Field Contributions to Molecular Qubit Spin Relaxation via T_1 Anisotropy 220
Appendix E: Supporting Information for Chapter VI: T_1 Anisotropy Elucidates Spin Relaxation Mechanisms in an S = 1 Chromium(IV) Optically Addressable Molecular Qubit 221
Appendix F: Supporting Information for Chapter VII: Spectroscopic Signatures of Phonon Character in Molecular Electron Spin Relaxation 222
Appendix G: Supporting Information for Chapter VIII: Slow Electron Spin Relaxation at Ambient Temperatures with Copper Coordinated by a Rigid Macrocyclic Ligand 223
Appendix H: Supporting Information for Chapter IX: Quantifying the Effects of Peripheral Substituents on the Spin-Lattice Relaxation of a Vanadyl Molecular Quantum Bit 224
Appendix I: Supporting Information for Chapter X: Ultrafast, All-Optical Coherence of Molecular Electron Spins in Room-Temperature Aqueous Solution 225

LIST OF ILLUSTRATIONS

Number *Page*
1.1 Principles of qubit measurements in EPR spectroscopy 4
1.2 Experimental methods and considerations for spin coherence 5
1.3 Representative electronic spin-based qubits 7
1.4 Regimes of decoherence in molecular electron spin qubits 8
1.5 Phonon involvement in spin-lattice relaxation 12
1.6 A general ligand field theory method for predicting decoherence in the spin-phonon regime from equilibrium molecular parameters . . . 17
1.7 Effect of geometric distortion on spin-phonon coupling terms 19
2.1 Overview of molecular electron spin qubits 35
2.2 The excited state origins of ground state spin-phonon coupling 38
2.3 Impact of symmetry on spin-phonon coupling 41
2.4 Orientation-dependent spin-phonon coupling coefficients for CuPc, $[Cu(bdt)_2]^{2-}$, and $[VO(dmit)_2]^{2-}$ 43
2.5 Thermally-weighted ligand field model for phthalocyanine qubits . . 46
2.6 Thermally-weighted ligand field model for dithiolate and diselenate qubits 48
2.7 Symmetry flowchart of spin-phonon coupling coefficients 50
3.1 Mechanistic studies of spin-lattice relaxation in S = ½ qubits 60
3.2 Geometries of ruffled metalloporphyrins 61
3.3 Temperature-dependent T_1 by pulse EPR X-band inversion recovery in 1% solid state powder dilutions of CuOEP in ZnOEP, CuTPP in NiTPP, and CuTiPP in NiTiPP 64
3.4 Calculated spin relaxation rates $1/T_1$ for the Cu porphyrin series . . . 66
3.5 Calculated vs. experimental $1/T_1$ log-log slopes for CuOEP and CuTiPP 69
3.6 Determination of the dominant vibrational mode energy for spin relaxation 70
4.1 MCD as a useful spectroscopic probe for spin relaxation 81
4.2 Compound scope for correlating MCD to spin relaxation rates 83
4.3 Assignment of electronic transitions through Gaussian band fitting of representative MCD and UV-vis-NIR absorption spectra 86

4.4 MCD spectral scope 87
4.5 Correlation between MCD and pulse EPR spin relaxation rates 92
4.6 Analysis of the spectrochemical series for spin relaxation 94
5.1 Highly coherent V(IV) and Cu(II) S = 1/2 compounds employed for analysis of T_1 anisotropy 105
5.2 Simulated orientation dependence of a pulsed EPR echo-detected field sweep (EDFS) 107
5.3 X-band T_1 anisotropy measured by inversion recovery at 100 K for isostructural solid state dilutions 108
5.4 Simulation of T_1 anisotropy for the Cu(acac)$_2$ sample 110
5.5 No correlation between the experimental T_1 anisotropy and the g-tensor or hyperfine tensor anisotropy 113
5.6 UV-vis-NIR absorption spectra for the molecular qubit complexes measured in this study 119
5.7 Totally symmetric vibrational modes considered for the DFT prediction of 100 K T_1 anisotropy 122
6.1 Molecular crystal structures and point groups of S = 1 Cr(o-tolyl)$_4$ and S = ½ Cu(acac)$_2$ 133
6.2 Anisotropy in Cr(IV) pulsed EPR 134
6.3 T_1 anisotropy at 40 K of Cr(o-tolyl)$_4$ and Cu(acac)$_2$ 136
6.4 Temperature dependence of T_1 anisotropy contributions for Cr(o-tolyl)$_4$ and Cu(acac)$_2$ 137
7.1 Measuring spin relaxation anisotropy 148
7.2 Variable-temperature, variable-field T_1 anisotropy (VTVH-T_1) 149
7.3 Comparison to local mode fitting 153
7.4 Single-crystal T_1 anisotropy for 1:1000 Cu(acac)$_2$ in Pd(acac)$_2$ 156
8.1 Comparison of copper N$_4$ macrocyclic S = ½ qubits 167
8.2 Crystallography of Cu($^{\mathrm{Mes}}$N$_6$)(OTf)$_2$ open and closed complexes . . . 169
8.3 Pulse EPR analysis of Cu($^{\mathrm{Mes}}$N$_6$)$^{2+}$ spin relaxation 171
8.4 Theoretical analysis of $^{\mathrm{Mes}}$N$_6$ ligand advantage for long spin lifetimes 173
9.1 Molecular structures of VOPc and VOPyzPz-DIPP 182
9.2 Pulse EPR T_1 anisotropy of VOPyzPz-DIPP and VOPc 185
9.3 Spin lattice relaxation measured by inversion recovery at 10 K 188
9.4 Spin-lattice relaxation of VOPyzPz-DIPP and VOPc as a function of temperature collected by inversion recovery at the powder line 189
10.1 Methods for detecting spin coherence 197

10.2 Ultrafast free induction decay at room temperature 200
10.3 Comparison between EPR and TRFE capabilities 203

LIST OF TABLES

Number *Page*
1.1 Application of orbital angular momentum operators to the real d-orbitals 15
2.1 Linear g_z spin-phonon coupling modes for VOPc and CuPc 40
3.1 Normal coordinate structural decomposition analysis of porphyrin distortions 63
3.2 Positions of local mode energies and Raman mixed ligand symmetric stretch peaks 71
5.1 Spin Hamiltonian g-tensor and A-tensor parameters 109
5.2 T_1 anisotropy ratios at 100 K for selected Cu(II) and V(IV) molecular qubits 111
5.3 T_1 anisotropy predictions via DFT $\partial g/\partial Q$ proxies 122
8.1 Comparison of crystallographic bond lengths and CW EPR values for copper N_4 macrocyclic complexes 174
8.2 Comparison of calculated vibrational modes and local mode fitting for copper N_4 macrocyclic complexes 174

NOMENCLATURE

Δ. Change in a quantity.

λ. Wavelength in nanometers.

ε. Molar absorptivity coefficient.

B. Magnetic field.

g value. A dimensionless quantity relating the magnetic moment of an electron to its spin.

M_S. Electron spin projection quantum number.

S. Total electron spin quantum number.

Å. Angstrom.

CW. Continuous wave.

d-d. Indicates a ligand field electronic transition.

DCM. Dichloromethane.

DFT. Density functional theory.

EPR. Electron paramagnetic resonance.

IR. Infrared.

LMCT. Ligand-to-metal charge transfer.

MCD. Magnetic circular dichroism.

MLCT. Metal-to-ligand charge transfer.

NIR. Near infrared.

Q. Nuclear coordinate.

TDDFT. Time-dependent density functional theory.

VH. Variable magnetic field.

VT. Variable temperature.

Chapter 1

INTRODUCTION: DECONVOLVING CONTRIBUTIONS TO DECOHERENCE IN MOLECULAR ELECTRON SPIN QUBITS—A DYNAMIC LIGAND FIELD APPROACH

- Adapted with permission from: Mirzoyan, R.; Kazmierczak, N. P.; Hadt, R. G. Deconvolving Contributions to Decoherence in Molecular Electron Spin Qubits: A Dynamic Ligand Field Approach. *Chemistry – A European Journal* **2021**, *27*, 9482–9494. DOI: https://doi.org/10.1002/chem.202100845.

1.1 Abstract

In the past decade, transition metal complexes have gained momentum as electron spin-based quantum bit (qubit) candidates due to their synthetic tunability and long achievable coherence times. The decoherence of magnetic quantum states imposes a limit on the use of these qubits for quantum information technologies, such as quantum computing, sensing, and communication. With rapid recent development in the field of molecular quantum information science, a variety of chemical design principles for prolonging coherence in molecular transition metal qubits have been proposed. Here we delineate the spin-spin, motional, and spin-phonon regimes of decoherence, outlining design principles for each. We show how dynamic ligand field models can provide insights into the intramolecular vibrational contributions in the spin-phonon decoherence regime. This minireview aims to inform the development of molecular quantum technologies tailored for different environments and conditions.

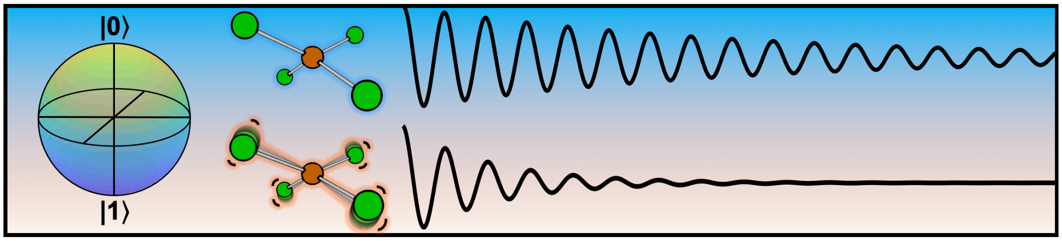

1.2 Introduction

1.2.1 Motivation

Near the beginning of the 20th century, quantum mechanics developed new fundamental rules that describe the natural world, constituting the first quantum revolution. The second quantum revolution now endeavors to control individual quantum systems, enabling powerful applications in computing, sensing, and communication.[1,2] The fundamental unit of quantum information science is the quantum bit (qubit), a two-level quantum system.[3] Paramagnetic molecules can serve as qubit platforms due to the Zeeman effect, wherein the M_S sublevels of an unpaired electron in a magnetic field generate an effective two-level system with an energy gap in the microwave frequency range (Figure 1.1A). The quantum states of electron spins can then be initialized, manipulated, and studied using microwave pulses in electron paramagnetic resonance (EPR) spectrometers.[4] Furthermore, paramagnetic transition metal complexes are synthetically tunable and can be attached to templated substrates and surfaces,[5] tethered to electrodes,[6] and integrated with superconducting resonators[7,8] to realize quantum technological devices tunable on the molecular scale.[9–15]

1.2.2 Defining and Using Quantum Coherence

An essential feature of quantum systems is the property of phase coherence (hereafter simply “coherence”), in which qubits in an ensemble retain their relative phase relations.[16] Interactions between the qubits and their environment cause the ensemble to lose coherence and collapse to a classically observable state, limiting the time in which uniquely quantum behavior can be observed. This process is known as decoherence.[16] Successful electron spin qubits in both sensing and computing must have long coherence times relative to their Larmor precession frequency, which governs the limiting timescale at which the electron spin qubit can change its quantum state. Using X-band EPR (~9.5 GHz), this timescale is on the order of 10 ns. To maintain phase information adequate for fault-tolerant quantum computations, the coherence time should be 10^4-10^5 times longer.[17] Therefore, understanding the contributions to coherence times is a critical factor for the development of technologies that exploit quantum information.[2]

In the simplest model, decoherence of an $S = ½$ system can be described by two mono-exponential processes, with time constants T_1 and T_2 based on the Bloch equations.[18] T_1 defines the time required for an ensemble of electron spins to relax back to thermodynamic equilibrium, a criterion satisfied when the Zeeman-split magnetic sublevels are populated according to a Boltzmann distribution. For an initial excess of excited spins, this requires dissipation of energy to a surrounding bath or lattice. T_1 is therefore often called the "spin-lattice" relaxation time, though the environment need not necessarily be a crystalline lattice. T_2 defines the time required for an ensemble of spins to lose their phase relations. This does not necessitate dissipation of energy to the lattice and arises from the differential couplings between qubit electron spins and spins in the bath. For this reason, T_2 is often called the "spin-spin" relaxation time. Both processes can be visualized by considering spin magnetization vectors projected onto a complex unit sphere known as the Bloch sphere (Figure 1.1A). A pure (coherent) state is represented by a vector extending towards a point on the surface of the sphere, while a mixed (partially or fully decohered) state is representing by a vector extending towards a point within the interior of the sphere.[3] As can be seen geometrically, longitudinal electron spin relaxation (T_1) necessarily destroys transverse magnetization (Figure 1.1B). Therefore, the upper limit to T_2 (Figure 1.1C) is defined by T_1, in which case T_2 is said to be T_1-limited. This regime is important to consider when seeking to increase the temperature at which coherence can be maintained and used.

The characteristic decoherence time constants can be determined experimentally using pulsed EPR spectroscopy. An initial state is prepared by a coherent pulse, which both excites members of the spin ensemble and synchronizes their phases. Experimental coherence times are defined herein by time constants T_2^{DD}, T_M, and T_2^*; each pertains to a time decay following a well-defined pulse sequence (Figure 1.2A). It should be noted that naming convention can differ, and some authors refer to T_2 and T_M interchangeably. T_2^* corresponds to the free-induction decay following a single $\pi/2$ pulse and is the simplest measurement of decoherence. T_M corresponds to the decay following a Hahn-echo pulse sequence, in which a π pulse removes dephasing due to static inhomogeneities in the magnetic environment (Figure 1.2A). T_2 as defined by Bloch cannot usually be measured in EPR owing to spectral diffusion (Figure 1.2B),[19] a process arising from the narrow bandwidth of the microwave radiation compared to the absorbance lineshape. In some cases, dynamic decoupling methods can more closely measure T_2 by filtering out quantum noise at the frequency corresponding to the interactions (typically hyperfine) that dominate spectral diffusion. The commonly used Carr-Purcell-Meiboom-Gill (CPMG) pulse sequence uses a train of "rephasing" π pulses, which can substantially diminish spectral diffusion effects in EPR dephasing.[20–22] While dynamical decoupling methods are powerful, the upper limit for coherence times are set by the molecular properties of the qubit.

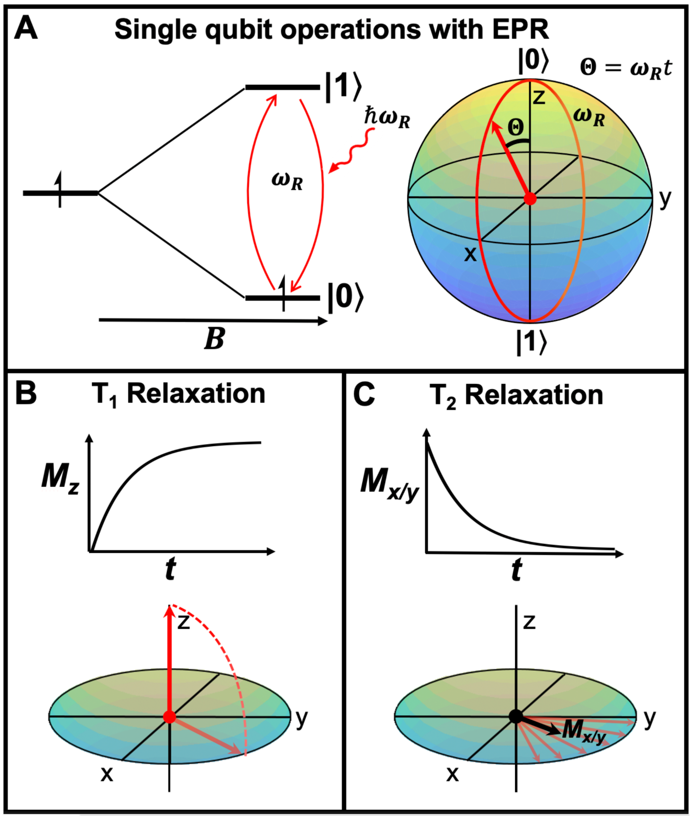

Figure 1.1: Principles of qubit measurements in EPR spectroscopy. (A) Generation of a qubit by application of a magnetic field. A resonant microwave pulse applied for length of time, t, predictably alters the polar angle, θ, in the Bloch sphere representation of the single qubit, allowing for microwave control of the quantum state. (B) T_1 (longitudinal) relaxation, as depicted by the recovery of net longitudinal magnetization M_z in the rotating frame representation. (C) T_2 (transverse) relaxation, as depicted by the decrease in the net transverse magnetization vector $M_{x/y}$ (black arrow) as the ensemble of spins (red arrows) interact with the environment and lose their phase coherence. The T_1 contribution to T_2 is not shown.

Thus, this minireview focuses on establishing design principles for long quantum coherence times through synthetically tunable chemical properties of the qubit and its environment.

1.2.3 The Idea of Decoherence Regimes

To understand factors leading to decoherence, it is useful to consider the terms of the spin Hamiltonian for the transition metal complex. A common model for decoherence is based on a quantum bath approach, in which the qubit and the bath are together considered as a closed quantum system.[23] The Hamiltonian of the

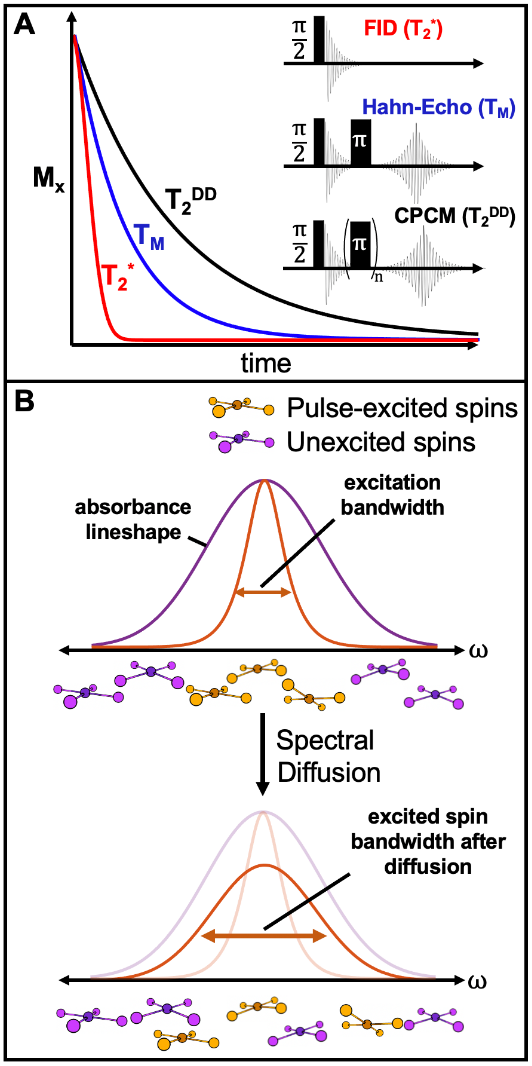

Figure 1.2: Experimental methods and considerations for spin coherence. (A) Overlay of FID ($T_2^{*}*$), Hahn-echo (T_M), and dynamically decoupled echo (T_2^{DD}) decays, together with the corresponding pulse sequences to measure these time constants. (B) Schematic illustration of spectral diffusion, in which magnetic interactions modify the resonant frequency of excited spins after excitation.

system is defined as $\boldsymbol{H} = \boldsymbol{H}_{spin} + \boldsymbol{H}_{bath} + \boldsymbol{H}_{int}$, where the spin Hamiltonian $\boldsymbol{H}_{spin}$ for a transition metal complex is given by:

$$\boldsymbol{H}_{spin} = \mu_e \boldsymbol{B_0} \boldsymbol{g} \widehat{\boldsymbol{S}} + \widehat{\boldsymbol{S}} \boldsymbol{A} \widehat{\boldsymbol{I}} + \widehat{\boldsymbol{S}} \boldsymbol{D} \widehat{\boldsymbol{S}}. \tag{1.1}$$

In order of appearance, Equation (1.1) contains the electronic Zeeman, hyperfine, and zero-field splitting terms. Here the external magnetic field is $\boldsymbol{B_0}$ and the electron and nuclear spin angular momenta are $\widehat{\boldsymbol{S}}$ and $\widehat{\boldsymbol{I}}$, with hyperfine tensor $\boldsymbol{A}$ and electronic g-tensor $\boldsymbol{g}$. The zero-field splitting tensor is given by $\boldsymbol{D}$ and is considered for systems in which the total electron spin is S > ½. The spin-bath interaction term $\boldsymbol{H}_{int}$ determines the decoherence properties of any molecular electron spin qubit.

A variety of strategies for increasing coherence times have been pursued, leading to different design principles for different goals and conditions. To prolong T_M, much emphasis has been placed on suppressing hyperfine interactions through nuclear spin dilution,[24–27] elimination,[28] substitution with nuclei having smaller magnetic moments,[27,29,30] and, more recently, "patterning,"[31] in which the neighboring nuclei of a lattice or ligand framework have a mismatch in their magnetic moments. These strategies suppress dipolar and hyperfine interaction terms in $\boldsymbol{H}_{int}$. The current record for the longest T_M in a transition metal complex is 0.7 ms at 10 K, which was observed for a six-coordinate V(IV) complex having a nuclear spin-free ligand and solvent environment (CS_2).[28] Inspired from atomic physics, another approach uses clock transitions, in which the Zeeman energy is centered at an avoided level crossing to suppress magnetic noise.[32–35] To prolong T_1, several studies have chosen structurally rigid ligand frameworks that suppress the effect of molecular vibrations and their modulation of spin-orbit coupling, with specific emphasis on building around the vanadyl (VO) moiety.[36–38] A recent strategy has targeted the minimization of ground state orbital angular momentum in a series of 3d and 4f metal complexes.[39] Despite possessing concentrated nuclear spins and a ligand framework that is structurally non-rigid, the isotropic ground state wave function enabled these qubits to reach μs coherence times at room temperature. To enable applications, molecular design is often inspired from a desired initialization or readout mechanism of the quantum state. For instance, optically addressable S = 1 molecular qubits, such as recently synthesized Cr(IV) complexes,[40] feature a spin-selective intersystem crossing in the excited state that enables a fluorescence-based readout of the quantum state. Such readout mechanisms were inspired[41] by the famous optically addressable solid-state electron spin qubits, such as nitrogen vacancy centers in diamond[42,43] and the divacancies in the 4H polytype of silicon carbide.[44] Alternatively, single qubit control may be pursued through the spatial resolution offered by metal organic frameworks (MOFs).[45,46] In accordance with the variety of experimental goals and design strategies, molecular qubit candidates display substantial structural diversity (Figure 1.3). Care must be taken to determine the dominant processes responsible for decoherence under a given set of conditions.

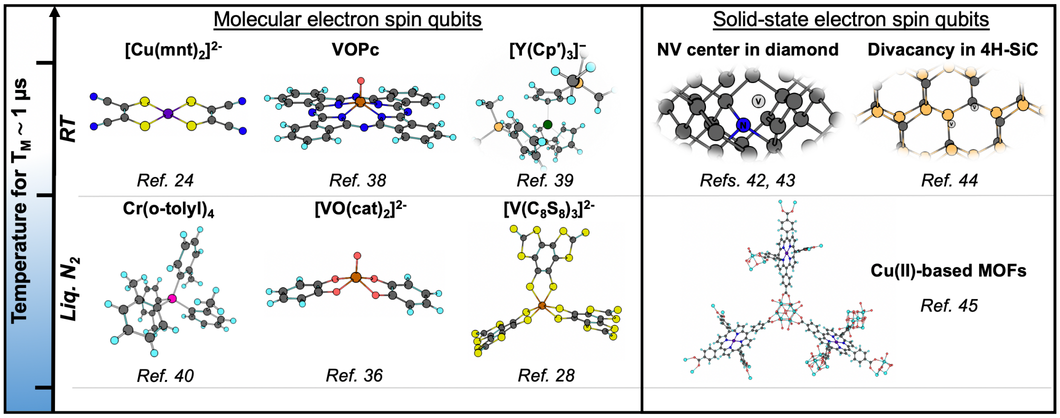

Figure 1.3: Representative electronic spin-based qubits.[24,28,36,38–40,42,44,45] Top row: representative qubits exceeding T_M = 1 μs at room temperature. Abbreviations: (mnt) = maleonitriledithiolate; VOPc = vanadyl phthalocyanine; Cp' = ($C_5H_4SiMe_3$); (cat) = catecholate. Atomic Color Scheme: Cu (purple), S (yellow), C (charcoal gray), V (orange), Cr (pink), O (red), N (blue), Si (dark yellow), H (cyan), Y (dark green).

The dominant decoherence processes of molecular qubits can be categorized into three distinct regimes: the spin-spin (Figure 1.4A), motional (Figure 1.4B), and spin-phonon limits (Figure 1.4C). In the spin-spin regime, the spin bath dominates T_M through electronic and nuclear spin flip-flops. In the motional limit, T_M is dominated by molecular tumbling (solution phase) or low amplitude librations (glassy solids), which dynamically change the portion of the anisotropic Zeeman tensor aligned with the external magnetic field. In the spin-phonon limit, T_M is limited by T_1, which is dominated by intramolecular vibrations that modulate the orbital angular momentum of the ground state. Each of the three regimes will be discussed in turn.

1.3 Spin-Spin and Motional Contributions to Decoherence

Electron spin qubits undergo decoherence in the presence of other electronic and nuclear spins in the environment due to the coupling of spin angular momenta. Electron and nuclear spins both on the qubit molecule and within the bath can undergo thermal energy-conserving flip-flops, which perturb the magnetic dipolar coupling of the electron spin qubit and induce decoherence.[47] Direct and indirect spin-spin interactions contributing to T_M are represented in Figure 1.4A. Spin-spin decoherence arises primarily through hyperfine coupling with nuclear spins in the solvent,[26,28] hyperfine coupling with nuclear spins on the ligands,[48] and direct spin flip-flops between electronic spin centers.[45,46] To minimize the latter contribution, dilution of the paramagnetic qubit in a matrix of a diamagnetic analog is a commonly

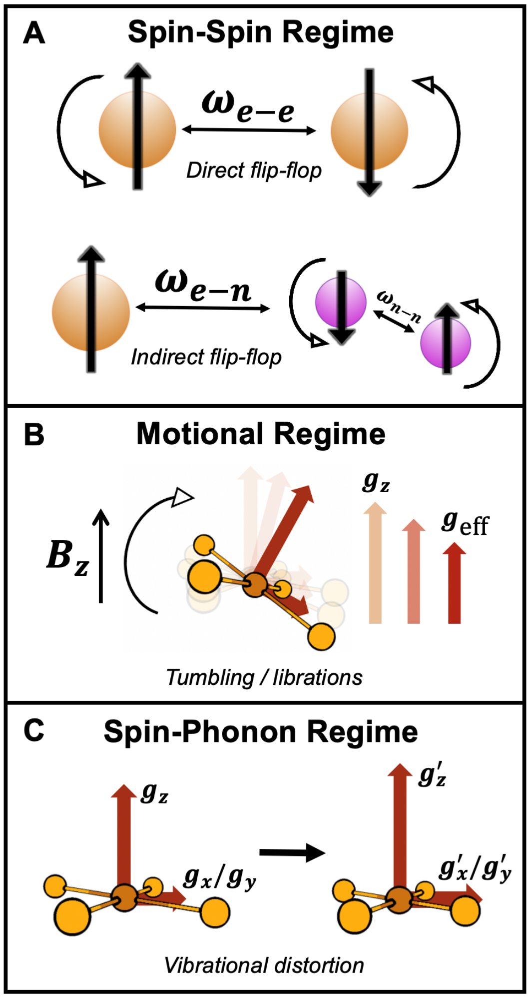

Figure 1.4: Regimes of decoherence in molecular electron spin qubits. (A) Dipolar flip-flops dominate the spin-spin decoherence regime, which occurs at low temperatures and in concentrated spin environments. Single solid black arrows represent magnetic dipole vectors, while double-headed arrows represent dipolar coupling (ω). Direct flip-flops occur when a pair of spins exchanges their spin angular momenta, while indirect flip-flops arise from interaction with nearby spin pairs. (B) Tumbling and librational dynamics characterize the motional decoherence regime, which occurs in liquids and glassy solids containing molecules with anisotropic Zeeman or hyperfine tensors. (C) Vibrationally-induced molecular distortions characterize the spin-phonon decoherence regime, which dominates at high temperatures in the solid phase.

employed strategy.[49] The suppression of hyperfine coupling is attained through nuclear-spin-free ligand scaffolds and spin-free solvents, such as carbon disulfide, which have shown great success.[28]

An additional key consideration is the spin-diffusion barrier,[50,51] in which nuclear spins that are within a 4-8 Å radius of the electron spin contribute only a small degree to decoherence.[52] Nuclei within the barrier couple strongly to the electron spin, which detunes them to other nuclei in the bath, reducing their participation in nuclear spin flip-flops. Experimental evidence for the spin-diffusion barrier has been obtained from a series of vanadyl complexes using carbon/sulfur ligand scaffolds to systematically vary the distance between the terminal hydrogens and the electron spin center.[53] Molecules containing hydrogen atoms only within 6 Å were found to have a sharp increase in coherence time, owing to strengthened coupling between the hydrogen-based nuclear spins and the vanadium-based unpaired electron. Some models for fitting T_2 data have incorporated the spin diffusion barrier radius.[26,54–56]

Additional decoherence mechanisms are possible whenever an electron spin qubit exhibits rotational and translational degrees of freedom in solutions or glasses. An ensemble of qubits with anisotropic $\boldsymbol{g}$ or $\boldsymbol{A}$ tensors can dephase through molecular rotations with respect to the applied magnetic field (Figure 1.4B), which alters the resonance frequency conditions and decreases T_M.[52] Due to the characteristic anisotropy of $\boldsymbol{g}$ and $\boldsymbol{A}$ in transition metal complexes, the T_M of transition-metal-based qubits is often more sensitive to orientation than that of organic radicals. Orientation-dependent T_M values for paramagnetic transition metal complexes in frozen solution have been attributed to small-angle librations (hindered rotations) at temperatures well below the glass-transition temperature of the frozen glasses. Such librations are not prevalent in crystals. Experimentally, strong T_M orientation dependence was observed for a Cr(V) tetratolyl-porphyin complex in the glassy state but not in crystals.[57] Orientation-dependent studies of T_M can therefore provide a selective diagnostic for librational decoherence processes. The role of the counterion structure in glasses has also been investigated. Through analyses of the temperature dependent T_M times, it was proposed that methyl rotors proximal to the electron spin have a detrimental impact on T_M.[58] However, similar T_M behavior has also been observed in systems with no methyl groups present.[49]

The well-studied class of V(IV) qubits contain experimental examples in each of the three decoherence regimes, providing for an instructive conceptual comparison. The electron spin relaxation of vanadyl phthalocyanine (VOPc) has been studied in a glassy frozen solution,[59] a pure crystalline solid,[38] and diamagnetically diluted crystalline dispersions in titanyl phthalocyanine (TiOPc) host at 1:10, 1:100, and 1:1000 concentrations.[38,49] At 300 K in 1:10 dilution, VOPc exists in the spin-spin regime, where T_M is significantly smaller than T_1 owing to electronic dipolar contributions to decoherence. However, the 1:1000 dilution displays $T_M \approx T_1$ at 300 K, indicating T_M is T_1 limited.[38] The increased dilution suppresses dipolar interactions and causes phonon contributions to dominate decoherence, moving VOPc from the spin-spin regime to the spin-phonon regime through sample preparation. Finally, the V(IV) qubit $(n{-}Bu_3NH)_2[V(C_6H_4O_2)_3]$ in a frozen glass has demonstrated 20% variation in T_M times as a function of field position, consistent with motional contributions to decoherence.[60] It is to be expected that other V(IV) qubits will demonstrate the same behavior. These examples show how sample preparation and measurement conditions can place a qubit into any one of the three decoherence regimes. Further research is needed to ascertain how spin-phonon contributions to decoherence change when a qubit moves from a crystalline to a motional environment, an effort which may prove key for applications in quantum sensing.

Crystal packing effects can also play a significant role in magnetic decoherence properties. A study comparing two different crystal packing modes of lanthanide-based nitroxide radicals showed that the structure with proximal intermolecular nitroxide spins possessed the stronger spin-spin exchange coupling.[61] Crystal packing thus modulates the strength of the spin-spin decoherence regime for magnetically undiluted crystals. Further research is required to elucidate the effect of ligand spin polarization on decoherence.

1.4 Phonon Contributions to Decoherence

In the crystalline solid phase, thermodynamic spin relaxation transfers energy to lattice phonons. At high temperatures, this relaxation process causes T_M to become T_1-limited,[62] defining the spin-phonon regime of decoherence. Two criteria must hold for spin-phonon mediated relaxation processes.[63,64] First, energy conservation must be satisfied, implying that only lattice processes matching the spin-flip energy can occur. This could arise through emission of a single phonon possessing the correct spin-flip energy (direct mechanism[16,65]), inelastic scattering of two phonons with the correct energy difference via a virtual state (Raman mechanism[16,65]), or two phonon relaxation through a real electronic excited state (Orbach mechanism[16,66]), as shown in Figure 1.5A. In dilute monometallic S = ½ qubits, contributions from the Orbach mechanism are often negligible owing to the lack of thermally accessible electronic excited states.[67] Second, there must be a nonzero transition probability for the energy to transfer from the spin to the lattice phonon, a criterion known as spin-phonon coupling. The theoretical underpinnings for spin-lattice relaxation in solids were developed by Van Vleck,[65,68] Pryce,[69] Orbach,[70] and others.[71,72]

1.4.1 Temperature Scaling

To diagnose the dominant phonon mechanism, early spin-phonon relaxation literature focused on deriving functional forms for how T_1 scales with temperature (T) and magnetic field (B). For example, treatment for S = ½ systems resulted in $1/T_1 \propto B^4T$ for the direct process and $1/T_1 \propto T^9$ and $1/T_1 \propto B^2T^7$ for the Raman process.[16] It is crucial to note, however, that these derivations use the Debye model, which describes crystal vibrations solely as acoustic phonons (i.e., displacement waves, Figure 1.5B) carrying momentum and possessing a linear dispersion relation.[73] Optical phonons (Figure 1.5B), which include the intramolecular vibrations commonly analyzed in molecular vibrational spectroscopy, are not considered in the Debye model. This assumption has two key consequences for a spin-phonon coupling model:[63,65,74] (1) relaxation takes place exclusively through scattering of acoustic phonons rather than optical phonons, and (2) the spin-phonon coupling constants for each phonon mode are equal or follow some predictable functional form, as no provision can be made for unique spin-phonon coupling for distinct intramolecular vibrations.[63] For more details on spin-phonon implications of the Debye model, see the perspective by Coronado, Gaita-Ariño and coworkers.[75]

The temperature scaling relationships derived from the Debye model often show excellent agreement with experiment for homogeneous extended solids at low temperatures, such as Tm^{2+} in alkaline earth fluorides.[76] However, the Debye model assumptions are no longer appropriate when localized molecular vibrations become thermally activated with increasing temperature. In an extended solid, such local modes may be attributed to defects in the crystal structure.[77,78] In a molecular solid, local modes correspond to optical phonons with large intramolecular vibrational character (Figure 1.5B).[73,79] Models for the temperature scaling of Raman relaxation through local modes have produced several new functional forms,[77,78] including $1/T_1 \propto T^3$, $1/T_1 \propto T^5$, and $1/T_1 \propto \exp(T)/(\exp(T)-1)^2$.

While useful as empirical tools for analyzing data, the proliferation of such functional forms points to the theoretical inability of the Debye model to describe the spin-phonon decoherence regime in molecular solids. In such materials, spin-lattice relaxation involves Raman processes with optical phonons, and the density of states for optical phonons is in general not homogeneous.[80,81] Furthermore, the

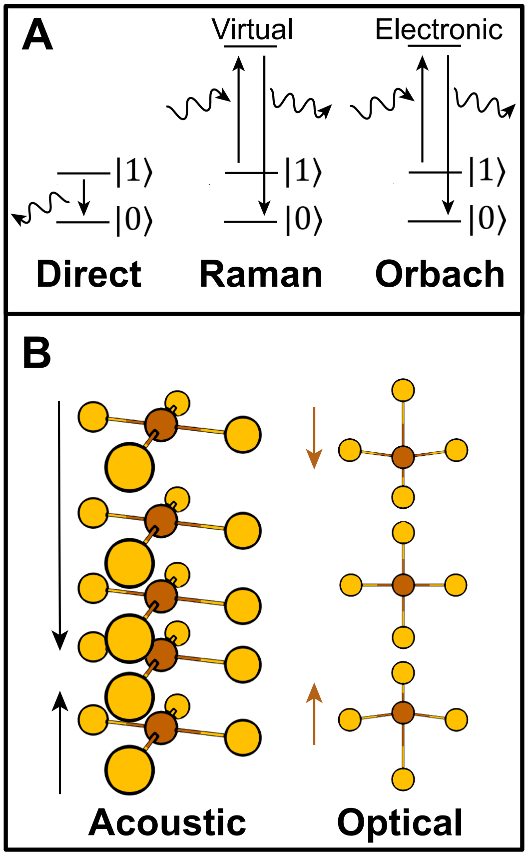

Figure 1.5: Phonon involvement in spin-lattice relaxation. (A) Mechanisms of phonon-induced relaxation. Zig-zag arrows represent phonon scattering. (B) Schematics of the two types of phonons involved in relaxation processes in molecular solids. Acoustic phonons are characterized by displacement waves, while optical phonons additionally involve intramolecular vibrations.

spin-phonon coupling terms in molecular solids may vary by orders of magnitude depending on the phonon mode under consideration.[80,82] These effects are not captured in the Debye model temperature scaling predictions, rendering deviations from experiment unsurprising.[79,83] Distinctly molecular models of spin-lattice relaxation are thus required to understand the spin-phonon regime and pinpoint the specific vibrational modes that contribute to decoherence.

1.4.2 Coupling Mechanisms

A second issue relates to the source of the spin-phonon coupling, which is a distinct consideration from the phonon mechanism (direct, Raman, Orbach). Coupling arises when phonons modulate the spin Hamiltonian; that is, $\partial \boldsymbol{H}_{spin}/\partial Q_i$ is nonzero for atomic displacements that take place along the vibrational coordinate Q_i of mode

i.[64,82] For an S = ½ qubit (Equation (1.1)), both the g-tensor ($\boldsymbol{g}$) and the hyperfine tensor ($\boldsymbol{A}$) can have significant nonzero derivatives with respect to nuclear motion along Q_i. Assuming weak coupling, this yields two types of terms contributing to the spin-phonon interaction:[64,84]

$$\frac{\partial \boldsymbol{H}_{spin}}{\partial Q_i} = \mu_e \boldsymbol{B_0} \cdot \frac{\partial \boldsymbol{g}}{\partial Q_i} \cdot \widehat{\boldsymbol{S}} + \widehat{\boldsymbol{S}} \cdot \frac{\partial \boldsymbol{A}}{\partial Q_i} \cdot \widehat{\boldsymbol{I}}. \tag{1.2}$$

Equation (1.2) gives first-order spin-phonon coupling terms for the direct process.[84] Mixed partial derivatives relate to the Raman process, but the magnitudes of the mixed partial derivatives are expected to trend similarly to the first derivatives.[80] Each phonon mode has unique spin-phonon coupling terms, which may be either zero or non-zero. Owing to larger modulations of the first coordination sphere of the spin bearing metal ion (Figure 1.5B), optical phonons exhibit much larger spin-phonon coupling terms than acoustic phonons.[64] Optical phonons therefore dominate spin-lattice relaxation when the temperature is high enough for their thermal population. Optical bands may be approximated by molecular vibrations at the gamma point (zero phonon momentum), enabling description of the Raman process solely through molecular quantities.[80] An active area of research seeks to understand the physical origins (i.e., molecular geometry and bonding) of the magnitudes of spin-phonon coupling coefficients under different experimental conditions.[64,82,85,86] For example, a recent study of the S = ½ organometallic [Cp(Ti)(cot)] complex found that it possesses a surprisingly long T_M, attributed to weak spin-phonon coupling with the d_{z^2} ground state.[87]

1.4.3 New Models

Two recent complementary approaches that go beyond the Debye model have gained new insights into relaxation in the spin-phonon regime. First, the *ab initio* spin dynamics approach of Lunghi, Sanvito, Sessoli, and coworkers seeks to computationally predict T_1 from the full phonon dispersion relation, calculating the unique spin-phonon coupling contribution from each phonon mode across the entire Brillioun zone. The predicted temperature scalings for T_1 are a good match for available experimental data.[64,83,84] A key breakthrough in high temperature spin-lattice relaxation modeling was achieved by using machine learning to predict the $\boldsymbol{g}$ and $\boldsymbol{A}$ tensor values as a function of molecular geometry.[83,84] This made second-order numerical differentiation of the $\boldsymbol{g}$ and $\boldsymbol{A}$ tensors computationally tractable for the first time, enabling *ab initio* prediction of the Raman relaxation processes dominating at high temperature.[84] Additionally, four-dimensional inelastic neutron scattering was recently used to map the phonon dispersion of a transition metal qubit, providing an experimental calibration of the phonon states responsible for magnetic relaxation.[88] The *ab initio* spin dynamics approach rigorously considers all spin-phonon coupling coefficients, but places less emphasis on interpreting the electronic structure origins of the $\boldsymbol{g}$ and $\boldsymbol{A}$ tensor derivatives.

A second approach uses ligand field theory and molecular vibrations to understand the origins of the dynamic Hamiltonian tensor values.[82,89] This method provides a chemical explanation of the factors responsible for spin-phonon coupling, along with a mode-by-mode description of which molecular vibrations contribute the most to decoherence across different coordination geometries and electronic structures. Such a description enables targeted molecular design focused on specific vibrational modes rather than the unspecific "rigidity" descriptor of the Debye model.[75] The ligand field method is outlined in the following section.

1.5 Dynamic Ligand Fields in Electron Spin Qubits

The ground states of free transition metal ions have intrinsic in-state orbital angular momentum, as the degenerate set of d orbitals can freely rotate into one another with no energy barrier. The g value in these cases can be predicted through the Landé formula and in general deviates strongly from the free-electron g value of 2.0023 (g_e). For example, a free Cu^{2+} ion with a ground state of $^2D_{5/2}$ has a predicted g value of 1.2. In the ligand fields encountered for molecular qubits, the ground state is orbitally nondegenerate, which quenches in-state orbital angular momentum. However, spin-orbit coupling between ground and excited states can reintroduce orbital angular momentum into the ground state (out-of-state orbital angular momentum). The impact on the g value from this orbital angular momentum can be expressed through the general perturbative expression for the g value of a given d electron ground state:[90]

$$g_i = g_e - 2\lambda \sum_{e \neq g} \frac{\left\langle \Psi_g \middle| \widehat{\boldsymbol{L}}_i \middle| \Psi_e \right\rangle \left\langle \Psi_e \middle| \widehat{\boldsymbol{L}}_i \middle| \Psi_g \right\rangle}{E_e}. \tag{1.3}$$

Here Ψ_g and Ψ_e represent ground and excited state wavefunctions, respectively, E_e represents the energy of Ψ_e relative to the ground state, $\widehat{\boldsymbol{L}}_i$ is an orbital angular momentum operator, and λ is the many-electron spin-orbit coupling constant. Note $\lambda = \pm\zeta_{3d}/2S$, where S is the total electron spin, ζ_{3d} is the one-electron spin-orbit coupling constant, and + and − are used for less than half filled and greater than half filled d^n shells, respectively. Taking D_{4h} $[\mathrm{CuCl_4}]^{2-}$ as an example, the g_z ($g_{\|}$) value is modified by spin-orbit coupling between the ${}^2B_{2g}$ (d_{xy}) excited state and the ${}^2B_{1g}$ ($d_{x^2-y^2}$) ground state. Table 1.1 gives the effect of $\widehat{\boldsymbol{L}}_{\boldsymbol{i}}$ on real d orbitals and can be used in conjunction with Equation (1.3) to derive a simple formula for g_z, where a factor η is used to account for the covalencies of the donor and acceptor orbitals of the ground and excited states:[91]

$$g_z = g_e - 2\frac{\lambda\eta \left\langle x^2 - y^2 \middle| \widehat{\boldsymbol{L}}_z \middle| xy \right\rangle \left\langle xy \middle| \widehat{\boldsymbol{L}}_z \middle| x^2 - y^2 \right\rangle}{E_{B_{2g}}} = g_e - \frac{8\lambda\eta}{E_{B_{2g}}}. \tag{1.4}$$

$\widehat{\boldsymbol{L}}_{\boldsymbol{x}}$	$\widehat{\boldsymbol{L}}_{\boldsymbol{y}}$	$\widehat{\boldsymbol{L}}_{z}$
$\widehat{\boldsymbol{L}}_{\boldsymbol{x}} d_{xz} = -id_{xy}$	$\widehat{\boldsymbol{L}}_{\boldsymbol{y}} d_{xz} = id_{x^2-y^2} - i\sqrt{3}d_{z^2}$	$\widehat{\boldsymbol{L}}_{\boldsymbol{z}} d_{xz} = id_{yz}$
$\widehat{\boldsymbol{L}}_{\boldsymbol{x}} d_{yz} = i\sqrt{3}d_{z^2} + id_{x^2-y^2}$	$\widehat{\boldsymbol{L}}_{\boldsymbol{y}} d_{yz} = id_{xy}$	$\widehat{\boldsymbol{L}}_{\boldsymbol{z}} d_{yz} = -id_{xz}$
$\widehat{\boldsymbol{L}}_{\boldsymbol{x}} d_{xy} = id_{xz}$	$\widehat{\boldsymbol{L}}_{\boldsymbol{y}} d_{xy} = -id_{yz}$	$\widehat{\boldsymbol{L}}_{\boldsymbol{z}} d_{xy} = -2id_{x^2-y^2}$
$\widehat{\boldsymbol{L}}_{\boldsymbol{x}} d_{x^2-y^2} = -id_{yz}$	$\widehat{\boldsymbol{L}}_{\boldsymbol{y}} d_{x^2-y^2} = -id_{xz}$	$\widehat{\boldsymbol{L}}_{\boldsymbol{z}} d_{x^2-y^2} = 2id_{xy}$
$\widehat{\boldsymbol{L}}_{\boldsymbol{x}} d_{z^2} = -i\sqrt{3}d_{yz}$	$\widehat{\boldsymbol{L}}_{\boldsymbol{y}} d_{z^2} = i\sqrt{3}d_{xz}$	$\widehat{\boldsymbol{L}}_{\boldsymbol{z}} d_{z^2} = 0$

Table 1.1: Application of orbital angular momentum operators to the real d-orbitals.

It should be noted that the η parameter can be derived from the spin densities of the metal ion and ligating atoms: a lower spin density on the metal center indicates a more covalent interaction, in which less spin on the metal is available to spin-orbit couple with d-d excited states. This proxy for covalency therefore takes into account the delocalization of spin density with the ligating environment. An important assumption here is that λ for the metal ion is much greater than that of the ligands, which justifies treating spin-orbit coupling only in the d-d manifold. The error in this approximation increases when heavy ligand atoms are present. However, contributions from ligand-based spin-orbit coupling may be incorporated into the model.

To minimize spin-phonon coupling, $\partial \boldsymbol{g}/\partial Q$ should be as small as possible (Equation (1.2)). By differentiating Equation (1.4) with respect to the ith vibrational coordinate, we obtain an analytical expression for the spin-phonon coupling coefficient for g_z:[82]

$$\frac{\partial g_z}{\partial Q_i} = 8\lambda \frac{\eta\left(\frac{\partial E_{B_{2g}}}{\partial Q_i}\right) - E_{B_{2g}}\left(\frac{\partial \eta}{\partial Q_i}\right)}{\left(E_{B_{2g}}\right)^2}. \tag{1.5}$$

The logic behind the ligand field model of decoherence is summarized in Figure 1.6. As was previously shown, the spin-phonon coupling coefficients for a wide variety of molecular electron spin qubits qualitatively track with increased T_M in the spin-phonon decoherence regime.[82] Crucially, Equation (1.5) expresses these coefficients in terms of spectroscopically observable and computationally accessible quantities: d-d ligand field transition energies $E_{B_{2g}}$, ligand-metal covalencies (η), and the many-electron spin-orbit coupling constant of the metal ion (λ). The energies of ligand field excited states of first-row transition metal complexes can be quantified by a combination of electronic absorption[91] and magnetic circular dichroism (MCD) spectroscopies.[92] However, highly covalent ligand-metal bonds, which are often present in molecular qubit candidates, can lead to low-energy, high-intensity charge transfer transitions. These, together with intra-ligand molecular excited states with large dipole allowed intensities (e.g., Soret and Q-bands in porphyrins and phthalocyanines), can obscure ligand field transitions even when using low temperature MCD. X-ray spectroscopies provide powerful approaches to overcome these limitations by gaining metal-centric electronic structure insights in highly covalent systems. For example, the covalencies of ligand-metal bonds can be quantified using metal L-edge[93,94] and ligand K-edge[95] X-ray absorption spectroscopies. Additionally, 2p3d resonant inelastic X-ray scattering (RIXS) can be utilized to directly measure spin-allowed and spin-forbidden ligand field excited state energies.[96,97] 1s2p RIXS can also provide L-edge-like data using hard X-rays through constant incident energy (CIE) cuts taken within the 1s-3d K pre-edge.[98] Therefore, combining inorganic electronic spectroscopies with the dynamic ligand field model can provide a quantitative experimental basis for understanding bonding and electronic structure contributions to molecular qubit coherence times.

Equation (1.5) suggests two approaches for engineering long coherence times in molecular electron spin qubits. First, the overall ground state orbital angular momentum can be minimized, as $\partial \boldsymbol{g}/\partial Q$ is lessened when g is small initially. This can occur by (1) decreasing the spin-orbit coupling constant, (2) increasing the excited state energy separation, (3) increasing the covalencies of ligand-metal bonds, or (4) engineering a ground state wave function that cannot engage in excited state spin-orbit coupling. Consideration of the d orbital rotations enables the latter strategy

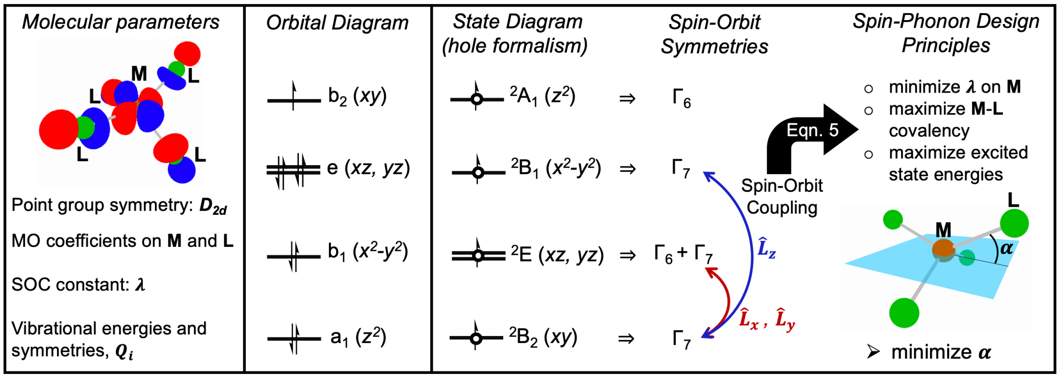

Figure 1.6: A general ligand field theory method for predicting decoherence in the spin-phonon regime from equilibrium molecular parameters (example: D_{2d} d^9 ML_4 complex). A molecular orbital diagram containing metal d-based orbitals can be mapped to a state diagram, and spin-orbit coupling contributions can be evaluated using the corresponding double group (shown in Bethe notation) to obtain molecular g values. With the aid of Equation (1.5), minimization of $\partial \boldsymbol{g}/\partial Q$ for the lowest-energy bending mode can be achieved by obtaining a planar equilibrium geometry (see also Figure 1.7).

through direct evaluation of orbital angular momentum matrix elements for S = ½ qubits. As shown in Table 1.1, the d_{z^2} orbital cannot rotate into any other d orbital about the z-axis, so a molecule with a d_{z^2} ground state should exhibit small spin-phonon coupling with the g_z transition. Experimentally, a yttrium complex with a partially covalent 4d_{z^2}/5s-based ground state demonstrated a μs T_M at room temperature, despite featuring ligands with nuclear spins, unoptimized magnetic dilution, and a non-rigid ligand framework.[39] This example establishes minimizing ground state orbital angular momentum as a powerful design principle for engineering molecular qubits within the spin-phonon decoherence regime.

Second, the magnitude of the vibrational derivatives can be directly decreased by employing ligand frameworks with few vibrational modes that can undergo spin-phonon coupling.[48,82] This can be accomplished by either (1) reducing the vibrational density of states at low energies,[62] as thermal phonon occupation is required for the Raman relaxation process, or (2) tailoring the coordination geometry to reduce spin-phonon coupling by symmetry.[48] Dynamic ligand field analysis of a $[CuCl_4]^{2-}$ model compound has illuminated how vibrational symmetry can engender an optimal coordination geometry for S = ½ Cu(II) qubits.[82] Depending on the counterion, $[CuCl_4]^{2-}$ can adopt a square planar (D_{4h}) or distorted tetrahedral (D_{2d}) crystal geometry.[99] These two structures are directly related by a low-energy bending mode (Figure 1.7A). Analyses of the ground and excited state potential energy surfaces (PESs) along this coordinate provide insight into the electronic structure origins of spin-phonon coupling over different structures. For example, at the D_{4h} geometry, there is no excited state distortion and therefore no excited state linear coupling term (Figure 1.7B, dashed blue line). The absence of linear excited state coupling eliminates linear spin-phonon coupling in the ground state. For D_{2d}, however, the excited state PES is shifted relative to the ground state (i.e., there is an excited state distorting force), giving rise to a non-zero excited state linear coupling term for the D_{2d} structure. This provides a mechanism for the amount of orbital angular momentum mixed into the D_{2d} ground state to dynamically fluctuate along Q_i (Figure 1.7B-C). This analysis demonstrates that new vibrational modes can be activated for spin-phonon coupling upon small modifications of the coordination geometry.[100–102]

Density functional theory (DFT) calculations confirm that the D_{4h} $[\mathrm{CuCl_4}]^{2-}$ g_z value exhibits linear spin-phonon coupling along only the totally symmetric stretching mode (i.e., breathing mode). However, upon distorting to the D_{2d} geometry, the bending distortion mode changes in symmetry from b_{2u} (in D_{4h}) to a_1 (in D_{2d}), thus activating it for linear spin-phonon coupling (Figure 1.7F). The spin-phonon coupling (arrow size) clearly increases as the distortion angle α departs from 180° and the slope of the g_z surface (i.e., $\partial g_z/\partial Q_\alpha$) increases. At $\alpha = 180°$, the surface flattens as linear spin-phonon coupling in the bending mode is removed. Examination of the covalency (Figure 1.7D) and excited state energies (Figure 1.7E) shows these quantities correlate strongly with the g_z value, as expected on the basis of Equations (1.4) and (1.5).[82] This model explains why Cu(II) transition metal complexes with the longest T_1 times host a square planar geometry around the metal center, while tetrahedrally distorted complexes exhibit shorter T_1 times.[79] While vibrational symmetry effects have so far been investigated in the context of discrete molecular qubits,[48] such strategies will likely also prove important in designing arrays of qubits in MOFs, where a large density of low-energy phonons leads to enhanced spin-phonon coupling.[45,46]

Notably, the gas phase equilibrium geometries of four-coordinate Cu(II) complexes are D_{2d}. However, ligand field strain through crystal packing effects can enforce geometries that would otherwise be out of equilibrium, similar to the concept of the entatic state in bioinorganic chemistry.[99,103] Cu complexes featuring symmetry- and distortion-altering intramolecular steric interactions have also been developed.

These interactions can strongly influence ground state redox potentials and reorganization energies, as well as the lifetimes of metal-to-ligand charge transfer excited states for Cu(I).[101,102,104] Similar ligand design approaches will enable systematic evaluation of how ligand field strain and secondary coordination sphere interactions contribute to coherence times Cu(II) qubit candidates.

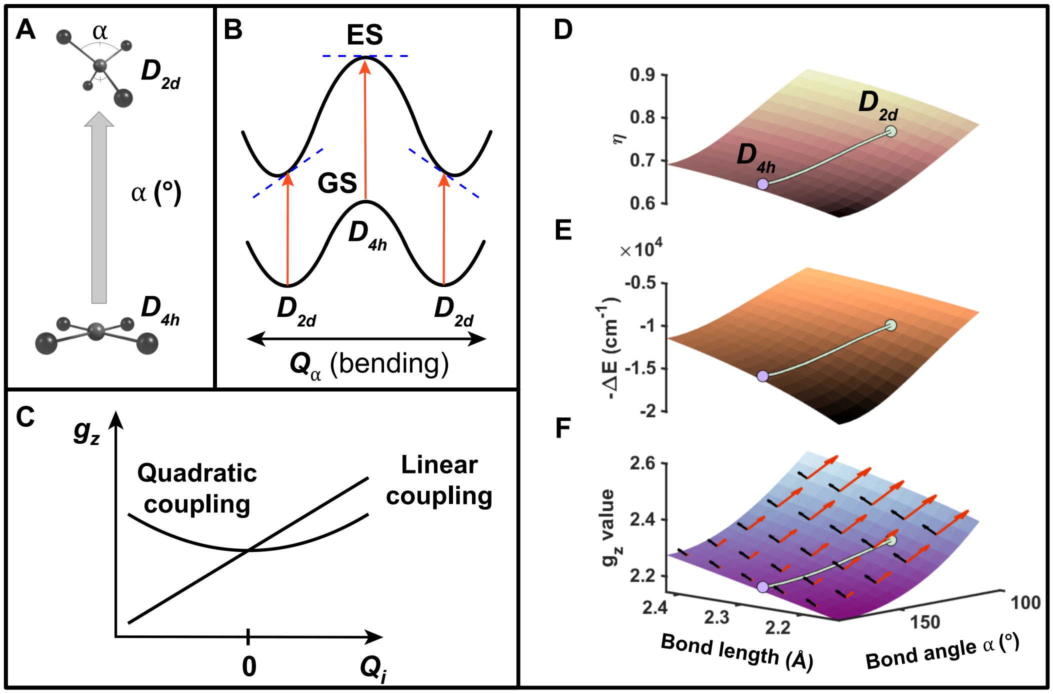

Figure 1.7: Effect of geometric distortion on spin-phonon coupling terms. (A) $[CuCl_4]^{2-}$ bending distortion from a D_{4h} to D_{2d} geometry, given by bond angle α. (B) Linear excited state coupling terms (dashed blue lines) give rise to ground state linear spin-phonon coupling terms. The ground and excited state equilibrium geometry mismatch at D_{2d} leads to linear coupling for the bending mode, while no such mismatch occurs in D_{4h}. (C) Linear versus quadratic spin-phonon coupling. X-axis tick represents ground state equilibrium geometry. (D) Variation of metal orbital contribution (1 - covalency) in $[CuCl_4]^{2-}$ as a function of geometry. (E) Variation of first excited state energy in $[CuCl_4]^{2-}$ as a function of geometry. (F) Variation of g_z in $[CuCl_4]^{2-}$ as a function of geometry. Arrows give the spin-phonon coupling terms along the symmetric stretch (black) and bending (red) modes, which correlate to the components of the g_z gradient. Symmetry coordinate mixing in the normal modes is less than 2%. Adapted from Ref.[82].

The interplay between factors in the dynamic ligand field model can be illustrated by recent studies comparing Cu(II) and V(IV) S = ½ qubit candidates.[49,62] It was experimentally shown that the T_1 of vanadyl phthalocyanine (VOPc) is longer than that of copper phthalocyanine (CuPc) at higher temperatures (>25 K) where the spin-phonon regime dominates,[49] with VOPc exhibiting coherence up to room temperature.[38] These results can be rationalized and quantitatively understood using the spin-phonon coupling factors found in Equation (1.5): (1) the energy of the ligand field excited state that spin-orbit couples with the ground state, (2) the covalencies of the ligand-metal bonds, and (3) the spin-orbit coupling constant. To the best of our knowledge, the specific ligand field transition contributions to the g values of CuPc and VOPc are not known experimentally, likely due to the intense, dominant intra-Pc contributions to the electronic absorption spectrum. For g_z, they were calculated to be similar in energy (22,165 and 22,745 cm^{-1}, respectively[82]), so (1) is likely not the distinguishing factor between CuPc and VOPc. Ligand-metal covalency in the ground state wave function is significantly larger in CuPc relative to VOPc, but this would suggest a longer coherence time for CuPc, so (2) is not the distinguishing factor. Thus, in the comparison between Cu(II) and V(IV)O in the same equatorial ligand set, the significantly reduced spin-orbit coupling constant of V(IV) in VOPc is of critical importance. Indeed, DFT calculations show that spin-phonon coupling coefficients between comparable vibrational modes of CuPc and VOPc differ primarily by the ratio of the spin-orbit coupling constants.[82]

In a comparison between four-coordinate $[\mathrm{Cu(II)(bdt)_2}]^{2-}$ (bdt=benzene-1,2-dithiolate) and six-coordinate $[\mathrm{V(IV)(bdt)_3}]^{2-}$, the observation of longer electron spin relaxation for the former was ascribed to increased covalency of the Cu(II)-S bonds. Interestingly, this is opposite of the behavior observed for CuPc vs VOPc, where longer coherence times were observed for the more ionic ground state. While $[\mathrm{Cu(bdt)_2}]^{2-}$ is square planar, $[\mathrm{V(bdt)_3}]^{2-}$ adopts a pseudo-octahedral coordination geometry and was calculated to have seventeen linear spin-phonon coupling active vibrational modes below 400 cm^{-1} for g_z; square planar $[\mathrm{Cu(bdt)_2}]^{2-}$ has only one for g_z.[82] Additionally, lower energy excited states in the six-coordinate V(IV) complexes, which increase ground state orbital angular momentum and thus sensitivity to spin-phonon coupling, may also be of critical importance for determining relaxation times. Thus, based on the ligand field theory model, the shorter coherence time in the six-coordinate V(IV) complex arises from increased spin-phonon coupling relative to the Cu(II) complex due to the different coordination environment, despite the lower spin-orbit coupling constant of the former. While substitution of sulfur with selenium in the ligands (forming benzene-1,2-diselenate, bds) increases the ligand-metal covalency, T_1 values were experimentally observed to decrease for both Cu(II) and V(IV). This likely arises because the heavy atom substitution decreases the frequency of the spin-phonon coupling active vibrational modes, thereby increasing the thermal population and total spin-phonon coupling, even though the spin-phonon coupling coefficient itself may decrease due to increased covalency.[62,82] An additional factor to consider is the significantly increased spin-orbit coupling constant of selenium relative to sulfur, which will also contribute to accelerated relaxation. The considerations in this Section demonstrate the critical importance of evaluating dynamic ligand field properties when comparing coherence times between different molecular qubit candidates, especially if they feature different first coordination spheres.

The ligand field model of spin-phonon coupling as described is general for understanding couplings in any S = ½ system. It has also been adapted for studying S > ½ systems. Here, modulation of $\boldsymbol{D}$ and $\boldsymbol{E}$ in the zero-field splitting Hamiltonian along vibrational coordinates enables a description of excited state intersystem crossing and single molecule magnet relaxation.[105] Further extensions of the ligand field model are possible to also account for hyperfine contributions[64] ($\partial \boldsymbol{A}/\partial Q$) to spin-lattice relaxation.

1.6 Summary and Outlook

The study of electron spin relaxation has a rich history and much is known. However, further understanding decoherence mechanisms at the molecular level is a key step towards the development of quantum technologies that can employ the versatility and tunability of coordination complexes. Here we have leveraged the idea of coherence regimes to highlight specific molecular contributions to decoherence. It is clear that the conditions (temperature, solid/solution phase) of the desired quantum application (computing/sensing) will define the specific design principles. In the spin-spin decoherence regime, decreasing spin-spin interactions through magnetic dilution and decreasing the concentration or gyromagnetic ratios of nuclear spins has the largest impact on prolonging T_M. In the motional regime, molecular tumbling and librational dynamics alter the resonance frequency conditions and decrease T_M. At higher temperatures in the solid state, T_M is limited by T_1. We find this spin-phonon regime particularly exciting, as it provides a means for fundamental studies of how specific atomic motions are coupled to dynamic electronic structure changes. These considerations are also crucial for understanding time-dependent magnetization phenomena beyond quantum information science, including single-molecule magnetism, spin crossover complexes, and the kinetics of photomagnetic processes. From considering dynamic ligand fields, several strategies for minimizing spin-phonon coupling have been characterized and applied to experimental case studies. It is important to note, however, that the specific molecular vibration(s) that are responsible for decoherence in the spin-phonon regime have yet to be experimentally assigned. In the future, we anticipate that the dynamic ligand field model will provide an analytical link between molecular vibrations and temperature dependent electron spin relaxation rates. This will facilitate experimental assignment of the decoherence-inducing vibrations, allowing for a more tailored synthetic design approach to prolonging T_M.

Careful examination of the various decoherence mechanisms also provides insights into applications beyond quantum computing. These considerations extend nicely to the development of qubits as molecular quantum sensors (qusors), which provide several attractive features: (1) the ability to target local regions of space on a molecular level, (2) novel coherence-based sensing mechanisms, and (3) a platform for fundamental studies of coherence in chemical microenvironments formed on electrode interfaces or in biological systems. In solution phases, including cases where qusors are immobilized on surfaces or bound to larger macromolecular structures (e.g., proteins), the magnitude of motional contributions to decoherence will be important to consider. By tailoring the ground state orbital angular momentum anisotropy and the molecular vibrations, it will be possible to design qusors that selectively sense rotational versus vibrational degrees of freedom and vice-versa, providing new insight into molecular dynamics in chemical microenvironments. Ligand sets with peripheral H-bond donors and acceptors may also provide a strategy to “lock-in” a specific molecular orientation and limit motional contributions. Additionally, it may be possible to sense the local electric fields in chemical microenvironments through their effects on T_1 and T_M, lending insight into the functional role of the local electrostatic environment. Previous work by Mims has shown that electron spin precession can be perturbed by an external electric field.[106] Electric field sensing has already been accomplished using solid state systems such as nitrogen vacancies in diamond,[9,107] but solid state sensors have inherently limited spatial resolution and tunability. An exciting molecular engineering challenge will be to tune and enhance qusor electric field sensitivity through noncentrosymmetric perturbations manifesting in odd parity ligand field components,[106] while still minimizing spin-phonon coupling. This level of detailed understanding will derive from incorporating electric field effects into the dynamic ligand field model and learning to describe and control vibrational symmetry, which remains an outstanding challenge in engineering molecular electron spin qubits.

While many approaches to prolonging coherence times have sought to make qubit frameworks more rigid, there are a variety of important geometric and electronic structure factors that are not captured by this description. Detailed ligand field analyses coupled to high-resolution inorganic spectroscopies are called for to understand the role of molecular "rigidity" and symmetry by defining the precise vibrational modes that contribute to spin-phonon coupling and tuning their frequencies through synthetic design strategies. This level of new molecular insight will guide fundamental studies of spin-phonon coupling over a broad range of one-, two-, and three-dimensional S = ½ systems, as well as the development of electron spin qubit and qusor constructs for use in quantum technologies.

References

[1] Dowling, J. P.; Milburn, G. J. Quantum Technology: The Second Quantum Revolution. *Philosophical Transactions: Mathematical, Physical and Engineering Sciences* **2003**, *361,* 1655–1674.

[2] Wasielewski, M. R. *et al.* Exploiting Chemistry and Molecular Systems for Quantum Information Science. *Nature Reviews Chemistry* **2020**, *4,* 490–504.

[3] Nielsen, M. A.; Chuang, I. L. *Quantum Computation and Quantum Information: 10th Anniversary Edition;* Cambridge University Press: Cambridge, 2010. DOI: 10.1017/CBO9780511976667.

[4] Schweiger, A.; Jeschke, G. *Principles of Pulse Electron Paramagnetic Resonance;* Oxford University Press: Oxford, UK; New York, 2001.

[5] Cimatti, I.; Bondì, L.; Serrano, G.; Malavolti, L.; Cortigiani, B.; Velez-Fort, E.; Betto, D.; Ouerghi, A.; B. Brookes, N.; Loth, S.; Mannini, M.; Totti, F.; Sessoli, R. Vanadyl Phthalocyanines on Graphene/SiC(0001): Toward a Hybrid Architecture for Molecular Spin Qubits. *Nanoscale Horizons* **2019**, *4,* 1202–1210.

[6] Cardona-Serra, S.; Gaita-Ariño, A. Vanadyl Dithiolate Single Molecule Transistors: The Next Spintronic Frontier? *Dalton Transactions* **2018**, *47,* 5533–5537.

[7] Urtizberea, A.; Natividad, E.; Alonso, P. J.; Pérez-Martínez, L.; Andrés, M. A.; Gascón, I.; Gimeno, I.; Luis, F.; Roubeau, O. Vanadyl Spin Qubit 2D Arrays and their Integration on Superconducting Resonators. *Materials Horizons* **2020**, *7,* 885–897.

[8] Bonizzoni, C.; Ghirri, A.; Atzori, M.; Sorace, L.; Sessoli, R.; Affronte, M. Coherent Coupling Between Vanadyl Phthalocyanine Spin Ensemble and

Microwave Photons: Towards Integration of Molecular Spin Qubits into Quantum Circuits. *Scientific Reports* **2017**, *7,* 13096.

[9] Dolde, F.; Fedder, H.; Doherty, M. W.; Nöbauer, T.; Rempp, F.; Balasubramanian, G.; Wolf, T.; Reinhard, F.; Hollenberg, L. C. L.; Jelezko, F.; Wrachtrup, J. Electric-Field Sensing Using Single Diamond Spins. *Nature Physics* **2011**, *7,* 459–463.

[10] Kucsko, G.; Maurer, P. C.; Yao, N. Y.; Kubo, M.; Noh, H. J.; Lo, P. K.; Park, H.; Lukin, M. D. Nanometre-Scale Thermometry in a Living Cell. *Nature* **2013**, *500,* 54–58.

[11] Mamin, H. J.; Kim, M.; Sherwood, M. H.; Rettner, C. T.; Ohno, K.; Awschalom, D. D.; Rugar, D. Nanoscale Nuclear Magnetic Resonance with a Nitrogen-Vacancy Spin Sensor. *Science* **2013**, *339,* 557–560.

[12] Hensen, B. *et al.* Loophole-Free Bell Inequality Violation Using Electron Spins Separated by 1.3 Kilometres. *Nature* **2015**, *526,* 682–686.

[13] Yu, Y. *et al.* Entanglement of Two Quantum Memories via Fibres over Dozens of Kilometres. *Nature* **2020**, *578,* 240–245.

[14] Abobeih, M. H.; Randall, J.; Bradley, C. E.; Bartling, H. P.; Bakker, M. A.; Degen, M. J.; Markham, M.; Twitchen, D. J.; Taminiau, T. H. Atomic-Scale Imaging of a 27-Nuclear-Spin Cluster Using a Quantum Sensor. *Nature* **2019**, *576,* 411–415.

[15] Graham, M. J.; Zadrozny, J. M.; Fataftah, M. S.; Freedman, D. E. Forging Solid-State Qubit Design Principles in a Molecular Furnace. *Chemistry of Materials* **2017**, *29,* 1885–1897.

[16] Standley, K. J.; Vaughan, R. A. *Electron Spin Relaxation Phenomena in Solids;* Springer US: Boston, MA, 1969. DOI: 10.1007/978-1-4899-6539-4.

[17] DiVincenzo, D. P. The Physical Implementation of Quantum Computation. *Fortschritte der Physik* **2000**, *48,* 771–783.

[18] Bloch, F. Nuclear Induction. *Physical Review* **1946**, *70,* 460–474.

[19] Kurshev, V. V.; Raitsimring, A. M. Carr-Purcell Train in the Conditions of Partial Excitation of Magnetic Resonance Spectrum. *Journal of Magnetic Resonance (1969)* **1990**, *88,* 126–129.

[20] Witzel, W. M.; Sarma, S. D. Multiple-Pulse Coherence Enhancement of Solid State Spin Qubits. *Physical Review Letters* **2007**, *98,* 077601.

[21] Morton, J. J. L.; Tyryshkin, A. M.; Brown, R. M.; Shankar, S.; Lovett, B. W.; Ardavan, A.; Schenkel, T.; Haller, E. E.; Ager, J. W.; Lyon, S. A. Solid-State Quantum Memory Using the ^{31}P Nuclear Spin. *Nature* **2008**, *455,* 1085–1088.

[22] Bluhm, H.; Foletti, S.; Neder, I.; Rudner, M.; Mahalu, D.; Umansky, V.; Yacoby, A. Dephasing Time of GaAs Electron-Spin Qubits Coupled to a Nuclear Bath Exceeding 200 μs. *Nature Physics* **2011**, *7,* 109–113.

[23] Breuer, H.-P.; Petruccione, F. *The Theory of Open Quantum Systems;* Oxford University Press: Oxford, 2007.

[24] Bader, K.; Dengler, D.; Lenz, S.; Endeward, B.; Jiang, S.-D.; Neugebauer, P.; van Slageren, J. Room Temperature Quantum Coherence in a Potential Molecular Qubit. *Nature Communications* **2014**, *5,* 5304.

[25] Graham, M. J.; Zadrozny, J. M.; Shiddiq, M.; Anderson, J. S.; Fataftah, M. S.; Hill, S.; Freedman, D. E. Influence of Electronic Spin and Spin–Orbit Coupling on Decoherence in Mononuclear Transition Metal Complexes. *Journal of the American Chemical Society* **2014**, *136,* 7623–7626.

[26] Yu, C.-J.; Graham, M. J.; Zadrozny, J. M.; Niklas, J.; Krzyaniak, M. D.; Wasielewski, M. R.; Poluektov, O. G.; Freedman, D. E. Long Coherence Times in Nuclear Spin-Free Vanadyl Qubits. *Journal of the American Chemical Society* **2016**, *138,* 14678–14685.

[27] Graham, M. J.; Krzyaniak, M. D.; Wasielewski, M. R.; Freedman, D. E. Probing Nuclear Spin Effects on Electronic Spin Coherence via EPR Measurements of Vanadium(IV) Complexes. *Inorganic Chemistry* **2017**, *56,* 8106–8113.

[28] Zadrozny, J. M.; Niklas, J.; Poluektov, O. G.; Freedman, D. E. Millisecond Coherence Time in a Tunable Molecular Electronic Spin Qubit. *ACS Central Science* **2015**, *1,* 488–492.

[29] Ardavan, A.; Rival, O.; Morton, J. J. L.; Blundell, S. J.; Tyryshkin, A. M.; Timco, G. A.; Winpenny, R. E. P. Will Spin-Relaxation Times in Molecular Magnets Permit Quantum Information Processing? *Physical Review Letters* **2007**, *98,* 057201.

[30] Bader, K.; Schlindwein, S. H.; Gudat, D.; Slageren, J. Molecular Qubits Based on Potentially Nuclear-Spin-Free Nickel Ions. *Physical Chemistry Chemical Physics* **2017**, *19,* 2525–2529.

[31] Jackson, C. E.; Lin, C.-Y.; Johnson, S. H.; Tol, J.; Zadrozny, J. M. Nuclear-Spin-Pattern Control of Electron-Spin Dynamics in a Series of V(IV) Complexes. *Chemical Science* **2019**, *10,* 8447–8454.

[32] Shiddiq, M.; Komijani, D.; Duan, Y.; Gaita-Ariño, A.; Coronado, E.; Hill, S. Enhancing Coherence in Molecular Spin Qubits via Atomic Clock Transitions. *Nature* **2016**, *531,* 348–351.

[33] Ghosh, S.; Datta, S.; Friend, L.; Cardona-Serra, S.; Gaita-Ariño, A.; Coronado, E.; Hill, S. Multi-Frequency EPR Studies of a Mononuclear Holmium Single-Molecule Magnet Based on the Polyoxometalate $[Ho^{III}(W_5O_{18})_2]^{9-}$. *Dalton Transactions* **2012**, *41,* 13697–13704.

[34] Zadrozny, J. M.; Gallagher, A. T.; Harris, T. D.; Freedman, D. E. A Porous Array of Clock Qubits. *Journal of the American Chemical Society* **2017**, *139,* 7089–7094.

[35] Giménez-Santamarina, S.; Cardona-Serra, S.; Clemente-Juan, J. M.; Gaita-Ariño, A.; Coronado, E. Exploiting Clock Transitions for the Chemical Design of Resilient Molecular Spin Qubits. *Chemical Science* **2020**, *11,* 10718–10728.

[36] Atzori, M.; Benci, S.; Morra, E.; Tesi, L.; Chiesa, M.; Torre, R.; Sorace, L.; Sessoli, R. Structural Effects on the Spin Dynamics of Potential Molecular Qubits. *Inorganic Chemistry* **2018**, *57,* 731–740.

[37] Atzori, M.; Morra, E.; Tesi, L.; Albino, A.; Chiesa, M.; Sorace, L.; Sessoli, R. Quantum Coherence Times Enhancement in Vanadium(IV)-based Potential Molecular Qubits: the Key Role of the Vanadyl Moiety. *Journal of the American Chemical Society* **2016**, *138,* 11234–11244.

[38] Atzori, M.; Tesi, L.; Morra, E.; Chiesa, M.; Sorace, L.; Sessoli, R. Room-Temperature Quantum Coherence and Rabi Oscillations in Vanadyl Phthalocyanine: Toward Multifunctional Molecular Spin Qubits. *Journal of the American Chemical Society* **2016**, *138,* 2154–2157.

[39] Ariciu, A.-M.; Woen, D. H.; Huh, D. N.; Nodaraki, L. E.; Kostopoulos, A. K.; Goodwin, C. A. P.; Chilton, N. F.; McInnes, E. J. L.; Winpenny, R. E. P.; Evans, W. J.; Tuna, F. Engineering Electronic Structure to Prolong Relaxation Times in Molecular Qubits by Minimising Orbital Angular Momentum. *Nature Communications* **2019**, *10,* 1–8.

[40] Bayliss, S. L.; Laorenza, D. W.; Mintun, P. J.; Kovos, B. D.; Freedman, D. E.; Awschalom, D. D. Optically Addressable Molecular Spins for Quantum Information Processing. *Science* **2020**, *370,* 1309–1312.

[41] Fataftah, M. S.; Freedman, D. E. Progress Towards Creating Optically Addressable Molecular Qubits. *Chemical Communications* **2018**, *54,* 13773–13781.

[42] Bar-Gill, N.; Pham, L. M.; Jarmola, A.; Budker, D.; Walsworth, R. L. Solid-State Electronic Spin Coherence Time Approaching One Second. *Nature Communications* **2013**, *4,* 1743.

[43] Warner, M.; Din, S.; Tupitsyn, I. S.; Morley, G. W.; Stoneham, A. M.; Gardener, J. A.; Wu, Z.; Fisher, A. J.; Heutz, S.; Kay, C. W. M.; Aeppli, G.

Potential for Spin-Based Information Processing in a Thin-Film Molecular Semiconductor. *Nature* **2013**, *503,* 504–508.

[44] Koehl, W. F.; Buckley, B. B.; Heremans, F. J.; Calusine, G.; Awschalom, D. D. Room Temperature Coherent Control of Defect Spin Qubits in Silicon Carbide. *Nature* **2011**, *479,* 84–87.

[45] Yu, C.-J.; Krzyaniak, M. D.; Fataftah, M. S.; Wasielewski, M. R.; Freedman, D. E. A Concentrated Array of Copper Porphyrin Candidate Qubits. *Chemical Science* **2019**, *10,* 1702–1708.

[46] Yu, C.-J.; von Kugelgen, S.; Krzyaniak, M. D.; Ji, W.; Dichtel, W. R.; Wasielewski, M. R.; Freedman, D. E. Spin and Phonon Design in Modular Arrays of Molecular Qubits. *Chemistry of Materials* **2020**, *32,* 10200–10206.

[47] Klauder, J. R.; Anderson, P. W. Spectral Diffusion Decay in Spin Resonance Experiments. *Physical Review* **1962**, *125,* 912–932.

[48] Santanni, F.; Albino, A.; Atzori, M.; Ranieri, D.; Salvadori, E.; Chiesa, M.; Lunghi, A.; Bencini, A.; Sorace, L.; Totti, F.; Sessoli, R. Probing Vibrational Symmetry Effects and Nuclear Spin Economy Principles in Molecular Spin Qubits. *Inorganic Chemistry* **2021**, *60,* 140–151.

[49] Follmer, A. H.; Ribson, R. D.; Oyala, P. H.; Chen, G. Y.; Hadt, R. G. Understanding Covalent versus Spin–Orbit Coupling Contributions to Temperature-Dependent Electron Spin Relaxation in Cupric and Vanadyl Phthalocyanines. *The Journal of Physical Chemistry A* **2020**, *124,* 9252–9260.

[50] Wald, L. L.; Hahn, E. L.; Lukac, M. Fluorine Spin Frozen Core in Pr^{3+}:LaF_3 Observed by Cross Relaxation. *Journal of the Optical Society of America B* **1992**, *9,* 789–793.

[51] Bloembergen, N. On the Interaction of Nuclear Spins in a Crystalline Lattice. *Physica* **1949**, *15,* 386–426.

[52] Eaton, S. S.; Eaton, G. R. Distance Measurements by CW and Pulsed EPR. In *Distance Measurements in Biological Systems by EPR*; Berliner, L. J.; Eaton, G. R.; Eaton, S. S., Eds.; Biological Magnetic Resonance Springer US: Boston, MA, 2000. DOI: 10.1007/0-306-47109-4_1.

[53] Graham, M. J.; Yu, C.-J.; Krzyaniak, M. D.; Wasielewski, M. R.; Freedman, D. E. Synthetic Approach To Determine the Effect of Nuclear Spin Distance on Electronic Spin Decoherence. *Journal of the American Chemical Society* **2017**, *139,* 3196–3201.

[54] Milov, A. D.; Salikhov, K. M.; Tsvetkov, Y. D. Phase Relaxation of Hydrogen Atoms Stabilized in Amorphous Matrices. *Fizika Tverdogo Tela* **1973**, *15,* 1187–1195.

[55] Zecevic, A.; Eaton, G. R.; Eaton, S. S.; Lindgren, M. Dephasing of Electron Spin Echoes for Nitroxyl Radicals in Glassy Solvents by Non-Methyl and Methyl Protons. *Molecular Physics* **1998**, *95,* 1255–1263.

[56] Canarie, E. R.; Jahn, S. M.; Stoll, S. Quantitative Structure-Based Prediction of Electron Spin Decoherence in Organic Radicals. *The Journal of Physical Chemistry Letters* **2020**, *11,* 3396–3400.

[57] Konda, R.; Du, J. L.; Eaton, S. S.; Eaton, G. R. Electron Spin Relaxation Rates for Nitridochromium(V) Tetratolylporphyrin and Nitridochromium(V) Octaethylporphyrin in Frozen Solution. *Applied Magnetic Resonance* **1994**, *7,* 185–193.

[58] Lin, C.-Y.; Ngendahimana, T.; Eaton, G. R.; Eaton, S. S.; Zadrozny, J. M. Counterion Influence on Dynamic Spin Properties in a V(IV) Complex. *Chemical Science* **2019**, *10,* 548–555.

[59] Bader, K.; Winkler, M.; van Slageren, J. Tuning of Molecular Qubits: Very Long Coherence and Spin-Lattice Relaxation Times. *Chemical Communications* **2016**, *52,* 3623–3626.

[60] Jackson, C. E.; Lin, C.-Y.; van Tol, J.; Zadrozny, J. M. Orientation Dependence of Phase Memory Relaxation in the V(IV) Ion at High Frequencies. *Chemical Physics Letters* **2020**, *739,* 137034.

[61] Pointillart, F.; Bernot, K.; Poneti, G.; Sessoli, R. Crystal Packing Effects on the Magnetic Slow Relaxation of Tb(III)-Nitronyl Nitroxide Radical Cyclic Dinuclear Clusters. *Inorganic Chemistry* **2012**, *51,* 12218–12229.

[62] Fataftah, M. S.; Krzyaniak, M. D.; Vlaisavljevich, B.; Wasielewski, M. R.; Zadrozny, J. M.; Freedman, D. E. Metal-Ligand Covalency Enables Room Temperature Molecular Qubit Candidates. *Chemical Science* **2019**, *10,* 6707–6714.

[63] Gatteschi, D.; Sessoli, R.; Villain, J. *Molecular Nanomagnets;* Oxford University Press: Oxford, 2006.

[64] Lunghi, A.; Sanvito, S. How Do Phonons Relax Molecular Spins? *Science Advances* **2019**, *5,* eaax7163.

[65] Van Vleck, J. H. Paramagnetic Relaxation Times for Titanium and Chrome Alum. *Physical Review* **1940**, *57,* 426–447.

[66] Orbach, R. Spin-Lattice Relaxation in Rare-Earth Salts. *Proceedings of the Royal Society of London A* **1961**, *264,* 458–484.

[67] Zhou, Y.; Bowler, B. E.; Eaton, G. R.; Eaton, S. S. Electron Spin Lattice Relaxation Rates for S = 1/2 Molecular Species in Glassy Matrices or Magnetically Dilute Solids at Temperatures between 10 and 300 K. *Journal of Magnetic Resonance* **1999**, *139,* 165–174.

[68] Van Vleck, J. H. Paramagnetic Relaxation and the Equilibrium of Lattice Oscillators. *Physical Review* **1941**, *59,* 724–729.

[69] Pryce, M. H. L.; Stevens, K. W. H. The Theory of Magnetic Resonance-Line Widths in Crystals. *Proceedings of the Physical Society. Section A* **1950**, *63,* 36–51.

[70] Orbach, R. On the Theory of Spin-Lattice Relaxation in Paramagnetic Salts. *Proceedings of the Physical Society* **1961**, *77,* 821–826.

[71] Abragam, A. *The Principles of Nuclear Magnetism;* Clarendon Press: London, 1961.

[72] Stevens, K. W. H. The Theory of Paramagnetic Relaxation. *Reports on Progress in Physics* **1967**, *30,* 189–226.

[73] Gu, L.; Wu, R. Origin of the Anomalously Low Raman Exponents in Single Molecule Magnets. *Physical Review B* **2021**, *103,* 014401.

[74] Casimir, H.; du Pré, F. Note on the Thermodynamic Interpretation of Paramagnetic Relaxation Phenomena. *Physica* **1938**, *5,* 507–511.

[75] Escalera-Moreno, L.; Baldoví, J. J.; Gaita-Ariño, A.; Coronado, E. Spin States, Vibrations and Spin Relaxation in Molecular Nanomagnets and Spin Qubits: a Critical Perspective. *Chemical Science* **2018**, *9,* 3265–3275.

[76] Sabisky, E. S.; Anderson, C. H. Spin-Lattice Relaxation of Tm^{2+} in CaF_2, SrF_2, and BaF_2. *Physical Review B* **1970**, *1,* 2028–2040.

[77] Castle, J. G.; Feldman, D. W.; Klemens, P. G.; Weeks, R. A. Electron Spin-Lattice Relaxation at Defect Sites; E Centers in Synthetic Quartz at 3 Kilo-Oersteds. *Physical Review* **1963**, *130,* 577–588.

[78] Castle, J. G.; Feldman, D. W. Resonance Modes at Defects in Crystalline Quartz. *Physical Review* **1965**, *137,* A671–A673.

[79] Fielding, A. J.; Fox, S.; Millhauser, G. L.; Chattopadhyay, M.; Kroneck, P. M.; Fritz, G.; Eaton, G. R.; Eaton, S. S. Electron Spin Relaxation of Copper(II) Complexes in Glassy Solution between 10 and 120K. *Journal of Magnetic Resonance* **2006**, *179,* 92–104.

[80] Albino, A.; Benci, S.; Tesi, L.; Atzori, M.; Torre, R.; Sanvito, S.; Sessoli, R.; Lunghi, A. First-Principles Investigation of Spin-Phonon Coupling in Vanadium-Based Molecular Spin Quantum Bits. *Inorganic Chemistry* **2019**, *58,* 10260–10268.

[81] Tesi, L.; Lunghi, A.; Atzori, M.; Lucaccini, E.; Sorace, L.; Totti, F.; Sessoli, R. Giant Spin-Phonon Bottleneck Effects in Evaporable Vanadyl-Based Molecules with Long Spin Coherence. *Dalton Transactions* **2016**, *45,* 16635–16643.

[82] Mirzoyan, R.; Hadt, R. G. The Dynamic Ligand Field of a Molecular Qubit: Decoherence through Spin-Phonon Coupling. *Physical Chemistry Chemical Physics* **2020**, *22,* 11249–11265.

[83] Lunghi, A.; Sanvito, S. Multiple Spin-Phonon Relaxation Pathways in a Kramer Single-Ion Magnet. *The Journal of Chemical Physics* **2020**, *153,* 174113.

[84] Lunghi, A.; Sanvito, S. The Limit of Spin Lifetime in Solid-State Electronic Spins. *The Journal of Physical Chemistry Letters* **2020**, *11,* 6273–6278.

[85] Escalera-Moreno, L.; Suaud, N.; Gaita-Ariño, A.; Coronado, E. Determining Key Local Vibrations in the Relaxation of Molecular Spin Qubits and Single-Molecule Magnets. *The Journal of Physical Chemistry Letters* **2017**, *8,* 1695–1700.

[86] Atzori, M.; Tesi, L.; Benci, S.; Lunghi, A.; Righini, R.; Taschin, A.; Torre, R.; Sorace, L.; Sessoli, R. Spin Dynamics and Low Energy Vibrations: Insights from Vanadyl-Based Potential Molecular Qubits. *Journal of the American Chemical Society* **2017**, *139,* 4338–4341.

[87] Camargo, L. C.; Briganti, M.; Santana, F. S.; Stinghen, D.; Ribeiro, R. R.; Nunes, G. G.; Soares, J. F.; Salvadori, E.; Chiesa, M.; Benci, S.; Torre, R.; Sorace, L.; Totti, F.; Sessoli, R. Exploring the Organometallic Route to Molecular Spin Qubits: The [CpTi(cot)] Case. *Angewandte Chemie International Edition* **2021**, *60,* 2588-2593.

[88] Garlatti, E.; Tesi, L.; Lunghi, A.; Atzori, M.; Voneshen, D. J.; Santini, P.; Sanvito, S.; Guidi, T.; Sessoli, R.; Carretta, S. Unveiling Phonons in a Molecular Qubit with Four-Dimensional Inelastic Neutron Scattering and Density Functional Theory. *Nature Communications* **2020**, *11,* 1751.

[89] Lunghi, A. Ligand-Field Contributions to Spin-Phonon Coupling in a Family of Vanadium Molecular Qubits from Multi-Reference Electronic Structure Theory. *arXiv:1912.04545 [cond-mat, physics:quant-ph]* **2019**.

[90] Ballhausen, C. J. *Introduction to Ligand Field Theory;* McGraw-Hill: New York, 1962.

[91] Solomon, E. I. Inorganic Spectroscopy—An Overview. *Comments on Inorganic Chemistry* **1984**, *3,* 227–320.

[92] Pavel, E. G.; Solomon, E. I. Recent Advances in Magnetic Circular Dichroism Spectroscopy. In *Spectroscopic Methods in Bioinorganic Chemistry*, Vol. 692; Solomon, E. I.; Hodgson, K. O., Eds.; American Chemical Society: Washington, DC, 1998.

[93] George, S. J.; Lowery, M. D.; Solomon, E. I.; Cramer, S. P. Copper L-Edge Spectral Studies: a Direct Experimental Probe of the Ground-State Covalency in the Blue Copper Site in Plastocyanin. *Journal of the American Chemical Society* **1993**, *115,* 2968–2969.

[94] Wasinger, E. C.; de Groot, F. M. F.; Hedman, B.; Hodgson, K. O.; Solomon, E. I. L-edge X-ray Absorption Spectroscopy of Non-Heme Iron Sites: Experimental Determination of Differential Orbital Covalency. *Journal of the American Chemical Society* **2003**, *125,* 12894–12906.

[95] Glaser, T.; Hedman, B.; Hodgson, K. O.; Solomon, E. I. Ligand K-Edge X-ray Absorption Spectroscopy: A Direct Probe of Ligand-Metal Covalency. *Accounts of Chemical Research* **2000**, *33,* 859–868.

[96] Van Kuiken, B. E.; Hahn, A. W.; Maganas, D.; DeBeer, S. Measuring Spin-Allowed and Spin-Forbidden d-d Excitations in Vanadium Complexes with 2p3d Resonant Inelastic X-ray Scattering. *Inorganic Chemistry* **2016**, *55,* 11497–11501.

[97] van Schooneveld, M. M.; Gosselink, R. W.; Eggenhuisen, T. M.; Al Samarai, M.; Monney, C.; Zhou, K. J.; Schmitt, T.; de Groot, F. M. F. A Multispectroscopic Study of 3d Orbitals in Cobalt Carboxylates: The High Sensitivity of 2p3d Resonant X-ray Emission Spectroscopy to the Ligand Field. *Angewandte Chemie International Edition* **2013**, *52,* 1170–1174.

[98] Lundberg, M.; Kroll, T.; DeBeer, S.; Bergmann, U.; Wilson, S. A.; Glatzel, P.; Nordlund, D.; Hedman, B.; Hodgson, K. O.; Solomon, E. I. Metal-Ligand Covalency of Iron Complexes from High-Resolution Resonant Inelastic X-ray Scattering. *Journal of the American Chemical Society* **2013**, *135,* 17121–17134.

[99] Szilagyi, R. K.; Metz, M.; Solomon, E. I. Spectroscopic Calibration of Modern Density Functional Methods Using $[CuCl_4]^{2-}$. *The Journal of Physical Chemistry A* **2002**, *106,* 2994–3007.

[100] Scaltrito, D. V.; Thompson, D. W.; O'Callaghan, J. A.; Meyer, G. J. MLCT Excited States of Cuprous Bis-Phenanthroline Coordination Compounds. *Coordination Chemistry Reviews* **2000**, *208,* 243–266.

[101] Mara, M. W.; Fransted, K. A.; Chen, L. X. Interplays of Excited State Structures and Dynamics in Copper(I) Diimine Complexes: Implications and Perspectives. *Coordination Chemistry Reviews* **2015**, *282-283,* 2–18.

[102] Stroscio, G. D.; Ribson, R. D.; Hadt, R. G. Quantifying Entatic States in Photophysical Processes: Applications to Copper Photosensitizers. *Inorganic Chemistry* **2019**, *58,* 16800–16817.

[103] Solomon, E. I.; Hadt, R. G. Recent Advances in Understanding Blue Copper Proteins. *Coordination Chemistry Reviews* **2011**, *255,* 774–789.

[104] Tsukuda, T.; Nakamura, A.; Arai, T.; Tsubomura, T. Luminescence of Copper(I) Dinuclear Complexes Bridged by Diphosphine Ligands. *Bulletin of the Chemical Society of Japan* **2006**, *79,* 288–290.

[105] Higdon, N. J.; Barth, A. T.; Kozlowski, P. T.; Hadt, R. G. Spin-Phonon Coupling and Dynamic Zero-Field Splitting Contributions to Spin Conversion Processes in Iron(II) Complexes. *The Journal of Chemical Physics* **2020**, *152,* 204306.

[106] Mims, W. B. *The Linear Electric Field Effect in Paramagnetic Resonance;* Clarendon Press: Oxford, 1976.

[107] Fujisaku, T.; Tanabe, R.; Onoda, S.; Kubota, R.; Segawa, T. F.; So, F. T.-K.; Ohshima, T.; Hamachi, I.; Shirakawa, M.; Igarashi, R. pH Nanosensor Using Electronic Spins in Diamond. *ACS Nano* **2019**, *13,* 11726–11732.

Chapter 2

THE IMPACT OF LIGAND FIELD SYMMETRY ON MOLECULAR QUBIT COHERENCE

- Adapted with permission from: Kazmierczak, N. P.; Mirzoyan, R.; Hadt, R. G. The Impact of Ligand Field Symmetry on Molecular Qubit Coherence. *Journal of the American Chemical Society* **2021**, *143*, 17305–17315. DOI: 10.1021/jacs.1c04605. © 2021 American Chemical Society.

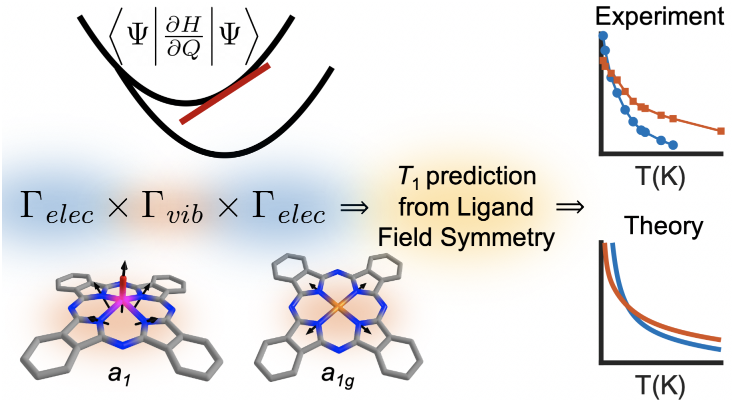

2.1 Abstract

Developing quantum bits (qubits) exhibiting room temperature electron spin coherence is a key goal of molecular quantum information science. At high temperatures, coherence is often limited by electron spin relaxation, measured by T_1. Here we develop a simple and powerful model for predicting relative T_1 relaxation times in transition metal complexes from dynamic ligand field principles. By considering the excited state origins of ground state spin-phonon coupling, we derive group theory selection rules governing which vibrational symmetries can induce decoherence. Thermal weighting of the coupling terms produces surprisingly good predictions of experimental T_1 trends as a function of temperature and explains previously confounding features in spin-lattice relaxation data. We use this model to evaluate experimental relaxation rates across S = ½ transition metal qubit candidates with diverse structures, gaining new insights into the interplay between spin-phonon coupling and molecular symmetry. This methodology elucidates the specific vibrational modes giving rise to decoherence, providing insight into the

origin of room temperature coherence in transition metal complexes. We discuss the outlook of symmetry-based modeling and design strategies for understanding molecular coherence.

2.2 Introduction

The use of paramagnetic transition metal complexes as molecular electron spin quantum bits (qubits) has generated considerable interest over the past decade (Figure 2.1A).[1–6] When placed into a magnetic field, the Zeeman effect splits the energies of the M_S sublevels into a quantum two-level system that can be leveraged for applications in computing, sensing, and communication (Figure 2.1B).[2,7] Among these, molecular quantum sensing constitutes a particularly exciting application,[2] as molecular electron spin qubits can be synthetically tuned and located in a targeted fashion within chemical microenvironments and interfaces to read out properties of relevance in areas such as catalysis and medicine. The microenvironments of interest often exist under ambient conditions. Thus, developing molecular qubits that operate at room temperature remains a key goal in the field.[1,8,9]

The utility of molecular electron spin qubits is limited by the phase memory time T_M, which describes how long phase relations are retained between members of the ensemble.[10] As temperature increases in spin-dilute environments, T_M becomes limited by T_1, the spin-lattice relaxation time. T_1 describes how quickly spin energy is transferred to the vibrational bath.[11] In solid lattices, this process is controlled by spin-phonon coupling.[12] Three mechanisms for spin-phonon coupling deteriorate the performance of molecular qubits at room temperature, known as the direct, Raman, and Orbach processes (Figure 2.1B).[10,13,14] The direct process dissipates spin energy through acoustic phonon emission and exerts the greatest contribution at low temperatures (e.g., < 10 K).[15] The Raman process dissipates spin energy through inelastic scattering of phonons from a virtual state, with acoustic phonons contributing at intermediate temperatures and optical phonons (i.e., local modes[6]) dominating at elevated temperatures near ambient conditions.[12,16] In $S = ½$ systems, the Orbach mechanism generally does not contribute strongly.[16] Room temperature coherence lifetimes of molecular electron spin qubits are controlled by spin-phonon coupling with the molecular vibrational modes.[4,17]

A natural question arises: which vibrational modes exhibit the strongest spin-phonon coupling? Vibrational modes higher in energy than about 400 cm^{-1} are not expected to contribute significantly to spin-lattice relaxation, as the Raman

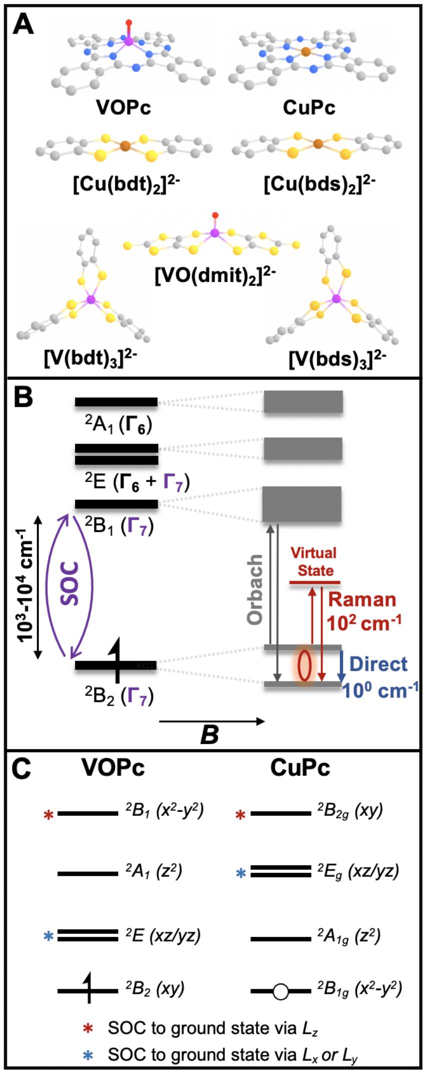

Figure 2.1: Overview of molecular electron spin qubits. (A) V(IV) and Cu(II) qubits considered in this study.[8,9,18,19] VOPc = vanadyl phthalocyanine; CuPc = copper phthalocyanine; $[Cu(bdt)_2]^{2-}$ = copper bis(1,2-benzenedithiolate); $[Cu(bds)_2]^{2-}$ = copper bis(1,2-benzenediselenate); $[VO(dmit)_2]^{2-}$ = vanadyl bis(1,3-dithiole-2-thione-4,5-dithiolate); $[V(bdt)_3]^{2-}$ = vanadium tris(1,2-benzenedithiolate); $[V(bds)_3]^{2-}$ = vanadium tris(1,2-benzenediselenate); (B) Electronic structure and relaxation mechanisms of molecular qubits. (Left) Electronic states (example: VOPc) in single-valued point groups and double groups (Bethe notation) inclusive of spin-orbit coupling. Charge-transfer states not shown. (Right) T_1 relaxation mechanisms. Atomic color scheme: C (grey), N (blue), O (red), S (yellow), Se (orange), Cu (brown), V (pink). H atoms not shown for clarity. (C) Qualitative crystal field state diagrams for VOPc and CuPc (hole formalism). Excited states with red (blue) asterisks spin-orbit couple to the corresponding ground states through L_z (L_x or L_y) angular momentum operators.

process requires thermal population of an existing phonon mode (see Supporting Information, Section 4).[10] While the phonon density of states and dispersion relation below 400 cm^{-1} can be probed using terahertz spectroscopy[20] and four-dimensional inelastic neutron scattering,[21] ascertaining the spin-phonon coupling of those modes remains an outstanding experimental challenge. In lieu of experimental evidence, several studies have sought to assign the most impactful spin-phonon coupling modes through computational studies.[17,22–24] There exists an emerging recognition of the importance of the symmetry of the vibrational mode, with recent studies empirically concluding that gerade modes exhibit heightened spin-phonon coupling over ungerade modes for square planar compounds.[22,24] However, no general theory yet exists for predicting which vibrational symmetries exert the greatest spin-phonon coupling and modeling the implications for temperature-dependent T_1. This hinders rational molecular design and constitutes an important challenge in the field.[6]

Here we derive group theory selection rules for determining vibrational modes that are active for spin-phonon coupling. We show that the coupling modes are those that are group theoretically allowed to undergo ligand field excited state distortions. These vibrational modes dynamically change the amount of ground state orbital angular momentum. We then show that a simple thermal weighting of molecular spin-phonon coupling coefficients furnishes very good agreement with relative trends in experimental spin-lattice relaxation rates, thus describing how different vibrations dominate T_1 over different temperature regimes. The resulting model predicts relative spin relaxation times (T_1), or phonon-limited coherence times (T_M) at high temperatures.

2.3 Ligand Field Paradigm for Electron Spin Relaxation

2.3.1 Symmetry Effects on Spin-Phonon Coupling

Spin-phonon coupling arises when some portion of the spin Hamiltonian is modulated by a vibrational mode.[6,25] The g tensor, $\boldsymbol{g}$, describing the Zeeman effect has been implicated as a major source of spin-phonon coupling in molecular qubits.[15,24] Therefore, to understand the impact of symmetry on spin-phonon coupling, we first turn to the molecular origins of the g values in a transition metal complex.

A free electron has an isotropic g value of $g_e = 2.0023$ owing to its intrinsic spin angular momentum; deviations from this value arise when the electron additionally possesses ground state orbital angular momentum, as quantified by the Landé formula. While the presence of a ligand field quenches orbital angular momentum in tetragonal transition metal complexes, spin-orbit coupling with ligand field excited states reintroduces orbital angular momentum into the ground state. Thus, changes in the g value arise from changes in spin-orbit coupling. In order for the ith vibrational mode to have a nonzero first-order spin-phonon coupling coefficient, $\partial \boldsymbol{g}/\partial Q_i$, the magnitude of spin-orbit coupling must therefore change as a function of the vibrational mode coordinate Q_i. The expression for the g value of a transition metal complex due to the spin-orbit perturbation is given by[26]

$$g_i = g_e - 2\lambda \sum_{e \neq g} \frac{\left\langle \Psi_g \middle| \widehat{\boldsymbol{L}_i} \middle| \Psi_e \right\rangle \left\langle \Psi_e \middle| \widehat{\boldsymbol{L}_i} \middle| \Psi_g \right\rangle}{E_e - E_g} \tag{2.1}$$

where λ is the many-electron spin-orbit coupling constant, Ψ_g and Ψ_e are the ground and excited states with energies E_g and E_e, respectively, $\widehat{\boldsymbol{L}_i}$ is an orbital angular momentum operator, and $i = x, y, z$ refer to the g tensor principal axes and the molecular quantization frame, which are aligned for the tetragonal qubits considered in this work. Equation (2.1) shows that the g values have a sensitive dependence on the energy gap between the ground and excited states involved in the spin-orbit coupling. (The precise excited states involved can be determined from double groups (Figure 2.1B) using Tables S13 and S14 and tables of d orbital rotations.[6,27]) If the ground and excited state potential energy surfaces reach a minimum at the same value of the vibrational coordinate Q_i, then the energy gap $E_e - E_g$ can at most vary quadratically as a function of Q_i, implying $\partial \boldsymbol{g}/\partial Q_i = 0$ at equilibrium (Figure 2.2A). However, if the equilibrium geometry of the excited state is different than that of the ground state equilibrium geometry along Q_i, the energy gap $E_e - E_g$ can vary linearly as a function of Q_i and give rise to $(\partial \boldsymbol{g}/\partial Q_i)_0 \neq 0$ (Figure 2.2B). We refer to such modes as the distorting modes.[27] The first-order coupling coefficient at equilibrium, $(\partial \boldsymbol{g}/\partial Q_i)_0$ (hereafter simply $\partial \boldsymbol{g}/\partial Q_i$), is predicted to exert the leading influence on spin-lattice relaxation times.[15,24] Therefore, the most important vibrational modes for spin-phonon coupling are precisely these distorting modes.[22]

Crucially, the excited state distortion can be expressed through a matrix element[27] involving vibrational perturbations of the ligand field Hamiltonian (H_{LF}):

$$\Delta Q_i = -\frac{\left\langle \psi^e_{elec} \middle| \left(\frac{\partial H_{LF}}{\partial Q_i}\right)_0 \middle| \psi^e_{elec} \right\rangle}{k_i}. \tag{2.2}$$

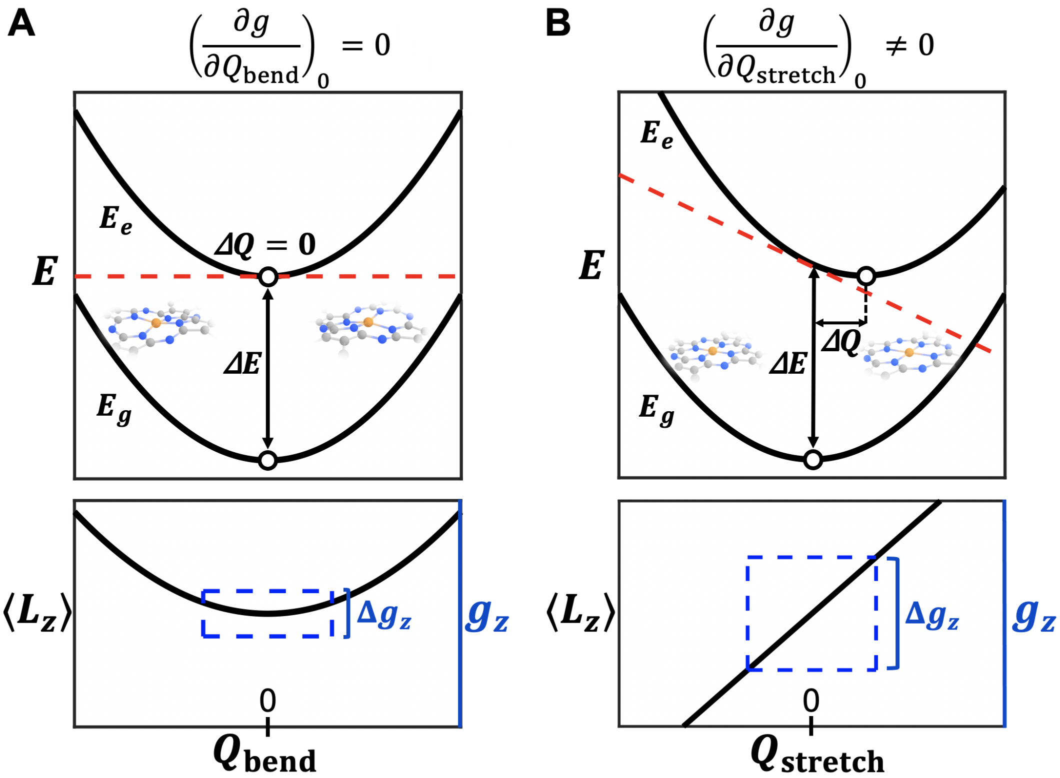

Figure 2.2: The excited state origins of ground state spin-phonon coupling. (A) Schematic potential energy surfaces for the b_{2u} bending mode in CuPc. The ground and excited state potential energy minima coincide, implying no excited state distortion and thus no linear spin-phonon coupling. (B) Schematic potential energy surfaces for the a_{1g} symmetric stretch in CuPc. The ground and excited state minima are offset, implying excited state distortion and linear ground state spin-phonon coupling.

Here ΔQ_i gives the excited state distortion along the vibrational mode Q_i, k_i is the force constant, and ψ^e_{elec} is the excited state wave function that spin-orbit couples into the ground state. The matrix element is evaluated at the ground state equilibrium geometry. The key utility of this expression lies in the application of group theory symmetry selection rules to the integral. The state symmetry of ψ^e_{elec} and Q_i (Γ_{elec} and Γ_{Q_i}, respectively) can be assigned through textbook techniques.[28] The ligand field Hamiltonian always has the totally symmetric irreducible representation in the molecular point group, so the derivative has the symmetry Γ_{Q_i}. Therefore, the symmetry of the integrand is given[27] by a direct triple product. For the integral to be nonzero, Equation (2.3) must contain the totally symmetric irreducible representation:

$$\Gamma_{elec} \times \Gamma_{Q_i} \times \Gamma_{elec} = a_1 + \ldots \tag{2.3}$$

Here a_1 in Equation (2.3) signifies the totally symmetric representation in the desired point group, and the excited state is group theoretically allowed to undergo distortion when the equivalent condition in Equation (2.4) is met:

$$[\Gamma_{elec} \times \Gamma_{elec}] = \Gamma_{Q_i}. \tag{2.4}$$

The square brackets in Equation (2.4) denote the symmetric direct product operation, appropriate for the product of Γ_{elec} with itself, and Γ_{Q_i} represents all mode symmetries that are allowed to couple.[27,29,30] This selection rule enables facile calculation of which vibrational symmetries will be able to exhibit linear spin-phonon coupling terms for a given coordination geometry and electronic structure. The coupling modes are those that are group theoretically allowed to undergo ligand field excited state distortions. For nondegenerate states, only the totally symmetric modes will couple, while other non-totally symmetric modes can couple for degenerate excited states. We note that this consideration is a more general basis for understanding forces in molecules (i.e., the Hellmann-Feynman force[31]), including those of relevance for transition metal photophysics[32,33] and those predicted by the Jahn-Teller theorem to give rise to the instability of orbitally degenerate states.[29]

To illustrate the power of this approach in understanding spin-phonon coupling contributions to decoherence in molecular qubits, we turn to a comparison between vanadyl phthalocyanine (VOPc) and copper phthalocyanine (CuPc) (Figure 2.1A).[19] VOPc belongs to the non-centrosymmetric point group C_{4v}, while CuPc belongs to the centrosymmetric point group D_{4h}. The electronic ground state of VOPc has the state symbol $^2B_2$ (d_{xy}), which spin-orbit couples with the $^2B_1$ ($d_{x^2-y^2}$) excited state to introduce orbital angular momentum into g_z (Figure 2.1C). The situation is reversed in CuPc owing to the hole formalism, with a $^2B_{1g}$ ($d_{x^2-y^2}$) ground state and a $^2B_{2g}$ (d_{xy}) excited state (Figure 2.1C). The relevant lowest lying excited state for g_z is nondegenerate in both cases. Because the direct product of any nondegenerate irreducible representation with itself gives the totally symmetric irreducible representation, Equation (2.4) reduces to $a_1 = \Gamma_{Q_i}$ for VOPc in order for $\partial g_z/\partial Q_i \neq 0$. An identical analysis holds for CuPc, where a_{1g} is the totally symmetric representation in D_{4h}. Thus, the group theory model predicts that the strongest spin-phonon coupling for g_z should arise from totally symmetric vibrational modes. Indeed, previous computational studies have observed that a_{1g} or a_1 modes exhibit large coupling coefficients,[22,24] with D_{2d} $\mathrm{CuCl_4^{2-}}$ possessing more spin-phonon coupling than D_{4h} $\mathrm{CuCl_4^{2-}}$ owing to a greater number of totally symmetric modes.[22]

Though totally symmetric vibrational modes dominate g_z coupling for both VOPc and CuPc, the change in point group between C_{4v} and D_{4h} nonetheless has important consequences for spin-phonon coupling. CuPc displays a single a_{1g} mode below 400 cm^{-1} corresponding to the totally symmetric Cu-N stretch (Figure 2.3A). Owing to the reduced number of irreducible representations in the C_{4v} point group, VOPc displays five total a_1 vibrational modes below 400 cm^{-1}, encompassing mixtures of both the symmetric stretch and metal out-of-plane motion Figure 2.3B). The portion of the vibrational density of states which matters for spin-phonon coupling is thus very different: CuPc possesses a lone linear coupling mode at 262 cm^{-1}, while VOPc possesses five spin-phonon active modes below 400 cm^{-1} (Table 2.1). Calculation of the $\partial g_z/\partial Q_i$ coefficients for CuPc and VOPc via calibrated density functional theory (DFT)[34] according to a previous procedure[22] (see also Supporting Information, Section 1) shows that the totally symmetric vibrations have the largest coefficients by orders of magnitude, confirming the group theory analysis (Figure 2.3C). The coefficient for CuPc is an order of magnitude larger than those for VOPc owing to the larger spin-orbit coupling constant of Cu(II) relative to V(IV).[19] For both VOPc and CuPc, only a very small portion of the vibrational density of states contributes to spin-phonon coupling for g_z (Figure 2.3A,B).

VOPc		CuPc	
E (cm^{-1})	$(\partial g_z/\partial Q)^2$	E (cm^{-1})	$(\partial g_z/\partial Q)^2$
42	5.5×10^{-8}	262	2.8×10^{-5}
178	1.5×10^{-6}		
262	6.3×10^{-7}		
317	2.9×10^{-6}		
395	1.9×10^{-6}		

Table 2.1: Linear g_z spin-phonon coupling modes for VOPc and CuPc. All modes have the totally symmetric representation.

A similar analysis can be performed for $\partial g_x/\partial Q_i$. For both VOPc and CuPc, orbital angular momentum is introduced to g_x principally via spin-orbit coupling with the d_{xz}/d_{yz} excited states, which are orbitally doubly degenerate and have the

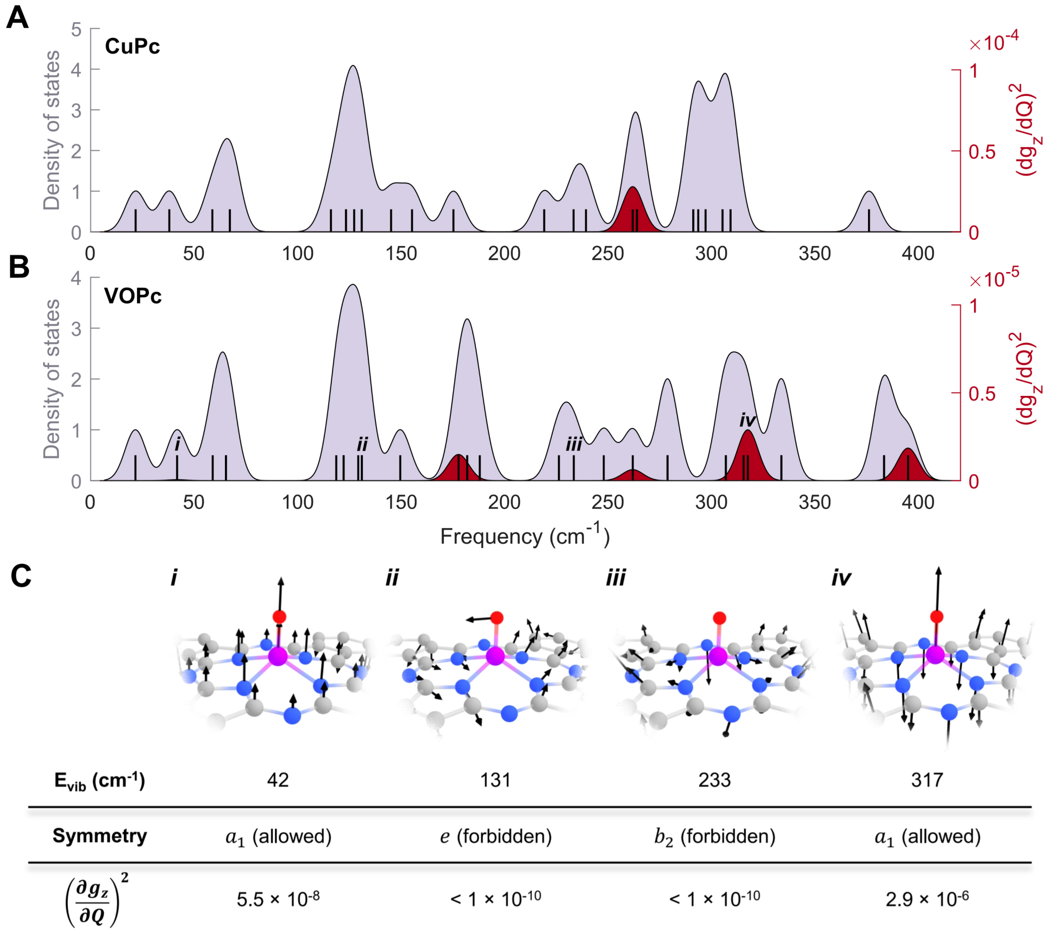

E_{vib} (cm^{-1})	42	131	233	317
Symmetry	a_1 (allowed)	e (forbidden)	b_2 (forbidden)	a_1 (allowed)
$\left(\frac{\partial g_z}{\partial Q}\right)^2$	5.5×10^{-8}	$< 1 \times 10^{-10}$	$< 1 \times 10^{-10}$	2.9×10^{-6}

Figure 2.3: Impact of symmetry on spin-phonon coupling. (A) Normalized vibrational density of states (lavender, left y-axis) and spin-phonon coupling active vibrations (red, right y-axis) for CuPc. (B) Normalized vibrational density of states (lavender, left y-axis) and spin-phonon coupling active vibrations (red, right y-axis) for VOPc. (C) Analysis of selected modes for VOPc. Arrows indicate atomic displacements; additional pictures are provided in Tables S3-S7. Symmetry selection rules are evaluated for the $^2B_1$ ($d_{x^2-y^2}$) excited state (g_z spin-phonon coupling) via Equation (2.4). $1{\times}10^{-10}$ constitutes the limit of numerical precision.

representations ^2E in C_{4v} and ^2E_g in D_{4h} (Figure 2.1C). Evaluation of Equation (2.4) for VOPc now yields $(a_1 + b_1 + b_2) = \Gamma_{Q_i}$, showing that a_1, b_1, and b_2 vibrational modes are able to have $\partial g_x/\partial Q_i \neq 0$ by symmetry. (a_2 is produced by the antisymmetric direct product and is therefore discarded.)[30] Similarly, Equation (2.4) for CuPc yields $\left(a_{1g} + b_{1g} + b_{2g}\right) = \Gamma_{Q_i}$, showing that multiple nondegenerate gerade modes are able to couple for g_x. Note that the gerade selection rule would hold true even if the electronic state symmetry were ungerade, because Equation

(2.4) contains the electronic symmetry twice. While group theory states which modes are allowed to couple by symmetry, as with any selection rule, this does not guarantee a large nonzero coefficient.[27]

Comparison between the coupling modes for CuPc and $[Cu(bdt)_2]^{2-}$ (bdt = 1,2-benzenedithiolate) illustrates the impact of descending in symmetry from D_{4h} to D_{2h} (Figure 2.4). Lower than 400 cm^{-1}, CuPc displays a single active mode with $\partial g_z/\partial Q_i$, the a_{1g} symmetric stretch. Two modes for CuPc display nonzero $\partial g_x/\partial Q_i$, including both the a_{1g} symmetric stretch and the b_{1g} antisymmetric stretching mode. The presence of the linearly coupling b_{1g} mode is enabled by the degeneracy of the ${}^2E_g$ electronic state (Figure 2.1C). However, no degenerate irreducible representations exist in the D_{2h} point group, so the d_{xz} and d_{yz} orbitals are split into the B_{2g} and B_{3g} representations. All electronic states implicated in the g_x and g_y spin-phonon coupling are nondegenerate for $[Cu(bdt)_2]^{2-}$, implying that only totally symmetric a_g vibrational modes will display linear coupling for all three canonical orientations. Indeed, examination of the spin-phonon coupling coefficients for $[Cu(bdt)_2]^{2-}$ shows that the most prominent coupling modes are the same for both $\partial g_z/\partial Q_i$ and $\partial g_x/\partial Q_i$ and possess a_g symmetry as predicted (Figure 2.4). The coupling b_{1g} mode from CuPc correlates to a b_{1g} mode in $[Cu(bdt)_2]^{2-}$, implying that the linear coupling of this antisymmetric stretch mode has been turned off by the descent in symmetry. Conversely, the b_{2g} in-plane scissoring mode in CuPc correlates to a_g symmetry for $[Cu(bdt)_2]^{2-}$ and is activated for g_z coupling. Thus, descent in symmetry from D_{4h} to D_{2h} retains the total number of linear coupling modes for g_x, but changes the identity of those modes (Figure 2.4). Similar behavior is observed for the C_{2v} qubit $[VO(dmit)_2]^{2-}$, with many a_1 modes exhibiting coupling for both g_x and g_z. Global molecular symmetry can impact the spin-phonon coupling modes even for apparently similar coordination geometries, a surprising result elucidated by group theory. This result establishes control of degenerate electronic excited states as an important design consideration for controlling activation of spin-phonon coupling vibrational modes.

A previous study of two D_{4h} Cu(II) complexes empirically concluded that gerade modes exhibited the strongest coupling.[24] Our work differs in two important ways. First, the present approach provides a predictive group theory analysis not dependent on a centrosymmetric point group. In addition to the C_{nv} point groups considered in this work, this will also enable extension of spin-phonon coupling symmetry analysis to qubits with trigonal coordination environments.[35,36] By analogy

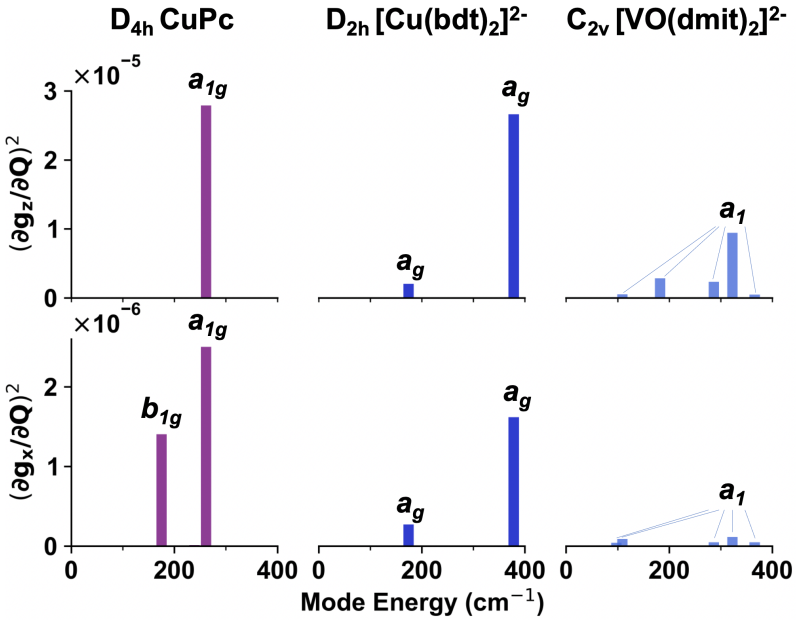

Figure 2.4: Orientation-dependent spin-phonon coupling coefficients for CuPc, $[Cu(bdt)_2]^{2-}$, and $[VO(dmit)_2]^{2-}$.

to gerade/ungerade, point groups containing the prime/double prime representations should see coupling only from the single-prime vibrational modes, as the double direct product of the electronic excited state in Equation (2.4) will yield a single-prime representation irrespective of the electronic representation, and the totally symmetric representation will always have a single-prime value. Furthermore, evaluation of Equation (2.4) for the D_{4h} point group reveals that the a_{2g} mode is not predicted to exhibit linear coupling despite possessing gerade symmetry. This prediction is in agreement both with previous calculations[24] and our own.

Second, a point of variance with the previous study[24] arises over the role of the degenerate e_g vibrations, which are found to couple in that study, but not predicted to couple by the present group theory analysis. This is because the present analysis has considered the spin-phonon coupling coefficients corresponding to the canonical orientations of the g tensor; namely, g_x, g_y, and g_z. By contrast, Santanni et al. averaged all nine $\partial \boldsymbol{g}/\partial Q$ values for the non-diagonalized g tensor.[24] Nonzero off-diagonal derivatives correspond to dynamic rotation of the principal axes of the g tensor. Indeed, the R_x and R_y rotation operators transform as e_g in D_{4h}, and pictures of the e_g vibrational modes show that the first coordination sphere undergoes a rigid rotation out of the xy-plane (Table S5). A minimal square-planar coordination environment such as D_{4h} $CuCl_4^{2-}$ does not posses e_g normal modes,[22] as these would correspond to pure rotational degrees of freedom. In CuPc, however, counter-rotation of the phthalocyanine ligand framework enables e_g normal modes. As local rotation does not affect bonding in the first coordination sphere, e_g vibrational modes do not dynamically alter g_x, g_y, and g_z, in accordance with our group theory predictions. Similarly, the non-coupling a_{2g} modes transform as R_z.

Our choice to consider only the canonical g tensor derivatives ($\partial g_x/\partial Q$, $\partial g_y/\partial Q$, and $\partial g_z/\partial Q$) is supported by two independent lines of experimental evidence: orientation-dependent T_1 trends and temperature-dependent T_1 trends. Modes with canonical versus off-diagonal g tensor derivatives are predicted to have distinct patterns of orientation dependence. As shown in Figure S18, modes with canonical g tensor derivatives are predicted to exhibit maximum and minimum coupling for molecules aligned along the principal tensor axes. By contrast, off-diagonal modes are predicted to exhibit maximum coupling at intermediate field positions in-between the canonical orientations. This provides an experimental test for whether canonical or off-diagonal modes dominate the observed T_1 behavior. Across a variety of systems, including D_{4h} Cu(II) coordination complexes,[37] C_{4v} nitridochromium(V) and oxochromium(V) complexes,[38,39] and organic nitroxide spin labels,[37] the minimum and maximum values of T_1 are found to coincide with the canonical orientations of the g tensor. These measurements encompass a range of temperatures from 50-130 K.[37] This experimental fact demonstrates that T_1 spin-lattice relaxation is driven not by rotational modes modulating the g tensor orientation, but by modes modulating the g_z and g_x, g_y principal values.[37,38,40] Corroborating this, we obtain superior predictions of experimental temperature-dependent T_1 times by including only the on-diagonal elements (vide infra). We note that T_M often reaches minimum experimental values at intermediate-field positions and maximum values at canonical orientations of the g tensor.[38] This phenomenon is ascribed to the impact of librations in the context of glassy frozen solution measurements,[38] but the e_g modes in CuPc induce the same type of rotational motion. This evidence indicates that rotational modes can impact T_M, but do not generally dominate T_1.

2.3.2 Thermally-Weighted Ligand Field Model of T_1

Once the $\partial \boldsymbol{g}/\partial Q$ values for molecular vibrations have been calculated,[22] relative T_1 times can be predicted using a simplified model of the Raman spin-lattice relaxation process in molecular solids. A simple functional form for attributing Raman relaxation to molecular vibrations has been proposed on the basis of the two-phonon Green's function[12] and used to fit experimental T_1 data.[24,41] We now employ this form to make comparative T_1 predictions informed by the preceding symmetry analysis:

$$\frac{1}{T_1} = A \sum_{i=1}^{3N-6} \left(\frac{\partial \boldsymbol{g}}{\partial Q_i} \right)^2 \frac{\exp\left[E_i/k_B T\right]}{\left(\exp\left[E_i/k_B T\right] - 1\right)^2}. \tag{2.5}$$

Here E_i is the energy of the lattice vibration, k_B is the Boltzmann constant, T is the lattice temperature, A is a proportionality constant to be determined by scaling to experimental data (Supporting Information, Section 5), and the sum is over all normal modes of vibration. A single scaling factor A is chosen for all molecules in each comparative T_1 prediction, ensuring that the relative T_1 ratios are unaltered by the scaling process. Modes without a first-derivative coupling term (Figure 2.2A) do not contribute to the sum. Owing to the exponentially vanishing thermal weighting factor, it is sufficient to consider only modes below 400 cm^{-1}. The prediction error due to this cutoff is estimated to be no greater than 5-10% at 300 K for the complexes considered (Figure S19), which has a negligible effect for a logarithmic scale. Here we present rate predictions using $\partial g_z/\partial Q_i$, while predictions using other elements of the Zeeman tensor are discussed in the Supporting Information Section 3 (Figures S11-S17). Equations (2.3), (2.4) and (2.5) together provide an analytical link between molecular vibrations and temperature-dependent electron spin relaxation rates.

Figure 2.5A shows the predicted temperature-dependent T_1 times for VOPc and CuPc, which are in good agreement with our previously obtained experimental data[19] considering the simplicity of the model employed. Equation (2.5) correctly predicts that VOPc has a longer T_1 than CuPc at room temperature. Furthermore, Equation (2.5) correctly predicts the existence of a T_1 crossover point at lower temperatures, below which CuPc displays the longer T_1 time. Though observed in multiple systems in the molecular qubit literature,[9,19] such crossover features have lacked a clear interpretation and have been attributed to variations in the Raman exponent under a Debye model treatment or local mode terms.[16,42,43]

We now show this phenomenon has a direct chemical interpretation in terms of molecular vibrations. As given in Table 2.1, VOPc possesses five linear coupling modes, while CuPc possesses only one. However, the magnitude of the spin-phonon coupling coefficient is significantly larger for the CuPc mode than for any of the VOPc modes, a fact explained by the difference in spin-orbit coupling coefficients between the two metals.[19,22] Additionally, the lone CuPc mode sits higher in energy

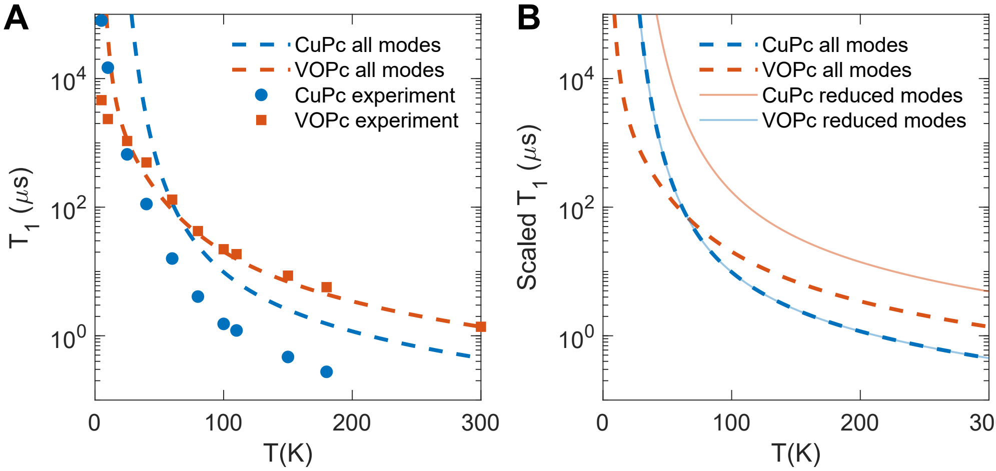

Figure 2.5: Thermally-weighted ligand field model for phthalocyanine qubits. (A) Comparison between T_1 model predictions (dashed lines) to experimental results from ref[19] (solid circles and squares). (B) Comparison between T_1 model predictions employing all modes with T_1 model predictions using a reduced subset of the vibrational modes. Dashed lines: all spin-phonon active modes. Solid lines: only the two strongest modes at 317 cm^{-1} and 395 cm^{-1} for VOPc and the single strongest mode at 262 cm^{-1} for CuPc. All T_1 predictions are scaled by the same factor A = 1.32×10^5 μs^{-1}, chosen so the VOPc all-modes prediction matches the experimental data at 300 K.

than three of the five VOPc modes. Thus, at the lowest temperatures modeled, the symmetric stretch of CuPc has negligible thermal population and minimal spin-phonon coupling. By contrast, VOPc possesses coupling modes as low as 42 cm^{-1} (Figure 2.3, Table 2.1), which are thermally populated at low temperature and contribute to VOPc having a shorter T_1 than CuPc. As the temperature increases, higher energy vibrational modes of both VOPc and CuPc become thermally populated, but the spin-phonon coupling coefficient is largest for the CuPc symmetric stretch. This manifests in a larger T_1 slope for CuPc versus VOPc. When all modes are populated near room temperature, the larger $\partial g_z/\partial Q_i$ of CuPc takes over, and VOPc has the longer coherence time at room temperature. The high and low temperature behavior of T_1 thus relate to the magnitude of $\partial g_z/\partial Q_i$ and the relative energy of the coupling vibrational modes, respectively. For these two molecules, ligand field symmetry is most important for a longer T_1 at low temperatures, while chemical bonding properties[6,19,22] contribute more strongly to a longer T_1 at high temperatures. The precise nature of this interplay will vary depending on the molecules analyzed.

The experimental T_1 crossover point is around 20 K, while the modeled crossover point is around 65 K (Figure 2.5, Table S2). If $\partial g_x/\partial Q_i$ derivatives are used instead of $\partial g_z/\partial Q_i$, the modeled crossover point is around 35 K. Thus, part of the uncertainty in the T_1 crossover temperature may arise from the choice of principal tensor derivative. Development of a model for anisotropic T_1 is called for to address this uncertainty. We note that the precise location of the crossover point likely also contains contributions from varying efficiencies of the direct process and Raman process operating on acoustic phonons. This may relate to effective acoustic phonon symmetry in the 1:1000 magnetic dilution data modeled here, as the 42 cm^{-1} linear coupling mode in VOPc contains displacements similar to an acoustic phonon (Figure 2.3C), and it has been suggested that acoustic phonons acquire spin-phonon coupling intensity through avoided crossings with low-lying optical phonons.[21]

The crossover behavior predicted in the model can be unambiguously assigned to the low-energy a_1 modes of VOPc by artificially manipulating the number of modes in the model. If only the two strongest-coupling modes of VOPc are considered (317 cm^{-1} and 395 cm^{-1}), no crossover is observed (solid orange line, Figure 2.5B). Indeed a crossover is barely observed upon simply deleting the a_1 mode at 42 cm^{-1}, indicating that low energy molecular vibrations produced by reduced symmetry can exert a large influence on the temperature-dependent T_1 times even when their spin-phonon coupling coefficients are small. The overall good agreement lends credence to the general use of this model to a priori predict the observation of room temperature coherence in any transition metal complex. Note that when modes of e_g and e symmetry (local rotations, vide supra) are included in the model through off-diagonal g tensor derivatives, they dominate the T_1 behavior for CuPc through thermal population owing to their low vibrational energy.[24] This eliminates the predicted T_1 crossover and fails to account for the power law exponents in the intermediate-temperature regime (50 – 125 K; see Figures S11 – S17 and discussion), further motivating our choice to use only the canonical g value derivatives.

To demonstrate the broad applicability of the thermally-weighted ligand field model, we provide T_1 predictions for $[\text{V(bdt)}_3]^{2-}$, $[\text{Cu(bdt)}_2]^{2-}$, $[\text{V(bds)}_3]^{2-}$, and $[\text{Cu(bds)}_2]^{2-}$ (bds = 1,2-benzenediselenate). Figure 2.6 shows the model predicts the same order of experimental high temperature T_1 times observed previously:[9] $[\text{Cu(bdt)}_2]^{2-}$ > $[\text{Cu(bds)}_2]^{2-}$ > $[\text{V(bdt)}_3]^{2-}$ > [V(bds)3]2-. Interestingly, the model predicts a near T_1 crossover between $[\text{Cu(bds)}_2]^{2-}$ and $[\text{V(bdt)}_3]^{2-}$ around 100 K, as observed experimentally at 60 K. In the high temperature regime, $[\text{Cu(bds)}_2]^{2-}$ is predicted to have a shallower slope than both $[V(bdt)_3]^{2-}$ and $[Cu(bdt)_2]^{2-}$, but a lower intercept than $[Cu(bdt)_2]^{2-}$. Substitution of selenium for sulfur decreases the $\partial g_z/\partial Q_i$ value for the $[Cu(bds)_2]^{2-}$ symmetric stretch relative to $[Cu(bdt)_2]^{2-}$, but also lowers the energy of that vibrational mode. The onset of symmetric stretch spin-phonon coupling thus occurs at lower temperature in $[Cu(bds)_2]^{2-}$ than $[V(bdt)_3]^{2-}$, but the high temperature magnitude of spin phonon coupling is greater in $[V(bdt)_3]^{2-}$ than $[Cu(bds)_2]^{2-}$ owing to the larger coefficients (Tables S8-S9), leading to the near T_1 crossover.

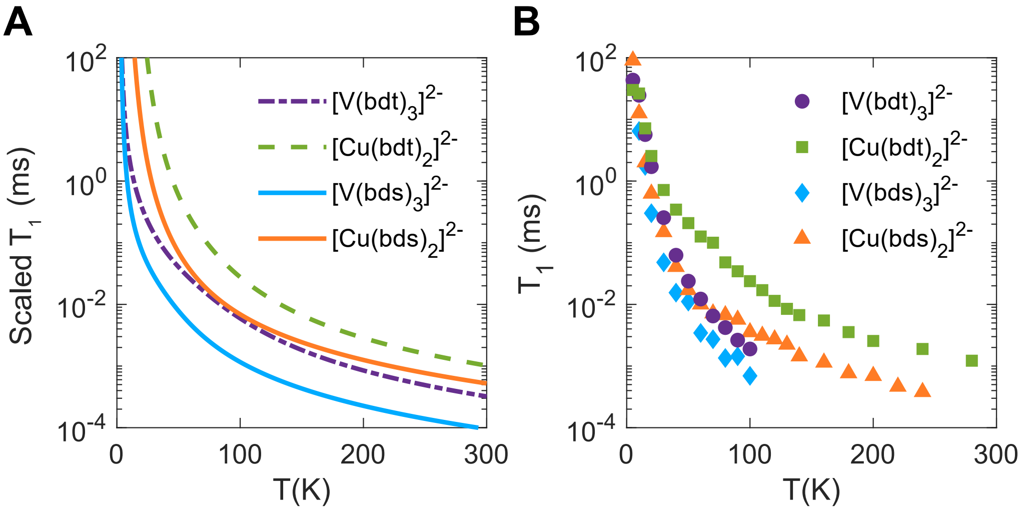

Figure 2.6: Thermally-weighted ligand field model for dithiolate and diselenate qubits. (A) T_1 predictions according to Equation (2.5). All T_1 predictions are scaled by the same factor $A = 1.01 \times 10^5\ \mu s^{-1}$, chosen to match the experimental data for $[Cu(bdt)_2]^{2-}$ at 280 K. (B) Comparison to experimental results from ref[9]. Theoretical predictions and experimental results are overlaid in Figure S10.

2.4 Discussion

It has become commonplace to fit temperature-dependent spin-lattice relaxation data with a set of polynomial and exponential functions derived from the Debye model description of direct, Raman, Orbach, and local mode relaxation processes. These fits yield values such as the Debye frequency and the Raman exponent. However, recent literature has demonstrated that Debye model parameters have no unambiguous chemical interpretation for molecular solids, as the Debye model makes incompatible assumptions regarding the nature of crystalline vibrations.[6] This hinders rational molecular design for quantum information science. A new molecular paradigm based on symmetry and vibrational principles is required.[4,6,24]

We argue that the present study provides a novel and attractive perspective for modeling T_1 on distinctly chemical grounds. Dynamic ligand field theory successfully predicts the magnitude[22] and symmetry-based selection rules for the spin-phonon coupling coefficients. Coupled with thermal weighting, this model successfully predicts relative T_1 trends and crossovers for a variety of structurally diverse molecular qubits. The group theory selection rules and functional forms employed for temperature-dependent T_1 times are explicitly grounded in physical quantities for molecular solids, unlike in the Debye model. Previous work has considered the role of bonding descriptors such as covalency, excited state energy, and the spin-orbit coupling constant in predicting the overall magnitudes of the spin-phonon coupling coefficients between different molecules.[19,22,23] These insights can be integrated with the group theory and thermal weighting approaches described herein. Beyond the magnetically-dilute crystals considered in this work, this model will also describe intramolecular contributions to T_1 for frozen glass and solution phase systems, though spin-spin and motional contributions will be important considerations as well.[6] We anticipate that the group theory methodology will yield insight into the molecular origins of T_1 times across a broad range of molecular electron spin qubits. Similar spin-orbit coupling expressions exist for organic radicals,[44–46] such as nitroxide spin labels, and will likely enable an analogous theory of spin-phonon coupling.[40] Analysis of transition metal qubits in trigonal coordination environments will expand the range of symmetries considered,[35,36] and applications to S > ½ optically addressable qubits may be enabled by applying group theory to zero-field splitting expressions.[47,48]

The simplicity of the model in this study necessarily comes with approximations and limitations that should be clearly acknowledged. First, the direct process is entirely ignored, so the model will fail at very low temperatures (<10 – 20 K).[12] Second, the phonon dispersion across the Brillouin zone is not taken into account. Optical phonons are approximated by gas-phase calculations at the Γ point and acoustic phonons are ignored, implying the model will fail whenever the solid does not possess low-temperature molecular vibrations (i.e., non-molecular solids). These systematic errors likely accounts for much of the temperature offsets between predicted and observed quantities such as crossover points; however, experimental[40] and theoretical[12] analyses suggests that acoustic phonons are not important at temperatures much above the direct process regime. Third, the quantity $\partial \boldsymbol{g}/\partial Q$ is used as a proxy for $\partial^2 \boldsymbol{g}/\partial Q_i \partial Q_j$, the Raman coupling term predicted by Redfield theory.[12] As a result, it is challenging to convert the present model into an absolute rate prediction. However, the model can be accurately calibrated by comparison to molecular spin qubits with known values of T_1, and the magnitude of the two derivatives are expected to trend similarly.[20] The scaling constants used to match the data in Figures 5 and 6 agree to within 30%, suggesting that a scaling constant around 1×10^5 μs^{-1} may be used to extend this model to complexes for which experimental data do not exist.

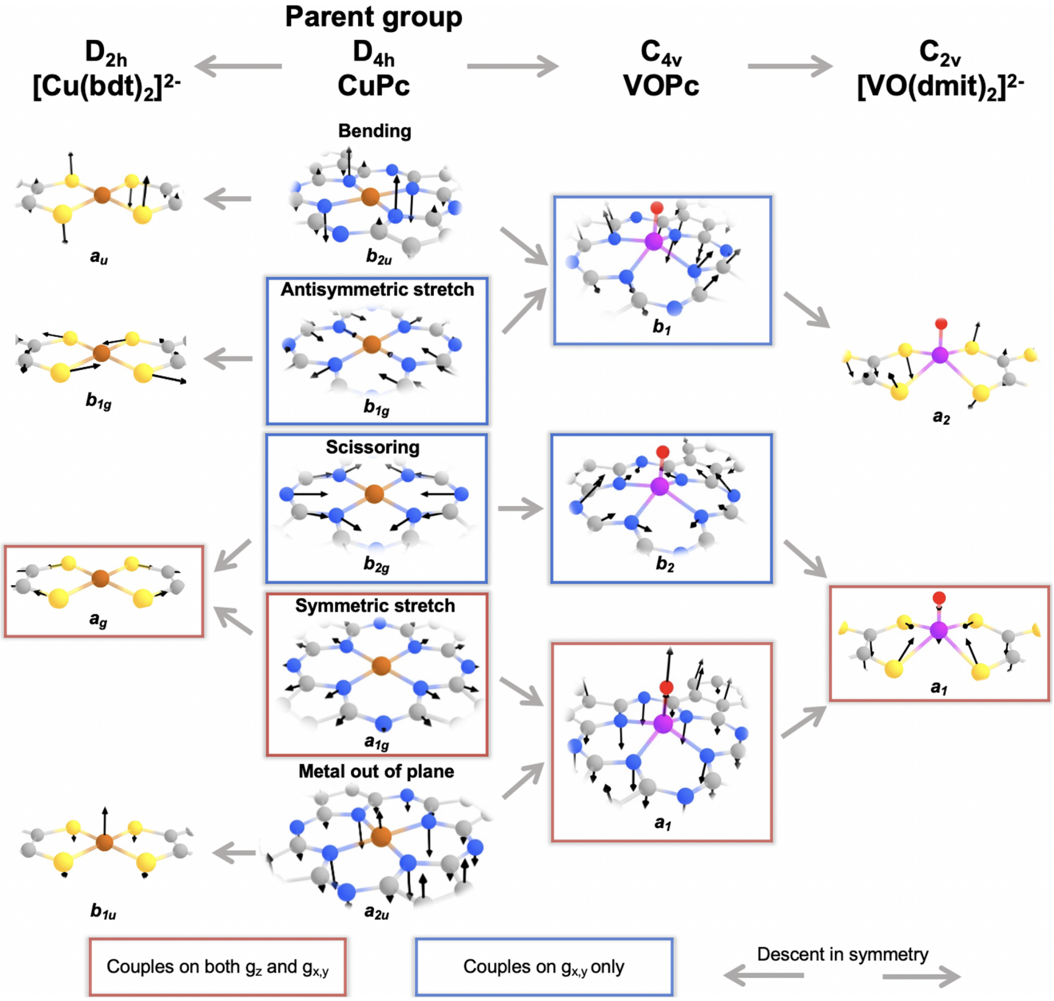

Figure 2.7: Symmetry flowchart of spin-phonon coupling coefficients. Convergent arrows indicate that vibrational modes mix under reduced-symmetry point groups, and boxes indicate the selection rules derived from Equation (2.4).

In this study, we have analyzed archetypal qubits from four point groups: D_{4h}, D_{2h}, C_{4v}, and C_{2v}. Because D_{2h}, C_{4v} and C_{2v} are all subgroups of D_{4h}, the impact of symmetry on spin-phonon coupling can be viewed through the perspective of descent in symmetry on the CuPc structure (Figure 2.7). True D_{4h} complexes such as CuPc and D_{4h} $CuCl_4^{2-}$ exhibit only a single g_z-active mode in the thermally accessible region, corresponding to the a_{1g} totally symmetric ligand-metal stretch (Table S5). The b_{1g} antisymmetric ligand-metal stretch and the b_{2g} scissoring mode are also able to couple for g_x. Descent in symmetry to C_{4v} activates the a_{2u} (D_{4h}) out-of-plane modes, which transform as a_1 in C_{4v}. Phthalocyanine ligand scaffolds support many such low-energy a_{2u} modes, with CuPc possessing four a_{2u} modes below 400 cm^{-1} (Table S5). These are activated for coupling in VOPc (Table 2.1, Table S4), resulting in a smaller T_1 slope than CuPc and a characteristic crossover point. Descent in symmetry to D_{2d} is known to activate new modes for spin-phonon coupling, as the b_{2u} bending mode in D_{4h} transforms as a_1 in the distorted D_{2d} point group.[22] Descent in symmetry to D_{2h} shuts down g_x spin-phonon coupling for the antisymmetric stretch b_{1g} mode while activating g_z coupling for the b_{2g} (D_{4h}) scissoring mode, which transforms as a_g in D_{2h}. The resulting a_g modes contain a mixture of symmetric stretch and scissoring character. This suggests that spin-phonon coupling could be decreased by selectively hindering scissoring and out-of-plane modes in lower symmetry point groups, a novel symmetry-based design strategy for molecular qubits.

In summary, we have developed a novel thermally-weighted dynamic ligand field model to describe and predict T_1 in molecular electron spin qubit candidates. The methodology has allowed for the determination of the specific vibrational modes that give rise to decoherence in the T_1-limited regime, ultimately elucidating the critical spin-phonon coupling, chemical bonding, and symmetry factors leading to room temperature coherence. It can be employed to a priori predict new S = ½ transition metal complexes that may exhibit this phenomenon. Group theory prediction of anisotropic spin-phonon coupling coefficients may prove particularly important in the context of quantum sensing, where anisotropic g values provide a key motivation for employing transition metal complexes as spectrally addressable quantum sensors.

We believe future modeling work in the spin-phonon coupling field will profit from combining this molecular group theory approach with *ab initio* spin dynamics modeling employing Redfield theory.[12,15,49,50] The strengths of these approaches complement each other: the former provides a direct connection to both chemical bonding parameters and analytical predictions of coupling terms, while the latter can simultaneously account for multiple relaxation mechanisms and predict the absolute relaxation rates without the need for a scaling parameter. Even when low symmetry molecules are considered *ab initio*, the descent in symmetry approach outlined in

Figure 2.7 can provide a rational analysis of the magnitudes of coupling coefficients for different modes. A combined approach will have greater interpretability and predictive power than either alone.

Finally, we note that development of spin-phonon coupling models to date has suffered from a lack of experimental constraints. While the temperature-dependent relaxation times provide a single vector of data to reference, modeling these data demands calculation of coupling coefficients for dozens or hundreds of vibrational modes. There exists no way to independently verify the accuracy of the calculated coefficients, and many combinations of spin-phonon coupling parameters could in principle account for similar temperature-dependent relaxation behavior. While *ab initio* models have been steadily improving in both theoretical rigor and fidelity to existing data, we believe new spectroscopic techniques are called for to garner insight into spin-phonon coupling, including the direct experimental observation of spin-phonon coupling coefficients.

References

[1] Atzori, M.; Sessoli, R. The Second Quantum Revolution: Role and Challenges of Molecular Chemistry. *Journal of the American Chemical Society* **2019**, *141,* 11339–11352.

[2] Wasielewski, M. R. *et al.* Exploiting Chemistry and Molecular Systems for Quantum Information Science. *Nature Reviews Chemistry* **2020**, *4,* 490–504.

[3] Graham, M. J.; Zadrozny, J. M.; Fataftah, M. S.; Freedman, D. E. Forging Solid-State Qubit Design Principles in a Molecular Furnace. *Chemistry of Materials* **2017**, *29,* 1885–1897.

[4] Escalera-Moreno, L.; Baldoví, J. J.; Gaita-Ariño, A.; Coronado, E. Spin States, Vibrations and Spin Relaxation in Molecular Nanomagnets and Spin Qubits: a Critical Perspective. *Chemical Science* **2018**, *9,* 3265–3275.

[5] Aromí, G.; Aguilà, D.; Gamez, P.; Luis, F.; Roubeau, O. Design of Magnetic Coordination Complexes for Quantum Computing. *Chemical Society Reviews* **2012**, *41,* 537–546.

[6] Mirzoyan, R.; Kazmierczak, N. P.; Hadt, R. G. Deconvolving Contributions to Decoherence in Molecular Electron Spin Qubits: A Dynamic Ligand Field Approach. *Chemistry – A European Journal* **2021**, *27,* 9482–9494.

[7] Nielsen, M. A.; Chuang, I. L. *Quantum Computation and Quantum Information: 10th Anniversary Edition;* Cambridge University Press: Cambridge ; New York, 1st ed.; 2010.

[8] Atzori, M.; Tesi, L.; Morra, E.; Chiesa, M.; Sorace, L.; Sessoli, R. Room-Temperature Quantum Coherence and Rabi Oscillations in Vanadyl Phthalocyanine: Toward Multifunctional Molecular Spin Qubits. *Journal of the American Chemical Society* **2016**, *138,* 2154–2157.

[9] Fataftah, M. S.; Krzyaniak, M. D.; Vlaisavljevich, B.; Wasielewski, M. R.; Zadrozny, J. M.; Freedman, D. E. Metal-Ligand Covalency Enables Room Temperature Molecular Qubit Candidates. *Chemical Science* **2019**, *10,* 6707–6714.

[10] Standley, K. J.; Vaughan, R. A. *Electron Spin Relaxation Phenomena in Solids;* Springer US: Boston, MA, 1969. DOI: 10.1007/978-1-4899-6539-4.

[11] Bloch, F. Nuclear Induction. *Physical Review* **1946**, *70,* 460–474.

[12] Lunghi, A.; Sanvito, S. The Limit of Spin Lifetime in Solid-State Electronic Spins. *The Journal of Physical Chemistry Letters* **2020**, *11,* 6273–6278.

[13] Van Vleck, J. H. Paramagnetic Relaxation Times for Titanium and Chrome Alum. *Physical Review* **1940**, *57,* 426–447.

[14] Orbach, R. Spin-Lattice Relaxation in Rare-Earth Salts. *Proceedings of the Royal Society of London A* **1961**, *264,* 458–484.

[15] Lunghi, A.; Sanvito, S. How Do Phonons Relax Molecular Spins? *Science Advances* **2019**, *5,* eaax7163.

[16] Zhou, Y.; Bowler, B. E.; Eaton, G. R.; Eaton, S. S. Electron Spin Lattice Relaxation Rates for S=1/2 Molecular Species in Glassy Matrices or Magnetically Dilute Solids at Temperatures between 10 and 300 K. *Journal of Magnetic Resonance* **1999**, *139,* 165–174.

[17] Escalera-Moreno, L.; Suaud, N.; Gaita-Ariño, A.; Coronado, E. Determining Key Local Vibrations in the Relaxation of Molecular Spin Qubits and Single-Molecule Magnets. *The Journal of Physical Chemistry Letters* **2017**, *8,* 1695–1700.

[18] Bader, K.; Winkler, M.; van Slageren, J. Tuning of Molecular Qubits: Very Long Coherence and Spin-Lattice Relaxation Times. *Chemical Communications* **2016**, *52,* 3623–3626.

[19] Follmer, A. H.; Ribson, R. D.; Oyala, P. H.; Chen, G. Y.; Hadt, R. G. Understanding Covalent versus Spin-Orbit Coupling Contributions to Temperature-Dependent Electron Spin Relaxation in Cupric and Vanadyl Phthalocyanines. *The Journal of Physical Chemistry A* **2020**, *124,* 9252–9260.

[20] Albino, A.; Benci, S.; Tesi, L.; Atzori, M.; Torre, R.; Sanvito, S.; Sessoli, R.; Lunghi, A. First-Principles Investigation of Spin-Phonon Coupling in Vanadium-Based Molecular Spin Quantum Bits. *Inorganic Chemistry* **2019**, *58,* 10260–10268.

[21] Garlatti, E.; Tesi, L.; Lunghi, A.; Atzori, M.; Voneshen, D. J.; Santini, P.; Sanvito, S.; Guidi, T.; Sessoli, R.; Carretta, S. Unveiling Phonons in a Molecular Qubit with Four-Dimensional Inelastic Neutron Scattering and Density Functional Theory. *Nature Communications* **2020**, *11,* 1751.

[22] Mirzoyan, R.; Hadt, R. G. The Dynamic Ligand Field of a Molecular Qubit: Decoherence through Spin-Phonon Coupling. *Physical Chemistry Chemical Physics* **2020**, *22,* 11249–11265.

[23] Lunghi, A. Ligand-Field Contributions to Spin-Phonon Coupling in a Family of Vanadium Molecular Qubits from Multi-Reference Electronic Structure Theory. *arXiv:1912.04545 [cond-mat, physics:quant-ph]* **2019**.

[24] Santanni, F.; Albino, A.; Atzori, M.; Ranieri, D.; Salvadori, E.; Chiesa, M.; Lunghi, A.; Bencini, A.; Sorace, L.; Totti, F.; Sessoli, R. Probing Vibrational Symmetry Effects and Nuclear Spin Economy Principles in Molecular Spin Qubits. *Inorganic Chemistry* **2021**, *60,* 140–151.

[25] Lunghi, A.; Totti, F.; Sessoli, R.; Sanvito, S. The Role of Anharmonic Phonons in Under-Barrier Spin Relaxation of Single Molecule Magnets. *Nature Communications* **2017**, *8,* 14620.

[26] Ballhausen, C. J. *Introduction to Ligand Field Theory;* McGraw-Hill: 1962.

[27] Solomon, E. I. Inorganic Spectroscopy—An Overview. *Comments on Inorganic Chemistry* **1984**, *3,* 227–320.

[28] Harris, D. C.; Bertolucci, M. D. *Symmetry and Spectroscopy: An Introduction to Vibrational and Electronic Spectroscopy;* Dover Publications: New York, 1989.

[29] Jahn, H. A.; Teller, E.; Donnan, F. G. Stability of Polyatomic Molecules in Degenerate Electronic States: I—Orbital Degeneracy. *Proceedings of the Royal Society of London. Series A - Mathematical and Physical Sciences* **1937**, *161,* 220–235.

[30] Atkins, P. W.; Friedman, R. S. *Molecular Quantum Mechanics;* Oxford University Press: Oxford ; New York, 5th ed.; 2010.

[31] Feynman, R. P. Forces in Molecules. *Physical Review* **1939**, *56,* 340–343.

[32] Wilson, R. B.; Solomon, E. I. Spectroscopic Studies of the Photoactive $^4T_{2g}$ Excited State of Hexaamminechromium(III). *Inorganic Chemistry* **1978**, *17,* 1729–1736.

[33] Wilson, R. B.; Solomon, E. I. Spectroscopic Studies of Photochemically Important Transition Metal Excited States. 2. The $^1T_{1g}$, $^3T_{1g}$, and $^5T_{2g}$ Excited States of Hexaamminecobalt(III). *Journal of the American Chemical Society* **1980**, *102,* 4085–4095.

[34] Szilagyi, R. K.; Metz, M.; Solomon, E. I. Spectroscopic Calibration of Modern Density Functional Methods Using $[CuCl_4]^{2-}$. *The Journal of Physical Chemistry A* **2002**, *106,* 2994–3007.

[35] Ariciu, A.-M.; Woen, D. H.; Huh, D. N.; Nodaraki, L. E.; Kostopoulos, A. K.; Goodwin, C. A. P.; Chilton, N. F.; McInnes, E. J. L.; Winpenny, R. E. P.; Evans, W. J.; Tuna, F. Engineering Electronic Structure to Prolong Relaxation Times in Molecular Qubits by Minimising Orbital Angular Momentum. *Nature Communications* **2019**, *10,* 3330.

[36] Fataftah, M. S.; Bayliss, S. L.; Laorenza, D. W.; Wang, X.; Phelan, B. T.; Wilson, C. B.; Mintun, P. J.; Kovos, B. D.; Wasielewski, M. R.; Han, S.; Sherwin, M. S.; Awschalom, D. D.; Freedman, D. E. Trigonal Bipyramidal V^{3+} Complex as an Optically Addressable Molecular Qubit Candidate. *Journal of the American Chemical Society* **2020**, *142,* 20400–20408.

[37] Du, J.-L.; Eaton, G. R.; Eaton, S. S. Temperature and Orientation Dependence of Electron-Spin Relaxation Rates for Bis(diethyldithiocarbamato)copper(II). *Journal of Magnetic Resonance, Series A* **1995**, *117,* 67–72.

[38] Konda, R.; Du, J. L.; Eaton, S. S.; Eaton, G. R. Electron Spin Relaxation Rates for Nitridochromium(V) Tetratolylporphyrin and Nitridochromium(V) Octaethylporphyrin in Frozen Solution. *Applied Magnetic Resonance* **1994**, *7,* 185–193.

[39] Du, J. L.; Eaton, G. R.; Eaton, S. S. Electron-Spin-Lattice Relaxation in Natural Abundance and Isotopically Enriched Oxo-chromium(V)bis (2-hydroxy-2-ethylbutyrate). *Journal of Magnetic Resonance, Series A* **1995**, *115,* 236–240.

[40] Du, J. L.; Eaton, G. R.; Eaton, S. S. Temperature, Orientation, and Solvent Dependence of Electron Spin-Lattice Relaxation Rates for Nitroxyl Radicals in Glassy Solvents and Doped Solids. *Journal of Magnetic Resonance, Series A* **1995**, *115,* 213–221.

[41] Camargo, L. C.; Briganti, M.; Santana, F. S.; Stinghen, D.; Ribeiro, R. R.; Nunes, G. G.; Soares, J. F.; Salvadori, E.; Chiesa, M.; Benci, S.; Torre, R.; Sorace, L.; Totti, F.; Sessoli, R. Exploring the Organometallic Route to Molecular Spin Qubits: The [CpTi(cot)] Case. *Angewandte Chemie International Edition* **2021**, *60,* 2588-2593.

[42] Castle, J. G.; Feldman, D. W.; Klemens, P. G.; Weeks, R. A. Electron Spin-Lattice Relaxation at Defect Sites; E Centers in Synthetic Quartz at 3 Kilo-Oersteds. *Physical Review* **1963**, *130,* 577–588.

[43] Castle, J. G.; Feldman, D. W. Resonance Modes at Defects in Crystalline Quartz. *Physical Review* **1965**, *137,* A671–A673.

[44] Stone, A. g Factors of Aromatic Free Radicals. *Molecular Physics* **1963**, *6,* 509–515.

[45] Un, S.; Atta, M.; Fontecave, M.; Rutherford, A. W. g-Values as a Probe of the Local Protein Environment: High-Field EPR of Tyrosyl Radicals in Ribonucleotide Reductase and Photosystem II. *Journal of the American Chemical Society* **1995**, *117,* 10713–10719.

[46] Sinnecker, S.; Rajendran, A.; Klamt, A.; Diedenhofen, M.; Neese, F. Calculation of Solvent Shifts on Electronic g-Tensors with the Conductor-Like Screening Model (COSMO) and Its Self-Consistent Generalization to Real Solvents (Direct COSMO-RS). *The Journal of Physical Chemistry A* **2006**, *110,* 2235–2245.

[47] Higdon, N. J.; Barth, A. T.; Kozlowski, P. T.; Hadt, R. G. Spin-Phonon Coupling and Dynamic Zero-Field Splitting Contributions to Spin Conversion Processes in Iron(II) Complexes. *The Journal of Chemical Physics* **2020**, *152,* 204306.

[48] Bayliss, S. L.; Laorenza, D. W.; Mintun, P. J.; Kovos, B. D.; Freedman, D. E.; Awschalom, D. D. Optically Addressable Molecular Spins for Quantum Information Processing. *Science* **2020**, *370,* 1309–1312.

[49] Briganti, M.; Santanni, F.; Tesi, L.; Totti, F.; Sessoli, R.; Lunghi, A. A Complete Ab Initio View of Orbach and Raman Spin-Lattice Relaxation in a Dysprosium Coordination Compound. *Journal of the American Chemical Society* **2021**, *143,* 13633–13645.

[50] Reta, D.; Kragskow, J. G. C.; Chilton, N. F. Ab Initio Prediction of High-Temperature Magnetic Relaxation Rates in Single-Molecule Magnets. *Journal of the American Chemical Society* **2021**, *143,* 5943–5950.

Chapter 3

DETERMINING THE KEY VIBRATIONS FOR SPIN RELAXATION IN RUFFLED COPPER(II) PORPHYRINS VIA RESONANCE RAMAN SPECTROSCOPY

- Adapted with permission from: Kazmierczak, N. P.; Lopez, N. E.; Luedecke, K. M.; Hadt, R. G. Determining the Key Vibrations for Spin Relaxation in Ruffled Cu(II) Porphyrins via Resonance Raman Spectroscopy. *Chemical Science* **2024**, *15*, 2380–2390. DOI: 10.1039/D3SC05774G. © 2024 The Royal Society of Chemistry.

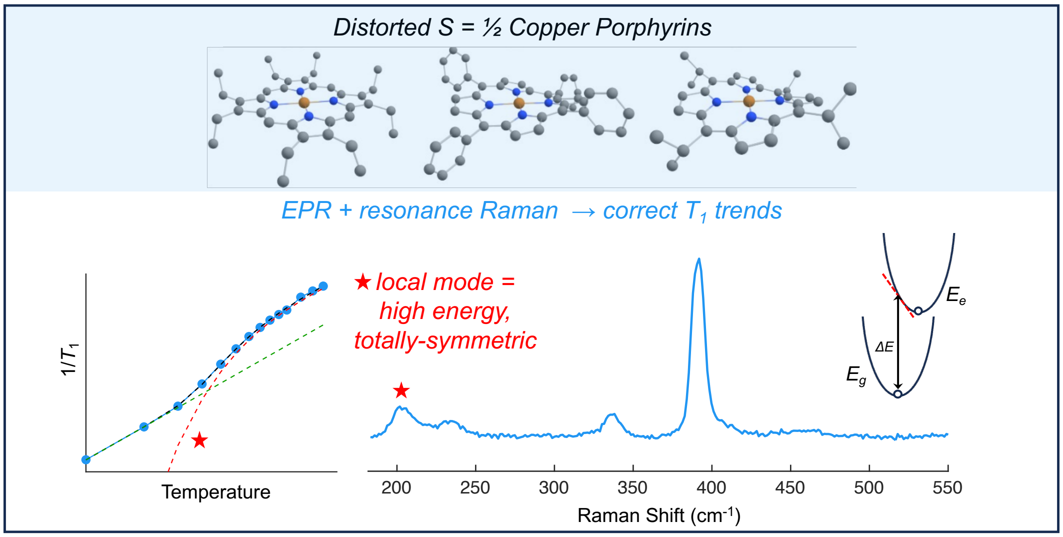

3.1 Abstract

Pinpointing vibrational mode contributions to electron spin relaxation (T_1) constitutes a key goal for developing molecular quantum bits (qubits) with long room-temperature coherence times. However, there remains no consensus to date as to the energy and symmetry of the relevant modes that drive relaxation. Here, we analyze a series of three geometrically-tunable S = ½ Cu(II) porphyrins with varying degrees of ruffling distortion in the ground state. Theoretical calculations predict that increased distortion should activate low-energy ruffling modes (~50 cm^{-1}) for spin-phonon coupling, thereby causing faster spin relaxation in distorted porphyrins. However, experimental T_1 times do not follow the degree of ruffling,

with the highly distorted copper tetraisopropylporphyrin (CuTiPP) even displaying room-temperature coherence. Local mode fitting indicates that the true vibrations dominating T_1 lie in the energy regime of bond stretches (~200 – 300 cm^{-1}), which are comparatively insensitive to the degree of ruffling. We employ resonance Raman (rR) spectroscopy to determine vibrational modes possessing both the correct energy and symmetry to drive spin-phonon coupling. The rR spectra uncover a set of mixed symmetric stretch vibrations from 200 – 250 cm^{-1} that explain the trends in temperature-dependent T_1. These results indicate that molecular spin-phonon coupling models systematically overestimate the contribution of ultra-low-energy distortion modes to T_1, pointing out a key deficiency of existing theory. Furthermore, this work highlights the untapped power of rR spectroscopy as a tool for building spin dynamics structure-property relationships in molecular quantum information science.

3.2 Introduction

The rise of molecular quantum information science has placed new importance on developing molecules with long-lasting electron spin coherence times (T_2), a parameter which sets the maximum length of time quantum information can be stored and processed.[1] At elevated temperatures, vibration-mediated spin relaxation (T_1) limits the maximum attainable value of T_2,[2] implying that vibrations effectively leak quantum information into the environment. While room-temperature electron spin coherence has been measured in a handful of S = ½ systems,[3–8] other key classes of molecular qubits, such as the Cr(IV) optically addressable qubits, remain limited to sub-liquid nitrogen temperatures owing to T_1-limited T_2.[9–12] Thus, understanding the relationship between molecular geometric / electronic structure and spin relaxation rates remains a key mechanistic goal of molecular quantum information science. The number of thermally-accessible vibrational modes that could potentially contribute to spin relaxation renders such investigations theoretically and spectroscopically challenging.

One approach to build T_1 mechanistic understanding is to employ theoretical models of the spin-relaxation process. Several models based on the easily-handled spin Hamiltonian have been proposed, but crucially, multiple expressions have been used for the spin-phonon coupling coefficient (Figure 3.1A). One can use derivatives of either the g-tensor[2,13–17] or the hyperfine tensor,[15,16] pick different elements of the tensor (on-diagonal only[2,5,13,14] vs. including off-diagonal[15–17]), and employ first[13–15] vs. second[16,18] derivatives. Depending on the theoretical choices made, different vibrational modes are predicted to dominate spin relaxation, ranging from ultra-low-energy e_g rotational modes (<50 cm^{-1})[19] to totally symmetric metal-ligand stretching modes (>200 cm^{-1}).[2,13,14] None of these spin Hamiltonian models can be considered mechanistically definitive due to two key issues: (1) derivatives of a spin Hamiltonian tensor do not constitute true matrix elements between spin states,[20] no matter how sophisticated the quantum master equation[21] used to handle the rate calculations, and (2) no spin Hamiltonian model successfully accounts for T_1 anisotropy, which instead requires analysis of spin-orbit wavefunctions.[20] At best, spin Hamiltonian models can predict the average temperature-dependent T_1 over all molecular orientations, functioning as a proxy for the true spin-orbit mechanism.[20] Further discrepancies arise when comparing the theoretically predicted temperature scaling of T_1 to experiment. On the basis of ultra-low-energy modes, contemporary *ab initio* models commonly predict flat, single-exponent power law behavior[19] for temperature-dependent T_1. However, experimental log-log plots of $1/T_1$ vs. temperature display marked curvature for most S = ½ molecular qubits, which has been interpreted by local mode fitting to indicate the contribution of molecular vibrational modes >100 cm^{-1} that give rise to a nonconstant power law exponent.[14,22,23] Experimentally-parameterized T_1 models have successfully reproduced this curvature for high-symmetry Cu(II) and V(IV) complexes,[14] but the curvature is not successfully predicted by *ab initio* models that emphasize ultra-low-energy modes.[19] We conclude that *ab initio* prediction of T_1 in S = ½ molecular qubits has not yet achieved satisfactory agreement with experimental data.

Alternatively, mechanistic understanding may be developed from experimentally-determined T_1 structure-property relationships. While relatively few such relationships have been explored in detail, one of the best-established connections has been demonstrated between the degree of first coordination sphere planarity and T_1 in four-coordinate Cu(II) S = ½ molecular qubits.[2] Two limiting geometries are possible: square planar (D_{4h}), in which the opposing L-M-L bond angle is 180°, and tetrahedral (T_d), in which the opposing L-M-L bond angle is 109.5°. From the D_{4h} geometry, ligated atoms can undergo distortion along the b_{2u} bending mode, which lowers the point group to D_{2d} and systematically decreases the L-M-L angle from 180° towards 109.5°. It has been experimentally demonstrated that planar structures have longer spin lifetimes (long T_1) than b_{2u}-distorted structures.[5,23] This result can be understood via application of group theory selection rules to the spin-phonon coupling problem.[13,14] In order for a vibrational mode to cause spin relaxation by altering the g value, it must transform as either a totally symmetric vibrational mode

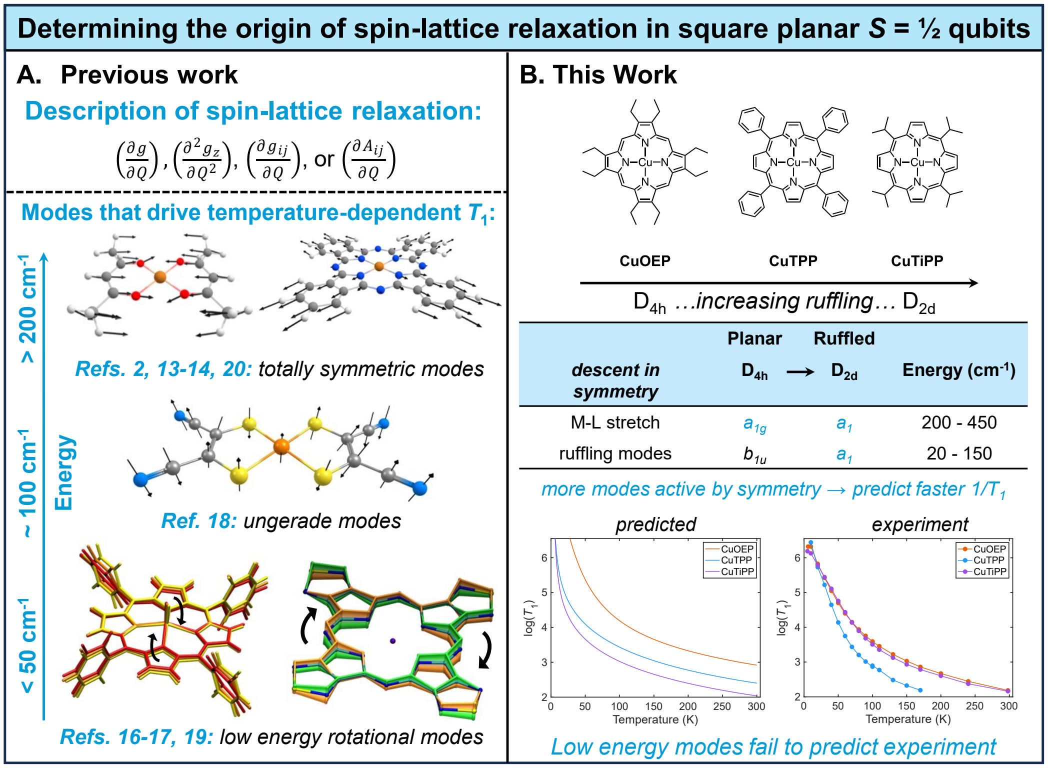

Figure 3.1: Mechanistic studies of spin-lattice relaxation in S = ½ qubits. (A) Previous theoretical studies have employed a variety of models for molecular spin-phonon coupling, leading to disparate predictions of modes with different energies and symmetries driving spin relaxation. Figures adapted with permission from refs.[17–20]. (B) This work systematically probes the effect of the b_{1u} ruffling distortion on spin relaxation in a series of copper porphyrins, finding that existing theory systematically overestimates the contribution of low-energy ruffling modes.

(a_1 or a_{1g}) or an excited state Jahn-Teller mode. In the D_{4h} geometry, the b_{2u} bending mode does not satisfy these symmetry requirements. However, once the equilibrium structure has been distorted along the bending motion in the D_{2d} point group, the bending mode now transforms as a_1 and can induce spin relaxation, as confirmed by calculation of $\partial g/\partial Q$ spin-phonon coupling coefficients.[13] This specific relationship illustrates a general principle: when a high-symmetry equilibrium structure is distorted along a non-totally-symmetric vibrational mode, that mode transforms as the totally symmetric representation in the new point group (Figure 3.1B, Supporting Information Section 4C) and can cause spin relaxation.[14]

Metalloporphyrins offer an attractive platform for extending T_1 structure-property relationships to new types of molecular geometries. Depending on the steric hindrance and substitutional pattern of peripheral moieties, porphyrins may adopt equilibrium geometries with saddled (b_{2u}), ruffled (b_{1u}), domed (a_{2u}), or waved (e_g) distortions, where the labels indicate the symmetry of the distorting vibrational mode in the D_{4h} point group.[24] The saddling distortion is equivalent to the same first coordination sphere bending distortion to D_{2d} described above (Figure 3.2B-C). By contrast, the b_{1u} ruffling distortion (Figure 3.2B-C) also results in a D_{2d} equilibrium geometry, but the first coordination sphere remains completely unaltered (Figure 3.2A). Instead, the porphyrin meso carbons are distorted above and below the plane of the first coordination sphere, rendering ruffling a secondary-sphere structural distortion. By analogy to the b_{2u} bending mode argument, the b_{1u} ruffling mode will transform as a_1 in the D_{2d} distorted point group, opening up the possibility of contributions to spin relaxation (Supporting Information Section 4C). Ruffling modes in porphyrins exist in the ultra-low energy range (~50 cm^{-1}), indicating that ruffled S = ½ porphyrins may show a decisive, unique contribution of low-energy modes to T_1.

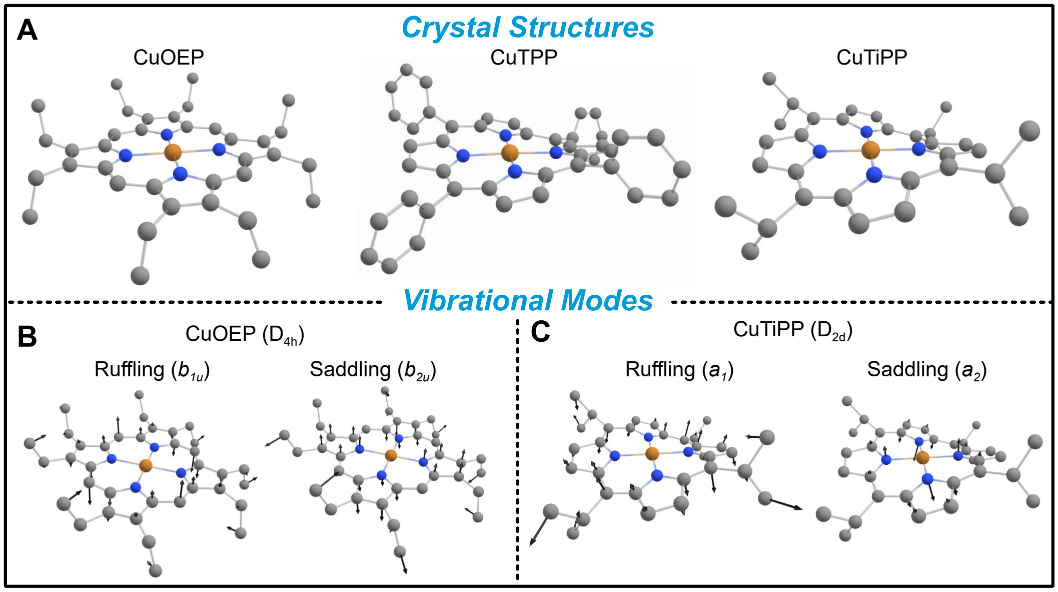

Figure 3.2: Geometries of ruffled metalloporphyrins. (A) Crystal structures demonstrate increasing static ruffling in the series CuOEP < CuTPP < CuTiPP. (B) Representative ruffling and saddling vibrational modes for CuOEP transform as non-totally-symmetric irreducible representations (irreps) due to the planar D_{4h} point group (ethyl groups neglected). Only the saddling mode alters the first coordination sphere geometry. (C) The static distortion of CuTiPP causes the ruffling vibration to transform as the totally-symmetric irrep in the new D_{2d} point group, while the saddling vibration remains non-totally-symmetric. H atoms omitted for clarity.

In this study, we measure temperature-dependent T_1 via pulse electron paramagnetic resonance (EPR) on a series of three Cu(II) metalloporphyrins (CuP) (Figure 3.1B, 3.2A): copper octaethylporphyrin (CuOEP), copper tetraphenylporphyrin (CuTPP), and copper tetraisopropylporphyrin (CuTiPP). CuOEP possesses a planar crystal structure, while CuTPP and CuTiPP exhibit increasing degrees of the ruffling distortion (Figure 3.2A). Computational modeling via density functional theory (DFT) suggests that T_1 times should decrease with increasing ruffling distortion. However, experimental T_1 measurements do not trend with ruffling: the planar CuOEP and highly ruffled CuTiPP display robust room-temperature coherence while the moderately ruffled CuTPP does not. The breakdown of the computational analysis can be attributed to an over-emphasis of the lowest energy ruffling mode. We then employ resonance Raman (rR) spectroscopy to detect the vibrational modes driving spin relaxation across this series and find a set of symmetric stretching vibrations in the 200 – 300 cm^{-1} region that trend with the experimentally observed T_1. Our results demonstrate that ultra-low energy modes do not drive spin relaxation in copper porphyrins, thereby distinguishing between conflicting theoretical models of spin relaxation (Figure 3.1A).

3.3 Results

To quantify the amount of distortion in a given metalloporphyrin crystal structure, we applied the normal coordinate structural decomposition (NSD) developed by Shelnutt[25] and implemented in the program by Kingsbury and Senge.[24] CuOEP was chosen as the undistorted control compound, as it displays no tendency towards ruffling and only slight amounts of waving (Table 3.1). The distorted ruffled structures were chosen according to two criteria: (a) ruffling should be by far the largest distortion of the porphyrin, and (b) there must exist a diamagnetic host matrix of comparable distortions for preparation of EPR solid-state dilution samples. CuTPP and CuTiPP satisfy criterion (a), with CuTPP having only a small secondary saddling distortion and CuTiPP having a very small secondary waving distortion. Regarding criterion (b), the corresponding Ni(II) porphyrins both display dominant ruffling distortions. The NiTPP matrix is closely matched to the CuTPP structure in both the primary magnitude of ruffling and the secondary saddling, while the NiTiPP matrix displays somewhat increased ruffling over the Cu structure (2.03 vs. 1.35) and an additional saddling distortion (0.46 vs. 0.00). These metrics indicate that the ruffling distortion increases in the series CuOEP < CuTPP < CuTiPP. Note that metalloporphyrins can crystallize in multiple phases: while the ruffled structure for

CuTPP is the more common polymorph in the Cambridge Structure Database,[26–28] there also exist two planar polymorphs.[29,30] Additionally, we obtained a new ruffled solvate crystal phase for CuTiPP through single crystal X-ray diffraction (Supporting Information Section 2C). We confirmed that all EPR sample preparations in this work adhered to the ruffled (or, for CuOEP and ZnOEP, planar) geometries via powder X-ray diffraction (PXRD) and Rietveld refinement for comparison to the single crystal structures (Supporting Information Section 2B, 4B). Good EPR sample agreement with the polymorphs used for the NSD analysis in Table 3.1 was found in all cases.

Distortion mode	Ruffling (b_{1u})	Sadding (b_{2u})	Doming (a_{2u})	Waving ($e_g(x)$)	Waving ($e_g(y)$)
CuOEP	0.00	0.00	0.00	0.11	0.05
CuTPP	1.18	0.22	0.00	0.00	0.00
CuTiPP	1.35	0.00	0.00	0.00	0.11
ZnOEP	0.00	0.00	0.00	0.16	0.06
NiTPP	1.27	0.27	0.00	0.00	0.00
NiTiPP	2.03	0.46	0.03	0.09	0.10

Table 3.1: Normal coordinate structural decomposition analysis of porphyrin distortions.

Temperature-dependent T_1 measurements were acquired for all three CuP species (Figure 3.3), prepared as 1% solid-state powder dilutions in the corresponding isostructural diamagnetic host (Table 3.1). Inversion recovery traces were acquired at field positions corresponding to both perpendicular (Figure 3.3B) and parallel (Figure 3.3C) orientations.[20] CuTPP exhibits the fastest spin relaxation of all CuP species at both field positions, with a particularly distinct relaxation trend at the perpendicular position. The comparatively fast spin relaxation is consistent with previous studies on Ti(III)/CuTPP bimetallic and monometallic congeners in solution,[31] as well as CuTPP embedded in a metal-organic framework (MOF),[32,33] which did not observe room-temperature coherence for CuTPP. CuOEP exhibits the slowest relaxation (i.e., longest T_1 time) at the perpendicular position, while CuTiPP exhibits the slowest relaxation at the parallel position; the orientation-averaged $1/T_1$ values are very similar for CuOEP and CuTiPP (Figure S36). Observer position differences in spin relaxation point to the presence of T_1 anisotropy for the three CuP species. T_1 anisotropy arises from the presence of anisotropic minority spin contri-

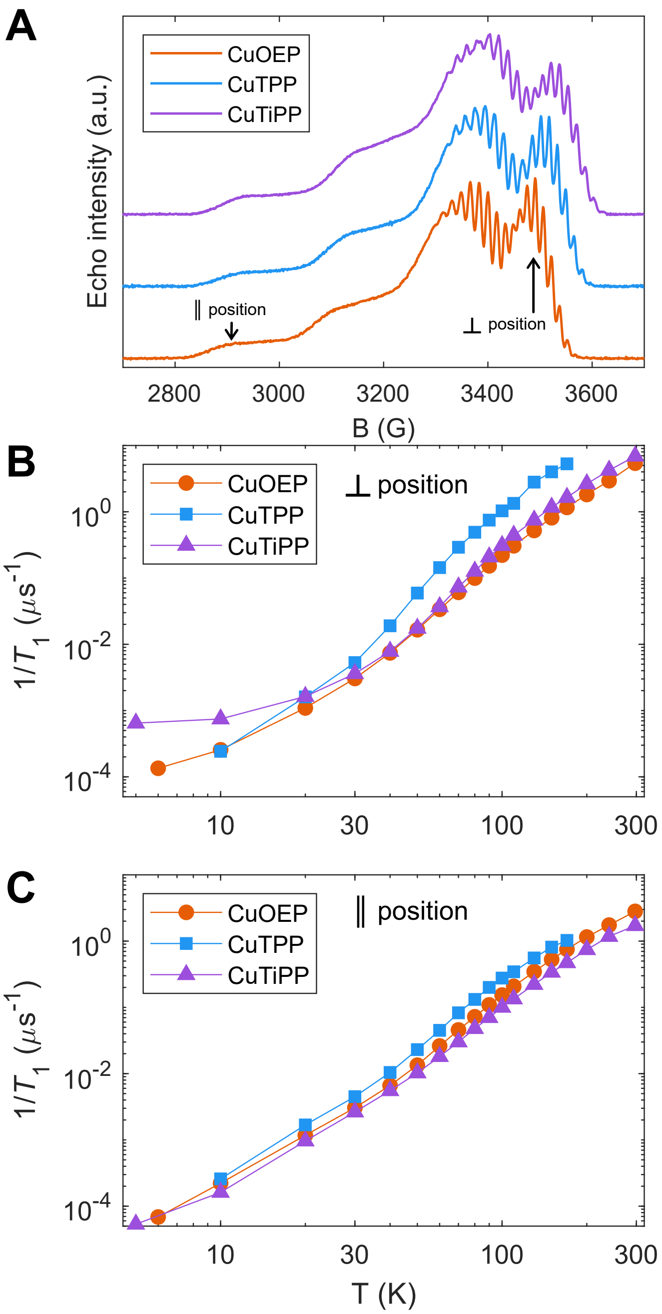

Figure 3.3: Temperature-dependent T_1 by pulse EPR X-band inversion recovery in 1% solid state powder dilutions of CuOEP in ZnOEP, CuTPP in NiTPP, and CuTiPP in NiTiPP. (A) Echo-detected field sweeps, with field positions selective for parallel and perpendicular molecular orientations indicated for CuOEP. The analogous field positions are chosen for CuTPP and CuTiPP. (B) Perpendicular position spin relaxation rates. (C) Parallel position spin relaxation rates.

butions in the ground state spin-orbit wavefunction and how they are modulated by totally symmetric vibrations.[20] Note that the T_1 values for all three porphyrins are quite similar at 20 K but diverge as temperature increases, indicating that higher-energy molecular vibrational modes are responsible for the differences between the compounds. Note also that CuOEP and CuTiPP display room-temperature (297 K) coherence, with T_1 and T_M (the phase memory time[2]) of 185 ns and 87 ns for CuOEP and 145 ns and 50 ns for CuTiPP at perpendicular orientations. To the best of our knowledge, room-temperature electron spin coherence has only been demonstrated in one previous CuN_4 molecular qubit, Cu(tmtaa)[5], and is not observed for copper phthalocyanine (CuPc).[22] CuTPP displays an extremely weak spin echo at room temperature, with T_1 and T_M of 60 and 49 ns at the perpendicular position. No echo was detectable at the CuTPP parallel position, and a room-temperature echo-detected field sweep could not be acquired. As such, we do not consider this signal robust enough for designation of CuTPP as a room-temperature coherent molecular qubit.

Since $1/T_1$ increases in the order CuOEP = CuTiPP << CuTPP, while ruffling increases in the order CuOEP < CuTPP < CuTiPP, the results of Figure 3.3 do not support the hypothesis that increased ruffling distortion activates new channels for spin relaxation. To examine the theoretical underpinnings of this notion, we performed molecular spin-phonon coupling calculations according to a previously published procedure to predict $1/T_1$ traces (Equation (3.1)).[14] The normal-mode derivatives of the principal values of the g tensor, $\partial g_i/\partial Q$, were averaged to obtain the spin-phonon coupling coefficients, thereby modeling the average $1/T_1$ relaxation across all orientations. Thermal weighting was applied via a two-phonon Green's function to model the temperature dependence of the Raman spin relaxation process.[16] An experimentally-calibrated proportionality constant of A = 1.01×10^5 μs^{-1} was used to convert the $1/T_1$ simulations into absolute rates.[14] This model has been shown to correctly predict the T_1 log-log slope of the molecular qubits CuPc and VOPc, as well as correctly ordering the relative T_1 for a series of four Cu(II) and V(IV) sulfur and selenium-ligated qubits.[14]

$$\frac{1}{T_1} = A \sum_{i=1}^{3N-6} \sum_{j=x,y,z} \frac{1}{3} \left(\frac{\partial g_j}{\partial Q_i}\right)^2 \frac{\exp\left[E_i/k_B T\right]}{\left(\exp\left[E_i/k_B T\right] - 1\right)^2} \tag{3.1}$$

Theoretical calculations predict that $1/T_1$ should increase in the order CuOEP < CuTPP < CuTiPP (Figure 3.4A; see Figure S51 for an overlay of theory and ex-

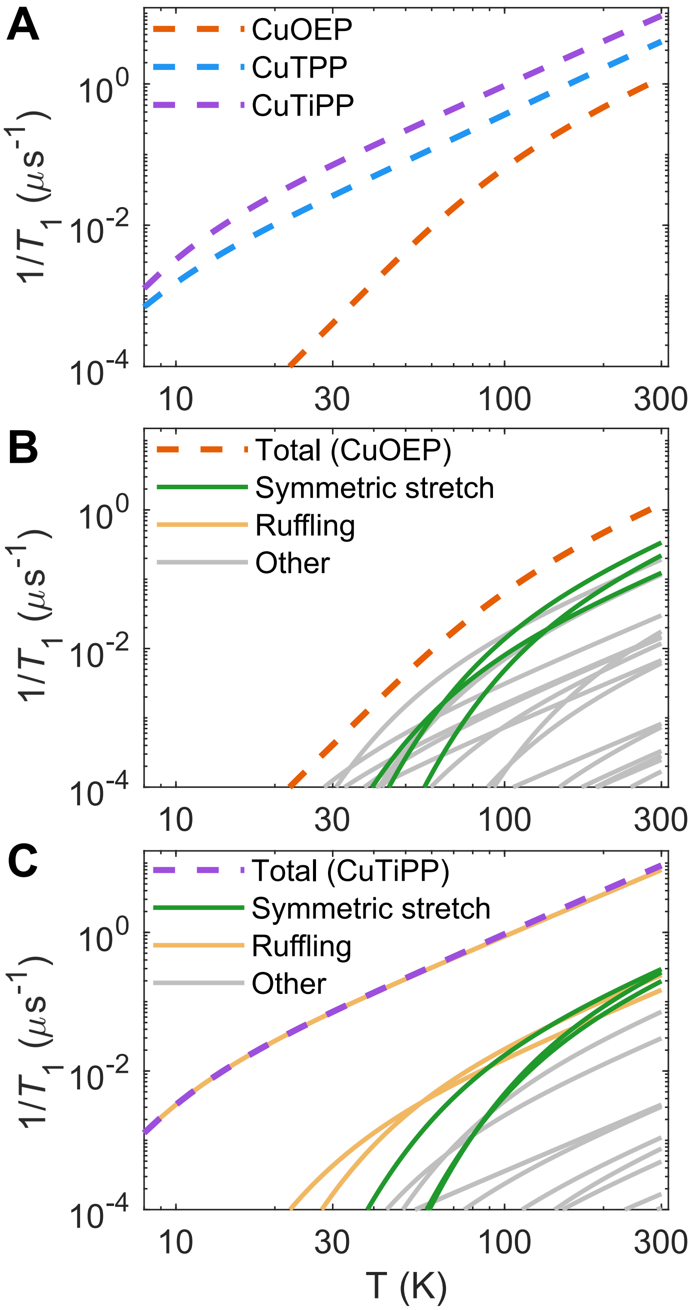

Figure 3.4: Calculated spin relaxation rates $1/T_1$ for the Cu porphyrin series. (A) Total calibrated relaxation rates. (B) Breakdown of individual vibrational mode contributions for planar CuOEP. Symmetric stretching modes dominate T_1 for T ≥ 100 K, while ruffling mode contributions are negligible. (C) Breakdown of individual vibrational mode contributions for ruffled CuTiPP. A single low-energy (26 cm^{-1}) ruffling mode dominates the calculated $1/T_1$ over the entire temperature range. Individual mode contributions are additive on a linear y-axis scale.

periment). This trend agrees with the order of increasing ruffling, but it does not agree with the experimental T_1 ordering. To understand the origin of the trend in the calculations, the individual vibrational mode contributions to $1/T_1$ are plotted for CuOEP (Figure 3.4B) and CuTiPP (Figure 3.4C); ruffled CuTPP follows similar behavior to ruffled CuTiPP (Figure S52). The contributions from each normal mode are additive towards the total rate of spin relaxation. All mode contributions have the same functional shape in accordance with the thermal weighting function, with two degrees of freedom: (1) a larger energy of the vibrational mode translates the $1/T_1$ contribution to the right, since the mode will not be thermally populated until higher temperatures, and (2) a larger $\partial g_i/\partial Q$ value shifts the $1/T_1$ contribution up on the plot, indicating that it mediates faster spin relaxation. For CuOEP, the calculated relaxation rate from ~30 – 70 K is set by low energy vibrational modes, mostly of an e_g rotational character with small amounts of symmetric stretch mixed in due to the waving distortion in CuOEP (Table 3.1). However, at 100 K and above, totally symmetric stretch modes take over the dominant contribution to spin relaxation (green lines, Figure 3.4B; Figure S38-S40, S54A). By contrast, spin relaxation for CuTiPP is predicted to be dominated by a single low energy ruffling mode at 26 cm^{-1} (Figure S46) over the entire temperature range studied (yellow lines, Figure 3.4C), which almost exactly matches the total $1/T_1$ calculated trace. The contribution from other modes, including the totally symmetric stretch, is predicted to be $< 15\%$ (Figure S54C). Therefore, molecular spin-phonon coupling calculations predict that the low-energy ruffling modes should dominate the $1/T_1$ for the ruffled porphyrins, and the absence of these distortion-activated modes in CuOEP should lead to a longer calculated spin lifetime. The room-temperature coherence of CuTiPP contradicts this prediction.

To determine the source of this discrepancy, we analyzed the temperature-dependent log-log slope of $1/T_1$. For a single power law process, such as those predicted by the Debye model for acoustic phonon spin relaxation,[34] the log-log slope should be constant. This behavior is often observed in experimental T_1 for inorganic lattices where the acoustic phonon branches drive T_1 over the entire Raman process temperature range.[34,35] However, variation in the log-log slope with temperature is common for molecular complexes. This behavior can originate from either (1) a crossover between two different spin relaxation processes (such as acoustic phonon relaxation vs. molecular vibration / local mode relaxation), or (2) the thermal population of higher-energy molecular vibrations, for which the innate spin relaxation contribution does not follow a power law form (Equation (3.1)).[14] In the first case, a sharp increase occurs in the log-log slope with increasing temperature, as a process that scales weakly with temperature gives way to a process that scales more strongly with temperature. In the second case, a smooth decrease occurs in the log-log slope with increasing temperature due to the thermal weighting functional form. The curvature of the log-log $1/T_1$ can then be used to pinpoint the energy of the contributing molecular vibration. Higher energy molecular vibrations display a larger and temperature-dependent log-log slope even at elevated temperatures. In contrast, the log-log slope of a low energy molecular vibration flattens out towards a constant value of 2 in the high temperature limit ($k_bT >> E_{\text{vib}}$), owing to the asymptotic behavior of the two-phonon Green's function.

Both CuOEP and CuTiPP display a temperature-dependent log-log slope (Figure 3.5A-B), which starts at a minimum below 10 K for the one-phonon direct process, peaks sharply at a value of ~4 at ~60 K, and then diminishes gradually towards ~2.5 at room temperature. The sharp increase from 10 – 60 K experimentally indicates a change in the relaxation process (case 1), wherein two-phonon scattering from a higher-energy molecular vibration (> 60 K) takes over from acoustic / pseudoacoustic phonons (< 30 K). The gradual decrease from 60 K towards room temperature indicates that one or more molecular vibrational modes controls spin relaxation over this region (case 2). By comparing these slopes to those of the theoretical calculations (Figure 3.4), the origin of the discrepancies with experiment can be ascertained. The calculated T_1 log-log slope for CuOEP matches the experimental behavior, which can be attributed in the calculation to the population of totally symmetric stretch modes above 60 K (Figure 3.5A, 3.4B). (Note that the calculations do not include acoustic phonons, so the divergence of the calculated log-log slope below 20 K is expected.) However, the calculated T_1 for CuTiPP displays a qualitatively incorrect log-log slope of 2 throughout the entire temperature range, while the experimental log-log slope peaks at a value of ~4.5 at 60 K. The calculated log-log slope of 2 arises from the 26 cm^{-1} ruffling mode (Figure 3.5B), which is predicted to dominate spin relaxation across all temperatures. A similar disagreement arises for CuTPP due to the same ruffling mode phenomenon (Figure S53, S55). We conclude that the calculated spin relaxation for CuOEP is in agreement with experiment, but the calculated spin relaxation for CuTiPP and CuTPP is incorrect due to overemphasis on the low-energy ruffling modes. Evidently, the ultra-low energy modes do not dominate spin relaxation in experiment.

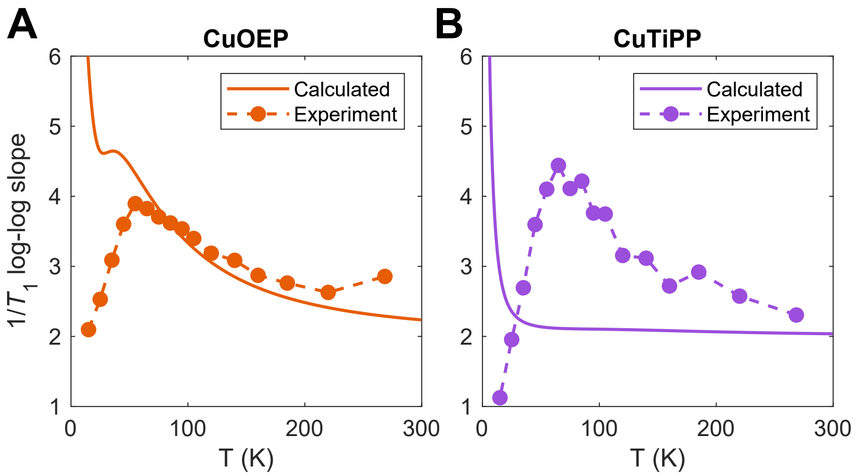

Figure 3.5: Calculated vs. experimental $1/T_1$ log-log slopes for (A) CuOEP and (B) CuTiPP.

To experimentally ascertain the energy range of the vibrational modes driving spin relaxation, local mode fits[22] to the $1/T_1$ data (Figure 3.6A-C) were carried out according to Equation (3.2). The least-squares fit was performed on the log-log data for equivalent residuals weighting across the entire temperature range.

$$\frac{1}{T_1} = aT^n + b\frac{\exp\left[E_{loc}/k_BT\right]}{(\exp\left[E_{loc}/k_BT\right]-1)^2} \tag{3.2}$$

The power law term accounts for a combination of the one-phonon direct process plus two-phonon Raman relaxation operating on low energy phonons; combining these reduces the number of free parameters to avoid overfitting. Lower temperature measurements ($<$ 10 K) would likely be needed to isolate the direct process contribution. It is well established that the Raman process in molecular solids need not follow the Debye model T^9 scaling,[36] so a variable exponent n is included. The second term has the same functional form as the two-phonon Green's function used for thermal weighting of molecular vibrational modes. In effect, this fitting postulates a single molecular vibration of energy E_{loc} capable of explaining the high-temperature T_1 values, while allowing for an unresolved collection of weakly-coupled low energy modes to determine the low-temperature T_1 values. All fits yield a local mode energy between 200 – 270 cm^{-1}, which fall in the energetic range of bond stretching vibrational modes. This analysis indicates that a similar type of vibrational mode likely determines T_1 in all three porphyrins. The fitted energy for CuTPP is lower than the fitted energies for CuOEP or CuTiPP, matching the room-temperature coherence observation for CuOEP and CuTiPP but not CuTPP. Local mode fitting on T_1 values collected at the parallel field position reinforces that the local mode energy for CuTPP is distinct from, and lower than, the mode energies for CuOEP and CuTiPP (Table S7). The local mode energies E_{loc} correlate better with the observed T_1 values than the coupling prefactor b, suggesting that vibrational mode energy shifts are principally responsible for the different T_1 values across the compound series (Table S8).

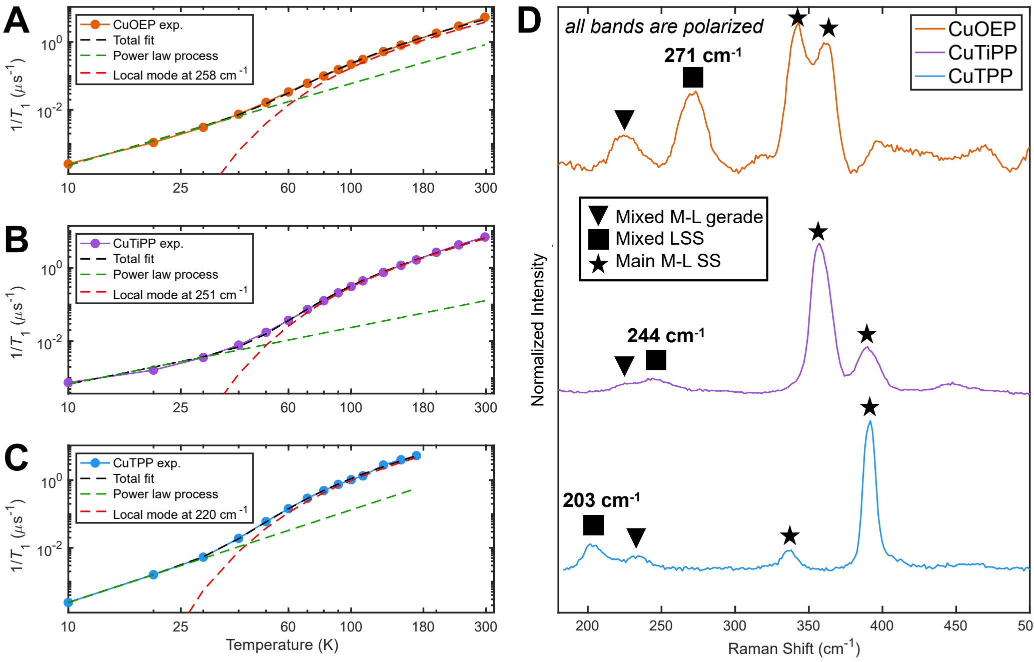

Figure 3.6: Determination of the dominant vibrational mode energy for spin relaxation. Local mode fitting at the perpendicular observer position according to Equation (3.1) for (A) CuOEP, (B) CuTiPP, and (C) CuTPP. (D) Resonance Raman spectroscopy obtained via 457.9 nm excitation (Soret preresonance enhancement). CuOEP collected in CS_2 at room temperature, while CuTiPP and CuTPP collected in C_6H_6 at room temperature. All peak positions are accurate to within 5 cm^{-1}.

rR spectroscopy was employed to identify vibrational modes in this energy range that could participate in spin-phonon coupling. Owing to selection rules of Raman scattering, only gerade modes are visible in centrosymmetric complexes. Furthermore, the A-term mechanism of Soret-band rR intensity enhancement selectively excites totally symmetric a_1 / a_{1g} modes,[37,38] which are precisely those modes predicted by group theory to have the correct symmetry for driving spin relaxation.[14] rR spectra for all three compounds display four main bands in the 200 – 400 cm^{-1} region, including two bands between 200 – 300 cm^{-1} (Figure 3.6D). Crucially, these latter bands appear lower in energy for CuTPP than for CuOEP or CuTiPP, in agreement with the relative rates of spin relaxation. All bands display a depolarization ratio less than 0.75 (Figures S22-S24), indicating at least some component of totally symmetric motion is present. The band positions in the solution-phase data are consistent within 8 cm^{-1} of rR spectra acquired in the solid state and display similar relative resonance enhancement (Table S2, Figure S25), indicating these reflect the vibrational structure present in the EPR samples as well. DFT frequency calculations of vibrations with Raman intensity display very good agreement with the experimental spectra and enable the assignment of the 300 – 400 cm^{-1} bands to totally symmetric metal-ligand stretching modes (Supporting Information Section 3C). The 200 – 300 cm^{-1} bands contain one instance of a mixed ligand symmetric stretch (LSS) and one instance of a mixed metal-ligand gerade mode with a principal contribution from non-totally symmetric motion. At least some symmetric motion must be admixed to account for the observation that all bands are polarized. Note the ordering of these latter two modes changes between the three CuP species.

Compound	Perpendicular orientation local mode (cm^{-1})	Raman mixed LSS mode (cm^{-1})
CuOEP	258	271
CuTiPP	251	244
CuTPP	220	203

Table 3.2: Positions of local mode energies and Raman mixed ligand symmetric stretch peaks.

Owing to the spin-phonon coupling group theory selection rule for totally symmetric vibrations, the mixed LSS mode energies were extracted from the rR spectra and compared with the local mode fits. Good agreement is found (Table 3.2), showing a $>$ 40 cm^{-1} distinction between the low energy CuTPP LSS mode (203 cm^{-1}) and those of CuOEP (271 cm^{-1}) and CuTiPP (244 cm^{-1}). This trend indicates that the energetic positioning of the LSS mode can explain the temperature-dependent T_1 results for the three CuP systems. In addition, the presence of a minor saddling distortion for CuTPP but not CuOEP or CuTiPP (Table 3.1) may lead to enhanced spin-phonon coupling, as saddling motions are known to be activated for spin relaxation via a first coordination sphere distortion. Porphyrin saddling contributions to T_1 will be analyzed in more detail in a future study. We conclude that high energy totally symmetric stretch modes, and not low-energy ruffling modes, control the relative T_1 ordering for CuOEP, CuTiPP, and CuTPP above 60 K.

3.4 Discussion

The failure of computational spin relaxation models to predict the correct high-energy stretching vibrational modes is not a unique feature of ruffled porphyrins. In several cases, molecular spin-phonon coupling models seem to have a bias toward over-emphasizing low energy modes, leading to predictions of ultra-low energy vibrations dominating T_1. However, such assignments often fail to account for the temperature-dependent T_1 curvature and log-log slope changes, such as in the case of *ab initio* modeling of vanadyl tetraphenylporphyrin (VOTPP).[19] Thus, such theoretical claims of low-energy phonon dominance should be treated with significant caution.

The origins of this computational low-energy bias are unclear, but likely relate to some of the approximations used to build the models. One possibility is that gas-phase DFT overestimates the amplitudes of low-energy vibrational modes, which should be more constrained in the solid-state. However, condensed-phase phonon calculations retain the same bias toward low energy modes.[19] Additionally, the use of full-g-tensor $\partial g_{ij}/\partial Q$ values for spin Hamiltonian matrix elements may overestimate the coupling of certain types of low energy modes, such as e_g rotations of the first coordination sphere, that do not dynamically change the total amount of minority spin mixing through the magnitude of spin-orbit coupling. Incorporation of spin-orbit coupling spin-flip matrix elements into *ab initio* T_1 modeling with quantum master equations may remedy this difficulty.

Experimentally, this work shows that rR spectroscopy is a powerful tool for building spin dynamics structure-property relationships by leveraging the selectivity for totally symmetric mode energies. Previous works have attempted to empirically correlate vibrations to features of spin relaxation through terahertz spectroscopy[39–42] or computation of the vibrational density of states.[5,32] However, terahertz or IR absorption spectroscopies rely on electric dipole selection rules that select for ungerade modes in centrosymmetric complexes. Group theory analysis has established a selection rule for spin-phonon coupling, which indicates that only gerade vibrations (predominately a_{1g} modes) are able to couple to the spins in centrosymmetric complexes.[14,17] Thus, IR or far-IR absorption spectroscopies do not probe the modes of relevance for spin-phonon coupling for square-planar complexes. Furthermore, the full vibrational density of states, or even atom-specific partial density of states, becomes very complicated in macrocyclic qubits like porphyrins, rendering statements about specific vibrational modes challenging. A-term enhanced rR spectra, however, have the key virtue of selectivity for the a_1 / a_{1g} modes most relevant to spin relaxation, making spectral correlations much more straightforward.

In addition, the magnitude of A-term resonance enhancement provided by excitation into a strongly dipole-allowed electronic absorption band is determined by the amount of excited state distortion through the electronuclear coupling integral.[37] This same term arises in the ligand field theory of spin-phonon coupling, where excited state distortion is required to observe nonzero $\partial g_i/\partial Q$.[14] Thus, there may be a connection between the magnitude of resonance enhancement and the magnitude of spin-phonon coupling itself. The caveat is that the electronic excited state of relevance is different for g-tensor contributions (d-d transition) vs. rR spectroscopy (charge transfer). In general, one cannot reliably acquire rR spectra for d-d bands, and many molecular qubits feature intense electronic transitions that obscure these transitions in electronic absorption spectra. The excited state distortions need not be the same between the two types of electronic excited states. Further work will investigate whether reliable information on spin relaxation can be extracted from the magnitude of A-term enhancement in rR spectra of molecular qubits.

3.5 Conclusions

This work probes the effect of the ruffling distortion on spin relaxation in a series of three copper porphyrins. Two of the three members of the series (CuOEP and CuTiPP) display room-temperature coherence, indicating the suitability of copper porphyrins as a new class of molecules for room-temperature molecular quantum information science applications. Unlike in the well-studied case of b_{2u} bending / saddling vibrations, increasing b_{1u} ruffling distortion does not correlate to decreased T_1 times, despite the mode transforming as a_1 in D_{2d}. This unexpected result may indicate that primary coordination sphere distortions are required to materially activate new vibrational modes for spin relaxation, and secondary sphere effects such as ruffling have too weak an influence on angular momentum and spin-orbit coupling to induce spin flips. Computational spin relaxation models fail to account for the insensitivity of T_1 to the ruffling distortion, indicating a direction for future theoretical efforts. rR spectroscopy successfully identifies a specific vibrational mode with totally symmetric character that correctly trends with the experimental T_1 local mode fits. Thus, this study indicates the primary vibrational modes responsible for S = ½ CuP spin relaxation above ~60 K correspond to bond stretches with totally symmetric character, not ultra-low energy modes of rotational character.

References

[1] Atzori, M.; Sessoli, R. The Second Quantum Revolution: Role and Challenges of Molecular Chemistry. *Journal of the American Chemical Society* **2019**, *141,* 11339–11352.

[2] Mirzoyan, R.; Kazmierczak, N. P.; Hadt, R. G. Deconvolving Contributions to Decoherence in Molecular Electron Spin Qubits: A Dynamic Ligand Field Approach. *Chemistry – A European Journal* **2021**, *27,* 9482–9494.

[3] Bader, K.; Dengler, D.; Lenz, S.; Endeward, B.; Jiang, S.-D.; Neugebauer, P.; van Slageren, J. Room Temperature Quantum Coherence in a Potential Molecular Qubit. *Nature Communications* **2014**, *5,* 5304.

[4] Fataftah, M. S.; Krzyaniak, M. D.; Vlaisavljevich, B.; Wasielewski, M. R.; Zadrozny, J. M.; Freedman, D. E. Metal-Ligand Covalency Enables Room Temperature Molecular Qubit Candidates. *Chemical Science* **2019**, *10,* 6707–6714.

[5] Amdur, M. J.; Mullin, K. R.; Waters, M. J.; Puggioni, D.; Wojnar, M. K.; Gu, M.; Sun, L.; Oyala, P. H.; Rondinelli, J. M.; Freedman, D. E. Chemical Control of Spin-Lattice Relaxation to Discover a Room Temperature Molecular Qubit. *Chemical Science* **2022**, *13,* 7034–7045.

[6] Atzori, M.; Tesi, L.; Morra, E.; Chiesa, M.; Sorace, L.; Sessoli, R. Room-Temperature Quantum Coherence and Rabi Oscillations in Vanadyl Phthalocyanine: Toward Multifunctional Molecular Spin Qubits. *Journal of the American Chemical Society* **2016**, *138,* 2154–2157.

[7] Atzori, M.; Morra, E.; Tesi, L.; Albino, A.; Chiesa, M.; Sorace, L.; Sessoli, R. Quantum Coherence Times Enhancement in Vanadium(IV)-based Potential Molecular Qubits: The Key Role of the Vanadyl Moiety. *J. Am. Chem. Soc.* **2016**, *138,* 11234–11244.

[8] Ariciu, A.-M.; Woen, D. H.; Huh, D. N.; Nodaraki, L. E.; Kostopoulos, A. K.; Goodwin, C. A. P.; Chilton, N. F.; McInnes, E. J. L.; Winpenny, R. E. P.; Evans, W. J.; Tuna, F. Engineering Electronic Structure to Prolong Relaxation Times in Molecular Qubits by Minimising Orbital Angular Momentum. *Nature Communications* **2019**, *10,* 3330.

[9] Laorenza, D. W.; Kairalapova, A.; Bayliss, S. L.; Goldzak, T.; Greene, S. M.; Weiss, L. R.; Deb, P.; Mintun, P. J.; Collins, K. A.; Awschalom, D. D.; Berkelbach, T. C.; Freedman, D. E. Tunable Cr^{4+} Molecular Color Centers. *Journal of the American Chemical Society* **2021**, *143,* 21350–21363.

[10] Bayliss, S. L.; Laorenza, D. W.; Mintun, P. J.; Kovos, B. D.; Freedman, D. E.; Awschalom, D. D. Optically Addressable Molecular Spins for Quantum Information Processing. *Science* **2020**, *370,* 1309–1312.

[11] Bayliss, S. L.; Deb, P.; Laorenza, D. W.; Onizhuk, M.; Galli, G.; Freedman, D. E.; Awschalom, D. D. Enhancing Spin Coherence in Optically Addressable Molecular Qubits through Host-Matrix Control. *Physical Review X* **2022**, *12,* 031028.

[12] Kazmierczak, N. P.; Luedecke, K. M.; Gallmeier, E. T.; Hadt, R. G. T_1 Anisotropy Elucidates Spin Relaxation Mechanisms in an S = 1 Cr(IV) Optically Addressable Molecular Qubit. *The Journal of Physical Chemistry Letters* **2023**, *14,* 7658–7664.

[13] Mirzoyan, R.; Hadt, R. G. The Dynamic Ligand Field of a Molecular Qubit: Decoherence through Spin-Phonon Coupling. *Physical Chemistry Chemical Physics* **2020**, *22,* 11249–11265.

[14] Kazmierczak, N. P.; Mirzoyan, R.; Hadt, R. G. The Impact of Ligand Field Symmetry on Molecular Qubit Coherence. *Journal of the American Chemical Society* **2021**, *143,* 17305–17315.

[15] Lunghi, A.; Sanvito, S. How Do Phonons Relax Molecular Spins? *Science Advances* **2019**, *5,* eaax7163.

[16] Lunghi, A.; Sanvito, S. The Limit of Spin Lifetime in Solid-State Electronic Spins. *The Journal of Physical Chemistry Letters* **2020**, *11,* 6273–6278.

[17] Santanni, F.; Albino, A.; Atzori, M.; Ranieri, D.; Salvadori, E.; Chiesa, M.; Lunghi, A.; Bencini, A.; Sorace, L.; Totti, F.; Sessoli, R. Probing Vibrational Symmetry Effects and Nuclear Spin Economy Principles in Molecular Spin Qubits. *Inorganic Chemistry* **2021**, *60,* 140–151.

[18] Escalera-Moreno, L.; Suaud, N.; Gaita-Ariño, A.; Coronado, E. Determining Key Local Vibrations in the Relaxation of Molecular Spin Qubits and Single-Molecule Magnets. *The Journal of Physical Chemistry Letters* **2017**, *8,* 1695–1700.

[19] Garlatti, E.; Albino, A.; Chicco, S.; Nguyen, V. H. A.; Santanni, F.; Paolasini, L.; Mazzoli, C.; Caciuffo, R.; Totti, F.; Santini, P.; Sessoli, R.; Lunghi, A.; Carretta, S. The Critical Role of Ultra-Low-Energy Vibrations in the Relaxation Dynamics of Molecular Qubits. *Nature Communications* **2023**, *14,* 1653.

[20] Kazmierczak, N. P.; Hadt, R. G. Illuminating Ligand Field Contributions to Molecular Qubit Spin Relaxation via T_1 Anisotropy. *Journal of the American Chemical Society* **2022**, *144,* 20804–20814.

[21] Lunghi, A. Toward Exact Predictions of Spin-Phonon Relaxation Times: An Ab Initio Implementation of Open Quantum Systems Theory. *Science Advances* **2022**, *8,* eabn7880.

[22] Follmer, A. H.; Ribson, R. D.; Oyala, P. H.; Chen, G. Y.; Hadt, R. G. Understanding Covalent versus Spin-Orbit Coupling Contributions to Temperature-Dependent Electron Spin Relaxation in Cupric and Vanadyl Phthalocyanines. *The Journal of Physical Chemistry A* **2020**, *124,* 9252–9260.

[23] Fielding, A. J.; Fox, S.; Millhauser, G. L.; Chattopadhyay, M.; Kroneck, P. M.; Fritz, G.; Eaton, G. R.; Eaton, S. S. Electron Spin Relaxation of Copper(II) Complexes in Glassy Solution between 10 and 120K. *Journal of Magnetic Resonance* **2006**, *179,* 92–104.

[24] Kingsbury, C. J.; Senge, M. O. The Shape of Porphyrins. *Coordination Chemistry Reviews* **2021**, *431,* 213760.

[25] Jentzen, W.; Song, X.-Z.; Shelnutt, J. A. Structural Characterization of Synthetic and Protein-Bound Porphyrins in Terms of the Lowest-Frequency Normal Coordinates of the Macrocycle. *The Journal of Physical Chemistry B* **1997**, *101,* 1684–1699.

[26] Fleischer, E. B.; Miller, C. K.; Webb, L. E. Crystal and Molecular Structures of Some Metal Tetraphenylporphines. *Journal of the American Chemical Society* **1964**, *86,* 2342–2347.

[27] Zeller, M.; DiMuzio, S. J.; Wilcox, R. J.; Hunter, A. D. CCDC 252379: Experimental Crystal Structure Determination. *CSD Communication* **2005**.

[28] Chen, C.; He, X.-T.; Hong, D.-L.; Wang, J.-W.; Luo, Y.-H.; Sun, B.-W. Tuning the Crystal Structures of Metal-Tetraphenylporphines via a Magnetic Field. *New Journal of Chemistry* **2018**, *42,* 12570–12575.

[29] He, H.-S. A Second Polymorph of (5,10,15,20-Tetraphenylporphyrinato)copper(II). *Acta Crystallographica Section E: Structure Reports Online* **2007**, *63,* m976–m977.

[30] Aparici Plaza, L.; Chojnacki, J. Influence of Chloroform on Crystalline Products Yielded in Reactions of 5,10,15,20-Tetraphenylporphyrin with HCl and Copper(II) Salts. *Acta Crystallographica Section C: Crystal Structure Communications* **2012**, *68,* m24–m28.

[31] von Kugelgen, S.; Krzyaniak, M. D.; Gu, M.; Puggioni, D.; Rondinelli, J. M.; Wasielewski, M. R.; Freedman, D. E. Spectral Addressability in a Modular Two Qubit System. *Journal of the American Chemical Society* **2021**, *143,* 8069–8077.

[32] Yu, C.-J.; von Kugelgen, S.; Krzyaniak, M. D.; Ji, W.; Dichtel, W. R.; Wasielewski, M. R.; Freedman, D. E. Spin and Phonon Design in Modular Arrays of Molecular Qubits. *Chemistry of Materials* **2020**, *32,* 10200–10206.

[33] Yu, C.-J.; Krzyaniak, M. D.; Fataftah, M. S.; Wasielewski, M. R.; Freedman, D. E. A Concentrated Array of Copper Porphyrin Candidate Qubits. *Chemical Science* **2019**, *10,* 1702–1708.

[34] Standley, K. J.; Vaughan, R. A. *Electron Spin Relaxation Phenomena in Solids;* Springer US: Boston, MA, 1969. DOI: 10.1007/978-1-4899-6539-4.

[35] Sabisky, E. S.; Anderson, C. H. Spin-Lattice Relaxation of Tm^{2+} in CaF_2, SrF_2, and BaF_2. *Physical Review B* **1970**, *1,* 2028–2040.

[36] Gu, L.; Wu, R. Origin of the Anomalously Low Raman Exponents in Single Molecule Magnets. *Physical Review B* **2021**, *103,* 014401.

[37] Albrecht, A. C. On the Theory of Raman Intensities. *The Journal of Chemical Physics* **1961**, *34,* 1476–1484.

[38] Rankin, J. G.; Czernuszewicz, R. S. Fingerprinting Petroporphyrin Structures with Vibrational Spectroscopy: Resonance Raman Spectra of Nickel and Vanadyl Etioporphyrins I and III. *Organic Geochemistry* **1993**, *20,* 521–538.

[39] Atzori, M.; Benci, S.; Morra, E.; Tesi, L.; Chiesa, M.; Torre, R.; Sorace, L.; Sessoli, R. Structural Effects on the Spin Dynamics of Potential Molecular Qubits. *Inorganic Chemistry* **2018**, *57,* 731–740.

[40] Albino, A.; Benci, S.; Tesi, L.; Atzori, M.; Torre, R.; Sanvito, S.; Sessoli, R.; Lunghi, A. First-Principles Investigation of Spin-Phonon Coupling in Vanadium-Based Molecular Spin Quantum Bits. *Inorganic Chemistry* **2019**, *58,* 10260–10268.

[41] Albino, A.; Benci, S.; Atzori, M.; Chelazzi, L.; Ciattini, S.; Taschin, A.; Bartolini, P.; Lunghi, A.; Righini, R.; Torre, R.; Totti, F.; Sessoli, R. Temperature Dependence of Spin-Phonon Coupling in [VO(acac)2]: A Computational and Spectroscopic Study. *The Journal of Physical Chemistry C* **2021**, *125,* 22100–22110.

[42] Camargo, L. C.; Briganti, M.; Santana, F. S.; Stinghen, D.; Ribeiro, R. R.; Nunes, G. G.; Soares, J. F.; Salvadori, E.; Chiesa, M.; Benci, S.; Torre, R.; Sorace, L.; Totti, F.; Sessoli, R. Exploring the Organometallic Route to Molecular Spin Qubits: The [CpTi(cot)] Case. *Angewandte Chemie International Edition* **2021**, *60,* 2588-2593.

Chapter 4

A SPECTROCHEMICAL SERIES FOR ELECTRON SPIN RELAXATION

- Adapted with permission from: Kazmierczak, N. P.*; Xia, K. T.*; Sutcliffe, E.; Aalto, J. P.; Hadt, R. G. A Spectrochemical Series for Electron Spin Relaxation. *Journal of the American Chemical Society* **2025**, *147*, 2849–2859. DOI: 10.1021/jacs.4c16571. © 2025 American Chemical Society.

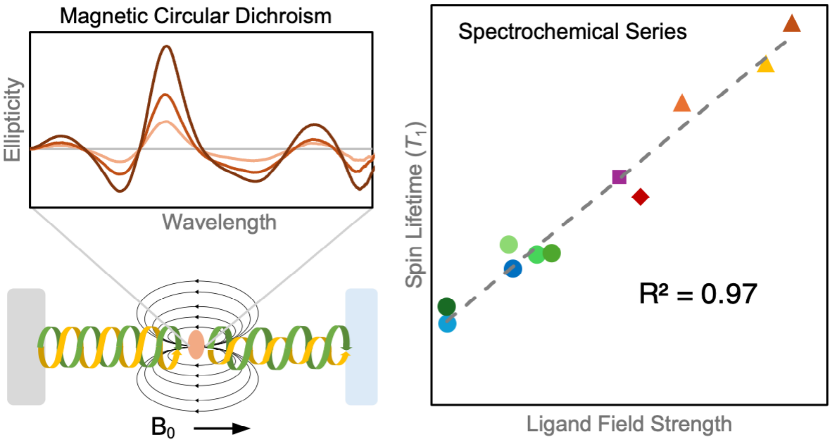

4.1 Abstract

Controlling the rate of electron spin relaxation in paramagnetic molecules is essential for contemporary applications in molecular magnetism and quantum information science. However, the physical mechanisms of spin relaxation remain incompletely understood, and new spectroscopic observables play an important role in evaluating spin dynamics mechanisms and structure-property relationships. Here, we use cryogenic magnetic circular dichroism (MCD) spectroscopy and pulse electron paramagnetic resonance (EPR) in tandem to examine the impact of ligand field (d-d) excited states on spin relaxation rates. We employ a broad scope of square-planar Cu(II) compounds with varying ligand field strength, including CuS_4, CuN_4, CuN_2O_2, and CuO_4 first coordination spheres. An unexpectedly strong correlation exists between spin relaxation rates and the average d-d excitation energy ($R^2 = 0.97$). The relaxation rate trends as the inverse eleventh power of the excited-state energies, whereas simplified theoretical models predict only an inverse second power depen-

dence. These experimental results directly implicate ligand field excited states as playing a critical role in the ground state spin relaxation mechanism. Furthermore, ligand field strength is revealed to be a particularly powerful design principle for spin dynamics, enabling formation of a spectrochemical series for spin relaxation.

4.2 Introduction

The spin dynamics properties of paramagnetic transition metal complexes have been studied since the earliest days of molecular magnetism,[1,2] but a resurgence of interest has accompanied the recent rise of molecular quantum information science.[3,4] S = ½ molecular complexes constitute a convenient two-level quantum system, fulfilling the requirements for a quantum bit (qubit). Molecular qubits possess the advantage of extreme miniaturization relative to other qubit platforms, though generation of large entangled arrays remains challenging.[5] Thus, molecular qubits are believed to possess advantages for quantum sensing applications in chemical microenvironments.[6–9]

To enact any quantum information protocol using a molecular qubit, it is necessary that a prepared spin state must retain its orientation and phase with high fidelity over a period of time. These spin states are typically generated in the presence of an applied magnetic field (B_0), such as in a pulse electron paramagnetic resonance (EPR) spectrometer.[10] However, electron spins possess an intrinsic magnetic dipole, causing them to interact with B_0. An electron spin placed in an antiparallel state to B_0 is out of equilibrium and experiences an energetically unfavorable repulsion (Figure 4.1A). Over time, such an electron will re-orient its spin so that the magnetic dipole re-aligns with B_0. This process, referred to as spin-lattice relaxation[11] and given by the time constant T_1, destroys the quantum information stored in the original state. Spin-lattice relaxation occurs through thermalizing interactions between the spin and vibrational modes, and thus proceeds much faster at elevated temperatures.[12] However, the mechanistic details of the spin-vibration coupling remain the subject of theoretical debate.[13] To realize the full potential of molecular quantum sensing, it is imperative to develop a more robust understanding of chemical factors affecting T_1.

Though spin relaxation occurs between the ground-state M_S sublevels, it has been suggested that electronic excited states may play an important role. Three distinct classes of spin relaxation models each predict a correlation between relaxation rates and the energy of the d-d (i.e., ligand field) excited states in transition metal complexes (Figure 4.1B). First, the popular spin Hamiltonian approaches model spin relaxation through the impact of vibrational modes on the g value, which controls the energy splitting between the ground-state M_S sublevels.[14–19] It is well known that an empirical correlation often exists between the orbital shift of the g value and the rate of spin relaxation,[20] with studies in both organic nitroxide radicals[21] and transition metal complexes.[14,22,23] Dynamic vibrational impacts on g are often roughly proportional to the static orbital contribution to g itself, so spin Hamiltonian models correctly predict faster relaxation for compounds with greater orbital angular momentum. Crucially, orbital contributions to g are produced by out-of-state spin-orbit coupling (SOC) between the ground state and excited d-d states.[10] The magnitude of this coupling is inversely proportional to the energy gap between the relevant d-d excited state and the ground state, so larger d-d excitation energies should lead to slower relaxation.[14] Second, it has been shown that shortcomings in the spin Hamiltonian model can be remedied by a wavefunction theory of spin relaxation that models the amount of ground-state minority spin.[24] The minority spin is produced by the same SOC mechanism as before, so the wavefunction theory predicts a similar relationship between d-d excitation energies and T_1. The d-d excitation energies may also be used to explain features of T_1 anisotropy.[24] Third, a recent approach has invoked virtual excitations to the d-d excited states as the primary driver of spin relaxation; these excitations become more feasible with reduced d-d excitation energy.[25]

Despite these predictions, there does not exist strong, direct experimental evidence for the impact of d-d excitation energies on T_1. The d-d transitions are weak in intensity because of the Laporte selection rule (ε = 10 – 100 M^{-1} cm^{-1}). If a compound has no spectral congestion from transitions involving ligands, the d-d transitions can be observed through UV-vis-NIR absorption spectroscopy (Figure 4.1E, top). However, many highly-coherent molecules possess extended π-conjugation and significant ligand–metal covalency. This induces intense charge transfer transitions (ε > 1000 M^{-1}cm^{-1}) across the visible spectrum, effectively masking the locations of the d-d states (Figure 4.1E, middle).[24] UV-vis-NIR absorption spectroscopy alone is thus insufficient to reliably quantitate d-d excitation energies across a broad scope of S = ½ molecules.

Magnetic circular dichroism (MCD) spectroscopy overcomes these limitations by selectively enhancing the strength of the d-d transitions. MCD is superficially related to the more familiar circular dichroism (CD) measurement; in both cases, a

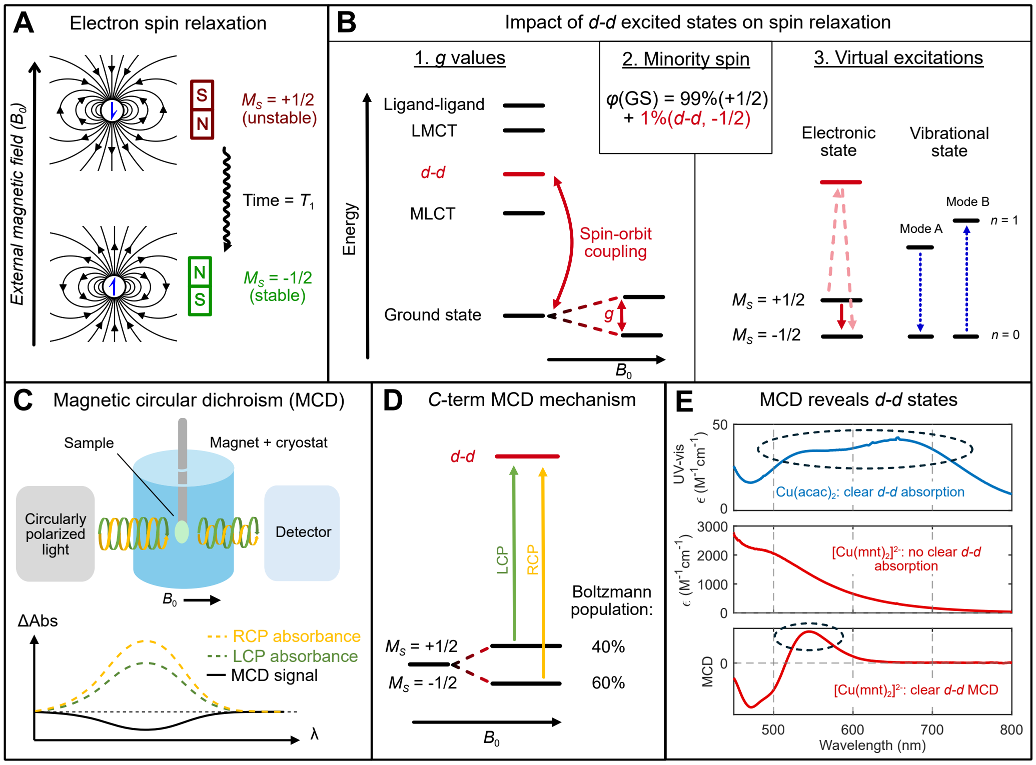

Figure 4.1: MCD as a useful spectroscopic probe for spin relaxation. (A) Electron spin relaxation arises from the reorientation of spin magnetic dipoles to align with an external magnetic field. (B) Excited states produced by transferring an electron between two d-orbitals (d-d transitions) play a key role in spin relaxation under multiple theoretical paradigms. (C) Schematic of the MCD instrument, which produces a signal based on differential absorption of left-handed and right-handed circularly polarized light (LCP/RCP) in the presence of a magnetic field. (D) Paramagnetic complexes produce an MCD signal through differential Boltzmann population of Zeeman sublevels, referred to as the C-term intensity mechanism. (E) The d-d transitions can be invisible in UV-vis-NIR absorption spectroscopy when buried under intense charge transfer transitions. MCD reveals ligand field transitions hidden in UV-vis-NIR absorption spectra (example data shown for Cu(acac)$_2$ and (PPh$_4$)$_2$[Cu(mnt)$_2$]).

signal is produced from differential absorption of left- and right-handed circularly polarized light (LCP/RCP) (Figure 4.1C).[26] However, the mechanism of dichroism is fundamentally distinct. In CD spectroscopy, signals can only arise when the molecule is chiral. MCD, however, does not require a chiral structure, and signals can arise even for achiral molecules, such as square-planar Cu(II) complexes[27–30] and related VO(IV) complexes.[31] Dichroism is instead produced by the interaction of an applied magnetic field with the molecule's electronic structure and magnetic moment. A variety of books and reviews have covered the mathematical theory and experimental history of MCD,[26,32–34] with notable applications to bioinorganic metal active sites.[35,36] Of relevance here, a major MCD intensity mechanism for paramagnetic molecules (referred to as the C-term mechanism) arises from unequal Boltzmann population of the ground-state Zeeman sublevels (Figure 4.1D). The population inequality increases as the temperature is decreased, so C-term MCD spectra are best acquired at cryogenic temperatures (2 – 20 K). In the presence of SOC, a transition from a particular Zeeman sublevel (say, $M_S = -1/2$) to a given excited state J will exhibit preferential absorption for RCP or LCP light. When the ground state is energetically well-separated from the excited states, the degree of this preference is often dominated by the strength of SOC in the excited state J.[37,38] Crucially, d-d excited states have much stronger SOC than charge transfer or ligand-based excited states, as the metal-centered SOC constant is typically up to an order of magnitude larger than on the ligand. Thus, d-d transitions intrinsically possess an amplified C-term MCD signal. MCD spectra can therefore resolve d-d transitions that are hidden beneath charge transfer transitions in the UV-vis-NIR absorption spectrum (Figure 4.1E, bottom).[39]

In this work, we leverage cryogenic MCD spectroscopy to accurately determine ligand field energies across a broad scope of square planar Cu(II) complexes (Figure 4.2).[13,24,40–45] The series includes molecules known to have long-lived spin lifetimes (e.g., $[Cu(mnt)_2]^{2-}$), as well as reference compounds not previously studied for their spin relaxation properties (e.g., $[Cu(ox)_2]^{2-}$). T_1 measurements at 100 K are subsequently acquired for each member of the series using matrix preparations identical or comparable to the MCD samples. This study provides the first direct experimental correlation between ligand field strength and spin relaxation rates. The unexpectedly strong correlation provides new insights into spin relaxation mechanisms and suggests that ligand field excited states dictate the spin dynamics behavior of transition metal complexes more than previously realized.

4.3 Results

4.3.1 Assigning d-d Transitions

To assign d-d bands, the first step is to acquire low-temperature MCD and UV-vis-NIR absorption spectra, which necessitates immobilization of the molecule in an optically transparent matrix. Three sample preparation techniques were used in this work (Supporting Information Section 1.3). First, the analyte can be dissolved into a polymer film, such as polystyrene (PS), poly(methyl methacrylate) (PMMA), or

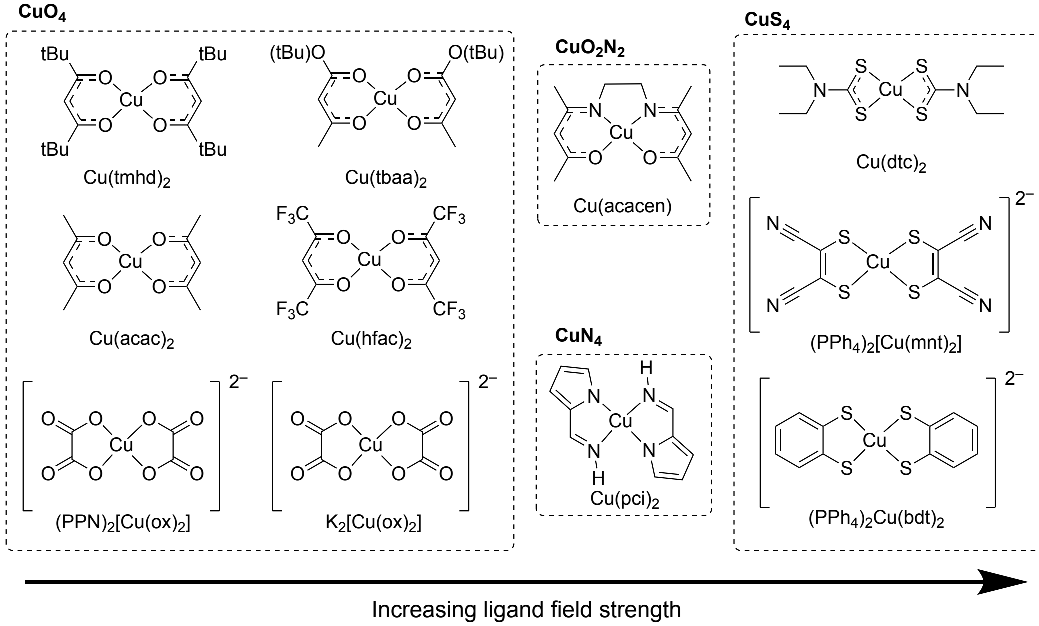

Figure 4.2: Compound scope for correlating MCD to spin relaxation rates. All compounds possess an approximately square-planar first coordination sphere in the absence of axial ligation. Ligand abbreviations: tmhd$^-$ = 2,2,6,6-tetramethylheptanedionate, tbaa$^-$ = tertbutylacetoacetate; acac$^-$ = acetylacetonate, hfac$^-$ = hexafluoroacetylacetonate, ox^{2-} = oxalate, acacen^{2-} = bis(acetylacetonato)ethylenediamine, pci$^-$ = pyrrolylcarbaldimine, dtc$^-$ = diethyldithiocarbamate, mnt^{2-} = maleonitriledithiolate, bdt^{2-} = benzenedithiolate.

polyvinyl alcohol (PVA), and drop-cast onto a quartz disc.[46,47] Polymer film samples generally have excellent optical properties permitting measurement of both MCD and absorption, but solubility can be limited, and the geometry of the compound is not crystallographically known. Second, the analyte can be dissolved into an optically glassing solvent and frozen in a homebuilt cell. This method can allow high solubility and good optical quality, but only a few solvents are optically transparent when frozen (such as butyronitrile, 2-methyl THF, and 3:7 glycerol:water).[48] Third, a solid crystalline powder of the analyte can be finely ground and suspended in fluorolube, referred to as a mull. Mull samples have a crystallographically-known geometry, but typically possess inferior optical quality, making it challenging to reliably measure absorption spectra. The sample preparation methods used for all compounds are tabulated in Table S1 in the Supporting Information.

Initially, we employed polymer films to simultaneously acquire C-term MCD and absorption spectra at cryogenic temperatures (2 – 20 K). Representative spectra for complexes from each class of coordinating ligand (e.g., CuS_4, CuN_4, CuN_2O_2, and CuO_4) are displayed in Figure 4.3, and full fitting information is provided in Supporting Information Section 5.2–5.3. While a few intense peaks are displayed in the absorption spectra, such as $Cu(dtc)_2$ at 430 nm (Figure 4.3A), many areas in the visible absorption spectra are comparatively flat and featureless, such as $Cu(pci)_2$ from 450 – 650 nm (Figure 4.3B). However, all compounds display clear structure in the MCD spectra. The flat absorption tail for $Cu(pci)_2$ is resolved into multiple signed bands in the MCD (Figure 4.3B). Similarly, multiple peaks are discernable in the $Cu(tmhd)_2$ MCD despite very low absorption (Figure 4.3D). These observations already suggest that the MCD spectra are successfully detecting d-d states that are not directly visible in the absorption spectra.

To quantitatively assign the d-d transitions, we performed Gaussian peak resolution to identify the spectral transitions (Figure 4.3).[39] Because MCD and absorption both arise from the same electronic states, we modeled Gaussian peaks as having the same energetic position and width in both spectra. The ratio of the MCD C-term and absorption transition moments (the latter is traditionally denoted as "D_0" in the MCD literature) can then be directly compared to give information about the nature of the excited state. In the linear limit, the C_0/D_0 ratio may be calculated according to Equation (4.1) (see also Supporting Information Section 5.1).[26,33,49] Here ε represents the molar absorptivity and $\Delta\varepsilon$ gives the MCD spectrum in units of differential molar absorptivity:[26]

$$\frac{C_0}{D_0} = \frac{k_B T}{\beta B}\frac{\Delta\varepsilon}{\varepsilon}. \tag{4.1}$$

It has been previously shown that a C_0/D_0 ratio around 0.1 is diagnostic of a d-d excited state, while a C_0/D_0 ratio around 0.01 is diagnostic of a charge transfer state.[50] In other words, d-d states have more intrinsic magnetic response per unit light absorption, owing to the enhanced metal-centered SOC.

Examination of the Figure 4.3 C_0/D_0 fits reveals important commonalities across all four compounds. $Cu(dtc)_2$ (Figure 4.3A) exhibits three bands from 21 000 – 16 000 cm^{-1} with C_0/D_0 ratios between 0.04 – 0.05; while somewhat small, such C_0/D_0 ratios are best assigned to d-d transitions. By contrast, the intense transition at 23 000 cm^{-1} possesses a C_0/D_0 ratio of only 0.016, and the higher-energy transitions have similar values. Thus, the 23 000 cm^{-1} band may be assigned to charge transfer, consistent with its intense extinction coefficient. The lowest-energy d-d band has a positive MCD sign, while the highest-energy assigned d-d band has a negative

MCD sign. Cu(pci)$_2$ (Figure 4.3B) possesses three strong d-d bands from 20 000 – 16 000 cm^{-1} with C_0/D_0 ratios around 0.08. The negative MCD peak at 19 970 cm^{-1} is especially prominent, despite not being resolved in the absorption spectrum. Cu(acacen) (Figure 4.3C) possesses a strong absorption peak at 18 600 cm^{-1} that is similar in appearance to the Cu(dtc)$_2$ charge transfer. However, the C_0/D_0 ratio is much larger at 0.062, indicating that this is a d-d transition in Cu(acacen). Furthermore, the transition has a prominent negative MCD sign, similar to the highest energy d-d transition in Cu(pci)$_2$. Finally, Cu(tmhd)$_2$ (Figure 4.3D) displays C_0/D_0 ratios at or above 0.1 for four d-d bands in the visible region, with a prominent negative MCD peak at 19 590 cm^{-1}. Note that in all four compounds, the highest-energy d-d band has a strong negative MCD signal, while the lowest-energy d-d band has a positive MCD signal. This spectral characteristic is conserved across the entire compound scope, enabling assignment of d-d transitions even when the UV-vis-NIR absorption spectrum cannot be obtained.

4.3.2 Comparing Ligand Field Strengths

Having identified the d-d transitions from C_0/D_0 fitting, the positions of the d-d bands across the compound scope may be compared (Figure 4.4). First, we examined the samples in randomly oriented matrices, either polymer films or frozen solutions (Figure 4.4A). In all eleven spectra, the d-d region is bookended by a negative MCD transition at higher energy and a positive MCD transition at lower energy. A total of four d-d transitions are expected for a d^9 Cu(II) complex. For some compounds, such as [Cu(bdt)$_2$]$^{2-}$, Cu(pci)$_2$, and Cu(hfac)$_2$, no extra resolved d-d peaks are observed in an intermediate energy range relative to the bookend transitions, though band asymmetry hints at extra transitions for Cu(pci)$_2$. These spectra also contain comparatively small energy gaps between the bookends, suggesting closely-spaced d-d manifolds. For other CuO$_4$ derivatives (Cu(acac)$_2$, Cu(tmhd)$_2$, and Cu(tbaa)$_2$), however, two additional prominent peaks are found between the bookend transitions. These observations account for all four d-d states in the MCD. Note that while the CuO$_4$ compounds do not have charge transfer transitions obscuring the d-d region, the four d-d states are not all individually resolved in the UV-vis-NIR absorption spectra. These MCD spectra thus provide enhanced ligand field information on all classes of compounds studied.

The sign of the MCD alone does not necessarily give an unambiguous indication of the precise d-d transitions, so calculations are valuable for conducting specific state assignments. In previous studies of rhombically-distorted C_{3v} Cu(II) metalloprotein

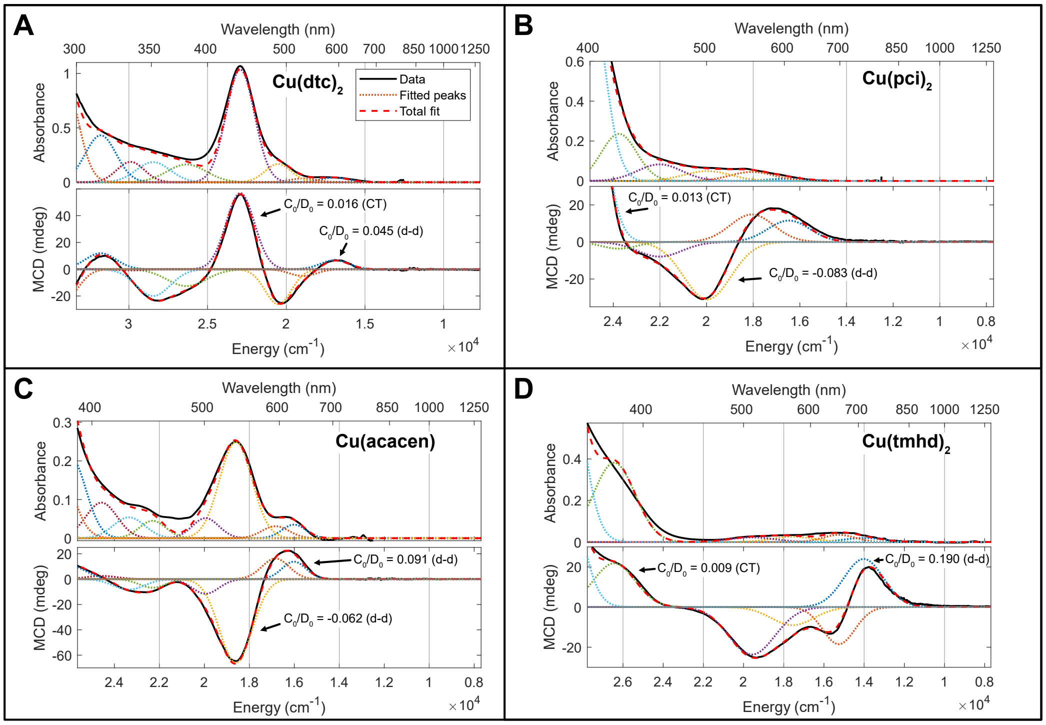

Figure 4.3: Assignment of electronic transitions through Gaussian band fitting of representative MCD and UV-vis-NIR absorption spectra. Relative intensity of transitions in MCD vs. absorbance is denoted by the C_0/D_0 ratio; a magnitude of ~0.01 is indicative of charge-transfer transitions, while ~0.1 is indicative of d-d transitions. (A) Cu(dtc)$_2$ MCD collected in PS film at ±2 T, 5.5 K – 10.0 K. (B) Cu(pci)$_2$ MCD in PS film at ±4 T, 5.0 K – 10.0 K. (C) Cu(acacen) MCD collected in PS film at ±2T, 5.0 K – 10.0 K. (D) Cu(tmhd)$_2$ MCD collected in PMMA film at ±2 T, 5.0 K – 20.0 K. All UV-vis-NIR absorption spectra are collected at the lowest temperature for which MCD data were measured. Two-point temperature subtractions eliminate temperature-independent features, yielding the pure C-term spectrum.

active sites, an intense negative MCD feature at the highest d-d excitation energy was assigned to a $xz/yz \rightarrow x^2 - y^2$ transition,[39] while a negative transition at highest d-d excitation energy arose from $z^2 \rightarrow x^2 - y^2$ in D_{4h} $CuCl_4^{2-}$.[30] However, the sign of MCD transitions can remain invariant in low symmetry systems even for multiple orderings of the excited states.[38] The expected band signs and energy orderings must be independently evaluated for the present D_{2h} complexes. Time-dependent density functional theory (TDDFT) calculations consistently assign the highest-energy state to the $x^2 - y^2 \rightarrow xy$ transition in D_{2h} symmetry (Supporting Information Section 7.1), while the lowest energy state is often (but not always) assigned to the $xz \rightarrow$

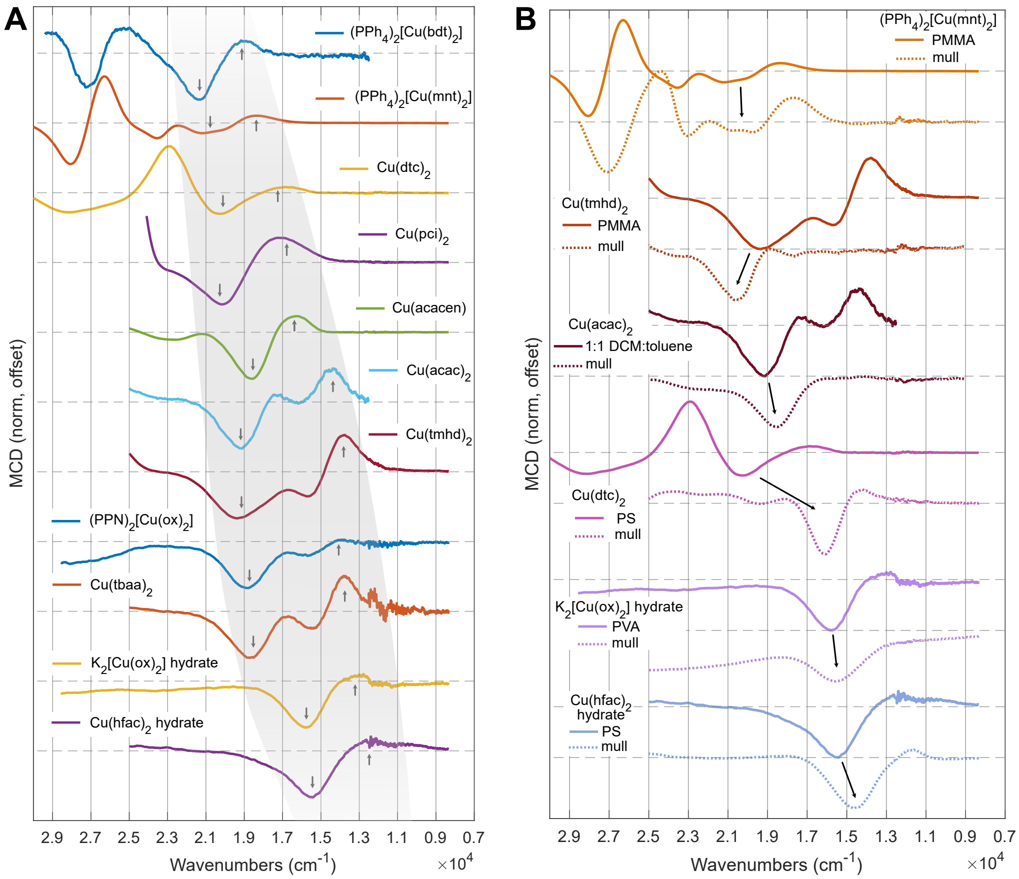

Figure 4.4: MCD spectral scope. (A) Comparison of MCD spectra across all compounds in disordered matrices (polymer film, solvent glass). Grey swathe indicates the region assigned to d-d transitions. Grey arrows indicate negative and positive features common to all spectra that bracket the d-d transitions. Matrices: $(PPh_4)_2[Cu(bdt)_2]$ in 1:1 butyronitrile:DCM, $(PPh_4)_2[Cu(mnt)_2]$ in PMMA, $Cu(dtc)_2$ in PS, $Cu(pci)_2$ in PS, Cu(acacen) in PS, $Cu(acac)_2$ in 1:1 DCM:toluene, $Cu(tmhd)_2$ in PMMA, $(PPN)_2[Cu(ox)_2]$ in PS, $Cu(tbaa)_2$ in PS, $K_2[Cu(ox)_2]$ in PVA, $Cu(hfac)_2$ in PS. (B) Comparison of matrix effects on MCD spectra for selected compounds. Polymer film or solution spectra are replicated from panel A. Arrows denote the shift in the prominent negative d-d MCD signal. Temperatures, fields and matrices are given for each spectrum in Supporting Information Section 5.1.1.

xy state. This analysis is consistent with the expected ordering for a nonbonding $x^2 - y^2$ orbital and π-donating ligands.

A substantial shift in ligand field strength was observed across the series (Figure 4.4A). The dithiolenes $[Cu(bdt)_2]^{2-}$ and $[Cu(mnt)_2]^{2-}$ possess the highest-energy d-d bands at an average of 20 460 cm^{-1} and 20 070 cm^{-1}, while the weakest ligand fields are displayed by $K_2[Cu(ox)_2]$ in PVA and $Cu(hfac)_2$ at 15 250 cm^{-1} and 15

230 cm^{-1}. This constitutes a 5000 cm^{-1} range, giving a 34% change in ligand field strength relative to the Cu(hfac)$_2$ endmember. The average d-d excitation energies are reliably ordered by the type of first coordination sphere: all CuS$_4$ > all CuN$_4$ > all CuN$_2$O$_2$ > all CuO$_4$. This is in good agreement with expectations from fundamental ligand field theory and with the observed CW EPR g values (Table S25). The O_4 acetylacetonate and oxalate donors possess lone pairs with facile mixing into the metal xz and yz orbitals, producing antibonding character, raising the orbital energy, and decreasing the gap to the xy acceptor. The antibonding character is visible in the xz donor NTOs from TDDFT (for example, Figure S122). Upon transitioning to N$_2$O$_2$ and N$_4$, the lone pairs are progressively removed, removing the π antibonding character and increasing the average transition energy. When moving to S_4, strong σ-donation leads to a high-lying σ^* xy acceptor orbital. The σ strength of the dithiolene ligands arises both from excellent orbital overlap of the diffuse S ligand and also close energetic matching of the S and metal orbitals, which can in some cases (such as for [Cu(mnt)$_2$]$^{2-}$) produce an inverted bonding regime.[51–55] Note that a weak MCD transition was detected at 8250 cm^{-1} for [Cu(mnt)$_2$]$^{2-}$ with a C_0/D_0 ratio of only 0.02 (Figures S26-S29). Though this donor orbital has the symmetry of the xz orbital, the low C_0/D_0 ratio indicates a predominantly charge transfer character. This assignment is in agreement with recent S K-edge 1s3p RIXS analysis, which concluded that a primarily LMCT character is the best description of the state.[56] Additionally, the TDDFT NTO donor orbital also displays primarily ligand character. Therefore, we do not include this transition in the calculation of the average d-d excitation energy for [Cu(mnt)$_2$]$^{2-}$. In sum, MCD spectroscopy assigns a ligand field strength ordering of CuS$_4$ > CuN$_4$ > CuN$_2$O$_2$ > CuO$_4$.

4.3.3 Impact of Axial Coordination

Close inspection of Figure 4.4A reveals that two different sample preparations of [Cu(ox)$_2$]$^{2-}$ possess significantly different d-d excitation energies. When prepared with the comparatively nonpolar PPN$^+$ counterion and dissolved in a non-coordinating PS film, (PPN)$_2$[Cu(ox)$_2$] displayed the $x^2 - y^2 \rightarrow xy$ transition with a strong negative MCD signal at 18 940 cm^{-1}. However, when prepared with the K$^+$ counterion and dissolved in the water-soluble PVA polymer, K$_2$[Cu(ox)$_2$] displayed a significant shift of the $x^2 - y^2 \rightarrow xy$ transition to 15 640 cm^{-1}. A concomitant shift in g_z from 2.255 to 2.322 was observed from (PPN)$_2$[Cu(ox)$_2$] in PS to K$_2$[Cu(ox)$_2$] in 30%:70% glycerol:water (a solution phase model of the PVA environment), consistent with an increase in ground-state orbital angular momentum from a weakened ligand field (Table S25). We posited that this shift could be explained by axial coordination of the alcohol groups in the PVA film, leading to a six-coordinate Cu(II) site with expanded equatorial bond lengths and a weakened σ^* interaction. Explicit solvation TDDFT calculations using the ORCA SOLVATOR[57] module support this interpretation (Supporting Information Section 7.4-7.5). In the absence of axial ligands, TDDFT predicts an $x^2 - y^2 \rightarrow xy$ energy of 19 150 cm^{-1} for $[\mathrm{Cu(ox)_2}]^{2-}$ (Table S29). Addition of explicit water solvation predicted a single axially coordinated H_2O molecule (Table S77), from which TDDFT predicted an $x^2 - y^2 \rightarrow xy$ energy of 16 480 cm^{-1} (Table S90). Addition of explicit methanol solvation predicted two axial alcohol coordination sites (Table S77), and TDDFT predicted an $x^2 - y^2 \rightarrow xy$ energy of 16 520 cm^{-1} (Table S94). The alcohol groups model the environment of the PVA matrix. Both explicit solvation approaches predict a band shift of about 2650 cm^{-1}, which is in good agreement with the experimental shift between the two sample matrices (3300 cm^{-1}). Note that the secondary peak near 16 000 cm^{-1} in the $\mathrm{(PPN)_2[Cu(ox)_2]}$ PS film may arise from an axially-coordinated species due to residual water, as this aligns with the PVA film. Additionally, a hydrated $\mathrm{Cu(hfac)_2}$ PS film possesses the weakest ligand field of all compounds studied; this compound commonly crystallizes as a hydrate with 1 – 2 axial waters ligated to the metal.[58,59] The axial ligation may be retained in the PS film and contribute to a weaker ligand field. These observations motivated further investigation of the role of axial coordination and the sample matrix in determining the measured ligand field strength.

MCD spectra in fluorolube mulls were acquired for six compounds and compared to the corresponding polymer film or solution spectra (Figure 4.4B). For $\mathrm{(PPh_4)_2[Cu(mnt)_2]}$, a slight overall redshift was observed in the mull, which may be attributed to the dielectric change in a crystalline powder. The band shape of the d-d transitions remained consistent, suggesting no major changes in compound geometry. Hydrated $\mathrm{K_2[Cu(ox)_2]}$ and $\mathrm{Cu(hfac)_2}$, which have crystallographic axial coordination, display minimal changes between the films and the mulls, suggesting the samples are axially coordinated in both sample preparations. $\mathrm{Cu(tmhd)_2}$ displays a blueshift of the $x^2 - y^2 \rightarrow xy$ transition, unique among the mull samples. Both $\mathrm{Cu(tmhd)_2}$ and $\mathrm{Cu(acac)_2}$ display a significant reduction in intensity of the lowest-energy positive MCD band, which is assigned to the $xz \rightarrow xy$ transition. The $x^2 - y^2 \rightarrow xy$ transition remains prominent and negative. The origin of this reduction is unclear, but may arise from increased conformational flexibility in the polymer/solution imparting enhanced electric dipole intensity to this transition.

Finally, $Cu(dtc)_2$ displays the most prominent change of all the compounds. The negative $x^2 - y^2 \rightarrow xy$ band shifts dramatically from over 20 000 cm^{-1} in the PS polymer film to just above 16 000 cm^{-1} in the mull, and the mull spectrum is more similar in appearance to the CuO_4 samples. This shift likely arises because $Cu(dtc)_2$ crystallizes as a staggered dimer, where the in-plane dtc ligand for one molecular unit provides out-of-plane axial coordination for the other molecular unit.[60] $Cu(dtc)_2$ likely dissociates into free square-planar monomers in the PS polymer film, supported by the lack of propensity to axial coordination in the explicit solvation DFT calculations (Table S77) and the observation of a strong S = ½ EPR signal. Thus, the strong mull MCD redshift for $Cu(dtc)_2$ is also explained by axial coordination.

4.3.4 Correlation to Spin Relaxation Rates

We next sought to correlate the observed MCD ligand field strengths to the rates of spin relaxation. Pulse EPR X-band inversion recovery measurements were conducted at 100 K and fit to stretched exponentials to extract T_1 (Figure 4.5A). The temperature was chosen to ensure that molecular vibrations localized to the first coordination sphere constituted the dominant driving force for spin relaxation, as opposed to low-energy phonons.[24] The correlation between d-d excited-state energies and spin relaxation rates has been theoretically predicted under a dominant two-phonon Raman relaxation mechanism with molecular vibrations at elevated temperatures (Figure 4.1B).[10,15] Spectral diffusion[10] is not a major factor at this temperature, so saturation recovery measurements are not needed. For most of the polymer film MCD samples, the films could be simply cut into strips and placed in an EPR tube. Strong CW and pulse EPR signals validated the dominant presence of magnetically dilute sites, with spin Hamiltonian parameters consistent with known molecular values in other matrices (Table S25). All T_1 measurements were collected at the most intense microwave absorption feature (powder line) to remove orientation effects, which is most appropriate for conducting the correlation analysis with the average d-d excitation energy.

To ensure that sample matrix differences did not affect the correlation analysis, EPR sample preparation was kept as close to the MCD sample preparation as possible (Table S1). For seven of the eleven samples, the MCD polymer film was reused for the EPR measurements, ensuring direct comparability. For $[Cu(ox)_2]^{2-}$, the coordinating PVA film was modeled by a 70%:30% water:glycerol solvent mixture, while the non-coordinating PS film was modeled by a toluene solvent system. $[Cu(bdt)_2]^{2-}$ and $Cu(acac)_2$ were run in glassing solvent mixtures for both MCD and EPR. Mull

MCD samples were necessarily excluded from the correlation analysis, as these paramagnetically concentrated powders do not display a spin echo in pulse EPR. There is some evidence that changing the matrix affects both the d-d excitation energies and the T_1 values in the same way (Figure 4.5B). For $[\mathrm{Cu(ox)_2}]^{2-}$, preparation in an axially-coordinating matrix ($\mathrm{K^+}$ counterion hydrate) lead to both a reduced d-d excitation energy (15 250 $\mathrm{cm^{-1}}$) and a reduced T_1 (254 ns) as compared to the preparation in a non-coordinating $\mathrm{PPN^+}$ matrix (d-d = 16 240 $\mathrm{cm^{-1}}$; T_1 = 480 ns). Therefore, while changes in the sample matrix can alter both the electronic structure and spin relaxation rates, these effects have been accounted for in the experimental design such that direct comparisons may be made.

A very strong correlation between the spin-lattice relaxation rates and the excited-state energies was observed (Figure 4.5B). A correlation plot of $\log(1/T_1)$ versus the average d-d excitation energy yields a linear fit with $R^2 = 0.966$. Notably, measured T_1 values at 100 K range from 8.15 μs ($[\mathrm{Cu(bdt)_2}]^{2-}$) to 308 ns ($\mathrm{Cu(hfac)_2}$), a change by a factor of 26.5 over the smaller value. However, the average d-d excitation energies for these two compounds are 20 460 $\mathrm{cm^{-1}}$ and 15 230 $\mathrm{cm^{-1}}$, respectively, which only constitutes a change by a factor of 1.34. The remarkable dependence of T_1 on comparatively small changes in excited-state energies is discussed below.

4.4 Discussion

We set out to quantify the surprisingly steep changes in T_1 with d-d excited-state energies and compare the experimental correlation to contemporary theoretical predictions. Denoting the average d-d excited-state energy as ΔE, we correlated $1/T_1$ and ΔE on a double logarithm plot to extract the effective power law scaling between the two variables. A linear fit to $\log(1/T_1)$ vs. $\log(\Delta E)$ gives a slope of approximately -11 (Figure 4.6A), implying $1/T_1 \propto \Delta E^{-11}$. This remarkable scaling is substantially stronger than would be naïvely predicted by examination of contemporary spin relaxation models.

To illustrate this unexpected result, we consider three main classes of spin relaxation models (Figure 4.1B): (1) spin Hamiltonian, (2) minority spin, and (3) virtual excitations. In the first class, the spin Hamiltonian g value itself scales as ΔE^{-1} according to a well-established relationship from 2nd-order perturbation theory (Equation (4.2), where $E_e - E_g = \Delta E$).[15,61]

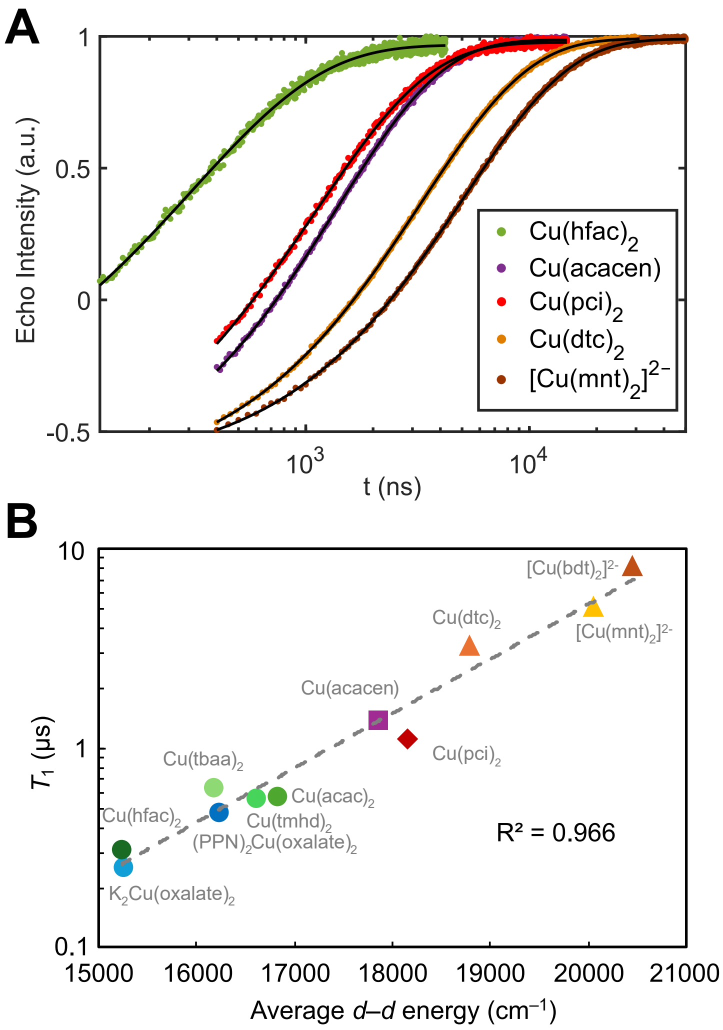

Figure 4.5: Correlation between MCD and pulse EPR spin relaxation rates. (A) Inversion recovery traces for selected compounds, acquired in the polymer matrix used for MCD ($Cu(hfac)_2$ in PS, Cu(acacen) in PS, $Cu(pci)_2$ in PS, $Cu(dtc)_2$ in PS, and $[Cu(mnt)_2]_2^-$ in PMMA). Stretched exponential fits yield the value of T_1. (B) Strong linear correlation between $\log(T_1)$ and the average d-d excited state energy determined from the MCD spectra. Error bars are smaller than the markers; tabulated in Table S26.

$$g_i = g_e - 2\lambda \sum_{e \neq g} \frac{\left| \left\langle \Psi_e \middle| \widehat{L}_i \middle| \Psi_g \right\rangle \right|^2}{E_e - E_g} \tag{4.2}$$

To connect the equilibrium g value to spin relaxation, it is common to differentiate Equation (4.2) with respect to a vibrational mode Q. The derivative, $\partial g / \partial Q$, is referred to as the spin-phonon coupling coefficient, and predicts the intrinsic propensity of a vibrational mode to induce spin relaxation. The leading order term in $\partial g/\partial Q$ scales as ΔE^{-2}.[14] Models using $\partial g/\partial Q$ as the spin relaxation coefficient will thus predict that $1/T_1$ scales somewhere between ΔE^{-2} or ΔE^{-4}, depending whether the $\partial g/\partial Q$ coefficient is squared or not.[14,15,19] The unclarity in coefficient squaring arises because $\partial g/\partial Q$ is a proxy for spin relaxation, rather than a true spin-flip matrix element amenable to Fermi's golden rule treatment.[24] For the second class of model, spin relaxation is proportional to the minority spin[24] in the ground-state wavefunction, which in turn is proportional to the out-of-state SOC. The minority spin in the ground-state wavefunction (Figure 4.1B) also scales[24] as ΔE^{-1}, so squaring the matrix element in Fermi's golden rule predicts $1/T_1 \propto \Delta E^{-2}$. In the third class, the Γ_{II} virtual transition mechanism (Figure 4.1B) similarly contains a ΔE^{-2} dependence from the virtual transitions,[25] though the scaling of the matrix elements is unclear. The ΔE^{-11} scaling of $1/T_1$ is therefore substantially stronger than would be naïvely predicted by examination of any of these models. Thus, contemporary theory only incompletely describes the impact of excited states on spin relaxation.

One possible explanation arises from ligand field theory analysis of inorganic bonding. Ligand field spin dynamics predicts[10,14,15] four separate factors impacting T_1: (1) the d-d excited-state energy, (2) the ligand–metal covalency, (3) the thermal population of the coupling vibrations, and (4) the magnitude of the excited-state vibronic coupling. Minimizing spin relaxation thus effectively constitutes an optimization problem in four dimensions. However, if multiple dimensions are tightly related in a series of molecules, it may be possible to obtain exceptionally steep apparent correlations. The Cu(II)–S compounds probed here are known to have highly covalent ligand–metal bonds, which produce an orbital reduction factor[62] that reduces the effective orbital angular momentum available for spin-vibration coupling.[51] Using the experimental EPR g values, we extracted effective orbital reduction factors for each compound (Supporting Information Section 6.3) that model the effects of bond covalency. Inclusion of covalency leads to a predicted scaling of $1/T_1 \propto \Delta E^{-5}$. While closer to experiment, this prediction still substantially underestimates the scaling. Alterations of the vibrational mode frequencies for different ligand frameworks may provide an additional contributing factor, though a full spin-phonon coupling analysis for all compounds is beyond the scope of the present study.

Irrespective of the theoretical details, this work demonstrates that ligand field strength can be an exceptionally powerful predictor for spin-lattice relaxation.

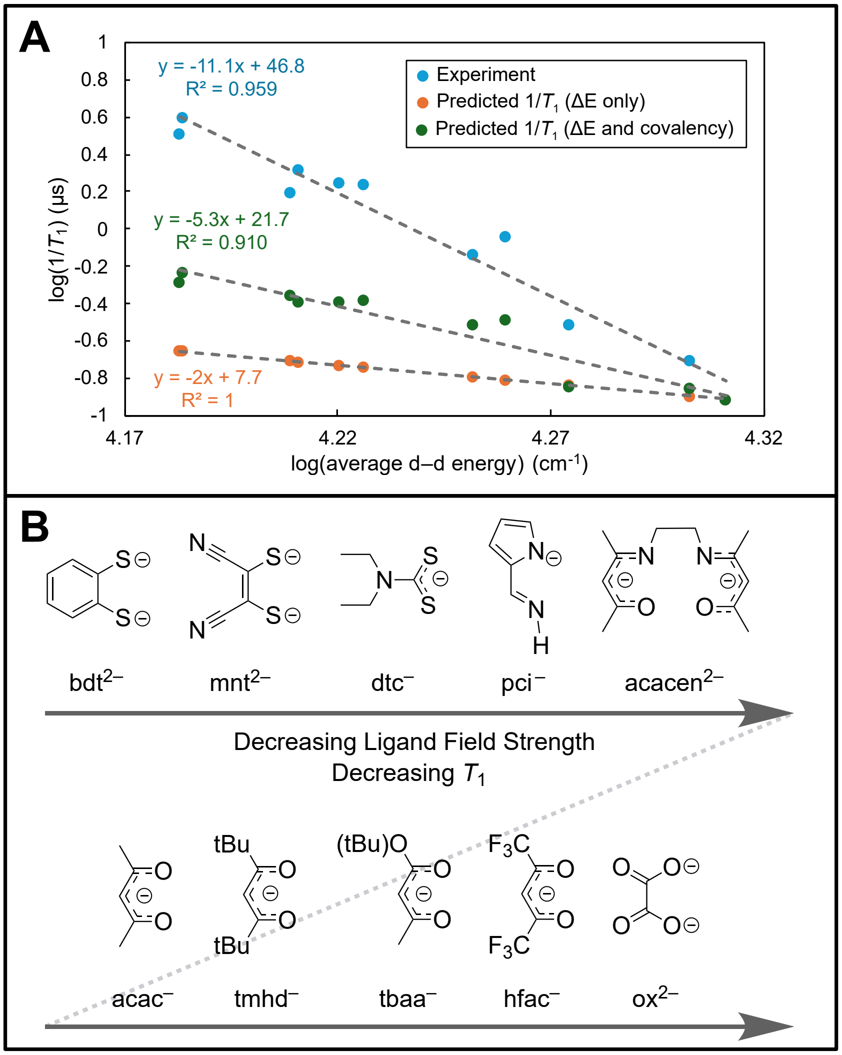

Figure 4.6: Analysis of the spectrochemical series for spin relaxation. (A) Log-log plot of predicted T_1 scaling with d-d excitation energies ($1/T_1 \propto \Delta E^{-2}$) compared to experimental scaling ($1/T_1 \propto \Delta E^{-11}$). (B) The spectrochemical series for spin relaxation.

Changing the d-d excitation energies by only 5000 cm^{-1} can be sufficient to alter T_1 by over a factor of 25. The logic of ligand field strength is furthermore a commonly employed synthetic design principle. For spin-based technological applications, great dividends may be produced by engineering compounds with the strongest possible ligand field strength. This can be accomplished in square-planar Cu(II) complexes both through strong-field ligands and through avoiding axial solvent coordination, which tends to weaken the ligand field. A similar approach should be applicable to square-pyramidal V(IV)O complexes, which are known to have long T_1 values.[63] On the basis of the MCD spectra, a spectrochemical series for spin relaxation can be formulated (Figure 4.6B).

4.5 Conclusions

By leveraging the selectivity of MCD spectroscopy, this study reports the first experimental demonstration of a strong correlation between ligand field strength and spin relaxation rates. This trend validates a general prediction of the ligand field approach to spin dynamics, showing that analysis of the static electronic structure can explain many spin dynamics phenomena.[10,14,15,24] The use of MCD spectroscopy enables quantification of ligand field strength even when the requisite bands cannot be detected in UV-vis-NIR absorption spectroscopy. As such, MCD is a valuable addition to the spectroscopic toolkit for studying spin relaxation mechanisms.

We emphasize that while spin relaxation is a ground-state process, the mechanism of spin relaxation is controlled by excited states. These electronic states are never populated during the process of spin relaxation, but they influence the motion of the electron spin through out-of-state SOC interactions and/or virtual excitations. MCD bands correlate to spin relaxation rates because MCD probes these relevant excited states. As such, it is essential to consider the full electronic state diagram when assessing spin relaxation mechanisms. Ligand field theory provides an indispensable tool for understanding the connection of spin properties to electronic structure design.

In the quest to produce molecules with long coherence times, formulation of reliable and practical synthetic guidelines for spin dynamics properties has been highly desired. Theories of spin relaxation have implicated multiple factors, including vibrational energy,[64,65] ligand–metal covalency,[45] coordination geometry,[63] as well as excited-state energy.[24,25] However, the very strong correlation demonstrated herein suggests that ligand field strength may be capable of predicting much, if not most, of the T_1 variation in planar Cu(II) compounds. Only a very small change in d-d excitation energy is required for a significant impact on the rate of spin relaxation. Furthermore, ligand field strength is more readily translated into practical synthetic strategies than theoretical concepts like spin-phonon coupling. By leveraging the ligand field strength design principle, further elongation of T_1 may likely be obtained across a range of paramagnetic complexes.

References

[1] Van Vleck, J. H. Paramagnetic Relaxation Times for Titanium and Chrome Alum. *Physical Review* **1940**, *57,* 426–447.

[2] Orbach, R. On the Theory of Spin-Lattice Relaxation in Paramagnetic Salts. *Proceedings of the Physical Society* **1961**, *77,* 821–826.

[3] Atzori, M.; Sessoli, R. The Second Quantum Revolution: Role and Challenges of Molecular Chemistry. *Journal of the American Chemical Society* **2019**, *141,* 11339–11352.

[4] Wasielewski, M. R. *et al.* Exploiting Chemistry and Molecular Systems for Quantum Information Science. *Nature Reviews Chemistry* **2020**, *4,* 490–504.

[5] Scholes, G. D. A molecular perspective on quantum information. *Proceedings of the Royal Society A: Mathematical, Physical and Engineering Sciences* **2023**, *479,* 20230599.

[6] Sun, L.; Yang, L.; Dou, J.-H.; Li, J.; Skorupskii, G.; Mardini, M.; Tan, K. O.; Chen, T.; Sun, C.; Oppenheim, J. J.; Griffin, R. G.; Dincă, M.; Rajh, T. Room-Temperature Quantitative Quantum Sensing of Lithium Ions with a Radical-Embedded Metal-Organic Framework. *Journal of the American Chemical Society* **2022**, *144,* 19008–19016.

[7] Xie, F.; Mao, H.; Lin, C.; Feng, Y.; Stoddart, J. F.; Young, R. M.; Wasielewski, M. R. Quantum Sensing of Electric Fields Using Spin-Correlated Radical Ion Pairs. *Journal of the American Chemical Society* **2023**, *145,* 14922–14931.

[8] Mullin, K. R.; Laorenza, D. W.; Freedman, D. E.; Rondinelli, J. M. Quantum Sensing of Magnetic Fields with Molecular Color Centers. *Physical Review Research* **2023**, *5,* L042023.

[9] Totoiu, C. A.; Follmer, A. H.; Oyala, P. H.; Hadt, R. G. Probing Bioinorganic Electron Spin Decoherence Mechanisms with an Fe_2S_2 Metalloprotein. *The Journal of Physical Chemistry B* **2024**, *128,* 10417–10426.

[10] Mirzoyan, R.; Kazmierczak, N. P.; Hadt, R. G. Deconvolving Contributions to Decoherence in Molecular Electron Spin Qubits: A Dynamic Ligand Field Approach. *Chemistry – A European Journal* **2021**, *27,* 9482–9494.

[11] Standley, K. J.; Vaughan, R. A. *Electron Spin Relaxation Phenomena in Solids;* Springer US: Boston, MA, 1969. DOI: 10.1007/978-1-4899-6539-4.

[12] Jackson, C. E.; Moseley, I. P.; Martinez, R.; Sung, S.; Zadrozny, J. M. A Reaction-Coordinate Perspective of Magnetic Relaxation. *Chemical Society Reviews* **2021**, *50,* 6684–6699.

[13] Kazmierczak, N.; Oyala, P.; Hadt, R. Spectroscopic Signatures of Phonon Character in Molecular Electron Spin Relaxation. *ACS Central Science* **2024**, *10,* 2353–2362.

[14] Mirzoyan, R.; Hadt, R. G. The Dynamic Ligand Field of a Molecular Qubit: Decoherence through Spin-Phonon Coupling. *Physical Chemistry Chemical Physics* **2020**, *22,* 11249–11265.

[15] Kazmierczak, N. P.; Mirzoyan, R.; Hadt, R. G. The Impact of Ligand Field Symmetry on Molecular Qubit Coherence. *Journal of the American Chemical Society* **2021**, *143,* 17305–17315.

[16] Lunghi, A.; Sanvito, S. How Do Phonons Relax Molecular Spins? *Science Advances* **2019**, *5,* eaax7163.

[17] Lunghi, A.; Sanvito, S. The Limit of Spin Lifetime in Solid-State Electronic Spins. *The Journal of Physical Chemistry Letters* **2020**, *11,* 6273–6278.

[18] Escalera-Moreno, L.; Suaud, N.; Gaita-Ariño, A.; Coronado, E. Determining Key Local Vibrations in the Relaxation of Molecular Spin Qubits and Single-Molecule Magnets. *The Journal of Physical Chemistry Letters* **2017**, *8,* 1695–1700.

[19] Santanni, F.; Albino, A.; Atzori, M.; Ranieri, D.; Salvadori, E.; Chiesa, M.; Lunghi, A.; Bencini, A.; Sorace, L.; Totti, F.; Sessoli, R. Probing Vibrational Symmetry Effects and Nuclear Spin Economy Principles in Molecular Spin Qubits. *Inorganic Chemistry* **2021**, *60,* 140–151.

[20] Abragam, A.; Bleaney, B. 1.11. Spin-Lattice Interaction. In *Electron Paramagnetic Resonance of Transition Ions*; Oxford University Press: Oxford, New York, 1970.

[21] Sato, H.; Kathirvelu, V.; Fielding, A.; Blinco, J. P.; Micallef, A. S.; Bottle, S. E.; Eaton, S. S.; Eaton, G. R. Impact of Molecular Size on Electron Spin Relaxation Rates of Nitroxyl Radicals in Glassy Solvents between 100 and 300 K. *Molecular Physics* **2007**, *105,* 2137–2151.

[22] Ariciu, A.-M.; Woen, D. H.; Huh, D. N.; Nodaraki, L. E.; Kostopoulos, A. K.; Goodwin, C. A. P.; Chilton, N. F.; McInnes, E. J. L.; Winpenny, R. E. P.; Evans, W. J.; Tuna, F. Engineering Electronic Structure to Prolong Relaxation Times in Molecular Qubits by Minimising Orbital Angular Momentum. *Nature Communications* **2019**, *10,* 3330.

[23] Albino, A.; Benci, S.; Tesi, L.; Atzori, M.; Torre, R.; Sanvito, S.; Sessoli, R.; Lunghi, A. First-Principles Investigation of Spin-Phonon Coupling in Vanadium-Based Molecular Spin Quantum Bits. *Inorganic Chemistry* **2019**, *58,* 10260–10268.

[24] Kazmierczak, N. P.; Hadt, R. G. Illuminating Ligand Field Contributions to Molecular Qubit Spin Relaxation via T_1 Anisotropy. *Journal of the American Chemical Society* **2022**, *144,* 20804–20814.

[25] Mariano, L. A.; Nguyen, V. H. A.; Petersen, J. B.; Bjørnsson, M.; Bendix, J.; Eaton, G. R.; Eaton, S. S.; Lunghi, A. The Role of Electronic Excited States in the Spin-Lattice Relaxation of Spin-1/2 Molecules. *arXiv:2407.01380 [physics]* **2024**.

[26] Mason, W. R. *Magnetic Circular Dichroism Spectroscopy;* Wiley: Hoboken, N.J, 1st ed.; 2007.

[27] Katô, H. Vibronically-Allowed d-d Transitions and the Magnetic Circular Dichroism of Cu^{2+} Complexes. *Molecular Physics* **1972**, *24,* 81–97.

[28] Katô, H.; Gohda, J. Magnetic Circular Dichroism of $Cu(acac)_2$, $Fe(acac)_3$, and $Co(acac)_3$. *Bulletin of the Chemical Society of Japan* **1973**, *46,* 636–637.

[29] Katô, H.; Kimura, T. The Magnetic Circular Dichroism of Some Copper(II) β-Diketone Chelate Complexes in Various Media. *Bulletin of the Chemical Society of Japan* **1974**, *47,* 732–734.

[30] Dick, A.; Rahemi, H.; Krausz, E. R.; Hanson, G. R.; Riley, M. J. The Highly Resolved Electronic Spectrum of the Square Planar $[CuCl_4]^{2-}$ Ion. *The Journal of Chemical Physics* **2008**, *129,* 214505.

[31] Van Stappen, C.; Maganas, D.; DeBeer, S.; Bill, E.; Neese, F. Investigations of the Magnetic and Spectroscopic Properties of V(III) and V(IV) Complexes. *Inorganic Chemistry* **2018**, *57,* 6421–6438.

[32] Kobayashi, N.; Muranaka, A.; Mack, J. *Circular Dichroism and Magnetic Circular Dichroism Spectroscopy for Organic Chemists;* Royal Society of Chemistry: Cambridge, 1st ed.; 2011.

[33] Paul N. Piepho, S. B. . S. *Group Theory in Spectroscopy: With Applications to Magnetic Circular Dichroism;* John Wiley: New York, 1st ed.; 1983.

[34] Nelson, Z.; Delage-Laurin, L.; Swager, T. M. ABCs of Faraday Rotation in Organic Materials. *Journal of the American Chemical Society* **2022**, *144,* 11912–11926.

[35] Solomon, E. I.; Heppner, D. E.; Johnston, E. M.; Ginsbach, J. W.; Cirera, J.; Qayyum, M.; Kieber-Emmons, M. T.; Kjaergaard, C. H.; Hadt, R. G.; Tian, L. Copper Active Sites in Biology. *Chemical Reviews* **2014**, *114,* 3659–3853.

[36] Jose, A.; Schaefer, A. W.; Roveda, A. C.; Transue, W. J.; Choi, S. K.; Ding, Z.; Gennis, R. B.; Solomon, E. I. The Three-Spin Intermediate at the O–O Cleavage and Proton-Pumping Junction in Heme–Cu Oxidases. *Science* **2021**, *373,* 1225–1229.

[37] Neese, F.; Solomon, E. I. MCD C-Term Signs, Saturation Behavior, and Determination of Band Polarizations in Randomly Oriented Systems with Spin S ≥ 1/2. Applications to S = 1/2 and S = 5/2. *Inorganic Chemistry* **1999**, *38,* 1847–1865.

[38] Gerstman, B. S.; Brill, A. S. Magnetic Circular Dichroism of Low Symmetry Cupric Sites. *The Journal of Chemical Physics* **1985**, *82,* 1212–1230.

[39] Gewirth, A. A.; Solomon, E. I. Electronic Structure of Plastocyanin: Excited State Spectral Features. *Journal of the American Chemical Society* **1988**, *110,* 3811–3819.

[40] Amdur, M. J.; Mullin, K. R.; Waters, M. J.; Puggioni, D.; Wojnar, M. K.; Gu, M.; Sun, L.; Oyala, P. H.; Rondinelli, J. M.; Freedman, D. E. Chemical Control of Spin-Lattice Relaxation to Discover a Room Temperature Molecular Qubit. *Chemical Science* **2022**, *13,* 7034–7045.

[41] Wansapura, C. M.; Juyoung, C.; Simpson, J. L.; Szymanski, D.; Eaton, G. R.; Eaton, S. S.; Fox, S. From Planar Toward Tetrahedral Copper(Il) Complexes: Structural and Electron Paramagnetic Resonance Studies of Substituent Steric Effects in an Extended Class of Pyrrolate-Imine Ligands. *Journal of Coordination Chemistry* **2003**, *56,* 975–993.

[42] Fielding, A. J.; Fox, S.; Millhauser, G. L.; Chattopadhyay, M.; Kroneck, P. M.; Fritz, G.; Eaton, G. R.; Eaton, S. S. Electron Spin Relaxation of Copper(II) Complexes in Glassy Solution Between 10 and 120K. *Journal of Magnetic Resonance* **2006**, *179,* 92–104.

[43] Bader, K.; Dengler, D.; Lenz, S.; Endeward, B.; Jiang, S.-D.; Neugebauer, P.; van Slageren, J. Room Temperature Quantum Coherence in a Potential Molecular Qubit. *Nature Communications* **2014**, *5,* 5304.

[44] Du, J.-L.; Eaton, G. R.; Eaton, S. S. Temperature and Orientation Dependence of Electron-Spin Relaxation Rates for Bis(diethyldithiocarbamato)copper(II). *Journal of Magnetic Resonance, Series A* **1995**, *117,* 67–72.

[45] Fataftah, M. S.; Krzyaniak, M. D.; Vlaisavljevich, B.; Wasielewski, M. R.; Zadrozny, J. M.; Freedman, D. E. Metal-Ligand Covalency Enables Room Temperature Molecular Qubit Candidates. *Chemical Science* **2019**, *10,* 6707–6714.

[46] Upton, A. H. P.; Williamson, B. E. Magnetic Circular Dichroism and Absorption Spectra of Hexacyanoferrate(III) in a Poly(vinyl alcohol) Film. *The Journal of Physical Chemistry* **1994**, *98,* 71–76.

[47] McNicholas, B. J.; Nie, C.; Jose, A.; Oyala, P. H.; Takase, M. K.; Henling, L. M.; Barth, A. T.; Amaolo, A.; Hadt, R. G.; Solomon, E. I.; Winkler, J. R.; Gray, H. B.; Despagnet-Ayoub, E. Boronated Cyanometallates. *Inorganic Chemistry* **2022**, *62,* 2959–2981.

[48] Drago, R. S. *Physical Methods for Chemists;* Orlando, Florida, U.S.A.: Saunders College Pub: Ft. Worth, 2nd ed.; 1992.

[49] Stephens, P. J. Magnetic Circular Dichroism. In *Advances in Chemical Physics*; John Wiley & Sons, Ltd: 1976. DOI: 10.1002/9780470142547.ch4.

[50] Solomon, E. I.; Bell III, C. B. Inorganic and Bioinorganic Spectroscopy. In *Physical Inorganic Chemistry: Principles, Methods, and Models*; Bakac, A., Ed.; John Wiley & Sons: 2010.

[51] Sarangi, R.; DeBeer George, S.; Rudd, D. J.; Szilagyi, R. K.; Ribas, X.; Rovira, C.; Almeida, M.; Hodgson, K. O.; Hedman, B.; Solomon, E. I. Sulfur K-Edge X-ray Absorption Spectroscopy as a Probe of Ligand−Metal Bond Covalency: Metal vs Ligand Oxidation in Copper and Nickel Dithiolene Complexes. *Journal of the American Chemical Society* **2007**, *129,* 2316–2326.

[52] Kirk, M. L.; McNaughton, R. L.; Helton, M. E. The Electronic Structure and Spectroscopy of Metallo-Dithiolene Complexes. In *Progress in Inorganic Chemistry*; Stiefel, E. I., Ed.; John Wiley & Sons, Inc.: Hoboken, NJ, USA, 2004. DOI: 10.1002/0471471933.ch3.

[53] Alvarez, S.; Vicente, R.; Hoffmann, R. Dimerization and Stacking in Transition-Metal Bisdithiolenes and Tetrathiolates. *Journal of the American Chemical Society* **1985**, *107,* 6253–6277.

[54] Hoffmann, R.; Alvarez, S.; Mealli, C.; Falceto, A.; Cahill, T. J. I.; Zeng, T.; Manca, G. From Widely Accepted Concepts in Coordination Chemistry to Inverted Ligand Fields. *Chemical Reviews* **2016**, *116,* 8173–8192.

[55] Hocking, R. K.; DeBeer George, S.; Raymond, K. N.; Hodgson, K. O.; Hedman, B.; Solomon, E. I. Fe L-Edge X-ray Absorption Spectroscopy Determination of Differential Orbital Covalency of Siderophore Model Compounds: Electronic Structure Contributions to High Stability Constants. *Journal of the American Chemical Society* **2010**, *132,* 4006–4015.

[56] Larsen, C. B.; Ledbetter, K.; Nascimento, D. R.; Biasin, E.; Qureshi, M.; Nowak, S. H.; Sokaras, D.; Govind, N.; Cordones, A. A. Metal-Ligand Covalency in the Valence Excited States of Metal Dithiolenes Revealed by S 1s3p Resonant Inelastic X-ray Scattering. *Journal of the American Chemical Society* **2024**, *146,* 28561–28571.

[57] Bannwarth, C.; Ehlert, S.; Grimme, S. GFN2-xTB—An Accurate and Broadly Parametrized Self-Consistent Tight-Binding Quantum Chemical Method with Multipole Electrostatics and Density-Dependent Dispersion Contributions. *Journal of Chemical Theory and Computation* **2019**, *15,* 1652–1671.

[58] Maverick, A. W.; Fronczek, F. R.; Maverick, E. F.; Billodeaux, D. R.; Cygan, Z. T.; Isovitsch, R. A. Structures of Anhydrous and Hydrated Copper(II) Hexafluoroacetylacetonate. *Inorganic Chemistry* **2002**, *41,* 6488–6492.

[59] Jain, A.; Kodas, T. T.; Corbitt, T. S.; Hampden-Smith, M. J. Chemical Vapor Deposition of Copper from (hfac)CuL (L = VTMS and 2-Butyne) in the Presence of Water, Methanol, and Dimethyl Ether. *Chemistry of Materials* **1996**, *8,* 1119–1127.

[60] Jian, F.; Wang, Z.; Bai, Z.; You, X.; Fun, H.-K.; Chinnakali, K.; Razak, I. A. The Crystal Structure, Equilibrium and Spectroscopic Studies of Bis(dialkyldithiocarbamate) Copper(II) Complexes $[Cu_2(R_2dtc)_4]$ (dtc=dithiocarbamate). *Polyhedron* **1999**, *18,* 3401–3406.

[61] Ballhausen, C. J. *Introduction to Ligand Field Theory;* McGraw-Hill: 1962.

[62] Gerloch, M.; Miller, J. R. Covalence and the Orbital Reduction Factor, k , in Magnetochemistry. *Progress in Inorganic Chemistry* **1968**, *10,* 1–47.

[63] Atzori, M.; Morra, E.; Tesi, L.; Albino, A.; Chiesa, M.; Sorace, L.; Sessoli, R. Quantum Coherence Times Enhancement in Vanadium(IV)-based Potential Molecular Qubits: the Key Role of the Vanadyl Moiety. *Journal of the American Chemical Society* **2016**, *138,* 11234–11244.

[64] Kazmierczak, N. P.; Lopez, N. E.; Luedecke, K. M.; Hadt, R. G. Determining the Key Vibrations for Spin Relaxation in Ruffled Cu(II) Porphyrins via Resonance Raman Spectroscopy. *Chemical Science* **2024**, *15,* 2380–2390.

[65] Kazmierczak, N. P.; Luedecke, K. M.; Gallmeier, E. T.; Hadt, R. G. T_1 Anisotropy Elucidates Spin Relaxation Mechanisms in an S = 1 Cr(IV) Optically Addressable Molecular Qubit. *The Journal of Physical Chemistry Letters* **2023**, *14,* 7658–7664.

Chapter 5

ILLUMINATING LIGAND FIELD CONTRIBUTIONS TO MOLECULAR QUBIT SPIN RELAXATION VIA T_1 ANISOTROPY

- Adapted with permission from: Kazmierczak, N. P.; Hadt, R. G. Illuminating Ligand Field Contributions to Molecular Qubit Spin Relaxation via T_1 Anisotropy. *Journal of the American Chemical Society* **2022**, *144*, 20804–20814. DOI: 10.1021/jacs.2c08729. © 2022 American Chemical Society.

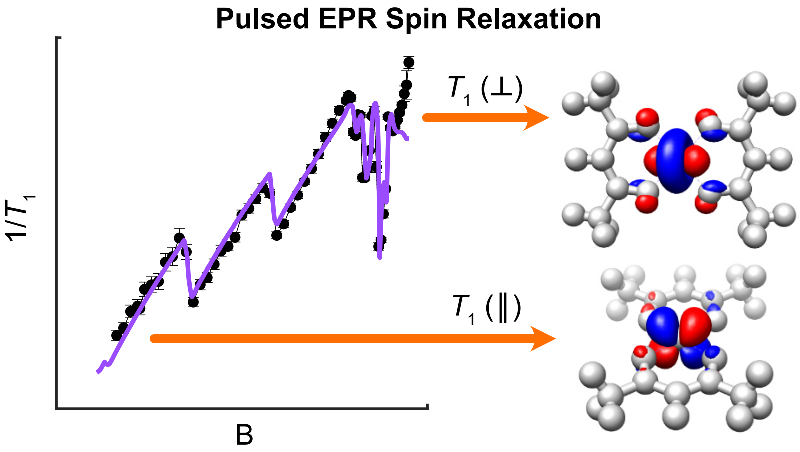

5.1 Abstract

Electron spin relaxation in paramagnetic transition metal complexes constitutes a key limitation on the growth of molecular quantum information science. However, there exist very few experimental observables for probing spin relaxation mechanisms, leading to a proliferation of inconsistent theoretical models. Here we demonstrate that spin relaxation anisotropy in pulsed electron paramagnetic resonance is a powerful spectroscopic probe for molecular spin dynamics across a library of highly coherent Cu(II) and V(IV) complexes. Neither the static spin Hamiltonian anisotropy nor contemporary computational models of spin relaxation are able to account for the experimental T_1 anisotropy. Through analysis of the spin-orbit coupled wavefunctions, we derive an analytical theory for the T_1 anisotropy that accurately reproduces the average experimental anisotropy of 2.5. Furthermore, compound-by-compound deviations from the average anisotropy provide a promising approach

for observing specific ligand field and vibronic excited state coupling effects on spin relaxation. Finally, we present a simple density functional theory workflow for computationally predicting T_1 anisotropy. Analysis of spin relaxation anisotropy leads to deeper fundamental understanding of spin-phonon coupling and relaxation mechanisms, promising to complement temperature-dependent relaxation rates as a key metric for understanding molecular spin qubits.

5.2 Introduction

The growth of quantum information science has inspired chemists to construct molecular systems that can function as quantum bits (qubits), which constitute the fundamental unit of quantum information.[1] One common approach uses Zeeman sublevels of a paramagnetic molecule in a magnetic field as the two level system.[2] Such systems are known as molecular electron spin qubits and enable quantum operations to be performed in a pulsed electron paramagnetic resonance (EPR) spectrometer.[3] Paramagnetic transition metal complexes are commonly employed for this purpose owing to their synthetic tunability, microwave spectral addressability, and potential for optical addressability in S > 1/2 systems. Such molecular qubit systems are highly miniaturized,[1] can be placed in materials and chemical microenvironments with a high degree of spatial precision,[4] and can exhibit quantum behavior at elevated temperatures, up to and including room temperature.[5]

Two key factors limit the performance of molecular electron spin qubits. The most fundamental problem is referred to as decoherence, measured by the time constant T_2, which determines the rate at which the electron spins lose phase synchronization.[3] At low temperatures, T_2 is dominated by magnetic fluctuations due to hyperfine couplings. At elevated temperatures, however, T_2 is dominated by the spin relaxation process, which destroys coherence through the interaction of the spin system with vibrational degrees of freedom (spin-phonon coupling). The spin relaxation rate is given by the time constant T_1. While several S = 1/2 qubits display coherence at room temperature,[5–9] optically addressable S = 1 qubits have so far not exceeded 40 K owing to the impact of spin-phonon coupling on T_1.[10–12] As room temperature quantum applications constitute a key area of interest for molecular qubit systems, this makes it imperative to completely understand the molecular factors controlling the spin relaxation rate.

Unfortunately, there exists an acute lack of experimental observables for understanding the mechanisms of spin relaxation, resulting in a proliferation of inconsistent theoretical models. The traditional approach has relied on analyzing the temperature dependence of the T_1 parameter from pulsed EPR or the τ parameter from alternating-current (AC) magnetometry. For many decades, these data were interpreted by fitting a plot of $1/T_1$ vs. temperature to equations derived from the Debye model from solid state physics. The fits were interpreted as giving the contributions of the direct, Raman, and Orbach relaxation processes.[13] However, recent reevaluation has demonstrated that the assumptions implicit in the Debye model are inappropriate for molecular systems, and the quality of Debye model fits to molecular temperature-dependent T_1 can be largely considered a phenomenological coincidence.[3,14–17] Modern molecular spin relaxation models instead define a spin-phonon coupling coefficient for each vibrational normal mode, together with a thermal weighting factor describing the population of the mode.[14,16,18–22] However, relevant molecular systems may possess dozens of thermally accessible vibrations, so these models possess many more parameters than experimental T_1 data points, rendering unique data fitting impossible. To circumvent this, spin-phonon coupling coefficients are computationally predicted via density functional theory[14,16,18,20,21] (DFT) or multireference wavefunction methods.[20,22] Here, again, there exists no consensus on the correct way to compute the coupling coefficient of relevance to S = 1/2 spin relaxation. Various models have proposed using the first-derivative of the g-tensor principal values with respect to a vibrational coordinate ($\partial g/\partial Q$),[14,18] the second derivative of the g-tensor,[19] the first derivative of the hyperfine tensor,[20,21], and the average of all nine g-tensor derivatives.[16] Unsurprisingly, these approaches lead to diverging predictions for which vibrational modes have the strongest impact on spin relaxation, with different studies implicating totally symmetric a_1 vibrations,[14,18] rotational e_g or e modes,[16] and ungerade bending modes.[19] The central problem is that T_1 temperature dependence is an insufficiently powerful experimental observable to discriminate between competing spin relaxation theories.

In this work, we show that T_1 anisotropy is an accessible and informative experimental observable for spin relaxation that has been under-utilized in the molecular qubit literature. We acquire T_1 anisotropy measurements through powder-pattern pulsed EPR for a library of highly coherent Cu(II) and V(IV) qubits (Figure 5.1), including both well-established molecular qubits (Figure 5.1B-F) and literature compounds that have not yet been studied in the context of quantum information science (Figure 5.1A). Existing T_1 models based on derivatives of the spin Hamiltonian cannot account for the observed T_1 anisotropy. Furthermore, the T_1 anisotropy shows no correlation with the static spin Hamiltonian parameters. We therefore derive a new theory for anisotropic spin relaxation based on the spin-orbit coupled wavefunctions instead of the spin Hamiltonian, and show that this theory accurately reproduces the average T_1 anisotropy. Finally, we demonstrate that compound-by-compound variations in the T_1 anisotropy provide a unique and promising spectroscopic approach for probing vibronic and ligand field contributions to spin relaxation. The T_1 anisotropy observable has the potential to discriminate between competing theoretical spin relaxation models, leading to a deeper fundamental understanding of spin-phonon coupling and spin relaxation mechanisms and, thus, a more rational design process for molecular electron spin qubits.

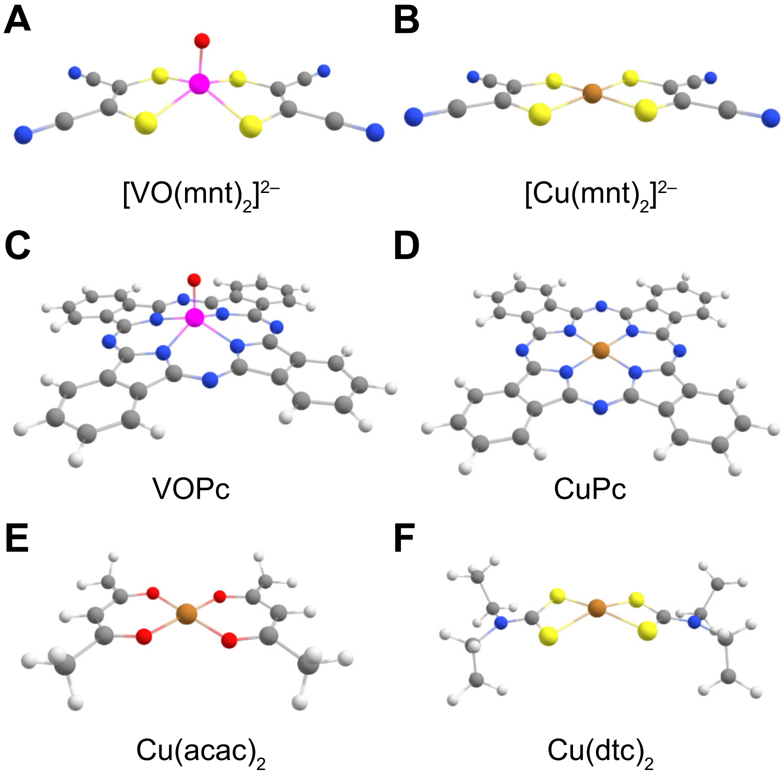

Figure 5.1: Highly coherent V(IV) and Cu(II) S = 1/2 compounds employed for analysis of T_1 anisotropy. (A) Vanadyl bis(maleonitriledithiolate), (B) copper bis(maleonitriledithiolate), (C) vanadyl phthalocyanine, (D) copper phthalocyanine, (E) copper bis(acetylacetonate), (F) copper bis(diethyldithiocarbamate). Color scheme: C = dark grey, H = white, N = blue, S = yellow, O = red, Cu = brown, V = pink.

5.3 Results

T_1 anisotropy refers to how the measured T_1 in pulsed EPR changes depending on the orientation of the molecular axes to the applied magnetic field.[23] As the molecules considered in this study possess axial or nearly-axial g-tensors, T_1 anisotropy will be discussed with reference to two orientations: $B \parallel g_z$ ("parallel orientation," z) and $B \perp g_z$ ("perpendicular orientation," x or y), where the z-axis for a tetragonal complex is approximately collinear with the principal symmetry axis extending out of the equatorial plane (Figure 5.2A). Note that single crystal measurements are not necessary to obtain T_1 anisotropy in pulsed EPR. Because $g_{\parallel} \neq g_{\perp}$, each orientation has a unique resonant field position, so setting the magnitude of the applied magnetic field selectively analyzes a subpopulation of molecules with a particular orientation, even when considering a microcrystalline powder or a frozen solution. Simulation of the metal hyperfine splitting from the I = 3/2 ^{63}Cu and ^{65}Cu nuclei (69% and 31% abundance, respectively) and the I = 7/2 ^{51}V nuclei (99.8% abundance), as well the differing nuclear g-factors for ^{63}Cu and ^{65}Cu (+1.48 and +1.58, respectively)[24], reveals that the complete EPR spectra are composed of a sum of hyperfine manifolds, each with its own characteristic orientation dependence (Figure 5.2B-C). Overlap between hyperfine manifolds means that some values of the applied magnetic field may probe two or more sub-populations of molecular orientations, each with a unique m_I value. For example, a T_1 measurement collected for the simulated Cu(II) spectrum at 3300 G (Figure 5.2B) would probe both molecules with an orientation of 45° (m_I = -1/2) and molecules with an orientation of 70° (m_I = -3/2). Nonetheless, it typically remains possible to acquire T_1 for pure parallel and perpendicular orientations. For Cu(II), 3050 G and 3575 G selectively probe the parallel orientation, while 3390 G and 3480 G selectively probe the perpendicular orientation (arrows in Figure 5.2B). For V(IV), 2900 G and 4200 G selectively probe the parallel orientation while 3400 G and 3500 G selectively probe the perpendicular orientation (arrows in Figure 5.2C). In this way, it remains possible to acquire $T_1(\perp)$ and $T_1(\parallel)$ from powder-pattern measurements.

X-band T_1 anisotropy measurements were conducted via inversion recovery at 100 K for isostructural diamagnetic solid state dilutions of 0.1% $(PPh_4)_2[VO(mnt)_2]$ in $(PPh_4)_2[MoO(mnt)_2]$,[25,26] 0.1% $(PPh_4)_2[Cu(mnt)_2]$ in $(PPh_4)_2[Ni(mnt)_2]$,[8] 0.1% VOPc in TiOPc,[27] 1% CuPc in ZnPc,[27] and 0.1% $Cu(acac)_2$ in $Pd(acac)_2$ (Figure 5.1A-E).[28] T_1 anisotropy measurements for 0.2% $Cu(dtc)_2$ in $Ni(dtc)_2$ (Figure 5.1F) at 100 K were previously reported by Eaton and Eaton,[23] so anisotropy information has been extracted from their data and included in this analysis. The choice of 100 K ensures spin relaxation will be dominated by the two-phonon Raman process operating on molecular vibrations,[14,29] while simultaneously allowing measurement of compounds lacking detectable room temperature coherence. The results are plotted

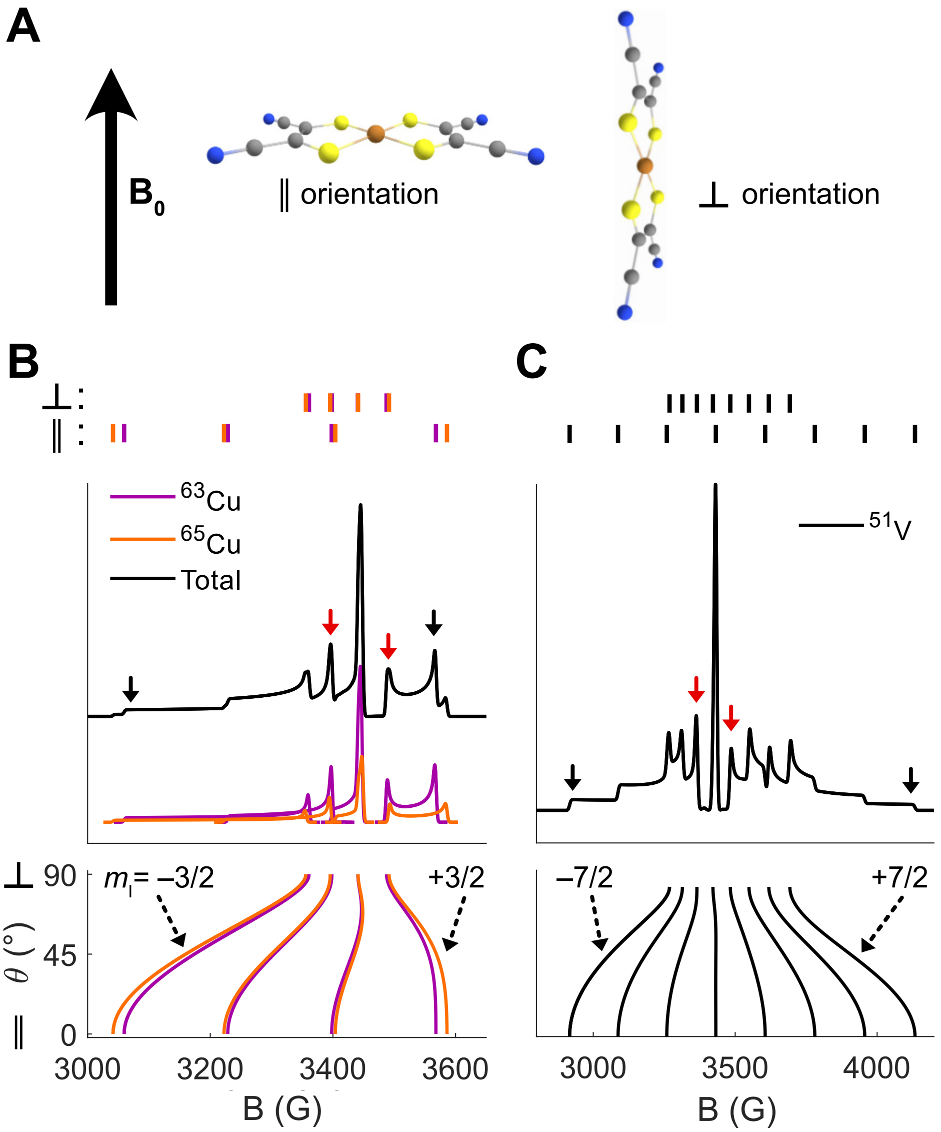

Figure 5.2: Simulated orientation dependence of a pulsed EPR echo-detected field sweep (EDFS). (A) Definition of the parallel and perpendicular orientations for a tetragonal Cu(II) complex. (B) Simulated Cu(II) EDFS and orientation dependence of the constituent hyperfine m_I manifolds for the spin Hamiltonian parameters $g_{\parallel}$ = 2.0912, $g_{\perp}$ = 2.0218, $A_{\parallel}$ = -500.1 MHz (-166.8 × 10^{-4} cm^{-1}), $A_{\perp}$ = -116.9 MHz (-39.0 × 10^{-4} cm^{-1}), ν = 9.7 GHz, taken from fits to the experimental [Cu(mnt)$_2$]$^{2-}$ CW EPR spectrum. (C) Simulated V(IV) EDFS and orientation dependence for the spin Hamiltonian parameters $g_{\parallel}$ = 1.9650, $g_{\perp}$ = 1.9863, $A_{\parallel}$ = -478.0 MHz (-159.4 × 10^{-4} cm^{-1}), $A_{\perp}$ = -167.8 MHz (-55.9 × 10^{-4} cm^{-1}), ν = 9.7 GHz, taken from fits to the experimental VOPc CW EPR spectrum. Black solid arrows indicate pure parallel orientations in the EDFS, while red solid arrows indicate pure perpendicular positions.

together with the simulated field positions for the perpendicular and parallel orientations for ease of interpretation (Figure 5.3). Stretching factors for the stretched exponential fits are reported in Figure S24.

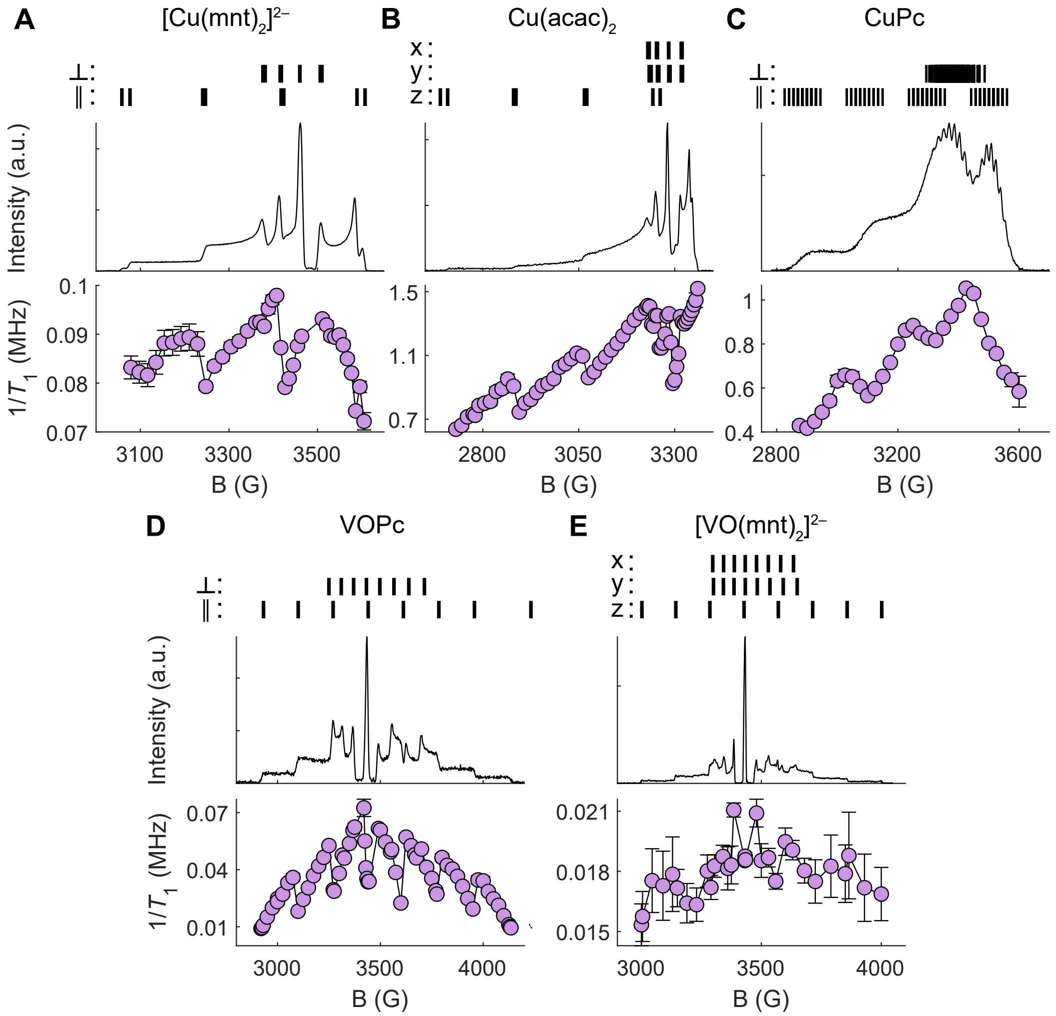

Figure 5.3: X-band T_1 anisotropy measured by inversion recovery at 100 K for isostructural solid state dilutions indicated in the text. (A) $[Cu(mnt)_2]^{2-}$, (B) $Cu(acac)_2$, (C) CuPc, (D) VOPc, (E) $[VO(mnt)_2]^{2-}$. Resonant field positions obtained from simulations of CW spectra (Figures S3-S7), with spin Hamiltonian parameters given in Table 5.1. For perfectly axial spin Hamiltonians in A, C, and D, the ⊥ label corresponds to x and y while the || label corresponds to z.

Some features of the T_1 anisotropy are common to all compounds analyzed. (i) For both Cu(II) and V(IV) compounds, relaxation is always fastest at the perpendicular orientation and slowest at the parallel orientation. (ii) Sharp discontinuities in the T_1 occur at the hyperfine turning points. These features arise from averaging over m_I subpopulations with different molecular orientations at the same resonant

Compound	g_x	g_y	g_z	g_{aniso}	$\lvert A_x \rvert$	$\lvert A_y \rvert$	$\lvert A_z \rvert$	A_{aniso}
$[\text{Cu(mnt)}_2]^{2-}$	2.022	2.022	2.091	0.222	117	117	500	0.234
Cu(dtc)$_2$*	2.018	2.018	2.083	0.195	129	129	501	0.257
Cu(acac)$_2$	2.052	2.048	2.261	0.184	78	70	564	0.132
CuPc	2.046	2.046	2.176	0.252	48	48	625	0.077
VOPc	1.986	1.986	1.965	0.437	168	168	478	0.351
$[\text{VO(mnt)}_2]^{2-}$	1.990	1.987	1.975	0.505	117	134	400	0.313

Table 5.1: Spin Hamiltonian g-tensor and A-tensor parameters for the samples analyzed in Figure 5.3, obtained from fits to the corresponding CW EPR spectra (Figures S3-S7). All hyperfine values in units of MHz. g_{aniso} is defined as $\left|(g_\perp - g_e)\left(g_\parallel - g_e\right)\right|$, where $g_e = 2.0023$ is the isotropic free-electron g value. A_{aniso} is defined as $\left|A_\perp / A_\parallel\right|$. See Table S1 for complete spin Hamiltonian simulation parameters. (*) Ref.[23]

field. For the example of $[\text{Cu(mnt)}_2]^{2-}$ (Figure 5.3A), an applied magnetic field of 3200 G probes only molecules from m_I = -3/2 with an orientation around 45°, while a field of 3250 G would probe both m_I = -3/2 with an orientation around 60° and m_I = -1/2 with an orientation around 0°, giving an average orientation around 30°. This leads to a discontinuous decrease in the spin relaxation rate at the hyperfine turning point. These features do not contain extra information content in themselves, but rather represent a by-product of performing the T_1 anisotropy measurement on a power-pattern sample. (iii) After accounting for the effect of the hyperfine turning points, $1/T_1$ varies approximately linearly between the parallel and perpendicular orientations. For single crystal EPR of Cu(dtc)$_2$ in a Ni(dtc)$_2$ matrix, Eaton and Eaton have demonstrated that $1/T_1$ varies linearly with $\sin^2\theta$, where θ is the orientation of the crystal between the parallel and perpendicular orientations (Figure 5.2).[23] Extending this idea to powder-pattern EPR, we have simulated the average angle $\overline{\theta}$ and $\overline{\sin^2\theta}$ probed at any given field position by using the spin Hamiltonian parameters (Table 5.1, Table S1). The observed $1/T_1$ patterns can be modeled well using only $\overline{\sin^2\theta}$ and a constant offset (Figure 5.4) (Supporting Information Section 5). Importantly, Eaton and Eaton's single crystal experiments show that $1/T_1$ does not change significantly with the nuclear spin projection m_I, so geometric averaging is sufficient to explain T_1 anisotropy.[23] The quality of our fit confirms that $1/T_1$ is indeed determined by the molecular orientation.

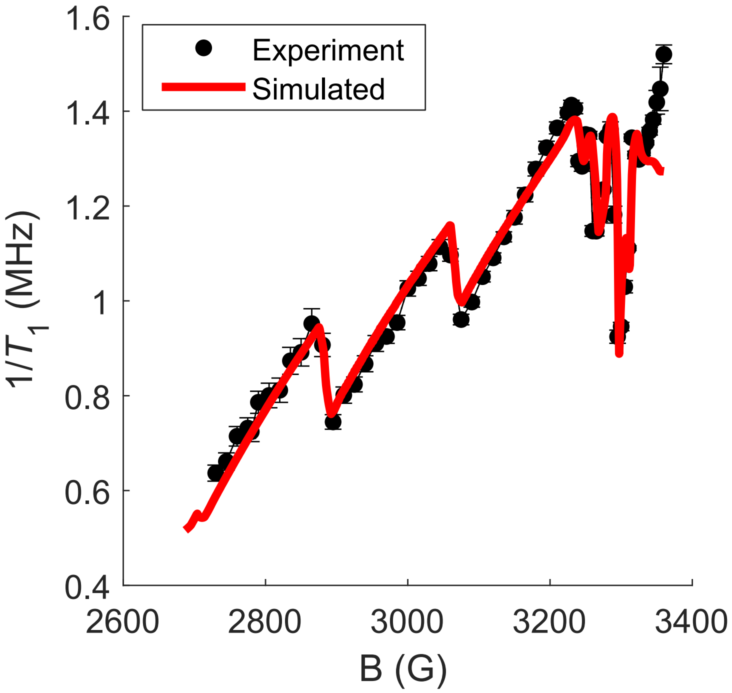

Figure 5.4: Simulation of T_1 anisotropy for the Cu(acac)$_2$ sample (X-band, inversion recovery, 100 K). The simulated red curve follows the functional form of $\overline{\sin^2\theta}$, where $\overline{\theta}$ is the average molecular orientation probed at any given observer field position.

^{14}N superhyperfine coupling smears out the orientation dependence for CuPc in Figure 5.3C. The Pascal's triangle distribution of superhyperfine absorption intensities from the four equivalent nitrogens leads to some curvature in $1/T_1$ as a function of field near the Cu hyperfine turning points. This is consistent, however, with an intrinsic linear variation in $1/T_1$ with the g-tensor orientation (Figure S30). Additionally, unique T_1 orientation effects from the ^{63}Cu and ^{65}Cu isotopes can be observed in Figure 5.3A at high fields (~3600 G). The isotope manifolds reach the parallel orientation at slightly different fields, resulting in staggered minima in $1/T_1$. Finally, note that Cu(acac)$_2$ possesses an EDFS signal at fields above the highest perpendicular turning point owing to the combination g- and A-tensor anisotropy and the presence of a strong nuclear quadrupole interaction (NQI).[28]

Owing to the linear variation of T_1 between the $g_{\|}$ and $g_{\perp}$ resonance positions, we can summarize the T_1 anisotropy by considering the spin relaxation rate at the parallel and perpendicular orientations. The T_1 anisotropy ratio is defined as:

$$T_1 \text{ anisotropy} = \frac{1/T_1(\perp)}{1/T_1(\|)}. \tag{5.1}$$

The T_1 anisotropy values extracted from Figure 5.3 are given in Table 5.2. Additionally, 100 K Q-band inversion recovery experiments (Figure S16) and 100 K X-band and Q-band picket fence saturation recovery experiments (Figures S17-S18) have been performed for selected compounds (Supporting Information Section 4). The T_1 anisotropy values are very similar between X- and Q-band and additionally between inversion recovery and saturation recovery (Table S2), validating T_1 anisotropy as an intrinsic molecular property rather than an artifact of spectral diffusion.[30] Owing to enhanced signal-to-noise, the X-band inversion recovery data (Figure 5.3) are most reliable and henceforth analyzed, additionally including the X-band CW saturation recovery value for Cu(dtc)$_2$ from ref[23].

Compound	T_1 anisotropy
$[\mathrm{Cu(mnt)_2}]^{2-}$	1.3
Cu(dtc)$_2$	2.3
Cu(acac)$_2$	2.4
CuPc	2.8
VOPc	6.0
$[\mathrm{VO(mnt)_2}]^{2-}$	1.2

Table 5.2: T_1 anisotropy ratios at 100 K for selected Cu(II) and V(IV) molecular qubits. All measurements except for Cu(dtc)$_2$ are performed at X-band and 100 K using inversion recovery. CW saturation recovery measurements for Cu(dtc)$_2$ are taken from ref.[23].

Over the six compounds considered, the average T_1 anisotropy is 2.7. Three of the four Cu compounds, Cu(acac)$_2$, Cu(dtc)$_2$, and CuPc, each have T_1 anisotropy values very close to the average. The final Cu compound, $[\mathrm{Cu(mnt)_2}]^{2-}$, and both vanadyl compounds, VOPc and $[\mathrm{VO(mnt)_2}]^{2-}$, each have T_1 anisotropy values significantly different from the 2.7 average. We now turn to the theoretical interpretation of the T_1 anisotropy metric, seeking to explain both the value of the average anisotropy and the reasons for compound-by-compound deviations from it.

5.4 Discussion

The linear orientation dependence of $1/T_1$ at intermediate orientations between parallel and perpendicular is significant, as it indicates that the orientation itself, rather than the rate of change of the orientation with respect to the resonant field, is the underlying predictor for spin relaxation. Notably, Hahn-echo measurements of T_m display a different trend: the decoherence rate $1/T_m$ is maximized near the intermediate orientation $\theta = 45°$, where $\partial B/\partial\theta$ is maximized, and minimized near the principal g-tensor orientations $\theta = 0°$ and $\theta = 90°$.[31,32] The T_m anisotropy has been interpreted as indicating that molecular rotations or librations dominate T_m, as these motions dynamically change θ and therefore the resonant field and effective Larmor frequency.[31] But for T_1, minimum and maximum values of the spin relaxation rate are obtained at the principal orientations $\theta = 0°$ and $\theta = 90°$, with the intermediate field position bearing no special significance. This indicates that rotational or librational motions likely do not dominate T_1, but rather vibrational modes that alter the principal g values ($g_{\|}$ and $g_{\perp}$) are implicated.[23,33,34] Note that isotopic substitution experiments for oxochromium(V)bis(2-hydroxy-2-ethylbutyrate) showed that both enriched ^{53}Cr (I = 3/2) and natural abundance Cr (90.5% I = 0) displayed no more than 10-20% changes in T_1, indicating that metal hyperfine is not the dominant contribution to spin relaxation in X-band EPR.[33]

We now demonstrate that several straightforward conjectures for interpreting T_1 based on existing spin Hamiltonian theories fail to account for the experimental results. First, it might be conjectured that the T_1 anisotropy would be directly proportional to the anisotropy of the principal g values, since the underlying spin Hamiltonian is itself anisotropic. However, this fails for two reasons. (1) The g value anisotropy is opposite to the T_1 anisotropy. Spin relaxation is slowest along the parallel orientation, but the orbital contribution to the g value is largest at the parallel orientation for the tetragonal complexes considered. Therefore, g value anisotropy would predict all T_1 anisotropy values should be less than 1, which is not observed. (Note that the sign of the many electron spin-orbit coupling constant is negative for Cu(II) (–830 cm^{-1}) but positive for V(IV) (+250 cm^{-1}), resulting in a single largest g value for Cu(II) ($g > g_e$) but a single smallest g value for V(IV) ($g < g_e$).[3,18] This does not reflect any fundamental difference in the axial electronic structure, as only the orbital contribution to the g value can interact with vibrations and contribute to relaxation.) (2) There is in fact no correlation between the T_1 anisotropy and the g-tensor anisotropy (Figure 5.5A), and similarly there exists no correlation between the T_1 anisotropy and the hyperfine tensor anisotropy (Figure 5.5B). Clearly, spin relaxation anisotropy cannot be predicted from consideration of the static spin Hamiltonian alone.

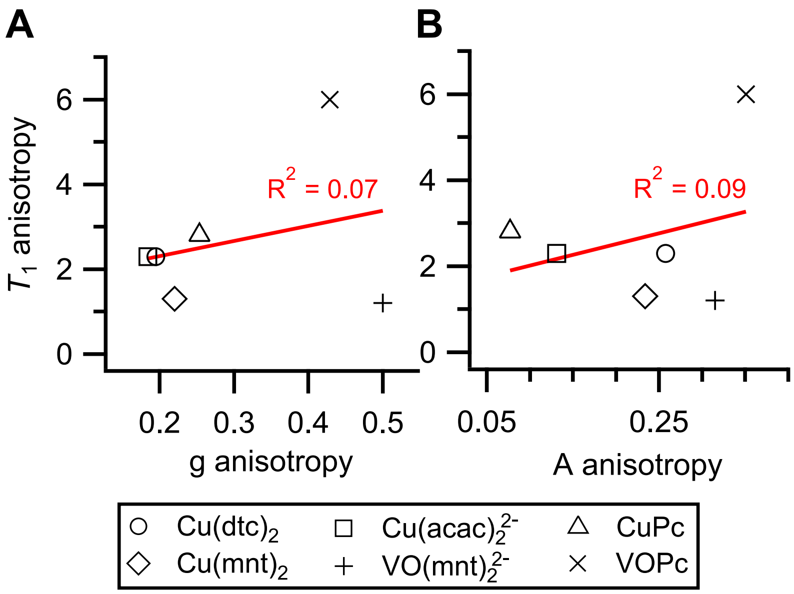

Figure 5.5: No correlation between the experimental T_1 anisotropy and the g-tensor or hyperfine tensor anisotropy. T_1 anisotropy is defined as in Equation (5.1). (A) g anisotropy is defined as $\left|(g_\perp - g_e)\,(g_\| - g_e)\right|$, where $g_e = 2.0023$ is the isotropic free-electron g value. (B) A anisotropy is defined as $\left|A_\perp\; A_\|\right|$. A and g anisotropy values are taken from Table 5.1.

A second straightforward conjecture is that spin relaxation along a given direction should be proportional to the vibronic derivative of the principal g value along that orientation; that is, $1/T_1(\|) \propto \partial g_\| / \partial Q$ and $1/T_1(\perp) \propto \partial g_\perp / \partial Q$, such that T_1 anisotropy $= (\partial g_\perp/\partial Q) \,/\, (\partial g_\|/\partial Q)$. However, this too fails. Previous DFT calculations of spin-phonon coupling coefficients have demonstrated that $\partial g_\|/\partial Q > \partial g_\perp/\partial Q$ for nearly all vibrational modes active for spin relaxation in tetragonal Cu(II) and V(IV) complexes, including CuPc and VOPc.[14,18] This is in fact the expected trend for the g-tensor derivatives: since the orbital contribution to the g-tensor is largest along the parallel orientation, the g-tensor modulation with respect to vibronic perturbation of the orbitals should also be largest along the parallel orientation. However, again, this fails to account for the experimental observation that spin relaxation is fastest at the perpendicular orientation, where the g value derivative is smallest. Note also that approaches which average all nine g-tensor derivatives[20] cannot account for spin relaxation anisotropy.

Finally, it may be argued that relaxation is fastest along the perpendicular orientation simply because there are more spins per Gauss in this region of the spectrum. However, examination of Figure 5.3 shows that $1/T_1$ does not track linearly with the EDFS intensity. This is exemplified by the m_I = +3/2 manifold of $[\mathrm{Cu(mnt)_2}]^{2-}$ (Figure 5.3A). Measurements of T_1 on natural abundance Cr(V) have demonstrated minimal changes in T_1 between the I = 0 region of the spectrum (90.5% abundance) and the I = 3/2 region (9.5% abundance), despite the large change in spins per Gauss. Eaton and Eaton also found T_1 anisotropy was very similar between single crystal and microcrystalline powder samples of $\mathrm{Cu(dtc)_2}$, despite differing spectral densities.[23] Given the failure of each of these simplified models, we believe a new theoretical approach outside of the spin Hamiltonian is required to interpret T_1 anisotropy.

5.4.1 Derivation of Average T_1 Anisotropy

To derive the correct value of the T_1 anisotropy for a $\mathrm{d^9}$ Cu(II) system, we develop an approach that uses the explicit forms of the spin-orbit coupled wavefunctions. First, we consider the case where the magnetic field is parallel to the molecular z-axis. The zeroth-order Kramers doublet ground state wavefunctions contain a single unpaired hole in the $d_{x^2-y^2}$ orbital, and the spin is aligned or anti-aligned along the z-axis. For the M_S = +1/2 Zeeman sublevel, this state is denoted as $|x^2-y^2,+_z\rangle$, with both the orbitals and spins quantized about the molecular z-axis. Via first-order perturbation theory, however, the spin-orbit coupling operator $\widehat{H}_{SOC} = \lambda\vec{L}\cdot\vec{S}$ introduces small contributions of other orbitals and spin orientations into the ground state wavefunction.[35] A more accurate picture of this state is thus given in Equation (5.2), as derived in Supporting Information Section 6, where λ is the many-electron spin-orbit coupling constant and E_{xy}, E_{xz}, and E_{yz} denote the energies of the respective ligand field excited states:

$$|0_z\rangle = |x^2-y^2,+_z\rangle - \frac{i\lambda}{E_{xy}}|xy,+_z\rangle - \frac{\lambda}{2E_{xz}}|xz,-_z\rangle + \frac{i\lambda}{2E_{yz}}|yz,-_z\rangle\,. \tag{5.2}$$

Notice that the spin in the xz and yz orbital components is pointing towards the negative z-axis, even though the wavefunction prior to the perturbation was a "spin-up" state. This is a consequence of the structure of the spin-orbit operator. The xz and yz orbitals are rotated into the ground state x^2-y^2 orbital via the L_x and L_y operators, which are connected via the dot product to S_x and S_y. These in turn are linear combinations of the raising and lowering spin operators S_+ and S_-. Since M_S = +1/2 cannot be raised any further for a S = 1/2 system, spin-orbit mixing of the xz and yz orbitals into the ground state via L_x and L_y requires a concomitant lowering of the M_S value to M_S = -1/2 via S_-. Note also that λ is on the order of 100s of $\mathrm{cm^{-1}}$, while the excited state energies are on the order of 10 000s of $\mathrm{cm^{-1}}$. This implies the M_S = -1/2 components constitute on the order of 1% of the nominally "M_S = +1/2" wavefunction.

Next, we consider the case where the magnetic field is perpendicular to the molecular z-axis, taken as B || x for simplicity. The orbitals remain quantized about the z-axis, which defines the electrostatic molecular bonding environment that gives the orbitals their shape. The spins, however, will orient along the x-axis due to the magnetic field, so we denote the x-quantized spin-up function as $+_x$. As derived in Supporting Information Section 6, we obtain:

$$|0_x\rangle = |x^2 - y^2, +_x\rangle - \frac{i\lambda}{E_{xy}}|xy, -_x\rangle - \frac{\lambda}{2E_{xz}}|xz, -_x\rangle + \frac{i\lambda}{2E_{yz}}|yz, +_x\rangle\,. \tag{5.3}$$

Crucially, the orbital components mixed in with the opposite spin direction have changed. While the parallel orientation saw xz and yz mixed in with opposite $M_S(z)$, the x orientation has xy and xz mixed in with opposite $M_S(x)$ orientation. Similarly, the y orientation will have xy and yz mixed with opposite $M_S(y)$ orientation. Because the xy orbital has a spin-orbit coupling mixing coefficient twice as large as that for xz and yz, this means the "spin-down" character in the nominally "spin-up" wavefunction will be larger for the perpendicular orientation and smaller for the parallel orientation.

The significance of these wavefunctions becomes clear when considering that spin-flip processes are associated with a change in the M_S value, and therefore should be dominated by that portion of the spin-orbit operator which mixes oppositely-signed spin functions into the ground state.[33] That is, relaxation along the parallel orientation is determined by how much xz and yz orbital mixing into the $x^2 - y^2$ ground state is modulated by a vibrational mode (Equation (5.2)). By contrast, $g_{||}$ is determined entirely by xy orbital mixing and not by xz and yz. The $\partial g_{||}/\partial Q$ value is determined by the degree to which xy orbital mixing with $x^2 - y^2$ ground state is modulated by the vibrational mode. Therefore, the spin-orbit wavefunction method yields distinct T_1 anisotropy predictions from those of the straightforward $\partial g/\partial Q$ method considered earlier.

An analytic expression for the T_1 anisotropy can be obtained by applying Fermi's golden rule to Equations (5.2) and (5.3) (Supporting Information Section 6), with the necessary approximations discussed and justified in Supporting Information Section 7. A single dominant vibrational mode Q is assumed at the temperature of the measurement, and $\partial E/\partial Q$ gives the vibronic coupling terms to the individual excited states, yielding:

$$\frac{1/T_1(\perp)}{1/T_1(\|)} = \frac{\frac{1}{E_{xy}{}^2}\left(\frac{\partial E_{xy}}{\partial Q}\right)^2 + \frac{1}{8E_{xz}{}^2}\left(\frac{\partial E_{xz}}{\partial Q}\right)^2 + \frac{1}{8E_{yz}{}^2}\left(\frac{\partial E_{yz}}{\partial Q}\right)^2}{\frac{1}{4E_{yz}{}^2}\left(\frac{\partial E_{yz}}{\partial Q}\right)^2 + \frac{1}{4E_{xz}{}^2}\left(\frac{\partial E_{xz}}{\partial Q}\right)^2}. \tag{5.4}$$

Making the additional approximation that all excited states have the same energy and all vibronic coupling terms are the same, Equation (5.4) simplifies to yield a numerical prediction for the average T_1 anisotropy:

$$\frac{1/T_1(\perp)}{1/T_1(\|)} = \frac{1 + \frac{1}{8} + \frac{1}{8}}{\frac{1}{4} + \frac{1}{4}} = \frac{5}{2}. \tag{5.5}$$

Thus, the spin-orbit wavefunction method predicts an average T_1 anisotropy of 2.5, in excellent agreement with the average experimental value of 2.7 (Table 5.2). We note that an alternate derivation using Elliott's relation[36,37] for condensed matter spin relaxation also yields a value of 2.5 for the average T_1 anisotropy (Supporting Information Section 7, Equations S29-S35), further supporting the reasonableness of the approximations involved.

It is useful to discuss the T_1 anisotropy derivation from a conceptual point of view. The origin of the 2.5 anisotropy prediction lies entirely with the different angular momentum matrix elements between excited states and the $x^2 - y^2$ ground state. The xy excited state has twice as much spin-orbit mixing as xz or yz. Upon squaring for the matrix element in Fermi's golden rule, the xy contribution becomes four times larger than xz or yz. However, vibrational modulation of a given excited state only contributes to spin-lattice relaxation if that excited state mixes spin-down character into a predominantly spin-up wavefunction or vice-versa. When the applied field is along the z-axis, only xz and yz are mixed into the wavefunction with opposite spin character. This gives a relative spin relaxation contribution of 1 + 1 = 2. When the applied field is along the x-axis, xy and xz are mixed with opposite spin character. This gives a relative spin relaxation of 4 + 1 = 5. Taking the ratio of these contributions gives the T_1 anisotropy prediction of 5/2.

5.4.2 Deviations from Average T_1 Anisotropy

While Cu(acac)$_2$, Cu(dtc)$_2$, and CuPc each have T_1 anisotropy values well-predicted by Equation (5.5), [Cu(mnt)$_2$]$^{2-}$ and [VO(mnt)$_2$]$^{2-}$ have T_1 anisotropy values significantly smaller than 2.5, while VOPc has a T_1 anisotropy significantly larger than 2.5 (Table 5.2). However, Equation (5.5) neglected changes in the spin relaxation contributions due to (a) differing excited state energies and (b) differing excited state vibronic coupling terms. We now seek to explain deviations from 2.5 in terms of these two chemical factors, the effects of which are retained in Equation (5.4). These terms offer unique connections between ligand field theory and observable spin relaxation phenomena.

Many highly coherent molecular qubit complexes employ π-conjugated ligand frameworks, with the result that the d-d transitions of relevance to Equation (5.4) are obscured by charge-transfer and intra-ligand transitions in the UV-vis-NIR spectra. However, a few d-d transitions are observable and informative. Cu(acac)$_2$ (Figure 5.6A) possesses two main d-d bands at 15 200 cm^{-1} with ε = 35 M^{-1} cm^{-1} and at 18 100 cm^{-1} with ε = 30 M^{-1} cm^{-1}. TDDFT calculations,[38] analysis of single-crystal absorption spectra[39], and magnetic circular dichroism[40,41] suggest that all four d-d transitions are contained within these two visible peaks, while the band at 26 200 cm^{-1}, ε = 340 M^{-1} cm^{-1} has been assigned as a low intensity $a_g \rightarrow b_{1u}$ ($d_{x^2-y^2} \rightarrow p_z$) charge transfer.[39] These d-d excited states are sufficiently close in energy that the equal-energy assumption in Equation (5.5) is reasonable, and indeed, Cu(acac)$_2$ possesses a T_1 anisotropy of 2.4, close to the 2.5 prediction of Equation (5.5).

The situation changes when considering the Cu(II) and V(IV) mnt complexes (Figure 5.6B-C). Though any d-d transitions in the visible region are obscured by charge transfer, both complexes possess d-d transitions observable in the near-IR (NIR): for [Cu(mnt)$_2$]$^{2-}$, at 8180 cm^{-1} with ε = 96 M^{-1} cm^{-1}; for [VO(mnt)$_2$]$^{2-}$, at 10 710 cm^{-1} with ε = 165 M^{-1} cm^{-1}, and an additional shoulder at 14 900 cm^{-1} with ε = 140 M^{-1} cm^{-1}. The 8180 cm^{-1} transition in [Cu(mnt)$_2$]$^{2-}$ has most recently been assigned to a single $b_{1g} \rightarrow b_{2g}$ transition in D_{2h} (hole formalism: $d_{xy} \rightarrow d_{xz}$) via TDDFT and DFT calculations,[42] in agreement with our TDDFT calculations (Table S6). The low energy of this transition arises from the strong d_{xz} π-bonding from the mnt ligand, which additionally manifests in measurable rhombicity in the NQI for [Cu(mnt)$_2$]$^{2-}$ owing to a non-axial electron density distribution at the Cu nucleus.[43] By contrast, NQI rhombicity is not observed for Cu(acac)$_2$ or Cu(dtc)$_2$, indicating the unique electronic structure produced by the mnt ligand.[43,44] Examination of Equation (5.4) indicates that an unusually small E_{xz} value would enhance spin relaxation along the parallel orientation (coefficient of 1/4) relative to the perpendicular orientation (coefficient of 1/8). This would tend to decrease the T_1 anisotropy for $[\mathrm{Cu(mnt)_2}]^{2-}$ from the theoretical average of 2.5, in agreement with the experimental value of 1.3. Note that the spin Hamiltonian parameters for $[\mathrm{Cu(mnt)_2}]^{2-}$ remain the same in solvents as strongly coordinating as pyridine and DMSO, indicating that solution-phase UV-vis-NIR spectra in dichloromethane accurately reflect the square-planar geometry in the solid-state dilution.[45] Similarly, the 10 710 cm^{-1} transition for $[\mathrm{VO(mnt)_2}]^{2-}$ has been assigned to the $d_{xy} \rightarrow d_{xz}$ and $d_{xy} \rightarrow d_{yz}$ electronic excitations (C_{2v}),[46] in agreement with our TDDFT calculations (Table S7). This would likewise tend to decrease the T_1 anisotropy for a d^1 system, in agreement with the low experimental T_1 anisotropy of 1.2 for $[\mathrm{VO(mnt)_2}]^{2-}$.

It is unclear if the low excited state energies explain the entirety of the T_1 anisotropy deviations for the mnt complexes, particularly in view of the neglect of orbital reduction factors in the derivation presented and the enhanced spin density delocalization in π-orbitals over σ-orbitals in square planar mnt complexes.[42,47? –49] In particular, L-edge X-ray absorption spectroscopy suggests that the d_{xy}-based ground state (D_{2h}) of $[\mathrm{Cu(mnt)_2}]^{2-}$ has 39% Cu character while the d_{xz}-based ground state in the oxidized analog $[\mathrm{Cu(mnt)_2}]^{-}$ has only 28% Cu character.[42] Regardless, the preceding analysis indicates a likely contribution from anisotropic excited state energies in determining T_1 anisotropy deviations for the mnt complexes.

CuPc displays two observable NIR transitions at 7920 cm^{-1}, ε = 8.6 M^{-1} cm^{-1} and 9400 cm^{-1}, ε = 11.0 M^{-1} cm^{-1} (Figure 5.6D), while VOPc displays a shoulder at 8640 cm^{-1}, ε = 20 M^{-1} cm^{-1} (Figure 5.6E). However, TDDFT modeling of both complexes shows these are not d-d transitions; they instead correspond to spin-flip transitions on the phthalocyanine ring from the a_{1u} donor orbital (Figures S33, S35). TDDFT predicts that the d-d transitions relevant to T_1 anisotropy are within 1500 cm^{-1} for both respective complexes (Tables S6-S7). Thus, there is no evidence of anisotropic excited state energy contributions to T_1 anisotropy in CuPc and VOPc. This is consistent with the near-average T_1 anisotropy of CuPc and calls for a different explanation of the unusually large T_1 anisotropy of VOPc.

To analyze VOPc, we consider the remaining terms in Equation (5.4): the vibronic excited state energy derivatives. Group theory selection rules have been developed that describe which vibrational mode symmetries are able to induce spin relaxation.[14] For a D_{4h} Cu(II) complex such as CuPc, only the totally symmetric stretch is fully allowed for spin relaxation, and the energies of all excited states may be expected to vary in a similar fashion as the ligand field strength increases along the vibrational coordinate Q. However, for a C_{4v} vanadyl complex such as VOPc,

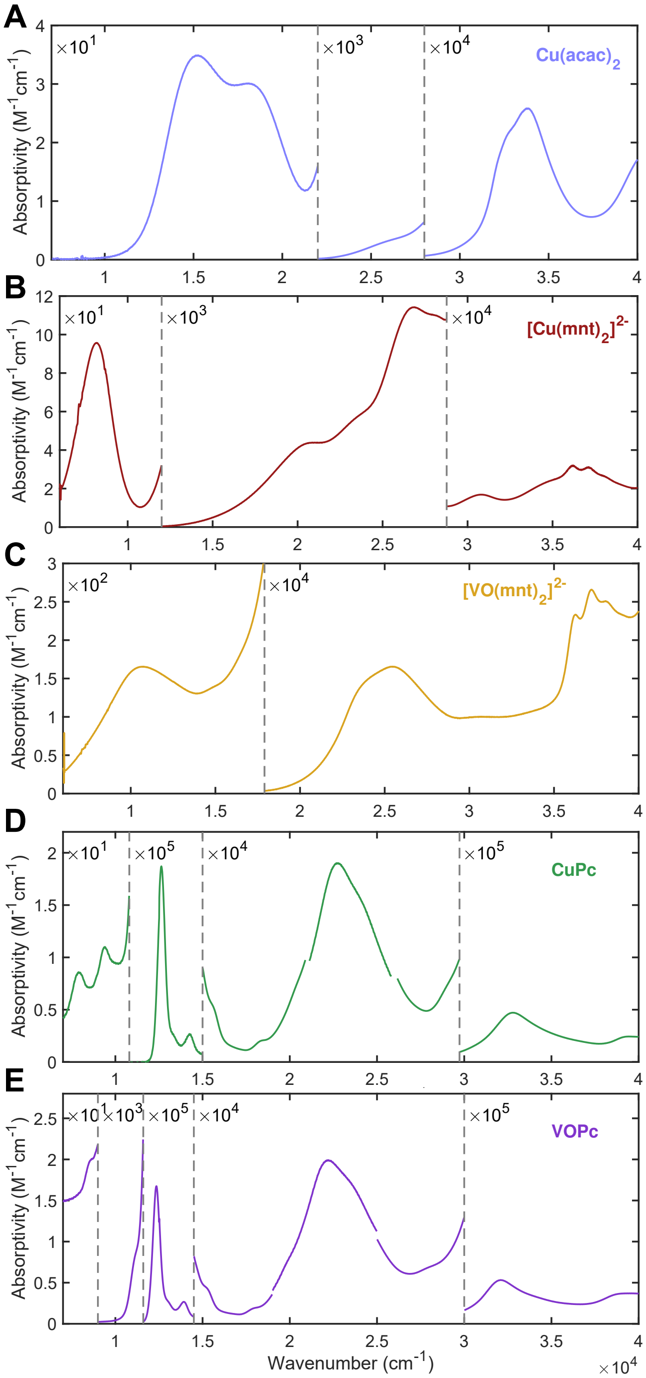

Figure 5.6: UV-vis-NIR absorption spectra for the molecular qubit complexes measured in this study. (A) Cu(acac)$_2$, (B) $(PPh_4)_2[Cu(mnt)_2]$, (C) $(PPh_4)_2[VO(mnt)_2]$, (D) CuPc, (E) VOPc. Cu(acac)$_2$, $[Cu(mnt)_2]^{2-}$, and $[VO(mnt)_2]^{2-}$ were measured in dichloromethane in a concentration range from 10 mM to 25 μM, while CuPc and VOPc were measured in concentrated H_2SO_4 from 10 mM to 1 μM. Dashed lines indicate order-of-magnitude changes in the y-axis scaling.

metal out-of-plane modes can additionally contribute to spin relaxation and mix with the symmetric stretch. The energy derivatives of such modes need not be equivalent across different excited states, as the out-of-plane motion may improve orbital overlap for some while worsening it for others. To test this idea, we have calculated the variation of the d-d excited state energies as a function of the symmetric stretch mode for the model complexes D_{4h} $\mathrm{CuCl_4^{2-}}$ and C_{4v} $\mathrm{VOCl_4^{2-}}$. The vibronic energy derivatives vary by no more than 15% between the different excited states for $\mathrm{CuCl_4^{2-}}$, consistent with no unusual contributions to T_1 anisotropy in CuPc (Table S20). For $\mathrm{VOCl_4^{2-}}$, however, the $d_{x^2-y^2}$ excited state has an energy derivative four times greater in magnitude than that of the d_{xz} and d_{yz} excited states (Table S21). Via Equation (5.4), $\partial E_{x^2-y^2}/\partial Q$ only contributes to spin relaxation along the perpendicular orientation, which would tend to increase the T_1 anisotropy. Thus, the anisotropic excited state energy derivatives rationalize the observed increase in T_1 anisotropy for VOPc. This mechanism for increased T_1 anisotropy is probably not dominant across all vanadyl complexes, however. The small T_1 anisotropy of $\mathrm{[VO(mnt)_2]^{2-}}$ suggests the low d_{xz}/d_{yz} excited state energies may play a larger role for the thiolate complex. Further work is needed to delineate the roles of different T_1 anisotropy mechanisms across a broad range of non-centrosymmetric compounds.

5.4.3 Computational Prediction of T_1 Anisotropy

The preceding sections have sought to establish an analytical ligand field theory framework for understanding the T_1 anisotropy parameter. It remains desirable, however, to obtain a facile workflow for computing the T_1 anisotropy through computational chemistry programs. While this question is not addressed fully in this work, we provide some preliminary observations. The Zeeman operator along a principal axis of the g-tensor is given by $\widehat{H_i} = g_i B_i \widehat{S_i}$ where i = x, y, or z. This operator is diagonal in the M_S(i) basis, implying that only the spin-up component of the nominally spin-up wavefunction can contribute to the g value. For the example of tetragonal d^9 Cu(II), only the mixing coefficient of the $|xy, +_z\rangle$ state contributes to g_z, despite the presence of $|xz, -_z\rangle$ and $|yz, -_z\rangle$ in the spin-orbit wavefunction (Equation (5.2)). Similarly, only the mixing coefficient of $|yz, +_x\rangle$ contributes to g_x, and only the coefficient of $|xz, +_y\rangle$ contributes to g_y. But since the perturbative contributions from $|yz\rangle$ and $|xz\rangle$ constitute the key opposite-spin components for z-orientation spin relaxation (Equation (5.4); Supporting Information Section 9), the quantity $\partial g_x/\partial Q + \partial g_y/\partial Q$ may be taken as an appropriate proxy for spin relaxation along the z-orientation. Note that this proxy does not justify the spin

Hamiltonian approach as a physical mechanism for spin relaxation, as g_x and g_y are entirely absent from the z-orientation spin Hamiltonian. Similarly, the average of $\partial g_z/\partial Q + \partial g_y/\partial Q$ and $\partial g_z/\partial Q + \partial g_x/\partial Q$ provides an appropriate proxy for spin relaxation along the perpendicular orientation where x and y are equally probed. This leads to the following proxy for T_1 anisotropy:

$$\frac{1/T_1(\perp)}{1/T_1(\|)} \approx \frac{\frac{\partial g_z}{\partial Q} + \frac{1}{2}\left(\frac{\partial g_x}{\partial Q} + \frac{\partial g_y}{\partial Q}\right)}{\frac{\partial g_x}{\partial Q} + \frac{\partial g_y}{\partial Q}}. \tag{5.6}$$

Using Equation (5.6), the standard computational methodology for obtaining $\partial g/\partial Q$ may be leveraged to predict the T_1 anisotropy.[14] While a full analysis will require computation and thermal weighting of all spin-phonon coupling coefficients in the thermally accessible window, this work is restricted to a simplified model using the single vibrational mode expected to have the largest impact on spin relaxation. This approach selects the totally symmetric vibrational mode with spin-phonon coupling coefficient larger than 1×10^{-7} that is lowest in energy, in accordance with previously-derived spin-phonon coupling selection rules[14] and thermal weighting statistics. These modes are pictured in Figure 5.7. The resulting single-mode T_1 anisotropy predictions (Table 5.3) display considerable agreement with the experimental T_1 anisotropy. The three Cu(II) complexes with T_1 anisotropy close to the theoretical 2.5 value (CuPc, Cu(acac)$_2$, and Cu(dtc)$_2$) are indeed predicted to have anisotropies close to that value. VOPc is successfully predicted to have an anomalously high T_1 anisotropy, while [VO(mnt)$_2$]$^{2-}$ is successfully predicted to have an anomalously low T_1 anisotropy. The lone compound with a seemingly incorrect prediction is [Cu(mnt)$_2$]$^{2-}$, which has a predicted T_1 anisotropy close to 2.5 despite the anomalously small experimental value. Nevertheless, the [Cu(mnt)$_2$]$^{2-}$ predicted T_1 anisotropy is indeed the smallest out of the Cu(II) complexes considered here. Further investigation is called for to ascertain if a rigorous thermally-weighted model across all vibrational modes is able to furnish a more accurate prediction for [Cu(mnt)$_2$]$^{2-}$, or if its unique electronic structure (vide supra) requires an alternative computational approach.

The preceding discussion explains the successful literature using the spin Hamiltonian $\partial g/\partial Q$-based models to model the T_1 temperature dependence, despite our finding that a spin-orbit wavefunction analysis is required to rigorously explain the T_1 anisotropy. Since spin relaxation along any principal tensor axis can be modeled by the sum of the $\partial g_i/\partial Q$ values along the other two tensor axes, the

Compound	DFT mode energy (cm^{-1})	DFT T_1 anisotropy	Experimental T_1 anisotropy
CuPc	261	2.2	2.8
$Cu(acac)_2$	212	2.3	2.4
$[Cu(mnt)_2]^{2-}$	118	2.1	1.3
$Cu(dtc)_2$	156	2.2	2.3
$[VO(mnt)_2]^{2-}$	134	0.6	1.2
VOPc	178	9.6	6.0

Table 5.3: T_1 anisotropy predictions via DFT $\partial g/\partial Q$ proxies (Equation (5.6)). At 100 K, $k_B T = 69.5$ cm^{-1}. See Table S22 for individual $\partial g/\partial Q$ values.

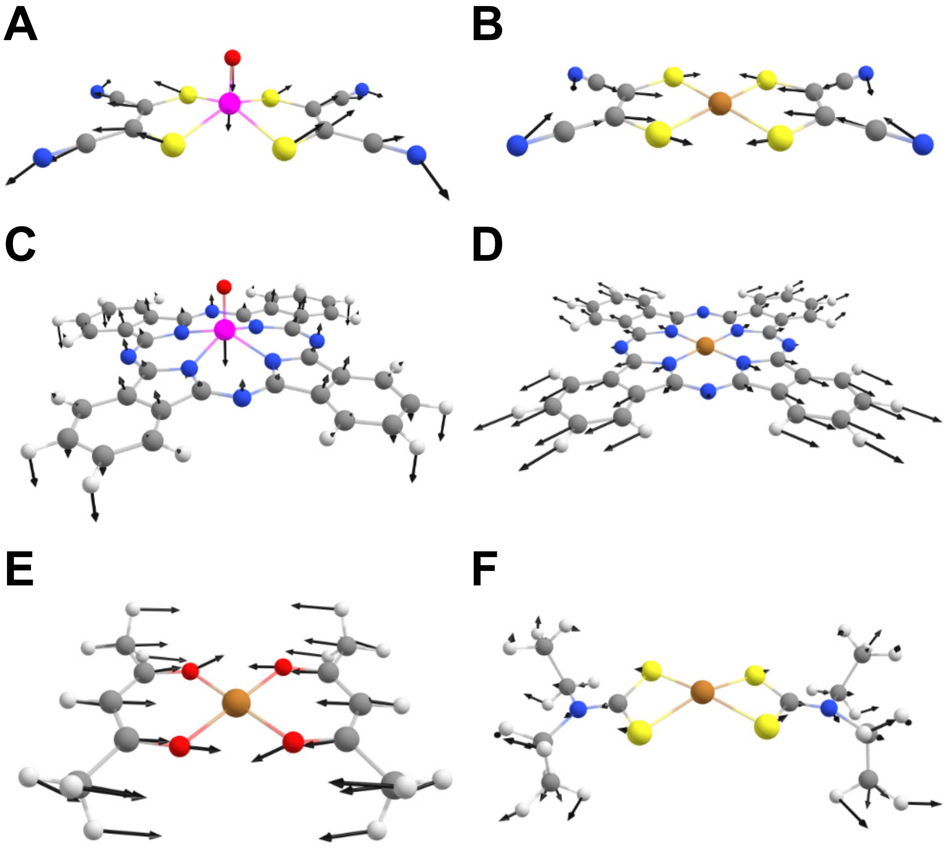

Figure 5.7: Totally symmetric vibrational modes considered for the DFT prediction of 100 K T_1 anisotropy.

orientation-averaged T_1 value can be expressed as the average of $\partial g_x/\partial Q$, $\partial g_y/\partial Q$, and $\partial g_z/\partial Q$. Such orientation-averaged predictions have proven sufficient to capture the major trends of T_1 temperature dependence, though exact quantitative agreement for molecular systems has not yet been achieved. However, on principled grounds, $\partial g/\partial Q$ must still be considered a proxy for spin relaxation rather than a fundamental descriptor of the spin-phonon coupling mechanism. Spin relaxation arises due to molecular vibrations when modulation of the spin-orbit coupling induces a transition matrix element between the spin-up and spin-down wavefunctions. By contrast, the g value describes the angular momentum content of the wavefunctions. This angular momentum is related to the spin-orbit coupling, but does not directly describe the transition matrix elements between M_S states, and therefore does not directly describe the spin relaxation mechanism. The principle of the spin Hamiltonian approach for spin-phonon coupling is to differentiate the spin Hamiltonian for the given system under analysis. When $\vec{B} \parallel g_z$, the Zeeman Hamiltonian reduces to precisely $g_z B_z \widehat{S}_z$ with no g_x or g_y terms included, and yet it is the $\partial g_x/\partial Q$ and $\partial g_y/\partial Q$ terms that are required to correctly model spin relaxation for $\vec{B} \parallel g_z$.

In a previous work, symmetry-based spin-phonon coupling selection rules were derived via group theory analysis of the ligand field theory $\partial g/\partial Q$ expression.[14] These selection rules are still valid in the orientation-selective T_1 model, provided the $\partial g/\partial Q$ proxy rules outlined above are followed: selection rules for $\partial g_z/\partial Q$ affect spin relaxation along the perpendicular orientation, while selection rules for $\partial g_x/\partial Q$ and $\partial g_y/\partial Q$ apply to both the perpendicular and parallel orientations. Fundamentally, these selection rules arise from considering the vibronic excited state coupling terms $\partial E/\partial Q$. It is therefore correct to choose the excited states corresponding to the opposite-spin spin-orbit coupled wavefunction components along the orientation of interest.

5.5 Conclusions

This study has demonstrated that T_1 anisotropy is a facile experimental observable for electron spin relaxation that reveals flaws in commonly-used spin Hamiltonian formalisms. Across a library of six highly coherent Cu(II) and V(IV) molecular qubit candidates, the average T_1 anisotropy is 2.7. Spin Hamiltonian $\partial g/\partial Q$ computational techniques either fail to predict anisotropy or incorrectly predict T_1 anisotropy less than 1, but the spin-orbit wavefunction method developed here correctly predicts an average value of 2.5. Deviations from the average 2.5 anisotropy are likely due to anisotropic excited state energies in the case of $[\mathrm{Cu(mnt)_2}]^{2-}$ and $[\mathrm{VO(mnt)_2}]^{2-}$ (T_1 anisotropy < 2.5) and anisotropic excited state vibronic coupling in the case of VOPc (T_1 anisotropy > 2.5), though further work is needed to quantify the contributions to T_1 anisotropy.

These results show that the commonly-used $\partial g/\partial Q$ formalism must be treated with caution, as it does not fully model the physics underlying S = 1/2 spin relaxation. The principal g-values are scalar-valued properties of a spin system that summarize the angular momentum content. They are not spin-flip matrix elements. Differentiation of a property, such as a g value, can do no better than provide a proxy for a true matrix element governing a time-dependent process.

From its inception, the spin Hamiltonian formalism was designed to accurately model energy levels, not wavefunctions.[50] For a d^1 or d^9 S = 1/2 system over the five d orbitals, the true Hilbert space has dimension 10, but the spin Hamiltonian representation compresses the wavefunction to a space of dimension 2. Information about the true wavefunctions is necessarily lost in this process, and this information has proven crucial to understanding the T_1 anisotropy of contemporary S = 1/2 molecular qubits. Analysis of the spin-orbit wavefunctions in the full Hilbert space recovers the correct matrix elements for molecular spin relaxation in tetragonal Cu(II) and V(IV) systems.

From an experimental spectroscopy perspective, development of the T_1 anisotropy metric holds exciting prospects for gaining new mechanistic insights into spin relaxation. Small changes in molecular bonding, symmetry, and electronic structure can manifest in large changes of the T_1 anisotropy, as witnessed by the divergent behaviors of CuPc and VOPc (identical ligands but different symmetries) or especially VOPc and $[VO(mnt)_2]^{2-}$ (both square pyramidal oxovanadium(IV) complexes, yet possessing the largest and smallest T_1 anisotropies observed in this work). This study has identified excited state energies and vibronic excited state energy derivatives as likely candidates for inducing these changes, indicating a key role for ligand field theory in understanding molecular qubit spin dynamics. However, much work remains to be done in correlating T_1 anisotropy across a wider range of ligands, molecular symmetries, and S > 1/2 systems. While our experiments have been conducted in diamagnetically diluted crystals, where spin relaxation is attributable to acoustic and optical phonons,[3,13] we note that it is equally possible to acquire T_1 anisotropy measurements on frozen solutions, where relaxation has been traditionally attributed to local modes due to the lack of long-range periodic ordering.[51] Comparison of the T_1 anisotropy between these different sample preparations will shed light on the importance of coupling to the host matrix in determining spin relaxation. A final exciting possibility involves acquiring temperature-dependent T_1 anisotropy patterns, which could enable detection of different vibrational and mechanistic (direct, Raman) contributions to spin relaxation in different temperature regimes through characteristic T_1 anisotropy signatures. We encourage other researchers to report T_1 anisotropy measurements to expand the scope of the mechanistic insights available. We believe T_1 anisotropy will ultimately stand side-by-side with temperature-dependent T_1 as a key observable for spin relaxation in molecular qubit systems.

References

[1] Wasielewski, M. R. *et al.* Exploiting Chemistry and Molecular Systems for Quantum Information Science. *Nature Reviews Chemistry* **2020**, *4,* 490–504.

[2] Atzori, M.; Sessoli, R. The Second Quantum Revolution: Role and Challenges of Molecular Chemistry. *Journal of the American Chemical Society* **2019**, *141,* 11339–11352.

[3] Mirzoyan, R.; Kazmierczak, N. P.; Hadt, R. G. Deconvolving Contributions to Decoherence in Molecular Electron Spin Qubits: A Dynamic Ligand Field Approach. *Chemistry – A European Journal* **2021**, *27,* 9482–9494.

[4] Yu, C.-J.; von Kugelgen, S.; Laorenza, D. W.; Freedman, D. E. A Molecular Approach to Quantum Sensing. *ACS Central Science* **2021**, *7,* 712–723.

[5] Atzori, M.; Tesi, L.; Morra, E.; Chiesa, M.; Sorace, L.; Sessoli, R. Room-Temperature Quantum Coherence and Rabi Oscillations in Vanadyl Phthalocyanine: Toward Multifunctional Molecular Spin Qubits. *Journal of the American Chemical Society* **2016**, *138,* 2154–2157.

[6] Fataftah, M. S.; Krzyaniak, M. D.; Vlaisavljevich, B.; Wasielewski, M. R.; Zadrozny, J. M.; Freedman, D. E. Metal-Ligand Covalency Enables Room Temperature Molecular Qubit Candidates. *Chemical Science* **2019**, *10,* 6707–6714.

[7] Amdur, M. J.; Mullin, K. R.; Waters, M. J.; Puggioni, D.; Wojnar, M. K.; Gu, M.; Sun, L.; Oyala, P. H.; Rondinelli, J. M.; Freedman, D. E. Chemical Control of Spin-Lattice Relaxation to Discover a Room Temperature Molecular Qubit. *Chemical Science* **2022**, *13,* 7034–7045.

[8] Bader, K.; Dengler, D.; Lenz, S.; Endeward, B.; Jiang, S.-D.; Neugebauer, P.; van Slageren, J. Room Temperature Quantum Coherence in a Potential Molecular Qubit. *Nature Communications* **2014**, *5,* 5304.

[9] Atzori, M.; Morra, E.; Tesi, L.; Albino, A.; Chiesa, M.; Sorace, L.; Sessoli, R. Quantum Coherence Times Enhancement in Vanadium(IV)-based

Potential Molecular Qubits: The Key Role of the Vanadyl Moiety. *Journal of the American Chemical Society* **2016**, *138,* 11234–11244.

[10] Laorenza, D. W.; Kairalapova, A.; Bayliss, S. L.; Goldzak, T.; Greene, S. M.; Weiss, L. R.; Deb, P.; Mintun, P. J.; Collins, K. A.; Awschalom, D. D.; Berkelbach, T. C.; Freedman, D. E. Tunable Cr^{4+} Molecular Color Centers. *Journal of the American Chemical Society* **2021**, *143,* 21350–21363.

[11] Wojnar, M. K.; Laorenza, D. W.; Schaller, R. D.; Freedman, D. E. Nickel(II) Metal Complexes as Optically Addressable Qubit Candidates. *Journal of the American Chemical Society* **2020**, *142,* 14826–14830.

[12] Fataftah, M. S.; Bayliss, S. L.; Laorenza, D. W.; Wang, X.; Phelan, B. T.; Wilson, C. B.; Mintun, P. J.; Kovos, B. D.; Wasielewski, M. R.; Han, S.; Sherwin, M. S.; Awschalom, D. D.; Freedman, D. E. Trigonal Bipyramidal V^{3+} Complex as an Optically Addressable Molecular Qubit Candidate. *Journal of the American Chemical Society* **2020**, *142,* 20400–20408.

[13] Standley, K. J.; Vaughan, R. A. *Electron Spin Relaxation Phenomena in Solids;* Springer US: Boston, MA, 1969. DOI: 10.1007/978-1-4899-6539-4.

[14] Kazmierczak, N. P.; Mirzoyan, R.; Hadt, R. G. The Impact of Ligand Field Symmetry on Molecular Qubit Coherence. *Journal of the American Chemical Society* **2021**, *143,* 17305–17315.

[15] Escalera-Moreno, L.; Baldoví, J. J.; Gaita-Ariño, A.; Coronado, E. Spin States, Vibrations and Spin Relaxation in Molecular Nanomagnets and Spin Qubits: a Critical Perspective. *Chemical Science* **2018**, *9,* 3265–3275.

[16] Santanni, F.; Albino, A.; Atzori, M.; Ranieri, D.; Salvadori, E.; Chiesa, M.; Lunghi, A.; Bencini, A.; Sorace, L.; Totti, F.; Sessoli, R. Probing Vibrational Symmetry Effects and Nuclear Spin Economy Principles in Molecular Spin Qubits. *Inorganic Chemistry* **2021**, *60,* 140–151.

[17] Gu, L.; Wu, R. Origin of the Anomalously Low Raman Exponents in Single Molecule Magnets. *Physical Review B* **2021**, *103,* 014401.

[18] Mirzoyan, R.; Hadt, R. G. The Dynamic Ligand Field of a Molecular Qubit: Decoherence through Spin-Phonon Coupling. *Physical Chemistry Chemical Physics* **2020**, *22,* 11249–11265.

[19] Escalera-Moreno, L.; Suaud, N.; Gaita-Ariño, A.; Coronado, E. Determining Key Local Vibrations in the Relaxation of Molecular Spin Qubits and Single-Molecule Magnets. *The Journal of Physical Chemistry Letters* **2017**, *8,* 1695–1700.

[20] Lunghi, A.; Sanvito, S. How Do Phonons Relax Molecular Spins? *Science Advances* **2019**, *5,* eaax7163.

[21] Lunghi, A.; Sanvito, S. The Limit of Spin Lifetime in Solid-State Electronic Spins. *The Journal of Physical Chemistry Letters* **2020**, *11,* 6273–6278.

[22] Reta, D.; Kragskow, J. G. C.; Chilton, N. F. Ab Initio Prediction of High-Temperature Magnetic Relaxation Rates in Single-Molecule Magnets. *Journal of the American Chemical Society* **2021**, *143,* 5943–5950.

[23] Du, J.-L.; Eaton, G. R.; Eaton, S. S. Temperature and Orientation Dependence of Electron-Spin Relaxation Rates for Bis(diethyldithiocarbamato)copper(II). *Journal of Magnetic Resonance, Series A* **1995**, *117,* 67–72.

[24] Stoll, S.; Schweiger, A. EasySpin, a Comprehensive Software Package for Spectral Simulation and Analysis in EPR. *Journal of Magnetic Resonance* **2006**, *178,* 42–55.

[25] McCleverty, J. A.; Locke, J.; Ratcliff, B.; Wharton, E. J. Transition Metal Dithiolene Complexes. Oxy-Metal Bis-1,2-Dithiolenes. *Inorganica Chimica Acta* **1969**, *3,* 283–286.

[26] Collison, D.; Mabbs, F. E.; Temperley, J.; Christou, G.; Huffman, J. C. Crystal and Molecular Structure of Bis(tetraphenylphosphonium) Bis(1,2-dicyanoethylene-1,2-dithiolato)oxovanadate(IV). Its Single-Crystal Electron Spin Resonance as a Pure Compound and Diluted in the Isomorphous Molybdenum(IV) Compound. *Journal of the Chemical Society, Dalton Transactions* **1988**, *(2),* 309–314.

[27] Follmer, A. H.; Ribson, R. D.; Oyala, P. H.; Chen, G. Y.; Hadt, R. G. Understanding Covalent versus Spin-Orbit Coupling Contributions to Temperature-Dependent Electron Spin Relaxation in Cupric and Vanadyl Phthalocyanines. *The Journal of Physical Chemistry A* **2020**, *124,* 9252–9260.

[28] Yen, T. F. *Electron Spin Resonance of Metal Complexes: Proceedings of the Symposium on ESR of Metal Chelates at the Pittsburgh Conference on Analytical Chemistry and Applied Spectroscopy, held in Cleveland, Ohio, March 4-8, 1968;* Springer US: Boston, MA, 1969. OCLC: 840289738.

[29] Eaton, S. S.; Eaton, G. R. Relaxation Mechanisms. In *eMagRes*; Wiley: 2016. _eprint: https://onlinelibrary.wiley.com/doi/pdf/10.1002/-9780470034590.emrstm1507 DOI: 10.1002/9780470034590.emrstm1507.

[30] Eaton, S. S.; Eaton, G. R. Multifrequency Pulsed EPR and the Characterization of Molecular Dynamics. In *Methods in Enzymology*, Vol. 563; Elsevier: 2015. DOI: 10.1016/bs.mie.2015.06.028.

[31] Du, J.-L.; More, K. M.; Eaton, S. S.; Eaton, G. R. Orientation Dependence of Electron Spin Phase Memory Relaxation Times in Copper(II) and Vanadyl Complexes in Frozen Solution. *Israel Journal of Chemistry* **1992**, *32,* 351–355.

[32] Jackson, C. E.; Lin, C.-Y.; van Tol, J.; Zadrozny, J. M. Orientation Dependence of Phase Memory Relaxation in the V(IV) Ion at High Frequencies. *Chemical Physics Letters* **2020**, *739,* 137034.

[33] Du, J. L.; Eaton, G. R.; Eaton, S. S. Electron-Spin-Lattice Relaxation in Natural Abundance and Isotopically Enriched Oxo-chromium(V)bis (2-hydroxy-2-ethylbutyrate). *Journal of Magnetic Resonance, Series A* **1995**, *115,* 236–240.

[34] Du, J. L.; Eaton, G. R.; Eaton, S. S. Temperature, Orientation, and Solvent Dependence of Electron Spin-Lattice Relaxation Rates for Nitroxyl Radicals in Glassy Solvents and Doped Solids. *Journal of Magnetic Resonance, Series A* **1995**, *115,* 213–221.

[35] Pake, G. E. *The Physical Principles of Electron Paramagnetic Resonance;* Frontiers in physics. Reading, Mass: W. A. Benjamin, Advanced Book Program: 2nd ed.; 1973.

[36] Žutić, I.; Fabian, J.; Das Sarma, S. Spintronics: Fundamentals and Applications. *Reviews of Modern Physics* **2004**, *76,* 323–410.

[37] Elliott, R. J. Theory of the Effect of Spin-Orbit Coupling on Magnetic Resonance in Some Semiconductors. *Physical Review* **1954**, *96,* 266–279.

[38] de Almeida, K. J.; Cesar, A.; Rinkevicius, Z.; Vahtras, O.; Ågren, H. Modelling the Visible Absorption Spectra of Copper(II) Acetylacetonate by Density Functional Theory. *Chemical Physics Letters* **2010**, *492,* 14–18.

[39] Dijkgraaf, C. Interpretation of the Polarized Absorption Spectra of Single Crystals of Copper Acetylacetonate. **1965**, *3,* 38–44.

[40] Katô, H.; Gohda, J. Magnetic Circular Dichroism of Cu(acac)$_2$, Fe(acac)$_3$, and Co(acac)$_3$. *Bulletin of the Chemical Society of Japan* **1973**, *46,* 636–637.

[41] Katô, H.; Kimura, T. The Magnetic Circular Dichroism of Some Copper(II) β-Diketone Chelate Complexes in Various Media. *Bulletin of the Chemical Society of Japan* **1974**, *47,* 732–734.

[42] Sarangi, R.; DeBeer George, S.; Rudd, D. J.; Szilagyi, R. K.; Ribas, X.; Rovira, C.; Almeida, M.; Hodgson, K. O.; Hedman, B.; Solomon, E. I. Sulfur K-Edge X-ray Absorption Spectroscopy as a Probe of Ligand−Metal Bond Covalency: Metal vs Ligand Oxidation in Copper and Nickel Dithiolene Complexes. *Journal of the American Chemical Society* **2007**, *129,* 2316–2326.

[43] White, L. K.; Belford, R. L. Quadrupole Coupling Constants of Square-Planar Copper(II)-Sulfur Complexes from Single-Crystal Electron Paramagnetic Resonance Spectroscopy. *Journal of the American Chemical Society* **1976**, *98,* 4428–4438.

[44] Soo, H.; Belford, R. L. Information from Forbidden Hyperfine Lines in Electron Paramagnetic Resonance. Copper Complexes. *Journal of the American Chemical Society* **1969**, *91,* 2392–2394.

[45] Billig, E.; Williams, R.; Bernal, I.; Waters, J. H.; Gray, H. B. The Electronic Structures of Square-Planar Metal Complexes. II. The Complexes of Maleonitriledithiolate with Copper(II), Nickel(II), Palladium(II), and Platinum(II). *Inorganic Chemistry* **1964**, *3,* 663–666.

[46] Atherton, N. M.; Winscom, C. J. Electron Spin Resonance and Electronic Structures of Vanadyl Bis(maleonitriledithiolene) and Vanadium Tris(maleonitriledithiolene). *Inorganic Chemistry* **1973**, *12,* 383–390.

[47] Kirk, M. L.; McNaughton, R. L.; Helton, M. E. The Electronic Structure and Spectroscopy of Metallo-Dithiolene Complexes. In *Progress in Inorganic Chemistry*; Stiefel, E. I., Ed.; John Wiley & Sons, Inc.: Hoboken, NJ, USA, 2004. DOI: 10.1002/0471471933.ch3.

[48] Williams, R.; Billig, E.; Waters, J. H.; Gray, H. B. The Toluenedithiolate and Maleonitriledithiolate Square-Matrix Systems. *Journal of the American Chemical Society* **1966**, *88,* 43–50.

[49] Szilagyi, R. K.; Lim, B. S.; Glaser, T.; Holm, R. H.; Hedman, B.; Hodgson, K. O.; Solomon, E. I. Description of the Ground State Wave Functions of Ni Dithiolenes Using Sulfur K-edge X-ray Absorption Spectroscopy. *Journal of the American Chemical Society* **2003**, *125,* 9158–9169.

[50] Stevens, K. W. H. 1—Spin Hamiltonians. In *Magnetism*; Rado, G. T.; Suhl, H., Eds.; Academic Press: 1963. DOI: 10.1016/B978-0-12-575301-2.50008-0.

[51] Fielding, A. J.; Fox, S.; Millhauser, G. L.; Chattopadhyay, M.; Kroneck, P. M.; Fritz, G.; Eaton, G. R.; Eaton, S. S. Electron Spin Relaxation of Copper(II) Complexes in Glassy Solution Between 10 and 120K. *Journal of Magnetic Resonance* **2006**, *179,* 92–104.

Chapter 6

T_1 ANISOTROPY ELUCIDATES SPIN RELAXATION MECHANISMS IN AN S = 1 CHROMIUM(IV) OPTICALLY ADDRESSABLE MOLECULAR QUBIT

- Adapted with permission from: Kazmierczak, N. P.; Luedecke, K. M.; Gallmeier, E. T.; Hadt, R. G. T_1 Anisotropy Elucidates Spin Relaxation Mechanisms in an S = 1 Cr(IV) Optically Addressable Molecular Qubit. *The Journal of Physical Chemistry Letters* **2023**, *14*, 7658–7664. DOI: 10.1021/acs.jpclett.3c01964. © 2023 American Chemical Society.

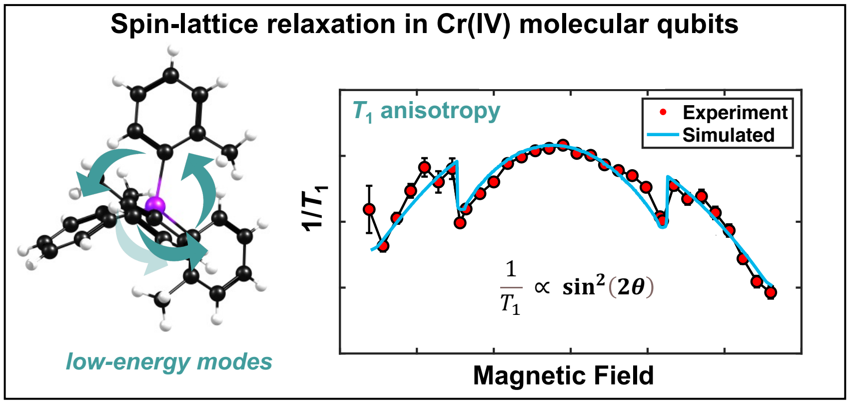

6.1 Abstract

Paramagnetic molecules offer unique advantages for quantum information science owing to their spatial compactness, synthetic tunability, room-temperature quantum coherence, and potential for optical state initialization and readout. However, current optically addressable molecular qubits are hampered by rapid spin-lattice relaxation (T_1) even at sub-liquid nitrogen temperatures. Here we use temperature- and orientation-dependent pulsed electron paramagnetic resonance (EPR) to elucidate the negative sign of the ground-state zero-field splitting (ZFS) and assign T_1 anisotropy to specific types of motion in an optically addressable S = 1 Cr(*o*-tolyl)$_4$ molecular qubit. The anisotropy displays a distinct $\sin^2(2\theta)$ functional form that is not observed in S = ½ Cu(acac)$_2$ or other Cu(II) / V(IV) microwave addressable molecular qubits. The Cr(*o*-tolyl)$_4$ T_1 anisotropy is ascribed to couplings between electron spins and rotational motion in low-energy acoustic or pseudo-acoustic

phonons. Our findings suggest that rotational degrees of freedom should be suppressed to maximize the coherence temperature of optically addressable qubits.

6.2 Introduction

The anionic nitrogen vacancy (NV^-) center in diamond constitutes one of the most widely implemented platforms for quantum sensing and imaging.[1] Substitutional replacement of two carbons in the diamond lattice with a nitrogen and a vacancy forms an S = 1 paramagnetic defect that exhibits selective photoluminescence behavior depending on the Zeeman sublevel that the spin occupies.[2,3] Furthermore, optical excitation of the NV^- center accumulates ground state spin polarization through a spin-selective intersystem crossing mechanism. These two features enable optical initialization and detection of quantum states in the Zeeman sublevels of the S = 1 defect, permitting a much greater degree of spatial localization than can be achieved with direct resonant microwave readout of the Zeeman sublevels. This functionality has enabled quantum sensing in a variety of applications,[1] including atomic scale magnetic resonance imaging of nuclear spin clusters,[4] probing intracellular molecular dynamics,[5] nanometer-scale thermometry with millikelvin accuracy inside a living cell,[6] imaging magnetic fields in live magnetotactic bacteria,[7] measuring local ion concentrations,[1] and strain/pressure sensing.[1] The main downsides of NV^- centers relate to the large bulk of the diamond lattice, the poor control over where the NV^- defects arise in the lattice, and the fixed nature of the NV^- center coherence properties.[8]

Production of molecules exhibiting the same optical initialization and readout capabilities would overcome these limitations of NV^- centers and open up molecular in situ and in vivo quantum sensing capabilities on the single nanometer scale. Multiple systems have been investigated on the basis of both S = 1 and S > 1 architectures,[9–11] but to date, the most successful molecules have been pseudo-T_d S = 1 Cr(IV) tetraaryl and tetraalkyl complexes[12,13] which display optical addressability and prolonged coherence times when diluted in non-isostructural diamagnetic matrices.[14] However, owing to fast spin relaxation, Cr(IV) molecular qubits do not display spin coherence at temperatures higher than ~60 K, at which point T_m becomes T_1 limited. This behavior is significantly inferior to that of both NV^- centers and microwave addressable S = ½ molecular qubits such as VOPc and $[Cu(mnt)_2]^{2-}$, which display coherence up to room temperature.[15–17] In particular, quantum sensing of biological systems would benefit greatly from the ability to perform room-temperature coherence measurements under ambient biochemical conditions. Therefore, to maximize the full potential of optically addressable molecular qubits, it is essential to identify and remove contributions to fast spin relaxation.

Recently, T_1 anisotropy has emerged as a novel technique for interrogating spin-phonon coupling contributions to spin relaxation and decoherence in S = ½ systems.[18] This approach can provide information regarding the vibrational contributions and mechanism of spin relaxation that is not accessible through more common temperature-dependent T_1 measurements. Here we apply this methodology to Cr(*o*-tolyl)$_4$, an S = 1 tetraaryl Cr(IV) optically addressable molecular qubit (Figure 6.1A). We find qualitatively different T_1 anisotropy patterns relative to Cu(acac)$_2$ (Figure 6.1B) and other copper(II) and oxovanadium(IV) S = ½ systems, indicating unique spin-phonon coupling contributions to spin relaxation.

6.3 Results and Discussion

The concept of T_1 anisotropy probes how the spin relaxation rate changes for molecules with different orientations relative to the spectrometer's applied magnetic field (B_0). In general, EPR spectra of powder or frozen solution samples can display resonance positions selective for these different molecular orientations, enabling access to orientation-specific relaxation rates without the need for single crystal experiments.[19] Cr(IV) qubits satisfy this requirement for orientation selectivity, as the microwave absorption spectrum of Cr(*o*-tolyl)$_4$ is composed of two transitions between the three M_S sublevels (Scheme 1C), and each spin transition occurs at a different resonance field depending on the molecular orientation (Figure 6.2A-B). By weighting these orientations with the fraction of molecules absorbing at the given field and averaging over the two spin transitions, we can define an average molecular orientation probed by EPR at any given resonance field (Figure 6.2C). At X-band, the pure parallel position can be addressed by performing pulsed EPR at 220 mT and 480 mT (lines atop Figure 6.2A). While no single position is uniquely selective for the perpendicular orientation, the Pake pattern horns at 280 mT and 410 mT display an average orientation around 80°, giving a close approximation to the pure perpendicular position behavior.

The identity of the $M_S = -1 \rightarrow 0$ and $M_S = 0 \rightarrow +1$ transitions depends upon the sign of the axial zero-field splitting (ZFS) parameter D. While a perfectly tetrahedral S = 1 molecule cannot display zero-field splitting owing to cubic symmetry and a lack of second-order spin-orbit interactions[20], Cr(*o*-tolyl)$_4$ crystallizes in the S_4 point group.[12] The sign of D is sensitive to changes in the electronic structure upon

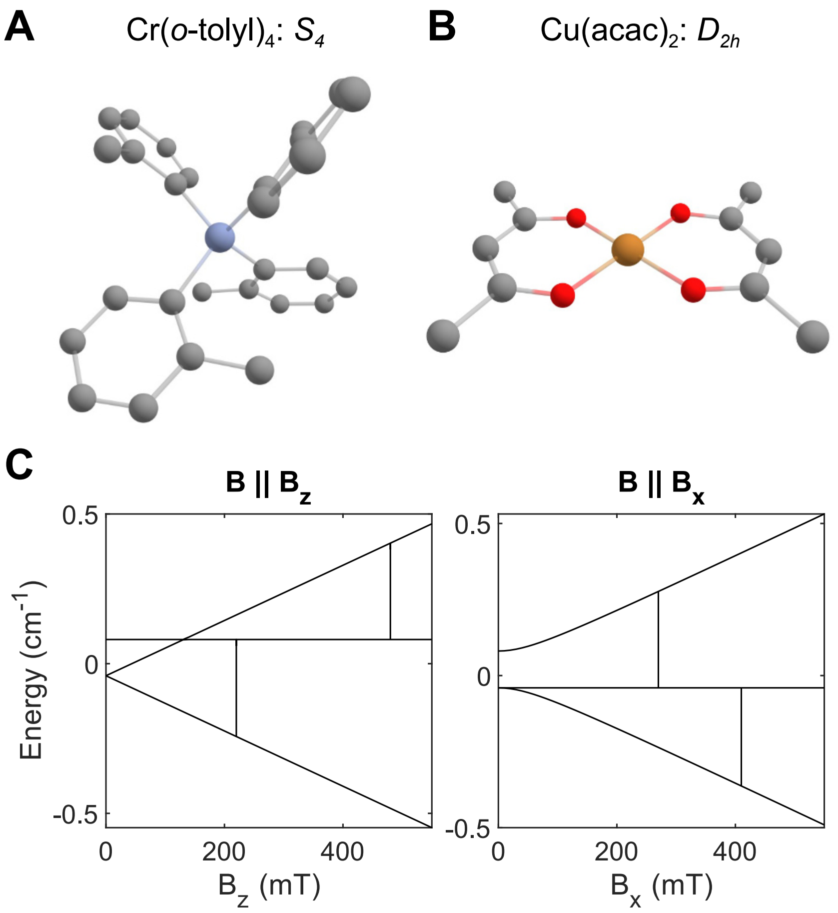

Figure 6.1: Molecular crystal structures and point groups of (A) S = 1 Cr(*o*-tolyl)$_4$ and (B) S = ½ Cu(acac)$_2$ (slight distortion from planarity). C = gray, Cr = blue, Cu = orange, and O = red. H atoms omitted for clarity. (C) Simulated Zeeman levels for Cr(*o*-tolyl)$_4$ with D = -0.121 cm^{-1}, as determined in this work. Vertical lines denote X-band EPR transitions at 9.6 GHz.

structural distortions from T_d to S_4 , including splitting of ligand field excited state energies and anisotropic orbital covalency.[20,21] Correct computational modeling of the sign of D is therefore essential for spin-phonon coupling calculations to accurately describe the electronic structure. While the absolute ZFS parameters for Cr(*o*-tolyl)$_4$ have been reported ($|D|$ = 0.121 cm^{-1}, $E \approx 0$ cm^{-1})[12], the sign of the ZFS has yet to be determined experimentally. To achieve this, we acquired variable-temperature Q-band echo-detected field sweeps (EDFSs) from 3.8 K - 50 K (Figure 6.2D). Soft microwave pulses were employed to suppress electron spin echo envelope modulation (ESEEM), which can add artifacts to EDFS spectra, and T_m was measured at several field positions and temperatures to ensure anisotropic T_m did not bias the EDFS intensity (Supporting Information Sections 3 – 4). As the

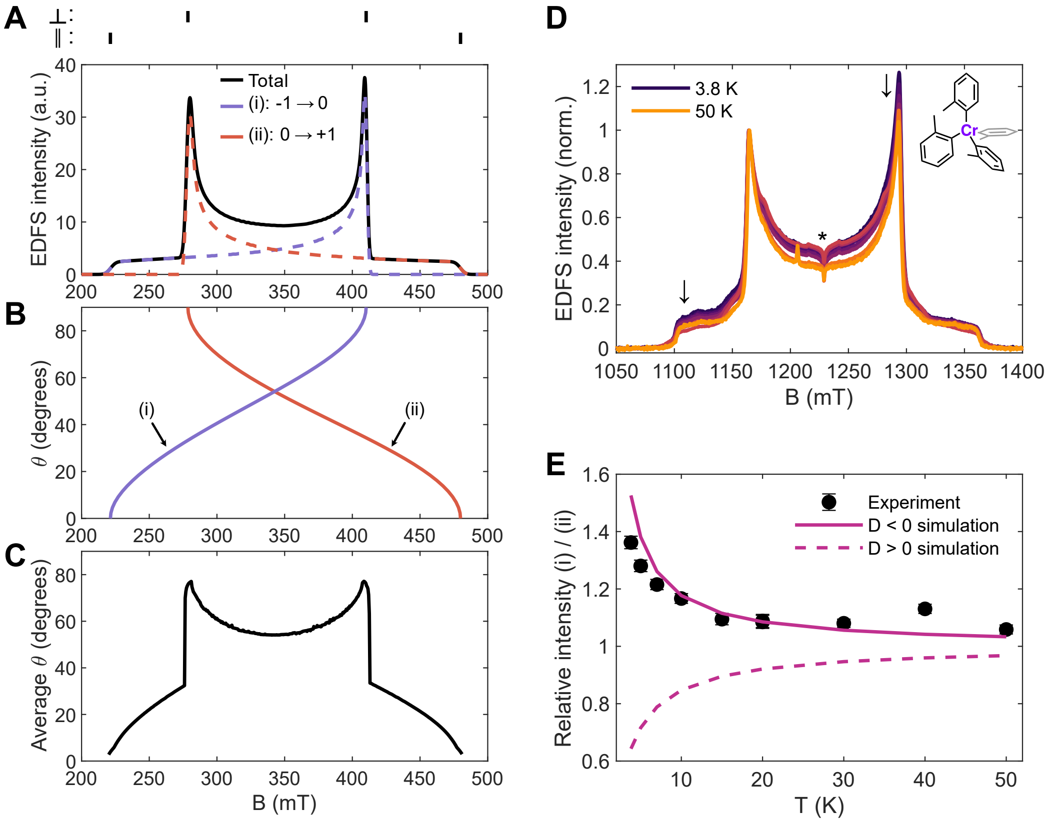

Figure 6.2: Anisotropy in Cr(IV) pulsed EPR. (A) Simulated X-band EDFS for Cr(o-tolyl)$_4$ showing the contributions from each spin transition in the case of $D < 0$. (B) Orientation of the molecule with respect to the value of B_0. $\theta = 0°$ indicates B_0 is parallel to the principal symmetry axis of the axial ZFS tensor. (C) Average orientation of the molecule over all spin transitions. (D) Variable-temperature Q-band EDFSs using soft pulses (π = 80 ns) and normalized to the peak at 1160 mT. * likely indicates an artifact due to cross-relaxation or a double-quantum transition (Supporting Information Section 3). (E) Comparison between experimental powder manifold intensities and simulations for $D < 0$ and $D > 0$.

sample temperature increases, the intensity of the spin transition spanning 1100 – 1290 mT decreases relative to the transition spanning 1160 – 1370 mT (arrows in Figure 6.2D). This behavior and corresponding simulation (Figure 6.2E) indicates that the former is the ground state $M_S = -1 \longrightarrow 0$ transition and that the sign of D is negative for Cr(o-tolyl)$_4$ (D = -0.121 cm^{-1}), consistent with calculations.[22,23] Note this sign differs from the pseudo-T_d Cr(IV) siloxide complex, Cr(DTBMS)$_4$, which exhibits $D > 0$.[24] This indicates that distortions away from T_d can produce categorically distinct electronic structure modifications in Cr(IV) complexes, which may lead to diverging spin-phonon coupling behavior.

Inversion recovery T_1 measurements at 40 K were conducted on a 1.8% dilution of Cr(*o*-tolyl)$_4$ into an isostructural diamagnetic Sn(*o*-tolyl)$_4$ matrix (Figure 6.3A-C). The slowest rates of spin relaxation were recorded at the pure parallel orientations, while the perpendicular orientations also displayed local minima in the spin relaxation rates (Figure 6.3B). Fastest spin relaxation was observed at the intermediate orientations closest to 45°, which are found both immediately to the outside of the Pake pattern horns and also in the very center of the spectrum (Figure 6.2C). The T_1 anisotropy pattern can be most nearly described by a $\sin^2(2\theta)$ functional form (Figure 6.3C), where θ is obtained from the orientation analysis in Figure 6.2. The $\sin^2(2\theta)$ function accounts for the slower spin relaxation along the canonical (parallel and perpendicular) orientations and faster spin relaxation along the intermediate orientations. Additionally, a $\sin^2(\theta)$ function and a linear function proportional to B (linear in the magnetic field) were considered. Note that the function linear in B does not directly depend upon the molecular angle θ and is therefore more precisely construed as isotropic field-dependent spin relaxation rather than true anisotropy (Supporting Information Section 5.3). This term may be understood as the slope of the Brons-van Vleck spin lifetime field dependence commonly observed in AC magnetometry, and this slope is indeed negative at X-band fields (0.3 mT) for common V(IV) qubits.[25] A least-squares fit of the inversion recovery data was conducted to quantify the relative contributions of different anisotropy functions (Supporting Information Section 5.1 and 5.3). The 40 K T_1 field dependence of Cr(*o*-tolyl)$_4$ can be described by this method as composed of 13% $\sin^2(2\theta)$, 6% $\sin^2(\theta)$, and 5% linear in B contributions, with a 76% constant (isotropic) component. This method of T_1 anisotropy analysis is applicable to any EPR-addressable S = 1 complex with an anisotropic powder spectrum.

Crucially, this behavior contrasts with that observed for tetragonal S = ½ Cu(II), V(IV), and Cr(V) compounds previously investigated by T_1 anisotropy at 100 K, in which fastest and slowest values of spin relaxation were always found at the canonical orientations.[18,19,26] To see if this was an effect of the temperature regime studied, we collected T_1 anisotropy at 40 K of 0.1% Cu(acac)$_2$ diluted in the isostructural diamagnetic matrix Pd(acac)$_2$ (Figure 6.3D-F). The 40 K Cu(acac)$_2$ completely follows the $\sin^2(\theta)$ functional form with no apparent significant contributions from $\sin^2(2\theta)$ (Figure 6.3F). The spin relaxation rate at the 45° orientation is simply the average of the rates at the canonical positions. These observations point to a qualitatively different origin of T_1 anisotropy in Cr(*o*-tolyl)$_4$ vs. Cu(acac)$_2$.

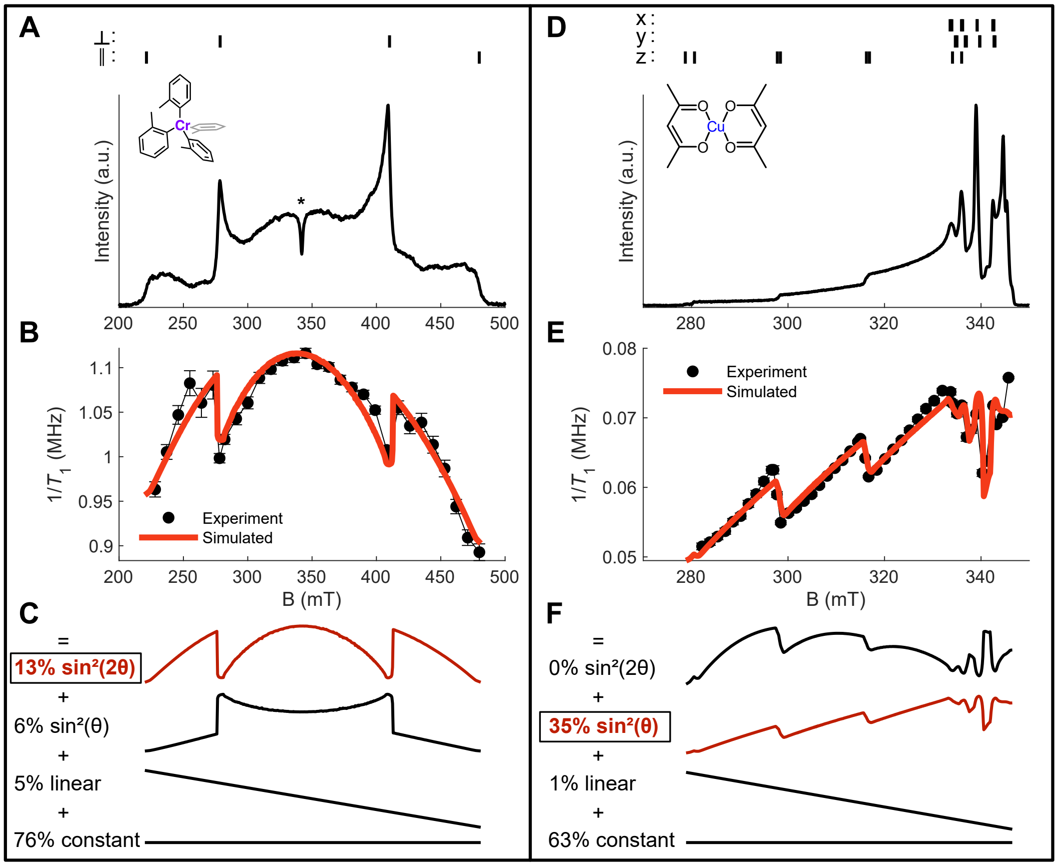

Figure 6.3: T_1 anisotropy at 40 K of (A-C) Cr(*o*-tolyl)$_4$ and (D-F) Cu(acac)$_2$. (A,D) X-band EDFSs. (B,E) T_1 anisotropy by inversion recovery, overlaid with best fit. (C,F) Orientation functions used to construct the T_1 anisotropy fit.

To ascertain the type of vibrations responsible for these distinct patterns, we probed the temperature dependence of the T_1 anisotropy for Cr(*o*-tolyl)$_4$ and Cu(acac)$_2$. We quantify the amount of T_1 anisotropy as a fraction of the largest $1/T_1$ over all field positions (Figure S17). Over the temperature range 7 K - 60 K, the amount of T_1 anisotropy for Cr(*o*-tolyl)$_4$ steadily decreases, with the dominant $\sin^2(2\theta)$ anisotropic contribution decreasing from 23% to 10% of the total T_1 (Figure 6.4). This decrease with increasing temperature indicates that $\sin^2(2\theta)$ anisotropy arises from very low energy degrees of freedom, likely acoustic or pseudo-acoustic phonons[27] (vide infra). Indeed, the isotropic field-dependent contribution to $1/T_1$ decreases at the same pace over this temperature range, and this contribution is commonly ascribed to the direct process of spin relaxation.[25] By contrast, the $\sin^2(\theta)$ T_1 anisotropy contribution increases sharply with temperatures for Cu(acac)$_2$, constituting only 0.5% of the total T_1 at 20 K but 62% at 100 K (Figure 6.4). Examination of the field-dependent T_1 for Cu(acac)$_2$ at 20 K validates that the spin relaxation anisotropy is greatly reduced (Figure S22), while the parallel and perpendicular T_1 at 100 K differ by a factor of 2.4, as observed and analyzed previously by our group.[18] This validates that the $\sin^2(\theta)$ anisotropy for Cu(acac)$_2$ arises from higher energy molecular vibrational modes (optical phonons) that are not thermally populated at 20 K. Thus, the T_1 anisotropies for Cr(*o*-tolyl)$_4$ vs. Cu(acac)$_2$ originate from different types of phonons. Note that both anisotropies are temperature-dependent in a manner consistent with the effect of thermal population of vibrational modes.[28–30] Anisotropic spectral diffusion was ruled out as a principal cause of the observed T_1 patterns for both compounds (Supporting Information Section 5.2).

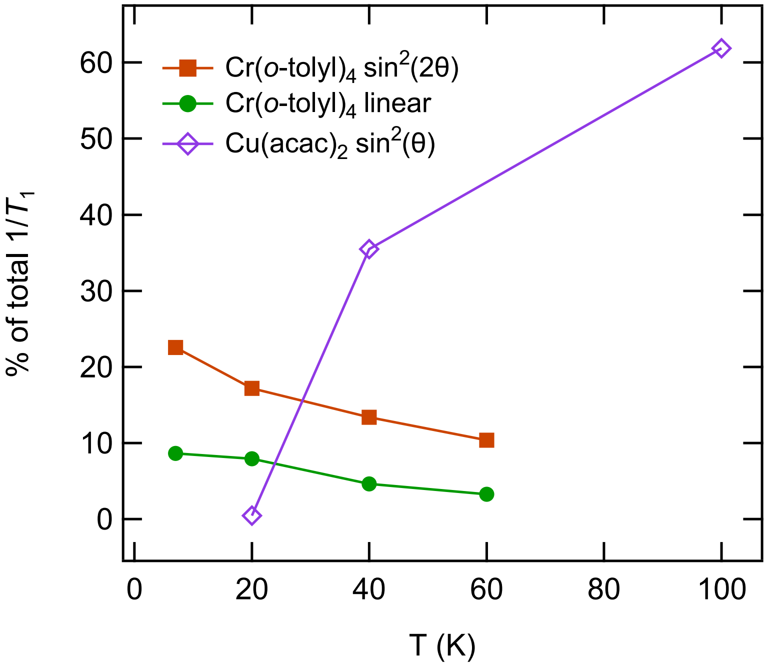

Figure 6.4: Temperature dependence of T_1 anisotropy contributions for Cr(*o*-tolyl)$_4$ and Cu(acac)$_2$.

A major attraction of the T_1 anisotropy methodology lies in the possibility of correlating the observed functional forms (e.g., $\sin^2(\theta)$ and $\sin^2(2\theta)$) to their origins in specific molecular degrees of freedom. Previous work has analyzed $\sin^2(\theta)$ spin relaxation anisotropy for Cu(II) and V(IV) molecular vibrations and shown it to be consistent with totally symmetric modes with metal-ligand stretching character[28,31,32] inducing relaxation through a modulation of the minority spin component of the ligand field wavefunction.[18] However, a new theoretical analysis is required to explain the $\sin^2(2\theta)$ anisotropy in Cr(*o*-tolyl)$_4$. While $\sin^2(2\theta)$ T_1 anisotropy has not been previously characterized, T_m anisotropy with a $\sin^2(2\theta)$ functional dependence has been observed in several S = ½ systems and has been attributed to rotational motion caused by librations.[33–35] This induces a change in resonant field position described by $\partial B_{res}/\partial\theta$, which is determined by the derivative of the projected g value, $\partial g/\partial\theta$. The derivative of the g-tensor $\partial g/\partial Q$ has been successfully used as a simplified model for the spin-phonon coupling coefficient describing spin relaxation, where in this case the vibrational mode Q is equal to a rotation θ, so there may be a connection between $\partial B_{res}/\partial\theta$ and spin relaxation in this context as well. Note that here rotational motion refers specifically to any molecular movement which causes rotation of principal tensor axes of the magnetic Hamiltonian. This does not necessarily imply rigid rotor molecular rotations, and possibilities include coupled rotations of different molecules in the solid-state unit cell (pseudo-acoustic or acoustic phonons), glassy librations, or molecular vibrations where the first coordination sphere and the extended ligand framework rotate in opposite directions (Supporting Information Section 6.1).

We therefore hypothesized that rotational motion from low-energy pseudo-acoustic or acoustic phonons may explain the $\sin^2(2\theta)$ functional form of the Cr(o-tolyl)$_4$ T_1 anisotropy. As the ZFS (D = -0.121 cm^{-1}) is smaller than the Zeeman splitting energy at X-band (0.32 cm^{-1} for g = 2 at 340 mT), we assume the spins are aligned along the applied magnetic field and treat the ZFS as a first-order perturbation to the Zeeman splitting of energy levels. Treating $\partial B_{res}/\partial\theta$ as a quantity proportional to the spin-flip matrix element for rotational motion, we obtain (Supporting Information Section 6):

$$\frac{1}{T_1} \propto \left|\frac{\partial B_{res}}{\partial\theta}\right|^2 = \frac{9D^2}{4\beta^2 g^2}\sin^2(2\theta). \tag{6.1}$$

Thus, the $\sin^2(2\theta)$ form is consistent with the expected T_1 anisotropy due to rotational motion. The decrease in the $\sin^2(2\theta)$ contribution to the T_1 anisotropy with increasing temperature also suggests that the rotational motion arises from low-energy acoustic or pseudo-acoustic phonons. The latter may carry significant rotational character when there are multiple molecules per unit cell,[27] as is the case here (Z = 10).[36] Further exploration of structurally diverse S = 1 complexes will be required to ascertain the generality of the rotational $\sin^2(2\theta)$ contributions.

The T_1 anisotropy for Cr(o-tolyl)$_4$ reduces in magnitude at higher temperatures as molecular vibrations begin to dominate spin relaxation through the Raman process.

It remains to be asked why the Cr(o-tolyl)$_4$ higher energy (> 100 cm^{-1}) molecular vibrations do not display T_1 anisotropy, while the Cu(acac)$_2$ totally symmetric vibrations display strong $\sin^2(\theta)$ anisotropy. This phenomenon is explained by a consideration of the orbital angular momentum matrix elements for a square planar vs. pseudo-T_d system. For D_{4h} Cu(acac)$_2$, the $d(x^2 - y^2)$ ground state has an orbital angular momentum matrix element with the $d(xy)$ excited state of squared modulus 4, while the matrix elements with $d(xz)$ and $d(yz)$ each have a squared modulus of only 1.33 These orbital angular momentum matrix elements control the amount of minority spin in the ground state wavefunction. Since the different excited states contribute to the wavefunction's minority spin along only some magnetic field orientations, the total minority spin for Cu(acac)$_2$ is greater for the perpendicular orientation than for the parallel orientation, thus giving rise to anisotropic relaxation.[18] However, in the cubic symmetry of the T_d point group, there can be no difference in matrix elements between the equivalent x, y, and z directions, so there can be no difference in the minority spin along different orientations. The small distortion from T_d required to produce nonzero ZFS[24,37] is evidently too small to yield a significant $\sin^2(\theta)$ T_1 anisotropy in Cr(o-tolyl)$_4$. Similar arguments were proposed to rationalize the presence of T_1 anisotropy in tetragonal nitridochromium(V) octaethylporphyrin and nitridochromium(V) tetratolylporphyrin, whereas the rhombic Cr(V)O(HEBA)$^{2-}$ complex did not display appreciable T_1 anisotropy.[26,38] Therefore, molecular vibrations (optical phonons) are likely to produce isotropic T_1 for Cr(o-tolyl)$_4$, in contrast to the previously analyzed tetragonal S = ½ systems.

In summary, our findings provide the first direct evidence for ascribing features of spin relaxation to specific types of motion in an optically addressable molecular qubit. These degrees of freedom are distinct from the totally symmetric optical phonons implicated in S = ½ microwave addressable molecular systems. As such, these experimental data are critical for defining the nature of spin-phonon couplings and the mechanism of T_1 in theoretical approaches seeking to model spin relaxation lifetimes. We note that the rotational motion contributions analyzed here likely do not dominate spin relaxation rates for T > 60 K, as the anisotropic component of the spin relaxation is reduced at higher temperatures due to the increased role of high energy molecular vibrations (Figure 6.4). Such structure-function relationships for spin dynamics will be essential for designing molecular optically addressable qubits displaying room temperature coherence.

References

[1] Schirhagl, R.; Chang, K.; Loretz, M.; Degen, C. L. Nitrogen-Vacancy Centers in Diamond: Nanoscale Sensors for Physics and Biology. *Annual Review of Physical Chemistry* **2014**, *65,* 83–105.

[2] Doherty, M. W.; Manson, N. B.; Delaney, P.; Jelezko, F.; Wrachtrup, J.; Hollenberg, L. C. L. The Nitrogen-Vacancy Colour Centre in Diamond. *Physics Reports* **2013**, *528,* 1–45.

[3] Fataftah, M. S.; Freedman, D. E. Progress Towards Creating Optically Addressable Molecular Qubits. *Chemical Communications* **2018**, *54,* 13773–13781.

[4] Abobeih, M. H.; Randall, J.; Bradley, C. E.; Bartling, H. P.; Bakker, M. A.; Degen, M. J.; Markham, M.; Twitchen, D. J.; Taminiau, T. H. Atomic-Scale Imaging of a 27-Nuclear-Spin Cluster Using a Quantum Sensor. *Nature* **2019**, *576,* 411–415.

[5] McGuinness, L. P.; Yan, Y.; Stacey, A.; Simpson, D. A.; Hall, L. T.; Maclaurin, D.; Prawer, S.; Mulvaney, P.; Wrachtrup, J.; Caruso, F.; Scholten, R. E.; Hollenberg, L. C. L. Quantum Measurement and Orientation Tracking of Fluorescent Nanodiamonds Inside Living Cells. *Nature Nanotechnology* **2011**, *6,* 358–363.

[6] Kucsko, G.; Maurer, P. C.; Yao, N. Y.; Kubo, M.; Noh, H. J.; Lo, P. K.; Park, H.; Lukin, M. D. Nanometre-Scale Thermometry in a Living Cell. *Nature* **2013**, *500,* 54–58.

[7] Le Sage, D.; Arai, K.; Glenn, D. R.; DeVience, S. J.; Pham, L. M.; Rahn-Lee, L.; Lukin, M. D.; Yacoby, A.; Komeili, A.; Walsworth, R. L. Optical Magnetic Imaging of Living Cells. *Nature* **2013**, *496,* 486–489.

[8] Graham, M. J.; Zadrozny, J. M.; Fataftah, M. S.; Freedman, D. E. Forging Solid-State Qubit Design Principles in a Molecular Furnace. *Chemistry of Materials* **2017**, *29,* 1885–1897.

[9] Fataftah, M. S.; Bayliss, S. L.; Laorenza, D. W.; Wang, X.; Phelan, B. T.; Wilson, C. B.; Mintun, P. J.; Kovos, B. D.; Wasielewski, M. R.; Han, S.; Sherwin, M. S.; Awschalom, D. D.; Freedman, D. E. Trigonal Bipyramidal V^{3+} Complex as an Optically Addressable Molecular Qubit Candidate. *Journal of the American Chemical Society* **2020**, *142,* 20400–20408.

[10] Wojnar, M. K.; Laorenza, D. W.; Schaller, R. D.; Freedman, D. E. Nickel(II) Metal Complexes as Optically Addressable Qubit Candidates. *Journal of the American Chemical Society* **2020**, *142,* 14826–14830.

[11] Lenz, S.; Bamberger, H.; Hallmen, P. P.; Thiebes, Y.; Otto, S.; Heinze, K.; Slageren, J. Chromium(III)-Based Potential Molecular Quantum Bits with Long Coherence Times. *Physical Chemistry Chemical Physics* **2019**, *21,* 6976–6983.

[12] Bayliss, S. L.; Laorenza, D. W.; Mintun, P. J.; Kovos, B. D.; Freedman, D. E.; Awschalom, D. D. Optically Addressable Molecular Spins for Quantum Information Processing. *Science* **2020**, *370,* 1309–1312.

[13] Laorenza, D. W.; Kairalapova, A.; Bayliss, S. L.; Goldzak, T.; Greene, S. M.; Weiss, L. R.; Deb, P.; Mintun, P. J.; Collins, K. A.; Awschalom, D. D.; Berkelbach, T. C.; Freedman, D. E. Tunable Cr^{4+} Molecular Color Centers. *Journal of the American Chemical Society* **2021**, *143,* 21350–21363.

[14] Bayliss, S. L.; Deb, P.; Laorenza, D. W.; Onizhuk, M.; Galli, G.; Freedman, D. E.; Awschalom, D. D. Enhancing Spin Coherence in Optically Addressable Molecular Qubits through Host-Matrix Control. *Physical Review X* **2022**, *12,* 031028.

[15] Bader, K.; Dengler, D.; Lenz, S.; Endeward, B.; Jiang, S.-D.; Neugebauer, P.; van Slageren, J. Room Temperature Quantum Coherence in a Potential Molecular Qubit. *Nature Communications* **2014**, *5,* 5304.

[16] Atzori, M.; Tesi, L.; Morra, E.; Chiesa, M.; Sorace, L.; Sessoli, R. Room-Temperature Quantum Coherence and Rabi Oscillations in Vanadyl Phthalocyanine: Toward Multifunctional Molecular Spin Qubits. *Journal of the American Chemical Society* **2016**, *138,* 2154–2157.

[17] Follmer, A. H.; Ribson, R. D.; Oyala, P. H.; Chen, G. Y.; Hadt, R. G. Understanding Covalent versus Spin-Orbit Coupling Contributions to Temperature-Dependent Electron Spin Relaxation in Cupric and Vanadyl Phthalocyanines. *The Journal of Physical Chemistry A* **2020**, *124,* 9252–9260.

[18] Kazmierczak, N. P.; Hadt, R. G. Illuminating Ligand Field Contributions to Molecular Qubit Spin Relaxation via T_1 Anisotropy. *Journal of the American Chemical Society* **2022**, *144,* 20804–20814.

[19] Du, J.-L.; Eaton, G. R.; Eaton, S. S. Temperature and Orientation Dependence of Electron-Spin Relaxation Rates for Bis(diethyldithiocarbamato)copper(II). *Journal of Magnetic Resonance, Series A* **1995**, *117,* 67–72.

[20] Deaton, J. C.; Gebhard, M. S.; Solomon, E. I. Transverse and Longitudinal Zeeman Effect on $[PPh_4][FeCl_4]$: Assignment of the Ligand Field Transitions and the Origin of the $^6A_1$ Ground-State Zero-Field Splitting. *Inorganic Chemistry* **1989**, *28,* 877–889.

[21] Griffith, J. S. *The Theory of Transition-Metal Ions;* Cambridge University Press: Cambridge, 1961.

[22] Sauza-de la Vega, A.; Pandharkar, R.; Stroscio, G. D.; Sarkar, A.; Truhlar, D. G.; Gagliardi, L. Multiconfiguration Pair-Density Functional Theory for Chromium(IV) Molecular Qubits. *JACS Au* **2022**, *2,* 2029–2037.

[23] Janicka, K.; Wysocki, A. L.; Park, K. Computational Insights into Electronic Excitations, Spin-Orbit Coupling Effects, and Spin Decoherence in Cr(IV)-Based Molecular Qubits. *The Journal of Physical Chemistry A* **2022**, *126,* 8007–8020.

[24] Bucinsky, L.; Breza, M.; Malček, M.; Powers, D. C.; Hwang, S. J.; Krzystek, J.; Nocera, D. G.; Telser, J. High-Frequency and -Field EPR (HFEPR) Investigation of a Pseudotetrahedral Cr^{IV} Siloxide Complex and Computational Studies of Related $Cr^{IV}L_4$ Systems. *Inorganic Chemistry* **2019**, *58,* 4907–4920.

[25] Atzori, M.; Morra, E.; Tesi, L.; Albino, A.; Chiesa, M.; Sorace, L.; Sessoli, R. Quantum Coherence Times Enhancement in Vanadium(IV)-based Potential Molecular Qubits: The Key Role of the Vanadyl Moiety. *Journal of the American Chemical Society* **2016**, *138,* 11234–11244.

[26] Konda, R.; Du, J. L.; Eaton, S. S.; Eaton, G. R. Electron Spin Relaxation Rates for Nitridochromium(V) Tetratolylporphyrin and Nitridochromium(V) Octaethylporphyrin in Frozen Solution. *Applied Magnetic Resonance* **1994**, *7,* 185–193.

[27] Kragskow, J. G. C.; Mattioni, A.; Staab, J. K.; Reta, D.; Skelton, J. M.; Chilton, N. F. Spin-Phonon Coupling and Magnetic Relaxation in Single-Molecule Magnets. *Chemical Society Reviews* **2023**, *52,* 4567–4585.

[28] Kazmierczak, N. P.; Mirzoyan, R.; Hadt, R. G. The Impact of Ligand Field Symmetry on Molecular Qubit Coherence. *Journal of the American Chemical Society* **2021**, *143,* 17305–17315.

[29] Lunghi, A.; Sanvito, S. The Limit of Spin Lifetime in Solid-State Electronic Spins. *The Journal of Physical Chemistry Letters* **2020**, *11,* 6273–6278.

[30] Santanni, F.; Albino, A.; Atzori, M.; Ranieri, D.; Salvadori, E.; Chiesa, M.; Lunghi, A.; Bencini, A.; Sorace, L.; Totti, F.; Sessoli, R. Probing Vibrational Symmetry Effects and Nuclear Spin Economy Principles in Molecular Spin Qubits. *Inorganic Chemistry* **2021**, *60,* 140–151.

[31] Mirzoyan, R.; Hadt, R. G. The Dynamic Ligand Field of a Molecular Qubit: Decoherence through Spin-Phonon Coupling. *Physical Chemistry Chemical Physics* **2020**, *22,* 11249–11265.

[32] Mirzoyan, R.; Kazmierczak, N. P.; Hadt, R. G. Deconvolving Contributions to Decoherence in Molecular Electron Spin Qubits: A Dynamic Ligand Field Approach. *Chemistry – A European Journal* **2021**, *27,* 9482–9494.

[33] Du, J.-L.; More, K. M.; Eaton, S. S.; Eaton, G. R. Orientation Dependence of Electron Spin Phase Memory Relaxation Times in Copper(II) and Vanadyl Complexes in Frozen Solution. *Israel Journal of Chemistry* **1992**, *32,* 351–355.

[34] Jackson, C. E.; Lin, C.-Y.; van Tol, J.; Zadrozny, J. M. Orientation Dependence of Phase Memory Relaxation in the V(IV) Ion at High Frequencies. *Chemical Physics Letters* **2020**, *739,* 137034.

[35] Eaton, S. S.; Eaton, G. R. Relaxation Mechanisms. In *eMagRes*; Wiley: 2016. DOI: 10.1002/9780470034590.emrstm1507.

[36] Bayliss, S.; Laorenza, D.; Mintun, P.; Kovos, B.; Freedman, D.; Awschalom, D. CCDC 1992356: Experimental Crystal Structure Determination. *Cambridge Crystallographic Data Centre* **2020**.

[37] Mowat, W.; Shortland, A. J.; Hill, N. J.; Wilkinson, G. Elimination Stabilized Alkyls. Part II. Neopentyl and Related Alkyls of Chromium(IV). *Journal of the Chemical Society, Dalton Transactions* **1973**, *(7),* 770–778.

[38] Du, J. L.; Eaton, G. R.; Eaton, S. S. Electron-Spin-Lattice Relaxation in Natural Abundance and Isotopically Enriched Oxo-chromium(V)bis (2-hydroxy-2-ethylbutyrate). *Journal of Magnetic Resonance, Series A* **1995**, *115,* 236–240.

Chapter 7

SPECTROSCOPIC SIGNATURES OF PHONON CHARACTER IN MOLECULAR ELECTRON SPIN RELAXATION

- Adapted with permission from: Kazmierczak, N. P.; Oyala, P. H.; Hadt, R. G. Spectroscopic Signatures of Phonon Character in Molecular Electron Spin Relaxation. *ACS Central Science* **2024**, *10*, 2353–2362. DOI: 10.1021/acscentsci.4c01177. © 2024 American Chemical Society.

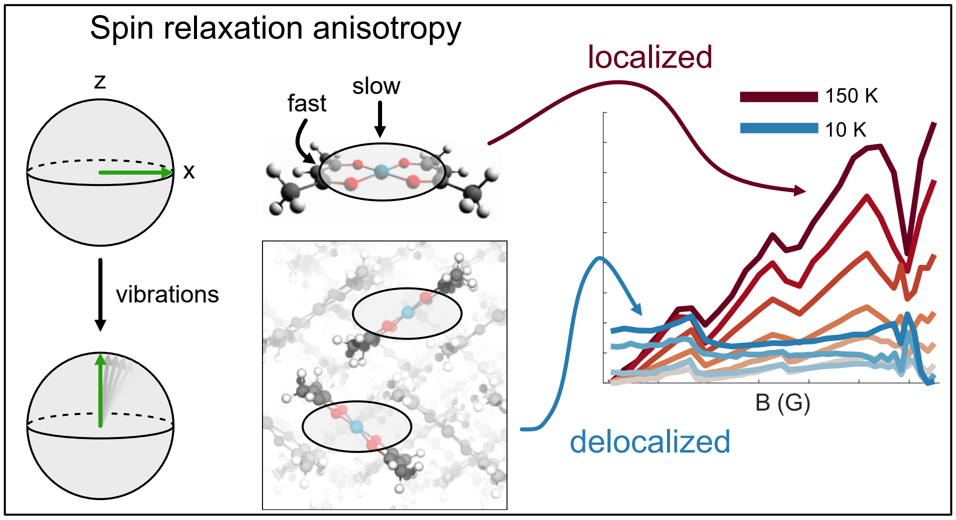

7.1 Abstract

Spin-lattice relaxation constitutes a key challenge for the development of quantum technologies, as it destroys superpositions in molecular quantum bits (qubits) and magnetic memory in single molecule magnets (SMMs). Gaining mechanistic insight into the spin relaxation process has proven challenging owing to a lack of spectroscopic observables and contradictions among theoretical models. Here, we use pulse electron paramagnetic resonance (EPR) to profile changes in spin relaxation rate (T_1) as a function of both temperature and magnetic field orientation, forming a two-dimensional data matrix. For randomly-oriented powder samples, spin relaxation anisotropy changes dramatically with temperature, delineating multiple regimes of relaxation processes for each Cu(II) molecule studied. We show that traditional T_1 fitting approaches cannot reliably extract this information. Single-crystal T_1 anisotropy experiments reveal a surprising change in spin relaxation symmetry

between these two regimes. We interpret this switch through the concept of a spin relaxation tensor, enabling discrimination between delocalized lattice phonons and localized molecular vibrations in the two relaxation regimes. Variable-temperature T_1 anisotropy thus provides a unique spectroscopic method to interrogate the character of nuclear motions causing spin relaxation and the loss of quantum information.

7.2 Introduction

Multiple emerging quantum technology concepts employ electron spins in paramagnetic molecules to store or process information.[1–3] For example, a quantum bit (qubit) is a two-level system able to process information through uniquely quantum degrees of freedom, such as superpositions. Qubit applications include quantum sensing, computing, and communication.[4] Paramagnetic molecules constitute a natural implementation of a qubit on the sub-nanometer scale, as the Zeeman sublevels of the unpaired electron spin satisfy the requirements of a two-level quantum system.[5] Additionally, molecular spin systems exhibiting a double-well potential can store information based on which stable spin state is adopted, referred to as the concept of a single molecule magnet (SMM).[2,6,7] In each case, information is encoded through the orientation and/or phase of the spin, so any process that dynamically alters the spin orientation on the Bloch sphere will have a deleterious impact on the proposed quantum technology.[8]

Spin-lattice relaxation constitutes one such detrimental process, denoted by the time constant T_1.[9] In the molecular qubit context, this process arises when electron spins exchange energy with vibrational modes of the molecule or the surrounding bath, causing spins in superpositions to re-align along the applied magnetic field and lose the quantum information (Figure 7.1A).[10] Because vibrational populations increase exponentially with temperature, spin-lattice relaxation (henceforth, simply referred to as "spin relaxation") must be minimized to obtain molecular quantum devices and sensing technologies functioning at non-cryogenic temperatures.[11]

A variety of experimental investigations have sought to characterize the mechanism of molecular spin relaxation in transition metal complexes. The most common measurement has been to determine T_1 by pulse electron paramagnetic resonance (EPR) at a fixed field position and analyze how it scales as a function of temperature. This can be used to extract approximate energies of the vibrational modes coupling to the spin.[12–14] From this, spin relaxation has been suppressed by using (i) high-symmetry complexes, such as square planar Cu(II), to reduce the number of totally-symmetric vibrations active for spin-phonon coupling,[15–18] (ii) increasing the energies of those modes to reduce their thermal population,[15,19] and (iii) reducing spin-orbit coupling through covalent metal-ligand bonding.[12,13,20] However, temperature-dependent T_1 measurements cannot unambiguously pinpoint the type of vibration driving relaxation, nor whether one or many vibrational modes dominate T_1. Disagreements also exist regarding the character of the molecular vibration and/or lattice phonon modes driving relaxation.[19,21] The challenge is that there does not yet exist a spectroscopic method for selecting a vibrational mode and measuring its contribution to T_1. New spectroscopic approaches are called for to clarify the nature of spin relaxation mechanisms.

Concurrently, a plethora of theoretical studies have sought to computationally predict the rate of S = ½ spin relaxation from either experimentally-calibrated models or first-principles. Such efforts have their roots in the seminal works of Van Vleck[22] and Orbach,[23,24] which analytically described mechanisms of relaxation. Recent works additionally incorporate the results of modern *ab initio* computational methods and quantum master equations.[25,26] Unfortunately, contemporary studies are rife with disagreement regarding the correct spin-phonon coupling Hamiltonian to employ. There exist two main types of S = ½ spin relaxation theories: those employing the spin Hamiltonian for the coupling terms, and those using a non-spin Hamiltonian approach. Of the former, there are at least four distinct models employing $\partial^2 g_i/\partial Q^2$,[27] $\partial \boldsymbol{g}/\partial Q$,[28] $\partial g_i/\partial Q$,[15,19] and $\partial \boldsymbol{A}/\partial Q$[21,29] coupling terms. Of the latter, there are at least three proposals based on spin-orbit wavefunction theory,[30] non-adiabatic spin-vibrational orbit interactions,[31] and virtual excitations to ligand field excited states.[32] Each choice describes the spin relaxation physics differently, consequently predicting qualitatively different vibrational modes to drive relaxation. Until a consensus is reached, it is imperative to improve these theoretical models using new types of data from experimental spectroscopy.

Recently, T_1 anisotropy has been introduced as a new spectroscopic observable for probing mechanisms of spin relaxation.[30,33] The principle of T_1 anisotropy stems from the orientation dependence of spin relaxation. When measuring spin relaxation via pulse EPR, an external magnetic field (B_0) is applied across the sample. B_0 can have various alignments with respect to individual molecules analyzed. For a square-planar Cu(II) complex, such as copper(II) bis(acetylacetonate) (Cu(acac)$_2$), alignment of B_0 passing at a right angle through the plane is referred to as the parallel orientation (θ = 0°) (Figure 7.1B). Conversely, B_0 contained within the plane is referred to as the perpendicular orientation (θ = 90°). If T_1 is measured for molecules at these orientations, different values may generally be obtained (Figure 7.1C-D). This is the core concept of T_1 anisotropy. Furthermore, a field-swept EPR spectrum will often contain natural statistical selectivity for different orientations at different magnetic field positions (Figure 7.1E), so T_1 anisotropy information can be collected even from randomly-oriented powder samples. Analysis of T_1 anisotropy has provided insight on how chemical bonding affects spin dynamics[30] and pinpointed the types of vibrations causing relaxation in S = ½ versus S = 1 molecular qubits.[33]

Here, we conduct a two-dimensional profiling of changes in T_1 by systematically altering both temperature and field, producing a full matrix of T_1 data along two independent axes (Figure S18). The field dimension yields anisotropy information at each temperature probed. We refer to this approach as variable-temperature, variable-field T_1 anisotropy (VTVH-T_1). We apply the VTVH-T_1 methodology to Cu(acac)$_2$ and copper octaethylporphyrin (CuOEP), both of which have been studied as molecular qubit candidates.[19,30] For powder samples of both compounds, the shape of the T_1 anisotropy changes between the high- and low-temperature limits, which enables assignment of different regimes of spin relaxation within a given compound. We show this information cannot be extracted in general from the temperature scaling of fixed-field T_1 measurements alone. Single-crystal VTVH-T_1 measurements further reveal that spin relaxation rates orient along the molecular axes at high temperatures, but switch to crystal lattice plane axes at low temperatures. This enables VTVH-T_1 to ascertain the localized vs. delocalized character of the vibrational modes driving spin relaxation. VTVH-T_1 provides a strikingly direct experimental portrait of spin relaxation mechanisms.

7.3 Results

7.3.1 Powder VTVH-T_1

We began by acquiring X-band pulse saturation recovery VTVH-T_1 measurements on randomly-oriented powder samples of 1:1000 Cu(acac)$_2$ in Pd(acac)$_2$ and 1:100 CuOEP in ZnOEP (Figure 7.2A-B). T_1 was acquired at a minimum of 25 field positions for each temperature and 10 temperature points (Supporting Information Section 13). Previously, CuOEP temperature-dependent T_1 has been measured by inversion recovery from 6 K to 294 K without analysis of anisotropy,[19] while Cu(acac)$_2$ anisotropy has been measured by inversion recovery at 20, 40, and 100 K without report of a temperature-dependent T_1 curve.[30,33] The use of saturation recovery in

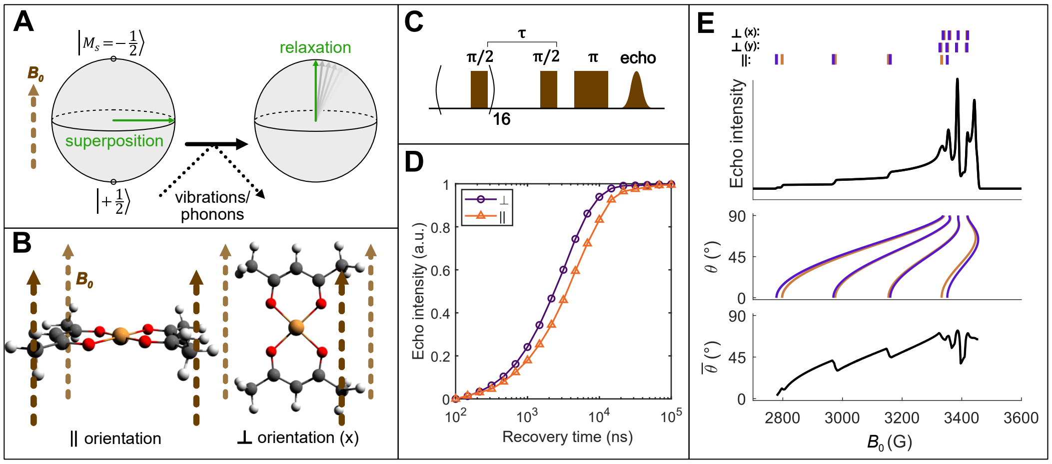

Figure 7.1: Measuring spin relaxation anisotropy. (A) Electron spin superpositions are destroyed by interactions with molecular vibrations or phonons that cause the spin to relax back to the applied magnetic field, B_0. (B) Parallel (θ = 0°) and perpendicular (θ = 90°) orientations of Cu(acac)$_2$ with respect to B_0. θ is the angle between B_0 and the normal vector of the CuO$_4$ plane. (C) Saturation recovery microwave pulse sequence used to measure electron spin relaxation in pulse EPR. (D) Saturation recovery reveals distinct spin relaxation rates for the parallel and perpendicular orientations (1:1000 Cu(acac)$_2$ in Pd(acac)$_2$ powder, 60 K). (E) The angular dependence of the EPR spectrum enables selectivity for different orientations at different magnitudes of B_0, even for a randomly-oriented Cu(acac)$_2$ powder. Orange ticks indicate resonance positions for the ^{63}Cu isotope, while purple ticks indicate resonance positions for the ^{65}Cu isotope.

the present work is important to reliably analyze low-temperature VTVH-T_1 without conflation of anisotropy and spectral diffusion (Supporting Information Sections 4 and 6). Complete saturation was not obtained under the fastest-relaxing temperature points (150 K for Cu(acac)$_2$ and 294 K for CuOEP), so inversion recovery was employed instead. Spectral diffusion is not anticipated to be an issue in the presence of fast spin-lattice relaxation. T_1 scales steeply with temperature, but changes in the anisotropy can be visualized by normalizing the data at each temperature to the slowest relaxation rate. This normalizes to the isotropic portion of the spin relaxation and enables comparison of the fraction of T_1 that is anisotropic at each temperature. Note that this normalization procedure removes the thermal dependence of the average T_1, so these anisotropy data provide independent information from that of traditional fixed-field temperature-dependent T_1 experiments.

Cu(acac)$_2$ does not display a quantifiable spin echo above 150 K, while CuOEP is room-temperature coherent via EPR, as observed previously.[19] At the highest

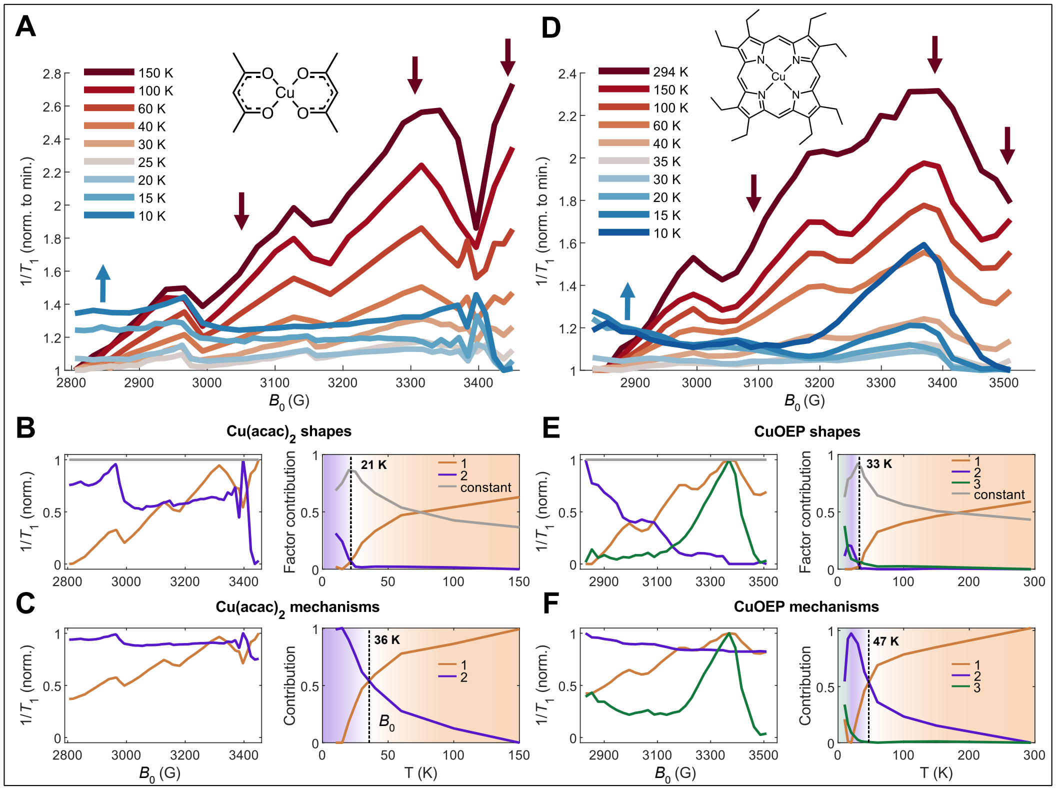

Figure 7.2: Variable-temperature, variable-field T_1 anisotropy (VTVH-T_1). (A) VTVH-T_1 for 1:1000 Cu(acac)$_2$ in Pd(acac)$_2$ powder sample. Red and blue arrows indicate decreasing and increasing anisotropy as temperature is reduced, respectively. Anisotropy traces at each temperature are normalized to the slowest relaxation rate at any field position. (B) VTVH-T_1 for 1:100 CuOEP in ZnOEP powder sample. (C-D) Bilinear factor analysis decomposition (Supporting Information Section 8) of the Cu(acac)$_2$ anisotropy data. (C) Two anisotropy patterns are extracted from the Cu(acac)$_2$ data. (D) Associated temperature dependence of the anisotropy patterns in panel C, corresponding to Cu(acac)$_2$ relaxation mechanism contributions. (E) Three anisotropy patterns are extracted from the CuOEP data. (F) Associated temperature dependence of the anisotropy patterns in panel E, corresponding to CuOEP relaxation mechanism contributions.

temperature of 150 K, Cu(acac)$_2$ displays a sawtooth linear increase in $1/T_1$ from low fields (parallel orientations) to high fields (perpendicular orientations), characteristic of a $\sin^2\theta$ T_1 anisotropy pattern for this molecule (Figure 7.2A, Figure S25).[30] This anisotropy form has been previously assigned to the impact of totally symmetric metal-ligand bond stretching vibrations.[30] The shape of the anisotropy remains constant with decreasing temperature from 150 to 25 K. However, the proportional contribution of the T_1 anisotropy to the total T_1 decreases significantly, from a maximum T_1 anisotropy ratio of 2.7 at 150 K to a minimum of 1.2 at 25 K. At

20 K and below, a new anisotropy shape grows in, with slowest relaxation at the highest fields and comparatively fast relaxation at the parallel orientation. The central hyperfine sawtooth discontinuity at 3150 G vanishes by 10 K, while the discontinuity at 2970 G becomes more prominent at 10 K, and the sharp patterns above 3350 G additionally change shape. Analogous changes are visible for CuOEP, where the $\sin^2\theta$ anisotropy pattern (Figure S37) decreases from 294 K to 35 K, and new shapes arise at 30 K and below (Figure 7.2B).

Visual inspection of a given anisotropy dataset (Figure 7.2A-B) indicates that only a small number of fundamental T_1 anisotropy patterns constitute the data, but the relative contributions of these patterns vary in different ways as a function of temperature. Thus, these anisotropy patterns likely arise from multiple underlying mechanisms of spin relaxation with distinct thermal dependencies, arising from the impact of different classes of phonons. We sought to quantify the relative proportions of each anisotropy pattern to extract mechanistic insight. Unlike in previous T_1 anisotropy studies,[30,33] however, a simple parametric form for T_1 as a trigonometric function of the angle θ could not be found for the low-temperature shapes.

We therefore employed a factor analysis procedure based on soft modeling to deconvolute the contributions of the distinct anisotropy patterns (Supporting Information Section 8).[34–37] The bilinear factor analysis decomposition represents the primary anisotropy data (Figures 7.2A-B) as the sum of fundamental anisotropy patterns (Figures 7.2C, 7.2E) that each possess their own unique temperature-dependent contributions (Figures 7.2D, 7.2F) subject to physical constraints like nonnegativity. This procedure is equivalent to a matrix factorization (Figure S17) and is sometimes referred to as model-free global analysis. Each fundamental anisotropy pattern spans across the full range of B_0 values. Thus, the temperature-dependent contributions track the evolution of the entire normalized anisotropy shape, which is different than extracting the temperature-dependent variation of T_1 at a fixed field. Likewise, the anisotropy patterns are extracted from over the entire range of temperature values. By extracting anisotropy information from the B_0 dimension, VTVH-T_1 provides independent information on spin relaxation not accessed in a fixed-field temperature-dependent T_1 experiment.

Applying this scheme to $\mathrm{Cu(acac)_2}$ successfully separates the two anisotropy patterns visible in the data. Relaxation mechanism #1 corresponds to the $\sin^2\theta$ anisotropy pattern (Figure 7.2C). The high-temperature mechanism #1 is shown to be more anisotropic than the low-temperature mechanism #2, consistent with the magnitudes of the anisotropies visible in the data. The crossover point between the two relaxation mechanisms is found to arise at 36 K (Figure 7.2D). CuOEP displays three distinct anisotropy patterns (Figure 7.2E), owing to the prominent bulge at 3350 G below 20 K (Figures S31-S36). The high-temperature pattern is dominant above 47 K (Figure 7.2F), a higher crossover point than observed for Cu(acac)$_2$. In summary, powder VTVH-T_1 indicates a low-temperature and a high-temperature regime of spin relaxation for both Cu(acac)$_2$ and CuOEP, demarcated by the 36 K and 47 K crossover points for each.

At this stage of the analysis, the different regimes can be assigned to relaxation dominated by different classes of phonons. Each phonon mechanism possesses its own characteristic anisotropy pattern, and the temperature dependences arise from thermal population of the relevant phonon modes. However, two important questions remain. First, does anisotropy give different information about relaxation mechanisms compared to traditional fixed-field temperature-dependent T_1 fitting? Second, can anisotropy extract any unique experimental information regarding the characteristics of the phonons participating in each relaxation mechanism? Both questions are answered affirmatively in the following sections.

7.3.2 Comparison to Temperature-Dependent T_1 Fitting

Assignment of direct, Raman, and local mode relaxation processes is commonly conducted by fitting the temperature scaling of T_1 at a fixed B_0 to power law and local mode functional forms.[8,12] We sought to compare these assignments to the spin relaxation regimes extracted from powder VTVH-T_1. Local mode fits to CuOEP saturation recovery data reveal two distinct contributions to the temperature scaling of T_1: a power law process dominant at low temperatures, and a molecular vibration dominant at high temperatures (Figure 7.3A, Supporting Information Section 5). The fits are in good agreement with a previous report employing inversion recovery data.[19] The crossover between the two contributions occurs at 64 K. This is reasonably close to the 47 K mechanism crossover observed by CuOEP VTVH-T_1 (Figure 7.2F), suggesting that the mechanism crossover detected is likely the same in both the temperature dimension and the anisotropy dimension.

However, the Cu(acac)$_2$ T_1 temperature scaling cannot be fit to two functional forms (Figure 7.3A). Unlike for CuOEP, the slope of $1/T_1$ vs. T is steeper at lower temperatures than at higher temperatures. This precludes use of a power law to fit the low-temperature data, which would dominate T_1 over the entire range and predict excessively fast spin relaxation at high temperature. A single local mode may be fit, but it does not satisfactorily capture the curvature of the data (Supporting Information Section 5). Fitting two or more local mode forms is of course mathematically possible, but the relationship to real mechanistic regimes of spin relaxation would be spurious, given the single curvature of the data.

Analysis of T_1 vs. T without functional fitting also fails to detect two mechanistic regimes for Cu(acac)$_2$. The curvature may be easily visualized through plotting the slope of log($1/T_1$) vs. log(T) (Figure 7.3B).[15,19] The CuOEP slope displays a maximum around 50 K that indicates a clear separation between two mechanistic regimes, while Cu(acac)$_2$ displays a monotonic decrease lacking clear features. We also acquired inversion recovery measurements of $1/T_1$ vs. T for Cu(acac)$_2$ with finer temperature resolution, yet no mechanistic separation could be ascertained (Figure S8-S9, Supporting Information Sections 3-4). A similar phenomenon was described in a recent report of spin relaxation in vanadyl tetrapyrazinoporphyrazine dyes (VOPyzPz-DIPP), where elaboration with peripheral substituents removed a visible mechanistic separation from $1/T_1$ vs. T.[38] Yet, as demonstrated, powder VTVH-T_1 measurements are able to unveil multiple mechanistic regimes for both Cu(acac)$_2$ and CuOEP (Figure 7.3C). Thus, the anisotropy information in VTVH-T_1 contains unique mechanistic insights not present in the traditional $1/T_1$ vs. T fitting approach.

7.3.3 Single-Crystal T_1 Anisotropy

We then sought to extract information about the character of the dominant vibrational mode in the different mechanistic regimes. While the high-temperature anisotropy shape for both Cu(acac)$_2$ and CuOEP can be nicely fit to the $\sin^2\theta$ form, the low-temperature shapes cannot easily be fit to a function of θ. Maximal care was taken to exclude spectral diffusion[10,39–41] as the source of these shapes, including probing the impact of the number of pulses, interpulse spacing, and pulse duration in the picket fence saturation recovery sequence (Figure S15), as well as the Cu(acac)$_2$ paramagnetic concentration dependence of the 20 K powder anisotropy shape (Figure S16). We conclude spectral diffusion is unlikely to be the cause of these powder anisotropy shapes.

To obtain the most detailed analysis of T_1 anisotropy, a single crystal of Cu(acac)$_2$ co-crystallized with Pd(acac)$_2$ in a 1:1000 ratio was prepared. The crystal was face-indexed by X-ray diffractometry and mounted for rotation along the [1 0 −1] axis to

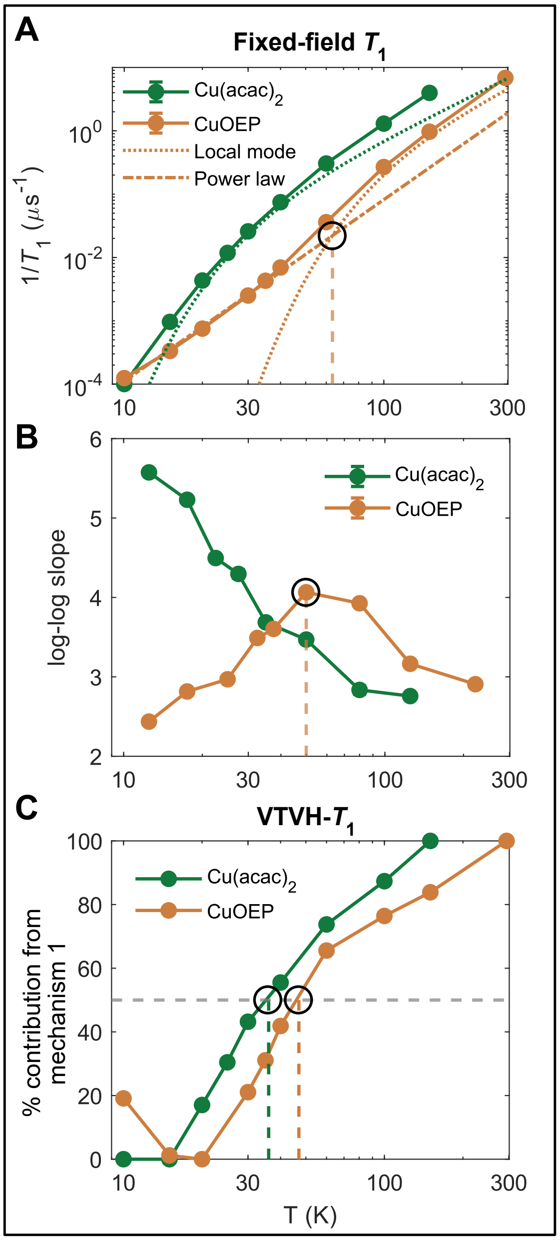

Figure 7.3: Comparison to local mode fitting. (A) Local mode fitting of temperature-dependent T_1 at fixed field positions selective for the perpendicular orientation (Cu(acac)$_2$: 3318 G, 9.7060 GHz; CuOEP: 3369 G, 9.6291 GHz). CuOEP is fit to two spin relaxation mechanisms, while Cu(acac)$_2$ can only be fit to one. (B) The slope of the graph in panel A indicates the power law scaling of $1/T_1$ vs. T at all temperatures, revealing two regimes for CuOEP but only one for Cu(acac)$_2$. (C) Percentage contribution of the high-temperature spin relaxation mechanism from VTVH-T_1 indicates two distinct regimes for both Cu(acac)$_2$ and CuOEP, despite the absence of clear features in $1/T_1$ vs. T for Cu(acac)$_2$.

access pure parallel and perpendicular positions (Supporting Information Section 9). A slight rhombic splitting exists between g_x and g_y.[30] DFT calculations of the g-tensor indicate the rotation about $[1\ 0\ -1]$ specifically accesses the g_x position, the smaller of the two perpendicular g values (Supporting Information Section 12). Single-crystal T_1 anisotropy experiments offer three significant advantages: (1) the ability to know the exact 360° molecular orientation through laboratory frame rotations, rather than inferring an angle between 0° and 90° from the resonant field position, (2) the ability to selectively probe different hyperfine transitions that would overlap in the powder spectrum, and (3) a vastly altered, sparse spectral density of states. The latter should reduce or eliminate spectral diffusion. Echo-detected field sweep (EDFS) linewidths as sharp as 10 G were obtained for the doped crystal (Figure 7.4A), additionally enabling selective T_1 measurements on ^{65}Cu and ^{63}Cu nuclear isotopes. Two metal sites with different molecular orientations exist in the isostructural Pd(acac)$_2$ and Cu(acac)$_2$ unit cells. Thus, two distinct Cu(II) hyperfine-split signals are observed at almost every crystal orientation, which we denote Cu$_A$ and Cu$_B$. An exception exists when the two molecules possess the same relative angle to the applied magnetic field, in which case the Cu$_A$ and Cu$_B$ resonances coincide. The Cu$_A$ and Cu$_B$ sites are equivalent by symmetry, related by a twofold screw axis along the b direction of the $P2_1/n$ space group.

Saturation recovery measurements for all ^{63}Cu peaks were acquired as a function of crystal orientation. At 100 K, $1/T_1$ varies almost linearly with B_0 for each hyperfine manifold (Figure 7.4B). For a given orientation, the relaxation rates are nearly equivalent for different values of M_I and for the ^{63}Cu and ^{65}Cu isotopes, despite the differing nuclear gyromagnetic ratios of the latter. The insensitivity to nuclear spin parameters indicates that Cu(II) spin relaxation at 100 K does not proceed through modulation of the hyperfine tensor, consistent with previous experimental[42] and theoretical[15,30] reports. By instead plotting $1/T_1$ vs. the molecular frame θ, a clear $\sin^2\theta$ dependence of spin relaxation is observed (Figure 7.4C), with slowest relaxation very close to the exact parallel position ($\theta = 5°$). This is fully consistent with the interpretation of the high-temperature powder anisotropy form for Cu(acac)$_2$.

A surprise arose when conducting this analysis at 20 K, which is within the low-temperature mechanism regime extracted from powder VTVH-T_1 (Figures 7.2 and 7.3). Unlike previous observations of T_1 anisotropy, a plot of $1/T_1$ vs. B_0 displays the opening of tilted ellipses (Figure 7.4D), where the semimajor axis sits approximately along a linear variation from parallel to perpendicular orientations. Widened ellipses are also visible at 10 K (Figure S63). The 20 K data has been reproduced with two separate crystals mounted in the pulse EPR instrument with two different sample mounting procedures (Supporting Information Section 9). The implication of an ellipse is that two distinct Cu(acac)$_2$ orientations possessing the same resonant field B_0 nonetheless have different spin relaxation rates. Since the resonant field B_0 is invariant to changes in the sign of θ, this could occur if orientations of $+\theta$ and $-\theta$ have different relaxation rates. Indeed, upon plotting $1/T_1$ vs. θ (the angle of B_0 to the molecular frame z-axis), the spin relaxation rate is not invariant to changes in the sign of θ for any particular Cu site (Figure 7.4E). Both Cu$_A$ and Cu$_B$ can be described instead by a phase-shifted $\sin^2\theta$, given as $\sin^2(\theta \pm \phi)$. The phase shift ϕ is equal and opposite for the two sites, and equal to 28° at 20 K. Thus, slowest spin relaxation for any given Cu(acac)$_2$ molecule arises at either +28° or −28°, and not at the molecular frame parallel orientation.

7.4 Discussion

We interpret the single-crystal T_1 anisotropy data by proposing the concept of a "spin relaxation tensor." Just as the g-tensor indicates how the Zeeman splitting changes as the magnetic field rotates relative to the molecular frame, so too the spin relaxation tensor indicates how the spin relaxation rate changes as the magnetic field rotates relative to the molecular frame. A formal definition of the spin relaxation tensor is given in Supporting Information Section 10. The g-tensor has principal axes, which indicate the orientations of largest and smallest Zeeman splitting. Likewise, the spin relaxation tensor has principal axes, which indicate the fastest and slowest spin relaxation rates.

Crucially, the principal axes of the spin relaxation tensor may or may not align with the molecular frame coordinate system (Figure 7.4F-G). The implications of tensor (mis-)alignment on the T_1 anisotropy can be illustrated graphically, where the spin relaxation tensor is visualized as an ellipse. The ellipse represents the different possible orientations of the applied field B_0, and the distance from the center of the ellipse represents the rate of spin relaxation at that orientation. At 100 K, the spin relaxation tensor aligns to the coordinate frame of the molecular point group, and the orientation of slowest spin relaxation coincides with the molecular z-axis (Figure 7.4F). This indicates that the dominant spin-phonon coupling process at 100 K is localized on individual molecules. At 20 K, by contrast, the spin relaxation tensor aligns to lattice planes in the crystal space group. In this scenario, the ori-

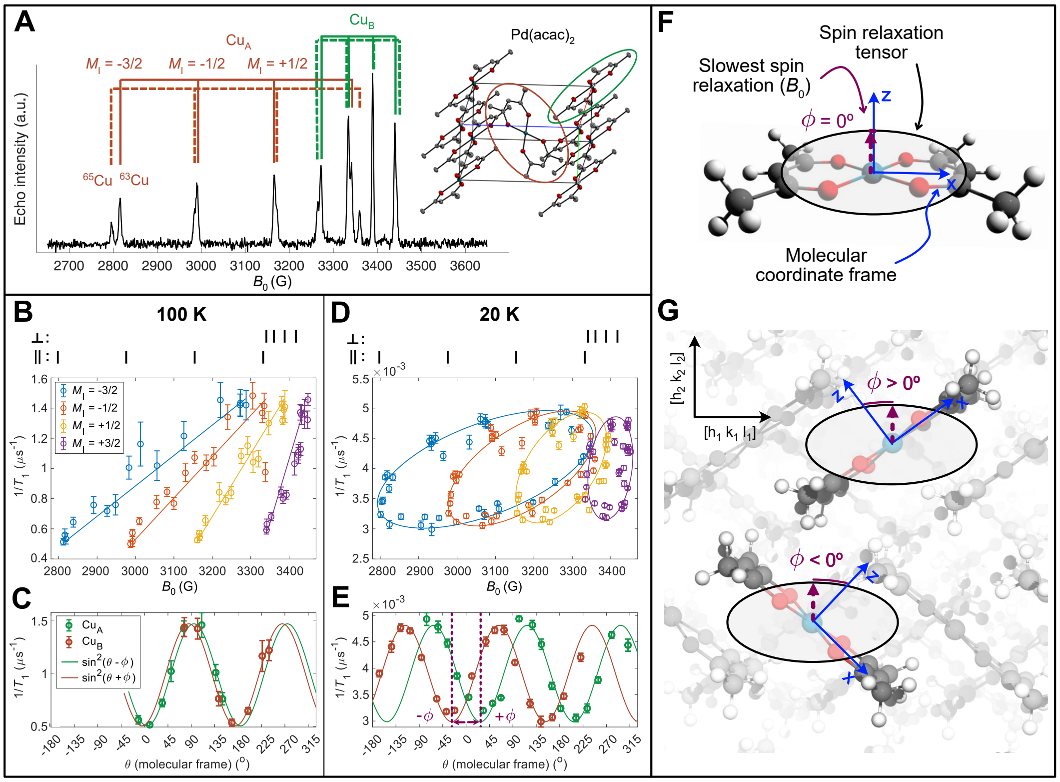

Figure 7.4: Single-crystal T_1 anisotropy for 1:1000 Cu(acac)$_2$ in Pd(acac)$_2$. (A) Example single-crystal EDFS at 100 K, together with assignments of the peaks to the two sites in the unit cell. (B) 100 K spin relaxation rate vs. B_0 indicates linear trends between parallel and perpendicular positions for each hyperfine manifold. Lines serve as a guide to the eye. (C) 100 K relaxation (M_I = -3/2) vs. molecular orientation reveals $\sin^2\theta$ angular dependence, with slowest relaxation very close to the pure parallel position (θ = 5°). (D) 20 K relaxation vs. B_0 displays elliptical T_1 patterns for each hyperfine manifold. (E) 20 K relaxation (M_I = -3/2) vs. field displays $\sin^2(\theta \pm \phi)$ angular dependence, with a large phase shift inducing slowest spin relaxation away from the parallel orientation (θ = 28°). (F) T_1 anisotropy determined by the local orientation of the molecular point group leads to $\sin^2\theta$ angular dependence, characteristic of localized spin-phonon coupling at 100 K. (G) T_1 anisotropy oriented along a lattice plane of the crystal unit cell can lead to $\sin^2(\theta \pm \phi)$ angular dependence with different phase shifts ϕ for each crystallographic site, characteristic of delocalized spin-phonon coupling at 20 K.

entation of slowest spin relaxation no longer coincides with the molecular z-axis, but with the orientation of the crystal lattice planes, and equal-and-opposite phase shifts (ϕ) may be obtained due to the angular orientation between the two Cu(acac)$_2$ molecules (Figure 7.4G). This behavior matches the experimental relaxation data at 20 K (Figure 7.4E), and a simple analytical model successfully predicts the observed $\sin^2(\theta \pm \phi)$ T_1 anisotropy form (Equation S9). Plots of $1/T_1$ vs. the laboratory frame orientation of the crystal (Ω) confirm that Ω does not determine $1/T_1$ at 100 K, while it partially determines $1/T_1$ at 20 K, and completely determines $1/T_1$ at 10 K, consistent with a dominant effect of the lattice orientation at low temperatures (Figures S56-S58). Because the spin relaxation tensor responds to the intermolecular crystal packing rather than the intramolecular bonding, this indicates that the dominant spin-phonon coupling process at 20 K is delocalized across multiple molecules.

The localized (100 K) and delocalized (20 K) phonon assignments obtained by single-crystal T_1 anisotropy correspond to the high- and low-temperature spin relaxation regimes obtained from powder VTVH-T_1 (Figure 7.2C-F). Therefore, the impact of different atomic motions can be disentangled based on their VTVH-T_1 spectroscopic signatures in the single-crystal and powder forms. The VTVH-T_1 methodology provides a uniquely direct handle for measuring the vibrational character of competing spin relaxation mechanisms.

If the spin relaxation tensor does not align with the molecular axes at low temperature, then there is also no reason to assume that it is axial (like the molecular g-tensor), or that any of its principal axes lie in the $(1\ 0\ -1)$ rotation plane interrogated in the single crystal experiments. While Figure 7.4F-G has depicted the spin-relaxation tensor as an ellipse in two-dimensions, it is actually a three-dimensional surface. Rotation of the crystal along multiple axes would enable characterization of the full tensor, so there are no limitations in principle for less-than-axial systems. However, this is beyond the scope of the present study. We note that the $[1\ 0\ -1]$ axis also produces a small rotation in the molecular xy plane in addition to the xz plane, but xy T_1 anisotropy is unlikely to explain the observed phase shifts (Figures S54-S55). The three-dimensional structure of the spin relaxation tensor would likely be required to simulate the low-temperature powder anisotropy shape.

The insights from single-crystal VTVH-T_1 anisotropy open up intriguing crystal engineering approaches for controlling lattice phonon involvement in spin relaxation. Changing the space group will probably change the observed single-crystal T_1 anisotropy significantly. Crystallization of a paramagnetic analyte in different diamagnetic host polymorphs or compounds may alter the phase shift properties in the low-temperature regime. We note that single-crystal T_1 anisotropy measurements at very low temperature (often <5 K) were reported on several inorganic lattices in the early days of EPR, including for Cr^{3+} ions in ruby,[9,43] as an experimental technique for detecting cross relaxation,[9] and in lanthanide-doped materials.[44,45] However, inorganic lattices lack the potential for tuning T_1 through intermolecular contacts.

We are aware of only one comparable single-crystal T_1 anisotropy study for a highly-coherent molecular crystal, reported by Eaton and Eaton in 1995, which examined Cu(dtc)$_2$ in Ni(dtc)$_2$ and Zn(dtc)$_2$ hosts.[46] The 100 K anisotropy in the isostructural Ni(dtc)$_2$ host agreed well with the patterns displayed by Cu(acac)$_2$ at 100 K (Figure 7.4B), but it is unknown if Cu(dtc)$_2$ also displays phase shift behavior at lower temperatures. Alteration of molecular packing through peripheral substituents may further probe the delocalized spin-phonon coupling regime—this effect may already be at play in the aforementioned VOPyzPz-DIPP system.[38] Finally, application of the VTVH-T_1 methodology to qubits embedded in metal-organic frameworks may provide a tunable means for engineering lattice phonon contributions in a high-symmetry environment.[47,48]

Powder VTVH-T_1 anisotropy contains broad potential to elucidate spin relaxation regimes not accessible by conventional local mode fitting. In the above analysis (Figure 7.2C-F), Cu(acac)$_2$ spin relaxation was shown to be dominated by a molecular vibration mechanism down to lower temperatures (>36 K) as compared to CuOEP (>47 K). This result is in good agreement with the ligand field spin dynamics model.[15] By density functional theory (DFT), Cu(acac)$_2$ has a lowest-energy totally symmetric vibration[30] at 212 cm^{-1}, whereas the corresponding vibration for CuOEP exists at 271 cm^{-1} by resonance Raman spectroscopy.[19] This change arises from having two bidentate ligands in Cu(acac)$_2$, which enables a low-energy totally symmetric scissoring mode that is not present in CuOEP.[15,30] The change in mechanism crossover point between CuOEP and Cu(acac)$_2$ likely arises from the increased thermal population of this mode in Cu(acac)$_2$. Discrimination between the impact of localized and delocalized phonons affects the design criteria for suppressing spin relaxation. If spin relaxation dominantly proceeds through localized modes, then the first coordination sphere of the molecule should be altered to suppress relaxation. Relevant strategies have been described in the literature, including stiffening the ligand framework to raise the metal-ligand stretching frequencies and strengthening the ligand field to reduce the orbital contribution to the g value.[20] Conversely, if delocalized modes dominantly drive spin relaxation, then intermolecular contacts / crystal packing effects should exhibit a greater impact. Relevant design criteria are less-well characterized, but may include the symmetry of the space group and the rotational freedom of the molecule in the lattice.[33] Powder VTVH-T_1 anisotropy can thus produce chemically interpretable design principles for controlling spin relaxation.

The present data invite detailed theoretical work to explain the change in coupling mechanism between the low- and high-temperature regimes, particularly as regards to the origin of the single-crystal phase shift. Initially, it might seem that a delocalized lattice phonon should still induce spin relaxation anisotropy obeying the molecular symmetry. Under the spin-orbit wavefunction model, T_1 anisotropy has been shown to arise from anisotropic spin-orbit coupling to ligand field electronic excited states.[30] This is a local property of the first coordination sphere, regardless of how delocalized the vibrational mode is. Alternatively, the delocalized phonons could induce spin flips involving multiple Cu centers (e.g., cross relaxation[9,48] or dipole-dipole mediated relaxation[29]). But this seems unlikely in view of the minimal paramagnetic concentration dependence of the Cu(acac)$_2$ 20 K powder anisotropy (Figure S16), as well as the dilute nature of the single-crystal samples. T_1 anisotropy has also recently been predicted through a non-adiabatic spin-vibrational orbit mechanism, though the predicted magnitude is orders of magnitude larger than observed experimentally.[31] The present anisotropy phenomena will thus provide a stringent test for development of improved spin relaxation theories.

Very recently, a new *ab initio* model has proposed that S = ½ spin relaxation occurs through virtual excitations to ligand field excited states.[32] Similar to the previously-reported spin-orbit wavefunction model,[30] this approach employs explicit anisotropic spin-orbit couplings to excited states, enabling accurate *ab initio* prediction of T_1 anisotropy within an open quantum systems framework. The model displays significantly more promising agreement with experiment than previous *ab initio* theories based on the spin Hamiltonian, including invariance to metal-based hyperfine coupling and the magnitude of the external magnetic field. However, one key point of disagreement with established experimental interpretation remains: the *ab initio* results were used to argue against the impact of high-energy molecular vibrations in driving spin relaxation. These vibrations have been experimentally interpreted to give rise to the curved local mode functional form in a plot of $1/T_1$ vs. T, such as that observed for CuOEP (Figure 7.3A). We note that the Cr(V) complexes employed in the *ab initio* predictions do not display clear local mode curvature - they behave more like Cu(acac)$_2$ than CuOEP in the present study. It is possible that only high-symmetry D_{4h} and C_{4v} compounds regularly display a dominant impact of a local mode, a result that would be consistent with previously derived group theory selection rules for spin-phonon coupling.[15] Nevertheless, the present VTVH-T_1 data show that Cu(acac)$_2$ and CuOEP alike display two distinct regimes of spin relaxation. For both compounds, this is most easily explained by high-energy molecular vibrations playing a major role at elevated temperatures. Therefore, accurate prediction of both temperature- and orientation-dependence in VTVH-T_1 constitutes an important test for *ab initio* spin dynamics models, which would be required to assert the dominant impact of low-energy phonons across all temperature regimes.

7.5 Conclusion

The VTVH-T_1 methodology uniquely probes the character of nuclear motions involved in spin relaxation and, thus, the loss of quantum information. The new mechanistic understanding gained from VTVH-T_1 will provide useful design principles for controlling spin relaxation across temperature regimes that differ by orders of magnitude, as well as diverse applications in molecular quantum information science ranging from quantum computing to room-temperature quantum sensing. Powder VTVH-T_1 measurements delineate multiple spin relaxation mechanisms operating in the same compound at different temperatures. Single-crystal VTVH-T_1 measurements characterize the orientation of the spin relaxation tensor, garnering insight into the localized vs. delocalized character of the vibrational/phonon modes coupled to the spin. The two-dimensional nature of the VTVH-T_1 methodology has proven crucial for extracting this information. The temperature dimension incorporates all the information attainable from functional fitting of $1/T_1$ vs. T, while the field dimension incorporates all the information attainable from T_1 anisotropy. Therefore, VTVH-T_1 provides the most complete picture of spin relaxation yet obtained from pulse EPR.

Until now, there has been no experimental spectroscopic method able to directly interrogate the character of the phonons causing spin relaxation. Information about spin relaxation has only been indirectly inferred from the temperature dependence of T_1. Yet, different phonons produce distinct anisotropy signatures, which can be used to directly detect competing spin relaxation mechanisms. By leveraging this insight, we constructed a direct spectroscopic probe for phonon character in spin relaxation. We believe this VTVH-T_1 approach will constitute the new gold standard for mechanistic studies of spin relaxation in molecular qubits.

References

[1] Wasielewski, M. R. *et al.* Exploiting Chemistry and Molecular Systems for Quantum Information Science. *Nature Reviews Chemistry* **2020**, *4,* 490–504.

[2] Chilton, N. F. Molecular Magnetism. *Annual Review of Materials Research* **2022**, *52,* 79–101.

[3] Coronado, E. Molecular Magnetism: From Chemical Design to Spin Control in Molecules, Materials and Devices. *Nature Reviews Materials* **2020**, *5,* 87–104.

[4] Wolfowicz, G.; Heremans, F. J.; Anderson, C. P.; Kanai, S.; Seo, H.; Gali, A.; Galli, G.; Awschalom, D. D. Quantum Guidelines for Solid-State Spin Defects. *Nature Reviews Materials* **2021**, *6,* 906–925.

[5] Atzori, M.; Sessoli, R. The Second Quantum Revolution: Role and Challenges of Molecular Chemistry. *Journal of the American Chemical Society* **2019**, *141,* 11339–11352.

[6] Gatteschi, D.; Sessoli, R. Quantum Tunneling of Magnetization and Related Phenomena in Molecular Materials. *Angewandte Chemie International Edition* **2003**, *42,* 268–297.

[7] Gatteschi, D.; Sessoli, R.; Villain, J. *Molecular Nanomagnets;* Oxford University Press: Oxford, 2006.

[8] Jackson, C. E.; Moseley, I. P.; Martinez, R.; Sung, S.; Zadrozny, J. M. A Reaction-Coordinate Perspective of Magnetic Relaxation. *Chemical Society Reviews* **2021**, *50,* 6684–6699.

[9] Standley, K. J.; Vaughan, R. A. *Electron Spin Relaxation Phenomena in Solids;* Springer US: Boston, MA, 1969. DOI: 10.1007/978-1-4899-6539-4.

[10] Mirzoyan, R.; Kazmierczak, N. P.; Hadt, R. G. Deconvolving Contributions to Decoherence in Molecular Electron Spin Qubits: A Dynamic Ligand Field Approach. *Chemistry – A European Journal* **2021**, *27,* 9482–9494.

[11] Escalera-Moreno, L.; Baldoví, J. J.; Gaita-Ariño, A.; Coronado, E. Spin States, Vibrations and Spin Relaxation in Molecular Nanomagnets and Spin Qubits: A Critical Perspective. *Chemical Science* **2018**, *9,* 3265–3275.

[12] Follmer, A. H.; Ribson, R. D.; Oyala, P. H.; Chen, G. Y.; Hadt, R. G. Understanding Covalent versus Spin-Orbit Coupling Contributions to Temperature-Dependent Electron Spin Relaxation in Cupric and Vanadyl Phthalocyanines. *The Journal of Physical Chemistry A* **2020**, *124,* 9252–9260.

[13] Fataftah, M. S.; Krzyaniak, M. D.; Vlaisavljevich, B.; Wasielewski, M. R.; Zadrozny, J. M.; Freedman, D. E. Metal-Ligand Covalency Enables Room Temperature Molecular Qubit Candidates. *Chemical Science* **2019**, *10,* 6707–6714.

[14] Atzori, M.; Tesi, L.; Morra, E.; Chiesa, M.; Sorace, L.; Sessoli, R. Room-Temperature Quantum Coherence and Rabi Oscillations in Vanadyl Phthalocyanine: Toward Multifunctional Molecular Spin Qubits. *Journal of the American Chemical Society* **2016**, *138,* 2154–2157.

[15] Kazmierczak, N. P.; Mirzoyan, R.; Hadt, R. G. The Impact of Ligand Field Symmetry on Molecular Qubit Coherence. *Journal of the American Chemical Society* **2021**, *143,* 17305–17315.

[16] Atzori, M.; Morra, E.; Tesi, L.; Albino, A.; Chiesa, M.; Sorace, L.; Sessoli, R. Quantum Coherence Times Enhancement in Vanadium(IV)-based Potential Molecular Qubits: The Key Role of the Vanadyl Moiety. *J. Am. Chem. Soc.* **2016**, *138,* 11234–11244.

[17] Amdur, M. J.; Mullin, K. R.; Waters, M. J.; Puggioni, D.; Wojnar, M. K.; Gu, M.; Sun, L.; Oyala, P. H.; Rondinelli, J. M.; Freedman, D. E. Chemical Control of Spin-Lattice Relaxation to Discover a Room Temperature Molecular Qubit. *Chemical Science* **2022**, *13,* 7034–7045.

[18] Fielding, A. J.; Fox, S.; Millhauser, G. L.; Chattopadhyay, M.; Kroneck, P. M.; Fritz, G.; Eaton, G. R.; Eaton, S. S. Electron Spin Relaxation of Copper(II) Complexes in Glassy Solution between 10 and 120K. *Journal of Magnetic Resonance* **2006**, *179,* 92–104.

[19] Kazmierczak, N. P.; Lopez, N. E.; Luedecke, K. M.; Hadt, R. G. Determining the Key Vibrations for Spin Relaxation in Ruffled Cu(II) Porphyrins via Resonance Raman Spectroscopy. *Chemical Science* **2024**, *15,* 2380–2390.

[20] Mirzoyan, R.; Hadt, R. G. The Dynamic Ligand Field of a Molecular Qubit: Decoherence through Spin-Phonon Coupling. *Physical Chemistry Chemical Physics* **2020**, *22,* 11249–11265.

[21] Garlatti, E.; Albino, A.; Chicco, S.; Nguyen, V. H. A.; Santanni, F.; Paolasini, L.; Mazzoli, C.; Caciuffo, R.; Totti, F.; Santini, P.; Sessoli, R.; Lunghi, A.; Carretta, S. The Critical Role of Ultra-Low-Energy Vibrations in the Relaxation Dynamics of Molecular Qubits. *Nature Communications* **2023**, *14,* 1653.

[22] Van Vleck, J. H. Paramagnetic Relaxation Times for Titanium and Chrome Alum. *Physical Review* **1940**, *57,* 426–447.

[23] Orbach, R. Spin-Lattice Relaxation in Rare-Earth Salts. *Proceedings of the Royal Society of London A* **1961**, *264,* 458–484.

[24] Orbach, R. On the Theory of Spin-Lattice Relaxation in Paramagnetic Salts. *Proceedings of the Physical Society* **1961**, *77,* 821–826.

[25] Lunghi, A. Toward Exact Predictions of Spin-Phonon Relaxation Times: An Ab Initio Implementation of Open Quantum Systems Theory. *Science Advances* **2022**, *8,* eabn7880.

[26] Escalera-Moreno, L. Towards the Coherent Control of Robust Spin Qubits in Quantum Algorithms. *arXiv:2303.12655* **2024**.

[27] Escalera-Moreno, L.; Suaud, N.; Gaita-Ariño, A.; Coronado, E. Determining Key Local Vibrations in the Relaxation of Molecular Spin Qubits and Single-Molecule Magnets. *The Journal of Physical Chemistry Letters* **2017**, *8,* 1695–1700.

[28] Santanni, F.; Albino, A.; Atzori, M.; Ranieri, D.; Salvadori, E.; Chiesa, M.; Lunghi, A.; Bencini, A.; Sorace, L.; Totti, F.; Sessoli, R. Probing Vibrational Symmetry Effects and Nuclear Spin Economy Principles in Molecular Spin Qubits. *Inorganic Chemistry* **2021**, *60,* 140–151.

[29] Lunghi, A.; Sanvito, S. How Do Phonons Relax Molecular Spins? *Science Advances* **2019**, *5,* eaax7163.

[30] Kazmierczak, N. P.; Hadt, R. G. Illuminating Ligand Field Contributions to Molecular Qubit Spin Relaxation via T_1 Anisotropy. *Journal of the American Chemical Society* **2022**, *144,* 20804–20814.

[31] Shushkov, P. A Novel Non-Adiabatic Spin Relaxation Mechanism in Molecular Qubits. *The Journal of Chemical Physics* **2024**, *160,* 164105.

[32] Mariano, L. A.; Nguyen, V. H. A.; Petersen, J. B.; Bjørnsson, M.; Bendix, J.; Eaton, G. R.; Eaton, S. S.; Lunghi, A. The Role of Electronic Excited States in the Spin-Lattice Relaxation of Spin-1/2 Molecules. *arXiv:2407.01380 [physics]* **2024**.

[33] Kazmierczak, N. P.; Luedecke, K. M.; Gallmeier, E. T.; Hadt, R. G. T_1 Anisotropy Elucidates Spin Relaxation Mechanisms in an S = 1 Cr(IV) Optically Addressable Molecular Qubit. *The Journal of Physical Chemistry Letters* **2023**, *14,* 7658–7664.

[34] Malinowski, E. R. *Factor Analysis in Chemistry;* Wiley: New York, 3rd ed.; 2002.

[35] de Juan, A.; Tauler, R. Multivariate Curve Resolution: 50 Years Addressing the Mixture Analysis Problem—A Review. *Analytica Chimica Acta* **2021**, *1145,* 59–78.

[36] de Juan, A.; Casassas, E.; Tauler, R. Soft Modeling of Analytical Data. In *Encyclopedia of Analytical Chemistry*; John Wiley & Sons, Ltd: 2006. _eprint: https://onlinelibrary.wiley.com/doi/pdf/10.1002/9780470027318.a5208 DOI: 10.1002/9780470027318.a5208.

[37] Wang, Y.-X.; Zhang, Y.-J. Nonnegative Matrix Factorization: A Comprehensive Review. *IEEE Transactions on Knowledge and Data Engineering* **2013**, *25,* 1336–1353.

[38] Lohaus, S. H.; Kazmierczak, N. P.; Luedecke, K. M.; Marx, B.; Nemykin, V. N.; Hadt, R. G. Quantifying the Effects of Peripheral Substituents on the Spin-Lattice Relaxation of a Vanadyl Molecular Quantum Bit. *Journal of Porphyrins and Phthalocyanines* **2024**, *28,* 383–389.

[39] Eaton, S. S.; Eaton, G. R. Saturation Recovery EPR. In *Biomedical EPR, Part B: Methodology, Instrumentation, and Dynamics*, Vol. 24/B; Eaton, S. R.; Eaton, G. R.; Berliner, L. J., Eds.; Kluwer Academic Publishers-Plenum Publishers: New York, 2005.

[40] Eaton, S. S.; Eaton, G. R. Multifrequency Pulsed EPR and the Characterization of Molecular Dynamics. In *Methods in Enzymology*, Vol. 563; Elsevier: 2015. DOI: 10.1016/bs.mie.2015.06.028.

[41] Harbridge, J. R.; Eaton, S. S.; Eaton, G. R. Electron Spin-Lattice Relaxation Processes of Radicals in Irradiated Crystalline Organic Compounds. *The Journal of Physical Chemistry A* **2003**, *107,* 598–610.

[42] Du, J. L.; Eaton, G. R.; Eaton, S. S. Electron-Spin-Lattice Relaxation in Natural Abundance and Isotopically Enriched Oxo-chromium(V)bis (2-hydroxy-2-ethylbutyrate). *Journal of Magnetic Resonance, Series A* **1995**, *115,* 236–240.

[43] Donoho, P. L. Spin-Lattice Relaxation in Ruby. *Physical Review* **1964**, *133,* A1080–A1084.

[44] Kiel, A.; Mims, W. B. Paramagnetic Relaxation Measurements on Ce, Nd, and Yb in $CaWO_4$ by an Electron Spin-Echo Method. *Physical Review* **1967**, *161,* 386–397.

[45] Mikkelson, R. C.; Stapleton, H. J. Anisotropic Spin-Lattice Relaxation Rates of Some Rare-Earth-Doped Lanthanum Trichlorides. *Physical Review* **1965**, *140,* A1968–A1982.

[46] Du, J.-L.; Eaton, G. R.; Eaton, S. S. Temperature and Orientation Dependence of Electron-Spin Relaxation Rates for Bis(diethyldithiocarbamato)copper(II). *Journal of Magnetic Resonance, Series A* **1995**, *117,* 67–72.

[47] Yu, C.-J.; Krzyaniak, M. D.; Fataftah, M. S.; Wasielewski, M. R.; Freedman, D. E. A Concentrated Array of Copper Porphyrin Candidate Qubits. *Chemical Science* **2019**, *10,* 1702–1708.

[48] Yu, C.-J.; von Kugelgen, S.; Krzyaniak, M. D.; Ji, W.; Dichtel, W. R.; Wasielewski, M. R.; Freedman, D. E. Spin and Phonon Design in Modular Arrays of Molecular Qubits. *Chemistry of Materials* **2020**, *32,* 10200–10206.

Chapter 8

SLOW ELECTRON SPIN RELAXATION AT AMBIENT TEMPERATURES WITH COPPER COORDINATED BY A RIGID MACROCYCLIC LIGAND

- Adapted with permission from: Espinosa, M. R.*; Guerrero, F.*; Kazmierczak, N. P.*; Oyala, P. H.; Hong, A.; Hadt, R. G.; Agapie, T. Slow Electron Spin Relaxation at Ambient Temperatures with Copper Coordinated by a Rigid Macrocyclic Ligand. *Journal of the American Chemical Society* **2025**, *147*, 14036–14042. DOI: 10.1021/jacs.5c00803. © 2025 American Chemical Society.
- * denotes co-first author contribution. M.R.E., F.G., and A.H. conducted chemical synthesis, characterization, and crystallography. M.R.E., F.G., A.H., and P.H.O. conducted experimental pulse and CW EPR data acquisition. N.P.K. conducted DFT calculations. N.P.K., M.R.E., and F.G. conducted analysis of CW and pulse EPR data. M.R.E., F.G., and N.P.K. co-wrote the initial manuscript. R.G.H. and T.A. conceptualized the study and provided guidance and resources. All authors contributed to the formulation of the project and have given approval to the published version of the manuscript.

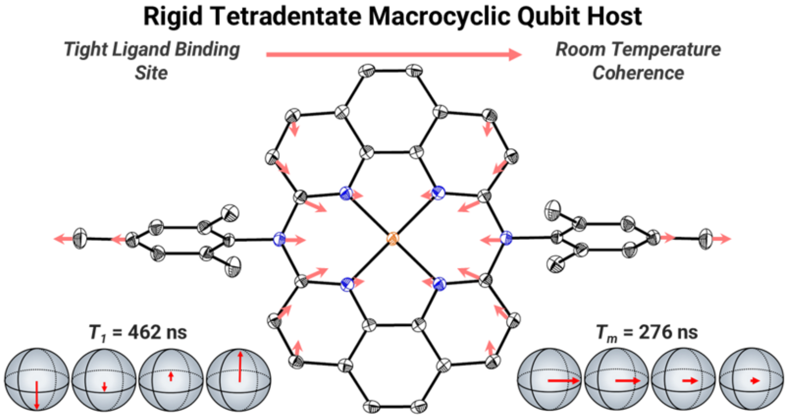

8.1 Abstract

Paramagnetic transition metal complexes can serve as quantum bits, storing phase information through unpaired electrons. Despite their promise, these systems often require low temperatures and tend to rapidly decohere. Recent efforts have sought to improve longitudinal relaxation (T_1), which provides an upper limit for phase coherence (T_m), by investigating existing literature compounds with reduced vibrational coupling and orbital angular momentum. However, synthetic strategies for improving T_1 through novel ligand design have remained scant. Here, we disclose the synthesis of a new modular macrocyclic ligand framework with four nitrogen donors (N_4) derived from phenanthroline that supports room temperature coherent Cu(II) spin centers. The optimized complex more than doubles the T_1 over the next best Cu(II)-N_4 compound and shows a room temperature coherence time (T_m) of 0.28 μs, close to previous reported values. This performance enhancement arises from a tight binding site with short Cu-N distances, resulting in a stronger ligand field and reduced thermal accessibility of symmetric vibrational modes. This work demonstrates a practical approach to enabling spin coherence at room temperature, a factor critical to accessing relevant quantum bits and biological sensors, through a designer macrocyclic ligand platform.

8.2 Introduction

Quantum information science leverages the known properties of superposition and entanglement to enable new technologies such as quantum computing, sensing, communication, and metrology.[1–4] The basic unit of information, the quantum bit or qubit, can be generated through commercially-available platforms such as the diamond nitrogen vacancy pair or superconducting loops.[5] Transition metal qubits provide a promising molecular alternative due to the ability to synthetically tune properties by changing the metal center, d electron configuration, ligand field, and spin delocalization.[1,6–13] This tunability also offers greater spectral addressability than organic radicals.[14,15] However, only a handful of transition metal systems are capable of maintaining phase coherence (T_m) at room temperature, making their potential practical implementation more challenging.[16–22]

Longitudinal relaxation (T_1) provides an upper limit for phase coherence (T_m)[23,24] and has been improved through optimization of orbital angular momentum and available vibrational modes.[16–22,25–29] For instance, Freedman et al. have shown in a series of copper (II) qubits that room temperature coherence can be achieved by reducing orbital angular momentum through changes to the molecular geometry.[16]

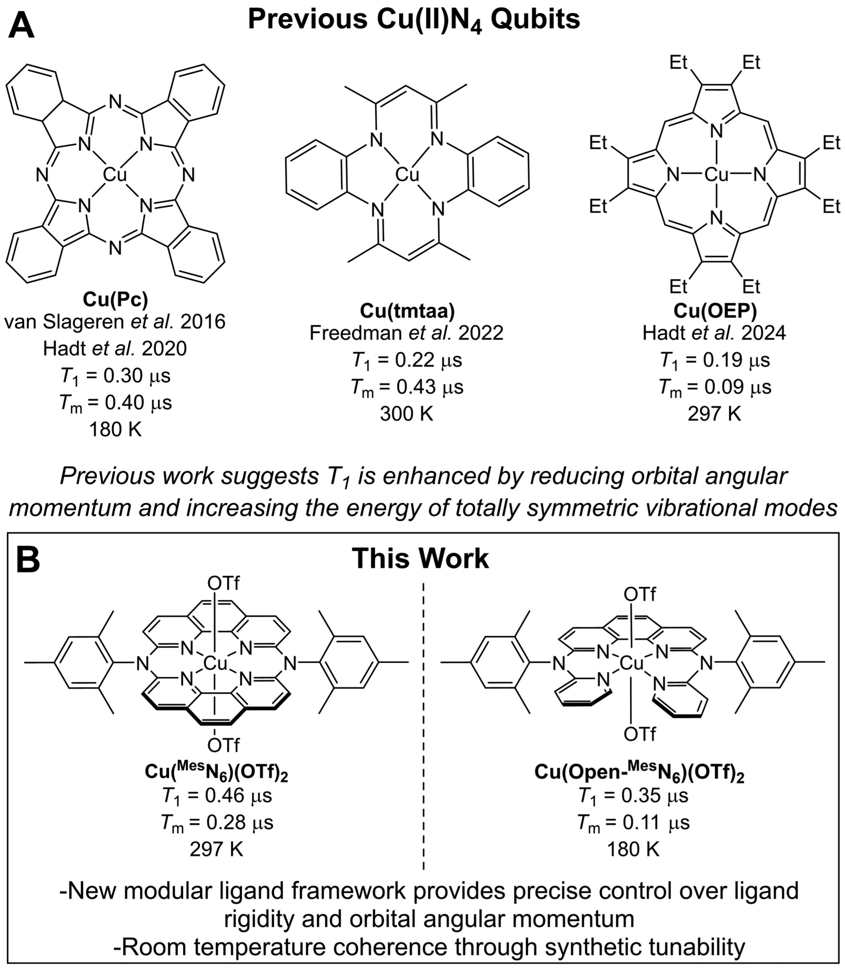

Figure 8.1: Comparison of copper N_4 macrocyclic S = ½ qubits. (A) Previous work investigating copper N_4 macrocyclic S = ½ qubits. (B) This work.

Smaller improvements in temperature dependent T_1 were demonstrated upon use of macrocyclic ligand. More recently, Hadt et al. have disclosed three copper (II) porphyrins where only two exhibit room temperature coherence despite their similar orbital angular momenta and coordination environment (Figure 8.1).[21] These observed differences were attributed to changes in the frequency of the metal-ligand symmetric stretch vibrational modes, which were experimentally determined through resonance Raman spectroscopy and local mode fitting of temperature-dependent T_1. Further work by Hadt and co-workers has detailed a new experimental observable, T_1 anisotropy, that compares T_1 across different magnetic field positions and therefore probes the influence of molecular orientation on spin relaxation.[29–31] This method has been used to determine the predominant spin relaxation pathway in Cu(II) and optically addressable Cr(IV) qubits. Lunghi et al. have investigated the relaxation dynamics of S = ½ Cr(V) coordination compounds through *ab initio* open quantum systems theory, emphasizing the crucial role of virtual transitions to high-energy electronic excited states in facilitating spin-relaxation.[32] Further exemplifying the importance of ligand field excited states, Hadt et al. have demonstrated a strong correlation between the relaxation rate of a series of Cu(II) coordination compounds and the average energy of the d-d electronic transitions measured by magnetic circular dichroism spectroscopy.[33] These studies highlight the importance of developing structure-property relationships in understanding qubit decoherence and developing improved systems.

Here, we report the synthesis of a new Cu(II) macrocyclic qubit that takes advantage of the known influence of orbital angular momentum and vibrational modes on T_1 to achieve longitudinal relaxation times at room temperature that are two times longer than the next best Cu(II)-N_4 system (Figure 8.1B). We show that these improvements are related to the tight binding site of our macrocyclic ligands based on phenanthroline (${}^{Mes}N_6$). Using field-dependent T_1 measurements, we show that T_1 anisotropy of ${}^{Mes}N_6$ is reduced compared to other Cu(II)-N_4 compounds and that symmetric vibrational modes are shifted to higher energies. The energy of the totally symmetric vibrational mode is further investigated computationally and experimentally through local mode fitting of the temperature-dependent T_1 data. These values are compared along with the orbital angular momentum data of existing macrocyclic Cu(II) compounds. We find that ${}^{Mes}N_6$ imparts high energy symmetric vibrational modes and decreases the orbital angular momentum through shorter Cu-N bonds. This enhanced rigidity results in improved longitudinal relaxation and similar phase coherence compared to existing systems.

8.3 Results and Discussion

We targeted a modular ligand framework that would allow us to systematically examine how rigidity influences spin coherence. To that end, we synthesized ${}^{Mes}N_6$, which tethers two phenanthrolines through 2,4,6-trimethyl aniline, in two high yielding SNAr steps with minimal work-up (See Supporting Information pages S3–S10). An open congener was produced by replacing one phenanthroline with two pyridines that are not linked (Open$-{}^{Mes}N_6$), allowing us to modify the metal-ligand vibrational modes while maintaining the Cu-N_4 coordination environment (See Supporting Information pages S3–S10).

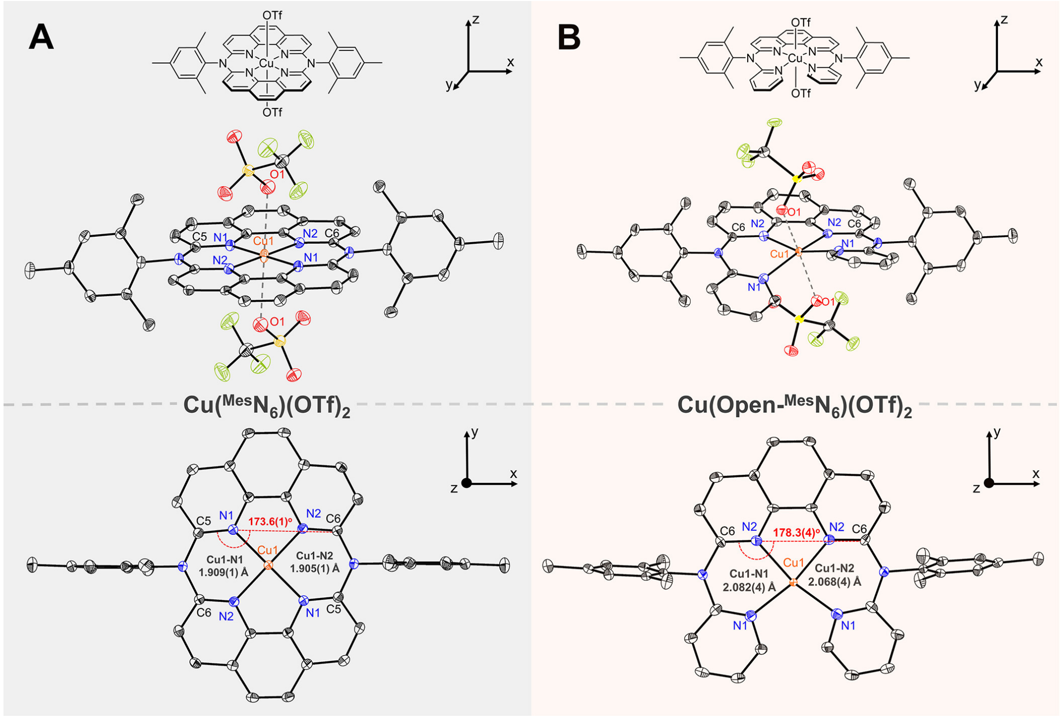

Figure 8.2: Crystal structures of (A) Cu($^{\mathrm{Mes}}$N$_6$)(OTf)$_2$ and (B) Cu(Open$-^{\mathrm{Mes}}$N$_6$)(OTf)$_2$ with top-down views omitting protons and triflate counter ions for clarity with thermal ellipsoids shown at 50% probability. Cu-N bond distances and angles in the closed macrocycle demonstrate a constrained binding site compared to the open congener which replaces a phenanthroline with two pyridines.

Crystallographic data of 1 and 2, demonstrated that $^{\mathrm{Mes}}$N$_6$ and Open$-^{\mathrm{Mes}}$N$_6$ were successfully metalated with Cu(II) triflate (Figure 8.2). The former shows a pseudo-D_{2h} square planar binding mode while the latter adopts a C_2 pseudo-tetrahedral geometry. Both structures have weak interactions with triflate counterions in the axial position (Cu-O distances of 2.660(1) and 2.319(3) Å for Cu($^{\mathrm{Mes}}$N$_6$)(OTf)$_2$ and Cu(Open$-^{\mathrm{Mes}}$N$_6$)(OTf)$_2$, respectively). Notably, the Cu-N bond lengths (1.909(1) and 1.905(1) Å) of the Cu($^{\mathrm{Mes}}$N$_6$)(OTf)$_2$ are significantly shorter than other Cu-N macrocyclic complexes like Cu(Pc), Cu(OEP), and Cu(tmtaa) (See Supporting Information pages S11–S23 for crystallographic histograms and tables).[34–36] In contrast, our structurally analogous open derivative shows longer Cu-N bond lengths (2.082(4) and 2.068(4) Å) than the aforementioned literature compounds. We propose that these differences are a consequence of the strain imparted on the phenanthroline by a more constrained ligand environment. The magnitude of this effect can also be measured by comparing the C-N-C bond angle along the binding edge of phenanthroline, where based on previously reported Cu(II) phenanthroline structures we expect to see angles between 175.08-178.09° (See Supporting Information pages S20–S23).[37–39] Compared to the literature compounds, we observe a similar C-N-C angle for Cu(Open$-^{\mathrm{Mes}}$N$_6$)(OTf)$_2$ of 178.34(4). However, in the macrocyclic analog this angle changes by about 5° and is smaller than other reported compounds, suggesting a more strained phenanthroline in Cu($^{\mathrm{Mes}}$N$_6$)(OTf)$_2$. These structural features indicate that the $^{\mathrm{Mes}}$N$_6$ ligand effectively squeezes the Cu(II) ion in the binding site, which results in enhanced σ donation and a stronger ligand field. We hypothesize that this relates to the rigidity of the new $^{\mathrm{Mes}}$N$_6$ ligand scaffold and its promise as a host for molecular qubits.

Newly synthesized Cu complexes were diluted in a structurally analogous diamagnetic matrix, and their spin relaxation behavior was characterized by X-band pulse electron paramagnetic resonance (EPR) (See Supporting Information pages S30–S38). Differences in the two new Cu(II) compounds are also apparent in the continuous wave (CW)-EPR spectrum, where the open structure distortion manifests as rhombic splitting (g_x = 2.042, g_y = 2.055, g_z = 2.225), while Cu($^{\mathrm{Mes}}$N$_6$)(OTf)$_2$ was well fit to an axial spin Hamiltonian (g_x = 2.038, g_y = 2.038, g_z = 2.150) (See Supporting Information pages S24–S29). The significantly larger g-values of the open structure arise from the weaker ligand field generated by the longer Cu-N bond distances (*vide infra*). Temperature-dependent T_1 and T_m data were collected at the field position with the highest signal to noise in the echo detected field sweep (EDFS). Cu($^{\mathrm{Mes}}$N$_6$)(OTf)$_2$ was shown to possess particularly slow spin relaxation (Figure 8.3A). Comparison to literature values of T_1 shows that this compound has longer spin lifetimes across all temperatures than the best molecules in the three other CuN$_4$ macrocycles (Figure 8.1A). The advantage of Cu($^{\mathrm{Mes}}$N$_6$)(OTf)$_2$ becomes most pronounced near room-temperature, a desirable regime for molecular quantum sensors. The T_1 value at room temperature (462 ns) is greater than twice as long as that of the nearest CuN$_4$ literature species, Cu(tmtaa) (220 ns). This improvement in longitudinal relaxation ensures that at room temperature, unlike Cu(tmtaa) which has a longer phase coherence under ambient conditions, Cu($^{\mathrm{Mes}}$N$_6$)(OTf)$_2$ is not T_1 limited (See Supporting Information page S39 for potential reasons for the shorter T_m). By contrast, the Cu(Open$-^{\mathrm{Mes}}$N$_6$)(OTf)$_2$ complex (Figure 8.3A) displays very fast spin relaxation below 60 K, inferior to all four other CuN$_4$ complexes. Above 100 K, this compound does overtake CuPc to have a longer T_1, but fast spin relaxation nonetheless prevents reliable detection of a spin echo above 180 K. The reduction in rigidity upon opening the macrocycle is clearly deleterious to spin relaxation properties.

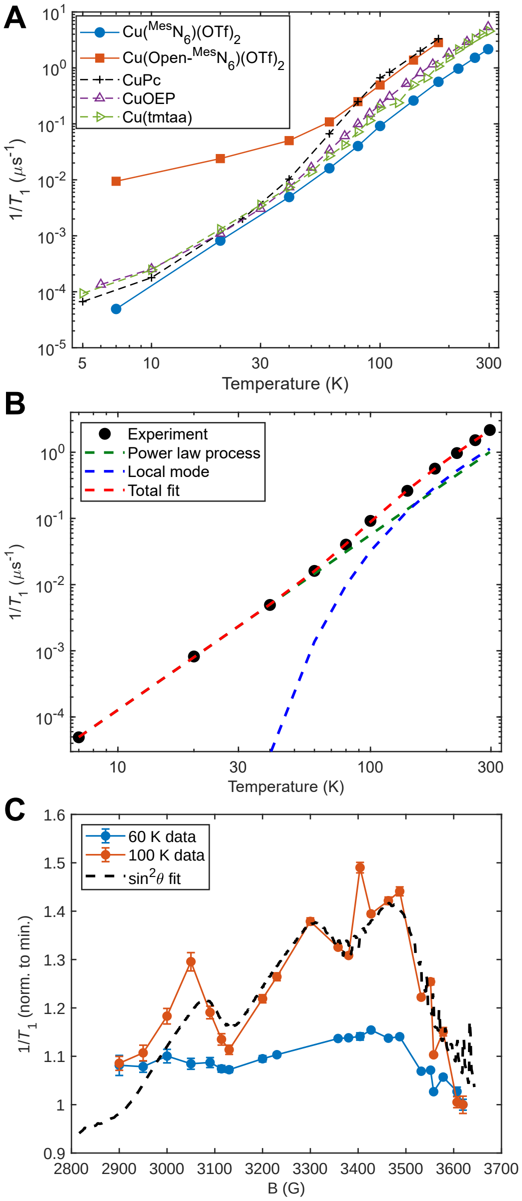

Figure 8.3: Pulse EPR analysis of Cu($^{Mes}N_6$)$^{2+}$ spin relaxation. (A) Comparison of Cu($^{Mes}N_6$)$^{2+}$ temperature-dependent T_1 (solid markers and lines) to previously studied CuN$_4$ macrocycles (open markers and dashed lines). (B) Local mode fitting of Cu($^{Mes}N_6$)(OTf)$_2$. (C) T_1 anisotropy confirms thermal population of M-L stretch modes is shifted to c.a. 100 K.

Local mode fitting (Figure 8.3B) reveals an effective molecular vibrational energy of 325 cm^{-1} for Cu($^{Mes}N_6$)(OTf)$_2$, which is higher than all other comparison CuN$_4$ complexes except Cu(tmtaa) (roughly 339 cm^{-1}, though the difference is within the previously reported fitting uncertainty).[16] The local mode relaxation process has been assigned to efficient spin flips induced by metal-ligand stretching vibrational modes; this observation suggests that the rigidity of the ${}^{\mathrm{Mes}}\mathrm{N}_6$ has reduced the thermal accessibility of these modes. The power law process ($1/T_1 \propto \mathrm{T}^{2.6}$) accounts for direct or Raman relaxation involving (pseudo-)acoustic and low-energy optical phonons. Recently, temperature-dependent T_1 anisotropy has been introduced as an independent method for detecting different vibrational regimes of spin relaxation (See Supporting Information page S40 for fitting information).[29] For S = ½ compounds, a $\sin^2 \theta$ functional form is diagnostic of high-energy stretching modes.[30,31] Indeed, the $\mathrm{Cu}({}^{\mathrm{Mes}}\mathrm{N}_6)(\mathrm{OTf})_2$ T_1 anisotropy data at 100 K can be successfully fit to the predicted $\sin^2 \theta$ shape, but the corresponding measurements at 60 K reveal that T_1 is mostly isotropic and not well-fit by this shape (Figure 8.3C). This confirms that anisotropic molecular stretching modes are not thermally populated until close to 100 K, in agreement with the relative contributions to the local mode fit (Figure 8.3B). This behavior stands in sharp contrast to CuOEP, which was recently shown to undergo the phonon/stretching mode regime transition around 45 K.[29] This suggests that the ${}^{\mathrm{Mes}}\mathrm{N}_6$ ligand has effectively detuned molecular vibrations from spin relaxation by making them too high in energy to be significantly thermally populated near room temperature.

DFT calculations shed light on the enhanced T_1 behavior of the ${}^{\mathrm{Mes}}\mathrm{N}_6$ ligand. Broadly speaking, contributions to spin relaxation may arise from either electronic structure (Figure 8.4A) or vibrational modes (Figure 8.4B). For the former, time-dependent DFT (TDDFT) calculations were used to predict the d-d excited-state energies, as these undergo spin-orbit coupling with the ground state to introduce orbital angular momentum and shifts in the g value. TDDFT indicates that the state produced by transferring an electron from d_{xy} to $d_{x^2-y^2}$ is significantly higher in energy for $\mathrm{Cu}({}^{\mathrm{Mes}}\mathrm{N}_6)(\mathrm{OTf})_2$ than for other CuN_4 complexes, including CuOEP (Figure 8.4A). This is consistent with enhanced σ donation due to the shorter Cu-N distance in $\mathrm{Cu}({}^{\mathrm{Mes}}\mathrm{N}_6)(\mathrm{OTf})_2$ and destabilization of $d_{x^2-y^2}$, while the d_{xy} orbital is little perturbed given its nonbonding character. This transition energy is known to be inversely related to the orbital g_z shift, and we indeed observe a significant decrease in g_z from CuOEP (2.195) to $\mathrm{Cu}({}^{\mathrm{Mes}}\mathrm{N}_6)(\mathrm{OTf})_2$ (2.150) accordingly (Table 8.1).[23] For $\mathrm{Cu}(\mathrm{Open}-{}^{\mathrm{Mes}}\mathrm{N}_6)(\mathrm{OTf})_2$, which possesses the longest average Cu-N bond lengths, g_z reaches its largest value across the series of 2.225. Increasing ground state orbital angular momentum is experimentally known[40] and theoretically predicted[17,23,41] to increase spin relaxation rates, so the strong σ donation is likely an important electronic factor contributing long T_1 in closed Cu($^{\mathrm{Mes}}$N$_6$)(OTf)$_2$.

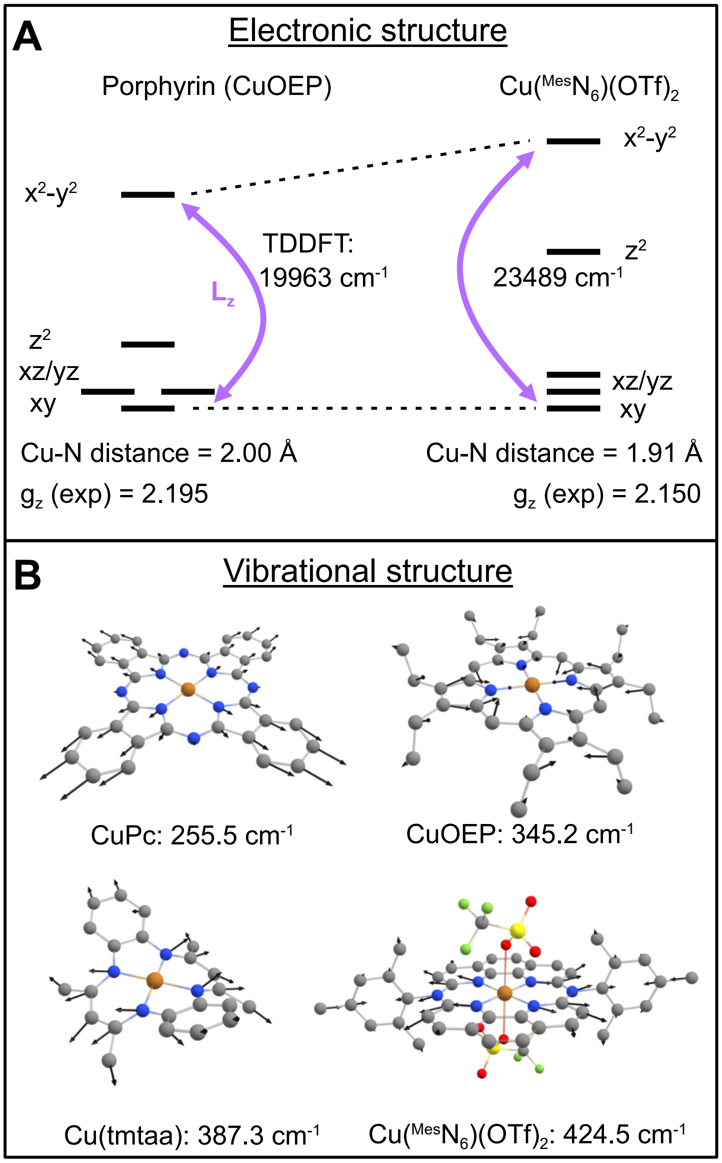

Figure 8.4: Theoretical analysis of $^{\mathrm{Mes}}$N$_6$ ligand advantage for long spin lifetimes. (A) Short Cu-N bond distances raise the computed energy of d-d transitions involved in spin-orbit coupling, leading to reduced ground state orbital angular momentum. (B) Ligand rigidity leads to a higher computed Cu-N stretching frequency than found in other highly coherent CuN$_4$ complexes. Calculations performed by (TD)DFT: see SI for details.

Additionally, the high local mode energy of Cu($^{\mathrm{Mes}}$N$_6$)(OTf)$_2$ suggests changes in relevant vibrational energies that distinguish it from CuOEP, CuPc, or Cu(Open$-^{\mathrm{Mes}}$N$_6$)(OTf)$_2$. Group theory predicts that only totally-symmetric

Compound	Cu-N bond length	g_z
Cu($^{Mes}N_6$)(OTf)$_2$	1.908	2.150
Cu(tmtaa)	1.927	2.17
CuPc	1.952	2.176
CuOEP	1.998	2.195
Cu(Open$-^{Mes}N_6$)(OTf)$_2$	2.075	2.225

Table 8.1: Comparison of crystallographic bond lengths[34–36] and CW-EPR g_z values.[16,21,28]

molecular vibrations are fully allowed to drive spin relaxation in axial S = ½ transition metal complexes.[25] With reduced symmetry, more vibrational modes are allowed to couple to the spin, tending to increase relaxation rates. Ignoring the counterions, Cu(Open$-^{Mes}N_6$)(OTf)$_2$ crystallizes in the C_2 point group, while Cu($^{Mes}N_6$)(OTf)$_2$ crystallizes approximately in the D_{2h} point group. It is therefore likely that opening the macrocycle allows more vibrations to couple to the spins, as well as reducing their energy through increased flexibility. To compare the CuN$_4$ macrocycles, DFT computations of the vibrational frequencies were conducted, and the totally-symmetric Cu-N stretching modes evaluated (Figure 8.4B; Table 8.2). Cu($^{Mes}N_6$)(OTf)$_2$ displays by far the highest such energy at 425 cm^{-1}, while that of CuPc is almost half that energy. The offsets between the main symmetric stretch energy and the local mode energy likely arise from having multiple coupled symmetric vibrational modes, which are aggregated in the phenomenological EPR fitting. The aforementioned contraction of metal-ligand bond lengths at the Cu(II) center by the $^{Mes}N_6$ ligand likely contributes to these high stretch energies, yielding reduced thermal mode population and enhanced values of T_1.

Compound	DFT symmetric stretch (cm^{-1})	Pulse EPR local mode (cm^{-1})
CuPc	255	236
CuOEP	345	258
Cu(tmtaa)	387	339
Cu($^{Mes}N_6$)(OTf)$_2$	425	325

Table 8.2: Comparison of calculated vibrational modes and local mode fitting.

While previous studies have implicated the role of metal-ligand stretching modes in driving spin relaxation,[21,23,25,27], it has been unclear how to synthetically combat this deleterious effect, given that metal-ligand stretching modes are necessarily present in any coordination complex. Here, we show that ligand design can produce tight binding pockets in rigid macrocycles; the tight binding compresses the equilibrium metal-ligand bond distances. This has two advantageous effects for spin relaxation: (1) it produces stronger σ-donation, which strengths the ligand field and reduces the ground state orbital angular momentum available for spin-phonon coupling, and (2) it stiffens the principal metal-ligand stretch vibrational modes, shifting them to a higher energy with reduced thermal population at room temperature. $^{\mathrm{Mes}}\mathrm{N}_6$ therefore represents an attractive, modular ligand framework for the design of high-performing molecular quantum systems for computing and biological sensing.

References

[1] Atzori, M.; Sessoli, R. The Second Quantum Revolution: Role and Challenges of Molecular Chemistry. *Journal of the American Chemical Society* **2019**, *141,* 11339–11352.

[2] Nielsen, M. A.; Chuang, I. L. *Quantum Computation and Quantum Information: 10th Anniversary Edition;* Cambridge University Press: Cambridge ; New York, 1st ed.; 2010.

[3] Ekert, A.; Jozsa, R. Quantum Computation and Shor's Factoring Algorithm. *Reviews of Modern Physics* **1996**, *68,* 733–753.

[4] MacFarlane, A. G. J.; Dowling, J. P.; Milburn, G. J. Quantum Technology: The Second Quantum Revolution. *Philosophical Transactions of the Royal Society of London. Series A: Mathematical, Physical and Engineering Sciences* **2003**, *361,* 1655–1674.

[5] Popkin, G. Quest for Qubits. *Science* **2016**, *354,* 1090–1093.

[6] Aromí, G.; Aguilà, D.; Gamez, P.; Luis, F.; Roubeau, O. Design of Magnetic Coordination Complexes for Quantum Computing. *Chemical Society Reviews* **2012**, *41,* 537–546.

[7] Gaita-Ariño, A.; Luis, F.; Hill, S.; Coronado, E. Molecular Spins for Quantum Computation. *Nature Chemistry* **2019**, *11,* 301–309.

[8] Graham, M. J.; Zadrozny, J. M.; Fataftah, M. S.; Freedman, D. E. Forging Solid-State Qubit Design Principles in a Molecular Furnace. *Chemistry of Materials* **2017**, *29,* 1885–1897.

[9] Harvey, S. M.; Wasielewski, M. R. Photogenerated Spin-Correlated Radical Pairs: From Photosynthetic Energy Transduction to Quantum Information Science. *Journal of the American Chemical Society* **2021**, *143,* 15508–15529.

[10] Troiani, F.; Affronte, M. Molecular Spins for Quantum Information Technologies. *Chemical Society Reviews* **2011**, *40,* 3119–3129.

[11] von Kugelgen, S.; Freedman, D. E. A Chemical Path to Quantum Information. *Science* **2019**, *366,* 1070–1071.

[12] Wasielewski, M. R. *et al.* Exploiting Chemistry and Molecular Systems for Quantum Information Science. *Nature Reviews Chemistry* **2020**, *4,* 490–504.

[13] Yu, C.-J.; von Kugelgen, S.; Laorenza, D. W.; Freedman, D. E. A Molecular Approach to Quantum Sensing. *ACS Central Science* **2021**, *7,* 712–723.

[14] von Kugelgen, S.; Krzyaniak, M. D.; Gu, M.; Puggioni, D.; Rondinelli, J. M.; Wasielewski, M. R.; Freedman, D. E. Spectral Addressability in a Modular Two Qubit System. *Journal of the American Chemical Society* **2021**, *143,* 8069–8077.

[15] Zhou, A.; Sun, Z.; Sun, L. Stable Organic Radical Qubits and their Applications in Quantum Information Science. *The Innovation* **2024**, *5,* 100662.

[16] Amdur, M. J.; Mullin, K. R.; Waters, M. J.; Puggioni, D.; Wojnar, M. K.; Gu, M.; Sun, L.; Oyala, P. H.; Rondinelli, J. M.; Freedman, D. E. Chemical Control of Spin–Lattice Relaxation to Discover a Room Temperature Molecular Qubit. *Chemical Science* **2022**, *13,* 7034–7045.

[17] Ariciu, A.-M.; Woen, D. H.; Huh, D. N.; Nodaraki, L. E.; Kostopoulos, A. K.; Goodwin, C. A. P.; Chilton, N. F.; McInnes, E. J. L.; Winpenny, R. E. P.; Evans, W. J.; Tuna, F. Engineering Electronic Structure to Prolong Relaxation Times in Molecular Qubits by Minimising Orbital Angular Momentum. *Nature Communications* **2019**, *10,* 3330.

[18] Atzori, M.; Morra, E.; Tesi, L.; Albino, A.; Chiesa, M.; Sorace, L.; Sessoli, R. Quantum Coherence Times Enhancement in Vanadium(IV)-based Potential Molecular Qubits: the Key Role of the Vanadyl Moiety. *Journal of the American Chemical Society* **2016**, *138,* 11234–11244.

[19] Atzori, M.; Tesi, L.; Morra, E.; Chiesa, M.; Sorace, L.; Sessoli, R. Room-Temperature Quantum Coherence and Rabi Oscillations in Vanadyl Phthalocyanine: Toward Multifunctional Molecular Spin Qubits. *Journal of the American Chemical Society* **2016**, *138,* 2154–2157.

[20] Bader, K.; Dengler, D.; Lenz, S.; Endeward, B.; Jiang, S.-D.; Neugebauer, P.; van Slageren, J. Room Temperature Quantum Coherence in a Potential Molecular Qubit. *Nature Communications* **2014**, *5,* 5304.

[21] Kazmierczak, N. P.; Lopez, N. E.; Luedecke, K. M.; Hadt, R. G. Determining the Key Vibrations for Spin Relaxation in Ruffled Cu(II) Porphyrins via Resonance Raman Spectroscopy. *Chemical Science* **2024**, *15,* 2380–2390.

[22] Fataftah, M. S.; Krzyaniak, M. D.; Vlaisavljevich, B.; Wasielewski, M. R.; Zadrozny, J. M.; Freedman, D. E. Metal–Ligand Covalency Enables Room Temperature Molecular Qubit Candidates. *Chemical Science* **2019**, *10,* 6707–6714.

[23] Mirzoyan, R.; Kazmierczak, N. P.; Hadt, R. G. Deconvolving Contributions to Decoherence in Molecular Electron Spin Qubits: A Dynamic Ligand Field Approach. *Chemistry – A European Journal* **2021**, *27,* 9482–9494.

[24] Zadrozny, J. M.; Freedman, D. E. Qubit Control Limited by Spin–Lattice Relaxation in a Nuclear Spin-Free Iron(III) Complex. *Inorganic Chemistry* **2015**, *54,* 12027–12031.

[25] Kazmierczak, N. P.; Mirzoyan, R.; Hadt, R. G. The Impact of Ligand Field Symmetry on Molecular Qubit Coherence. *Journal of the American Chemical Society* **2021**, *143,* 17305–17315.

[26] Fielding, A. J.; Fox, S.; Millhauser, G. L.; Chattopadhyay, M.; Kroneck, P. M.; Fritz, G.; Eaton, G. R.; Eaton, S. S. Electron Spin Relaxation of Copper(II) Complexes in Glassy Solution between 10 and 120K. *Journal of Magnetic Resonance* **2006**, *179,* 92–104.

[27] Mirzoyan, R.; Hadt, R. G. The Dynamic Ligand Field of a Molecular Qubit: Decoherence through Spin–Phonon Coupling. *Physical Chemistry Chemical Physics* **2020**, *22,* 11249–11265.

[28] Follmer, A. H.; Ribson, R. D.; Oyala, P. H.; Chen, G. Y.; Hadt, R. G. Understanding Covalent versus Spin–Orbit Coupling Contributions to Temperature-Dependent Electron Spin Relaxation in Cupric and Vanadyl Phthalocyanines. *The Journal of Physical Chemistry A* **2020**, *124,* 9252–9260.

[29] Kazmierczak, N. P.; Oyala, P. H.; Hadt, R. G. Spectroscopic Signatures of Phonon Character in Molecular Electron Spin Relaxation. *ACS Central Science* **2024**, *10,* 2353–2362.

[30] Kazmierczak, N. P.; Hadt, R. G. Illuminating Ligand Field Contributions to Molecular Qubit Spin Relaxation via T_1 Anisotropy. *Journal of the American Chemical Society* **2022**, *144,* 20804–20814.

[31] Kazmierczak, N. P.; Luedecke, K. M.; Gallmeier, E. T.; Hadt, R. G. T_1 Anisotropy Elucidates Spin Relaxation Mechanisms in an S = 1 Cr(IV) Optically Addressable Molecular Qubit. *The Journal of Physical Chemistry Letters* **2023**, *14,* 7658–7664.

[32] Mariano, L. A.; Nguyen, V. H. A.; Petersen, J. B.; Björnsson, M.; Bendix, J.; Eaton, G. R.; Eaton, S. S.; Lunghi, A. The Role of Electronic Excited States in the Spin-Lattice Relaxation of Spin-1/2 Molecules. *Science Advances* **2025**, *11,* eadr0168.

[33] Kazmierczak, N. P.; Xia, K. T.; Sutcliffe, E.; Aalto, J. P.; Hadt, R. G. A Spectrochemical Series for Electron Spin Relaxation. *Journal of the American Chemical Society* **2025**, *147,* 2849–2859.

[34] Brown, C. J. Crystal Structure of β-Copper Phthalocyanine. *Journal of the Chemical Society A: Inorganic, Physical, Theoretical* **1968**, *0,* 2488–2493.

[35] Pak, R.; Scheidt, W. R. Structure of (2,3,7,8,12,13,17,18-Octaethylporphinato)copper(II). *Acta Crystallographica Section C: Crystal Structure Communications* **1991**, *47,* 431–433.

[36] Hotz, R. P.; Bereman, R. D.; Purrington, S. T.; Singh, P. X-Ray Crystal Structure of 6,17-dimethyl-8, 15-diphenyl-dibenzo [b,i][1,4,8,11]tetraazacyclotetradecinato copper(II): The More Sterically-Crowded Isomer. *Journal of Coordination Chemistry* **1995**, *34,* 159–167.

[37] Valle, H. U.; Riley, K. M.; Russell, D. E.; Wolgemuth, D. K.; Voges-Haupt, C. F.; Rogers, T. A.; Redd, S. L.; Stokes, S. L.; Emerson, J. P. Synthesis, Characterization, and Structure of a [Cu(phen)$_2$(OTf)]OTf Complex: An Efficient Nitrogen Transfer Pre-catalyst.. *ChemistrySelect* **2018**, *3,* 5143–5146.

[38] Seidel, R. W.; Dietz, C.; Oppel, I. M. A Polymeric Arched Chain and a Chair-like M$_2$L$_2$-Metallamacrocycle Crystal Engineered of [M(phen)]$^{2+}$ (M = Cu, Cd; phen = 1,10-Phenanthroline) Corner Units and the Bent Ligand 4,4-Dithiodipyridine. *Zeitschrift für anorganische und allgemeine Chemie* **2011**, *637,* 94–101.

[39] Uvarova, M. A.; Nefedov, S. E. Reactions of PhenCuX$_2$ (X = OOCMe, O$_3$SCF$_3$) with 3,5-Dimethylpyrazole: Effect of the Anion Nature on the Composition and Structure of the Complexes. *Russian Journal of Coordination Chemistry* **2020**, *46,* 125–136.

[40] Abragam, A.; Bleaney, B. 1.11. Spin-Lattice Interaction. In *Electron Paramagnetic Resonance of Transition Ions*; Oxford University Press: Oxford, New York, 1970.

[41] Albino, A.; Benci, S.; Tesi, L.; Atzori, M.; Torre, R.; Sanvito, S.; Sessoli, R.; Lunghi, A. First-Principles Investigation of Spin–Phonon Coupling in Vanadium-Based Molecular Spin Quantum Bits. *Inorganic Chemistry* **2019**, *58,* 10260–10268.

Chapter 9

QUANTIFYING THE EFFECTS OF PERIPHERAL SUBSTITUENTS ON THE SPIN-LATTICE RELAXATION OF A VANADYL MOLECULAR QUANTUM BIT

- Electronic version of an article published as: Lohaus, S. H.; Kazmierczak, N. P.; Luedecke, K. M.; Marx, B.; Nemykin, V. N.; Hadt, R. G. Quantifying the Effects of Peripheral Substituents on the Spin-Lattice Relaxation of a Vanadyl Molecular Quantum Bit. *Journal of Porphyrins and Phthalocyanines* **2024**, *28*, 383–389. DOI: 10.1142/S1088424624500329. © 2024 World Scientific Publishing Company, https://www.worldscientific.com/worldscinet/jpp. Used with permission.

9.1 Abstract

Electron spin superpositions represent a critical component of emergent quantum technologies in computation, sensing, encryption, and communication. However, spin relaxation (T_1) and decoherence (T_m) represent major obstacles to the implementation of molecular quantum bits (qubits). Synthetic strategies have made substantial progress in enhancing spin coherence times by minimizing contributions from surrounding electron and nuclear spins. For room-temperature operation, however, the lifetime of spin coherence becomes limited by coupling with vibrational modes of the lattice. Using pulse electron paramagnetic resonance (EPR) spectroscopy, we measure the spin-lattice relaxation of a vanadyl tetrapyrazinoporphyrazine complex appended with eight peripheral 2,6-diisopropylphenol groups (VOPyzPz-DIPP) and compare it to the relaxation of the archetypical vanadyl phthalocyanine molecular qubit (VOPc). The added peripheral groups lead to distinctly different spin relaxation behavior. While similar relaxation times are observed at low temperature and ambient conditions, significant changes are observed for the orientation dependence of T_1 at 100 K, as well as the temperature dependence of T_1 over the intermediate temperature range spanning ~10 – 150 K. These results can be tentatively interpreted as arising from loosened spin-phonon coupling selection rules and a greater number of accessible acoustic and optical modes contributing to the spin relaxation behavior of VOPyzPz-DIPP relative to VOPc.

9.2 Introduction

The development of quantum computation and sensing is limited by the coherence times of current quantum bits (qubits) of information. In contrast to a or binary bit, a qubit can carry more information due to its ability to form superpositions of such states. For a successful quantum computation, the coherence time of the superposition, or phase memory time, T_m, must be at least 10^4 times longer than that of an individual quantum operation;[1,2] in electron paramagnetic resonance (EPR), the operation time corresponds to a microwave pulse of ~8 ns. Electron spins are attractive qubit candidates, as they can take on superpositions of their M_S sublevels in applied magnetic fields and can be manipulated and sensed by established methods. S = ½ Cu(II) and vanadyl phthalocyanines (CuPc/VOPc) are among some of the most highly studied molecular qubits; VOPc also represents one of the rare transition metal systems exhibiting measurable spin coherence up to room temperature.[3–6] Phthalocyanines can also be deposited onto surfaces for device fabrication[7] and integrated with solid-state systems into hybrid quantum architectures.[8,9] However, as temperature increases, vibrational modes of the molecules and phonons of the crystal become populated and interact with spins. This spin-lattice relaxation limits the coherence of the spin states and becomes critical for room temperature implementation of qubits, such as quantum sensors in biological systems.

Several design strategies have been explored for tuning the spin relaxation and spin decoherence rates in transition metal complexes. Spin coherence times can be improved by reducing interactions with nuclear spins through ligand substitutions,[10] especially when using nuclear-spin-free ligands.[11] Often, the bottleneck of spin coherence times arises from fast spin relaxation, which necessarily destroys coherent states in the transverse plane of the Bloch sphere. Slow spin relaxation is achieved in square-planar or square-pyramidal transition metal complexes, where the spin-orbit coupling becomes quenched by the ligand field,[1,6,12] minimizing spin-phonon coupling. Systems with a single unpaired electron (S = 1/2), such as Cu(II) or V(IV), generally yield slow spin relaxation due to the absence of Orbach relaxation involving low-lying electronic excited states. However, a better understanding of structural effects on spin-lattice relaxation is crucial for mitigating molecular qubit decoherence at room temperature.

Hadt and co-workers have previously developed a ligand-field model to describe the couplings between optical modes and the M_S sublevels of $S = 1/2$ systems.[6,12,13] From the development of a group theoretical selection rule, it was determined that only totally symmetric (bond-stretching) modes are fully allowed to undergo linear spin-phonon couplings. This selection rule derives from the fact that ligand field excited states distort along totally symmetric modes. These vibronic couplings change the degree of spin-orbit coupling between the ground and excited states, which can modulate ground-state orbital angular momentum and minority spin contributions in the ground-state wavefunction, thus leading to spin relaxation. Notably, changes in molecular symmetry will also lead to changes in vibrational symmetries, including the number of totally symmetric irreducible representations.[6,14] Furthermore, ligand perturbations can also change the energies of acoustic and optical modes and, therefore, their thermal population. Indeed, systematic correlations between molecular structure, vibrational mode symmetries, and spin relaxation have provided invaluable mechanistic insight related to the magnitude of T_1 and its temperature dependence.

Nemykin and co-workers have recently presented a detailed spectroscopic study of a new vanadyl complex related to VOPc: vanadyl tetrapyrazinoporphyrazine with eight peripheral 2,6-diisopropylphenol groups (VOPyzPz-DIPP, Fig. 9.1b). Here, we quantify the spin-lattice relaxation time, T_1, of VOPyzPz-DIPP in solid state dilutions, as well as its T_1 orientation dependence at 100 K. VOPyzPz-DIPP exhibits room temperature coherence with a T_1 comparable to VOPc. It also exhibits a slightly longer T_1 at 5 K despite the peripheral groups that introduce additional phonon modes. There exists, however, a dramatic difference in the nature of the T_1 temperature dependence between the two vanadyl complexes, especially in the intermediate temperature range (10 - 100 K) where VOPyzPz-DIPP relaxes more rapidly than VOPc. This relaxation behavior is tentatively assigned to increased spin-phonon couplings between the spin and new low-energy vibrational degrees of freedom introduced by the PyzPz-DIPP ligand. Thus, this study provides new insights into the spin-phonon coupling contributions to T_1 over a large temperature regime.

9.3 Materials and Methods

9.3.1 Materials

VOPc and titanyl phthalocyanine (TiOPc) were purchased from Sigma-Aldrich. VOPc was diluted by the isostructural diamagnetic TiOPc in a ratio of 1:100 as described in a previous study,[4] resulting in a bright primary-blue polycrystalline powder. VOPyzPz-DIPP was prepared as described previously.[15] As shown in Fig. 9.1, VOPyzPz-DIPP has an analogous structure to VOPc. A 3D interactive

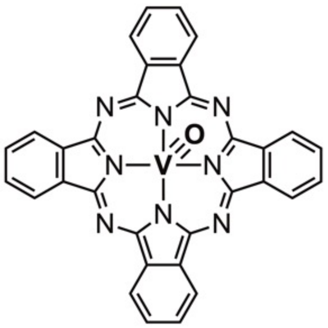

(a) VOPc

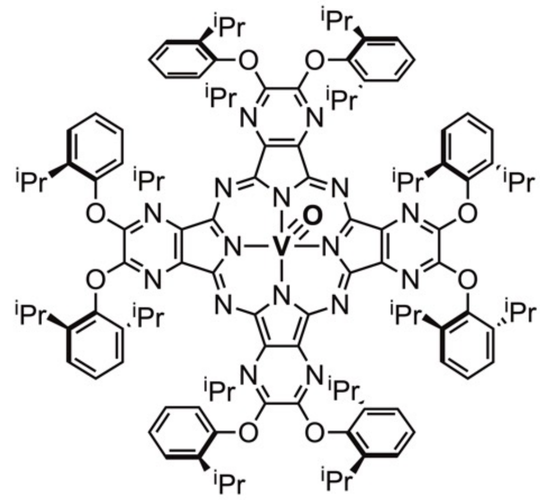

(b) VOPyzPz-DIPP

Figure 9.1: Molecular structures of (a) VOPc and (b) VOPyzPz-DIPP.

rendering of the VOPyzPz-DIPP molecule is available from the CCDC database (ref no. 2208789). For EPR measurements, VOPyzPz-DIPP was also diluted by its diamagnetic titanyl counterpart, TiOPyzPz-DIPP, in a ratio of 1:100. The resulting material is a deep dark green powder (photos of the materials and the UV-vis spectrum of VOpyzPz-DIPP are included in the SI). The color hues used to visualize the data in Figs. 2-4 represent the colors of the actual materials (with tints and shades adjusted for clarity). The X-ray powder diffraction of VOPyzPz-DIPP (Fig. S19) shows contributions from a crystalline structure on top of broad amorphous-like peaks. The crystal unit cell for VOPyzPz-DIPP is large, with a cubic lattice parameter of 37.267, which may lead to a partial loss of long-range order in the EPR diamagnetic dilution.

9.3.2 Electron Paramagnetic Resonance (EPR)

Continuous wave (CW) EPR was performed at X-band by a Bruker EMX instrument at 77 K using a liquid nitrogen immersion dewar. CW spectra were fitted using EasySpin[16] to extract g values and hyperfine parameters (Figs. S3-S4).

Pulse EPR enables the measurement of the spin relaxation dynamics. Pulse X-band EPR experiments were conducted with a Bruker ELEXSYS E580 pulse EPR spectrometer, using a Bruker MD-4 resonator. Temperature control was achieved using an Oxford Instruments CF935 cryogen flow cryostat using liquid helium and a Mercury iTC temperature controller. By selecting different high-power microwave pulse sequences, both T_1 and T_m can be measured. Due to spin-spin interactions, spins in different environments precess at slightly different frequencies causing phase decoherence (T_m). This was probed using Hahn-echo pulse sequences, $\pi/2 - \tau - \pi - \tau-$echo, by increasing τ and observing the decrease in the integrated echo intensity. Echo-detected field sweep (EDFS) spectra employed the same two-pulse Haho-echo sequence while scanning through different magnetic fields. Thermal equilibration through spin-lattice relaxation (T_1), realigns the spins back with the external magnetic field. This relaxation was detected by inversion recovery experiments, which added an initial spin flip π pulse to the sequence: $\pi - t - \pi/2 - \tau - \pi - \tau-$echo ($\tau$ is a fixed constant and t is the variable time delay).

Besides measuring T_1, inversion recovery traces may also contain relaxation by spectral diffusion, where excited spins exchange energy with spins outside of the microwave pulse bandwidth.[17] This additional (fast) relaxation pathway becomes particularly prominent at low temperatures when the spin lifetimes are long. To isolate this effect from the actual spin-lattice relaxation, saturation recovery measurements were also performed (see Section S3.2). This technique implements a series of eight initial π pulses, saturating spectral diffusion and diminishing its contributions to the subsequent inversion recovery measurements.

9.4 Results and Discussion

Hahn-echo measurements of T_m at X-band show a stretch exponential decay of the echo intensity convoluted by hyperfine modulations (Figs. S15-S17). The modulations arise from interactions with coupled nuclear spins on ligand atoms (H and N) and inhibit a quantitative determination of T_m. Nonetheless, as shown qualitatively in Fig. S18, the phase-memory time seems larger for VOPyzPz-DIPP than for VOPc. This validates the strategy of adding bulky ligand substituents to improve spin coherence by increasing the distance between spin centers as proposed in[15]. Additional experiments are required for a detailed analysis of T_m; we focus here on the spin-lattice behavior, T_1.

The EDFSs for VOPc and VOPyzPz-DIPP are similar (Fig. 9.2b), reflecting comparable spin Hamiltonian parameters and first coordination spheres. The g values and hyperfine parameters extracted from CW EPR measurements are presented in Table S1 and agree well with previous studies.[3–5] The spectrum of VOPyzPz-DIPP has an additional feature (marked by an asterisk) attributable to an organic radical with a g value of 2.003. CW EPR shows that it stems from the TiOPyzPz matrix (Fig. S6). This feature is also captured by CW EPR in VOPc, in accordance with previous studies.[3,4] The presence of such a radical signal, however, does not affect the measurement of T_1 at other field positions.

T_1 was measured by inversion recovery and as a function of the external field at 100 K (Fig. 9.2c). The relaxation is anisotropic and becomes monotonically faster towards the center of the spectrum. Vanadyl porphyrins and phthalocyanines possess axial g- and A-tensors with $g_{\parallel} < g_{\perp}$ and $|A_{\parallel}| > |A_{\perp}|$, where parallel and perpendicular refer to the orientation of the external field with respect to g_z (the z-axis is approximately collinear with the principal symmetry axis, out of the equatorial plane in Fig. 9.1). Since the perpendicular and parallel spin Hamiltonian parameters are distinct, different field positions measure different orientations, and single crystals are not required to measure T_1 anisotropy. Calculations of the hyperfine splitting of VOPc with the I = 7/2 ^{51}V nucleus show the field positions of parallel and perpendicular orientations in Fig. 9.2a.[5] We probe pure parallel contributions at 294 mT, while the isolated contribution of perpendicular orientations is measured at 337 mT (see arrows in Fig. 9.2b). T_1 is longest at the parallel position and decreases linearly through intermediate orientations towards the perpendicular orientation.

VOPc and several other molecular qubits show similar relaxation behavior.[5] However, previous measurements exhibited sharp discontinuities at the hyperfine turning points (i.e., steps and peaks of the EDFS spectrum). These discontinuities arise due to the excitation of new M_I subpopulations with different rates of spin relaxation. Notably, the relaxation of VOPyzPz-DIPP is insensitive to the hyperfine turning points. A possible origin of this effect lies in the partially amorphous nature of the material as measured by XRD (Fig. S19). The local behavior around the V(IV) spin center seems unaffected, as seen by the sharp turning points of the EDFS spectra, but long-range structural disorder would affect the propagation of phonon modes at

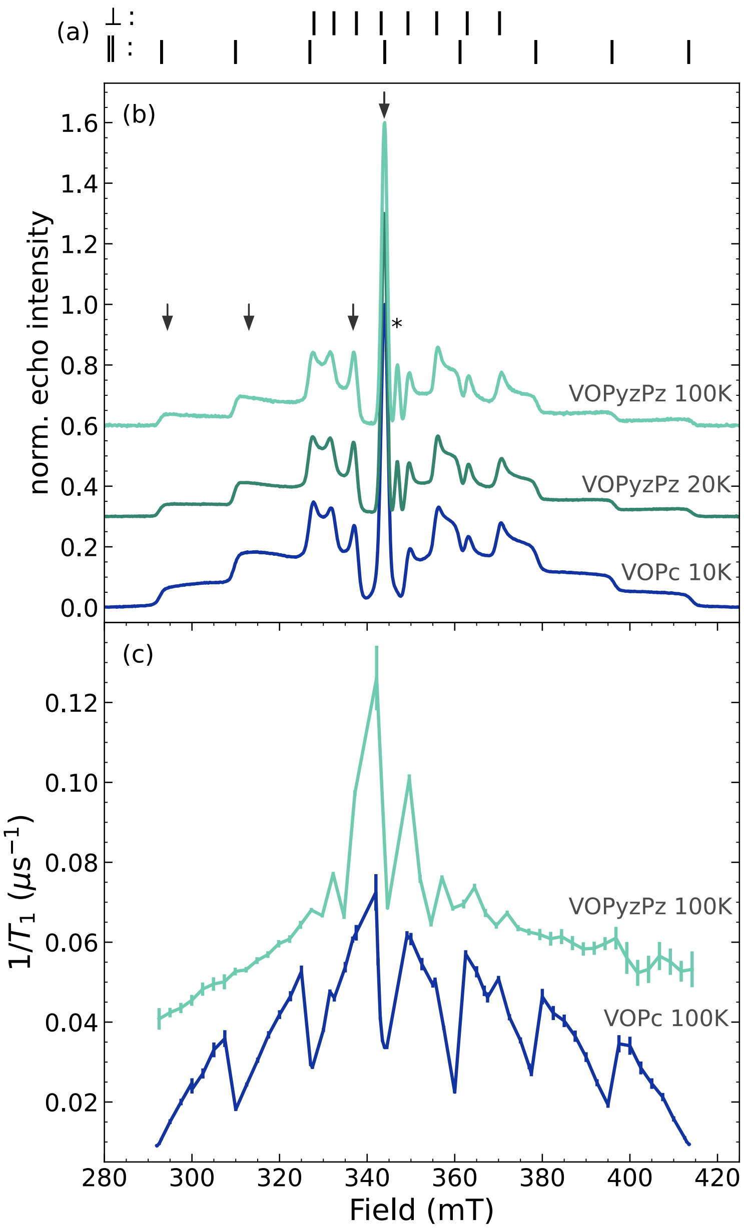

Figure 9.2: Pulse EPR T_1 anisotropy of VOPyzPz-DIPP and VOPc. (a) Simulated orientation dependence of VOPc, showing where parallel and perpendicular orientations of the molecular principal axis with respect to the external field are probed. (b) EDFS of VOPyzPz-DIPP (20 K and 100 K) and VOPc (10 K).[5] Arrows indicate field positions selected for temperature-dependent T_1 measurements. Asterisk denotes the feature resulting from an organic radical in the TiO matrix. (c) Spin-lattice relaxation time T_1 at 100 K as a function of the external magnetic field measured by inversion recovery experiments. Error bars show the 95% confidence interval of the fits using Eq. (9.2).

low energies. Structural symmetries might become lifted, allowing long wavelength glassy phonons to partake in the relaxation and cause a blurring of the hyperfine turning points. Future research directions include quantifying such an effect of structural disorder on spin-lattice relaxation.

The anisotropy parameter for VOPyzPz-DIPP can be computed by taking the ratio of T_1 at the parallel and perpendicular field positions (Eq. (9.1)):

$$T_{1,anisotropy} = \frac{1/T_1(\perp)}{1/T_1(\|)} = 2.2. \tag{9.1}$$

The T_1 anisotropy of 2.2 is close to the average predicted value of 2.5 from explicit forms of the spin-orbit wave functions.[5] Interestingly, the T_1 anisotropy of VOPc deviated significantly from 2.5 in a previous study, exhibiting a value of 6.0. This deviation from 2.5 was attributed to the square pyramidal geometry of VOPc, which breaks the planar symmetry and allows for additional modes to undergo spin-phonon and vibronic coupling. Different modes can contribute to the T_1 anisotropy through anisotropic vibronic couplings, which can result in a deviation from the average value of 2.5. Since both VOPc and VOPyzPz-DIPP have the same local symmetry around the vanadyl center, the different T_1 anisotropies suggest that additional long-range phonon modes may play an important role in the spin-lattice relaxation of VOPyzPz-DIPP. Such modes could arise from low energy vibrations of the peripheral groups and from glassy modes of the amorphous structure.

To further explore the vibrational contributions to the T_1 of VOPyzPz-DIPP, we performed inversion recovery measurements on VOPyzPz-DIPP and VOPc between 5 K and room temperature (Figs. 3 and 4). Data for VOPc are consistent with previous studies.[3,4] Temperature-dependent T_1 was measured at various field positions (arrows in Fig. 9.2a). All fields exhibited similar temperature behavior; thus, we focus on the powder line (i.e., the field position with the strongest signal intensity at 343 mT), while data for other field positions are presented in Section S3.2.

Inversion recovery quantifies the intensity of the echo measured at different delay times after the inversion pulse. As shown in Fig. 9.3a, the polarization of the spins (sign of the echo intensity) relaxes back to equilibrium with increasing delays. At 10 K (Fig. 9.3a), VOPyzPz-DIPP relaxes faster than VOPc. T_1 can be obtained by fitting the data to Eq. (9.2),

$$I(t) = A \exp\left(\left(\frac{t}{T_1}\right)^{\beta}\right) + I_0 \tag{9.2}$$

where β is a stretching factor that describes the deviation from a pure exponential decay. As seen from the smaller fit residuals in Fig. 9.3b, the relaxation of VOPyzPz-DIPP is better expressed by such a stretched exponential over the entire time interval, as compared to the relaxation of VOPc. Values of β are also closer to unity for VOPyzPz-DIPP at low temperatures (Fig. S12–S13), indicating that it follows a simpler decay process. This simpler decay is a desirable feature for implementing qubits into real devices as it improves their controllability.[10] For VOPc, we attempted biexponential fits that have been proposed to separate the slow spin-lattice relaxation from a fast spectral diffusion. Such fits (that omit β), however, gave even larger residuals. We therefore moved to collect measurements of T_1 by saturation recovery, particularly at low temperatures where relaxation is slower and more affected by spectral diffusion. As shown in Fig. S14, saturation recovery indeed measures slower spin-lattice relaxations. It captures, however, the same temperature dependence of T_1 as the inversion recovery measurements presented here. The spectral diffusion measurements, therefore, validate the time constants obtained from fitting VOPc T_1 data with stretched exponential functions, despite the larger residuals obtained.

Fig. 9.4a shows $1/T_1$ measured by inversion recovery at the powder line (344 mT) as a function of temperature. Our experiments reproduce the behavior of VOPc reported previously,[4] showing two different temperature regimes depicted by the dashed lines. This change in slope (plotted in Fig. 9.4b) indicates that different relaxation processes are active at these different temperature ranges. Other porphyrin-based qubits show an analogous temperature dependence with a change of slope around 40–60 K.[14] The behavior of VOPyzPz-DIPP is surprising, following a simple power law (solid green line) with no clear switch in the relaxation mechanism with temperature. Its spin-lattice relaxation time is faster than VOPc for most of the temperature range, reaching approximately the same values at room temperature. At 5 K, however, T_1 appears longer for VOPyzPz-DIPP, which is corroborated by the saturation recovery measurements (see Fig. S14). At temperatures above 5 K, vibrational modes become more populated. Adding the peripheral groups to the molecule raises the number of available modes, particularly of low-energy phonons that are more accessible at low temperatures. The partial amorphous nature of the lattice could also add low energy vibrations enhancing this effect further. This

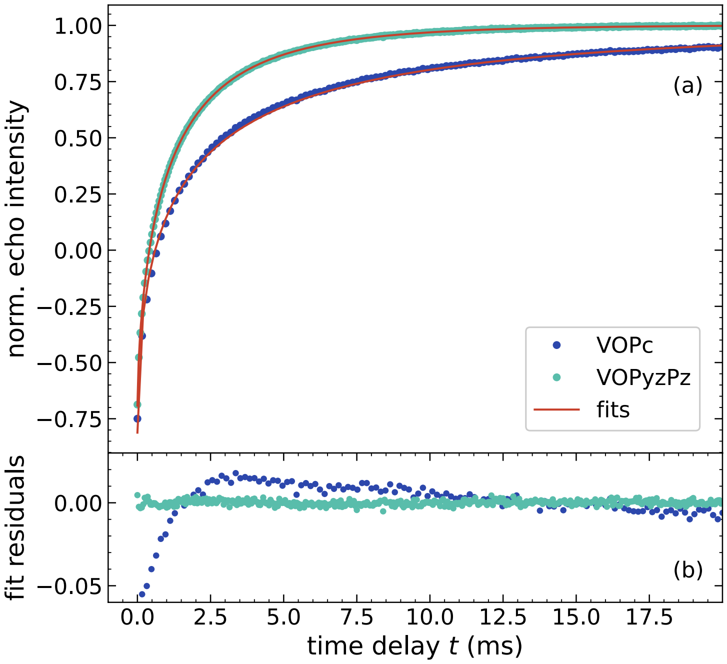

Figure 9.3: Spin lattice relaxation measured by inversion recovery at 10 K. (a) Normalized integrated echo intensity of VOPyzPz and VOPc (markers) with stretch exponential fits (solid lines). (b) Fitting residuals corresponding to fits of panel a.

enhanced phonon population could explain the steeper slope of T_1 of VOPyzPy-DIPP at low temperatures compared to VOPc.

Spin-lattice coupling reflects the dependency of electronic states on deformations of the lattice due to vibrations. This dependency follows different mechanisms for different phonon energies. At very low temperatures, the energy of the phonons is of the same magnitude as the Zeeman splitting, allowing a direct excitation or absorption of phonons by spins. The probability of such a relaxation scales linearly with temperature[18] and typically involves acoustic phonons with large wavelengths that cause minimal molecular distortions. At temperatures below 4 K, deviations from this linear behavior caused by phonon bottleneck effects have been reported for CuPc.[19]

When two phonons become involved in a Raman spin relaxation event, higher energy vibrational modes can participate, as only the difference in their energy must match the spin-flip transition energy. Starting from a second-order spin-phonon Hamiltonian, a two-phonon Green's function formalism predicts an exponential temperature dependence for such a two-phonon spin scattering ($\propto \exp(E_{loc}/k_B T)$).[20] Given the functional form, this process becomes particularly important at higher temperatures

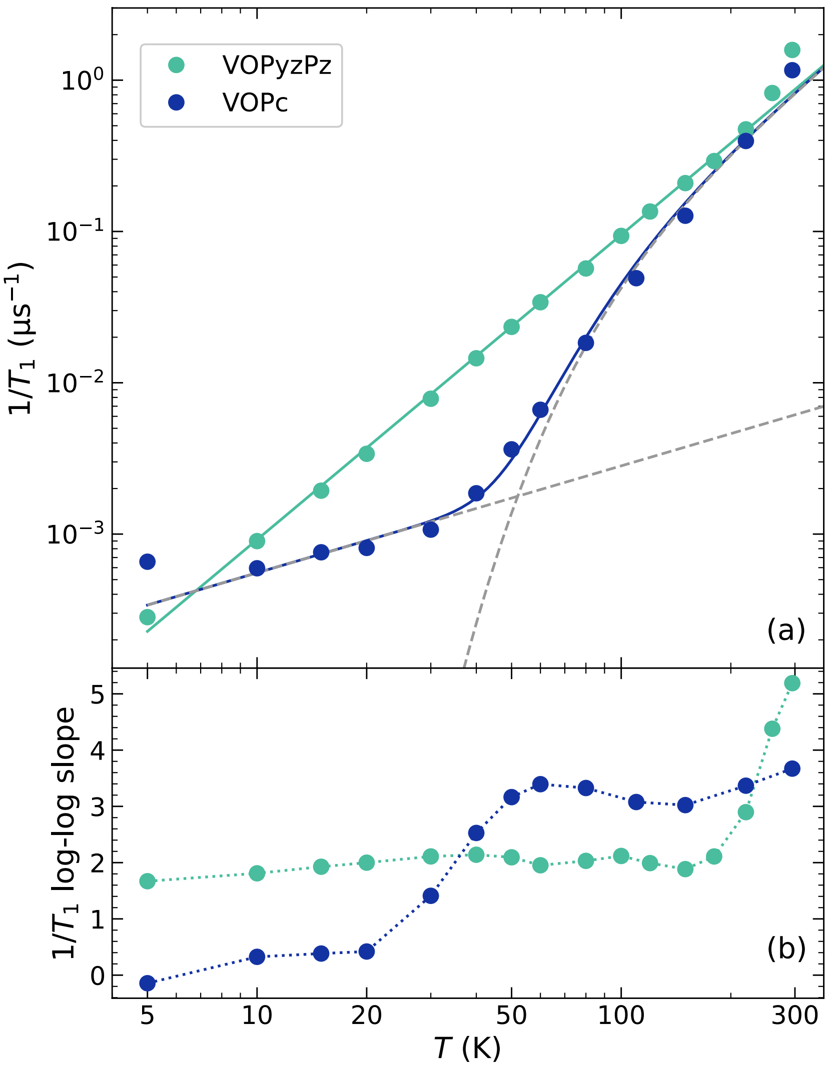

Figure 9.4: Spin-lattice relaxation of VOPyzPz-DIPP and VOPc as a function of temperature collected by inversion recovery at the powder line (344 mT). (a) Experimental $1/T_1$ data (markers) fitted by Eq. (9.4) as described in the text (solid lines). Dashed lines show individual contributions to the fit from a power law and local modes in VOPc. Fitting errors are smaller than the marker sizes. (b) Slope of $1/T_1$ computed in a log-log scale, revealing changes in the temperature dependence of T_1.

where optical phonon modes dominate. On the other hand, the low-energy (acoustic) phonon behavior of crystals is often described using a Debye model (where the phonon density of states follows a quadratic energy dependence up to a Debye temperature θ_D, at which all modes have become thermally accessible). Applying the Debye model to the same spin-phonon Hamiltonian gives a power-law temperature dependence for the spin relaxation ($\propto T^n$).[21] In the low-temperature limit (θ_D

$>> T$) an exponent of $n = 7$ is obtained (which has been a traditional assumption[18,22]), but n is usually smaller for molecular crystals, reaching a value of 2 in the high-temperature limit ($\theta_D << T$).[21] All contributions are summarized in Eq. (9.3):[4]

$$\frac{1}{T_1} = a_{dir}T + a_{1,Ram}\left(\frac{T}{\theta_D}\right)^n + a_{2,Ram}\frac{e^{E_{loc}/k_BT}}{(e^{E_{loc}/k_BT} - 1)^2} \tag{9.3}$$

$$\frac{1}{T_1} \approx aT^n + b\frac{e^{E_{loc}/k_BT}}{(e^{E_{loc}/k_BT} - 1)^2}. \tag{9.4}$$

Since the direct process is prevalent only near liquid helium temperatures, we avoid overfitting by combining the direct and Raman terms (Eq. (9.4)) as previously proposed.[14]

As shown in Fig. 9.4a, the relaxation of VOPc is well-fitted by Eq. (9.4). It follows power law behavior at low temperatures ($n = 0.7$, straight dashed line in Fig. 9.4a), while local modes around $E_{loc} = 233$ cm^{-1} dominate the relaxation above 50 K (in a previous study that included all terms of Eq. (9.3), the local mode energy was fitted to 295 cm^{-1}).[4] The data point at 5 K was not included in the fit, because it deviates from the T_1 behavior measured by saturation recovery (see Fig. S13). However, fits to the saturation recovery measurements that include data at 5 K result in a similar exponent of $n = 0.6$. Such a low power law exponent suggests that relaxation involving two phonons is limited and that the direct mechanism dominates at these temperatures. The energy of the local mode that controls the high-temperature behavior falls within the energy range of totally-symmetric modes containing metal-ligand bond-stretching character, which is consistent with our previous ligand field model for VOPc.[6] The behavior of VOPc is hence dictated by strong coupled optical modes around 233 cm^{-1} at elevated temperatures (> 50 K), while two-phonon processes are inefficient below 40 K, resulting in a spin-lattice relaxation that increases only weakly with temperature.

The relaxation of VOPyzPz-DIPP follows a single power law behavior from 5 K up to room temperature with $n = 2.0$. There is no single mode that dominates any part of the spectrum, but rather an unresolved collection of acoustic and optical phonon modes. VOPyzPz-DIPP reaches the same value of T_1 as VOPc, however, suggesting that a local mode at similar energies may play an important role at room temperature. Interestingly, a power-law exponent of 2 is predicted in the high-temperature limit of a Debye model ($\theta_D << T$).[21] This implies that VOPyzPz-DIPP has a low Debye temperature where vibrational modes that contribute to a Raman relaxation are populated already at low temperatures. We note that a Debye model is not required to reach this result. By assuming that the phonon modes are well populated, $E_{ph} << T$, the exponential local mode expression (last term in Eq. (9.4)) can be expanded into a Taylor series with a leading term that also scales as T^2. This can be visualized in Fig. 9.4a where the exponential term (blue curve) reaches the same asymptote as the power law fit with $n = 2$ (green curve) beyond room temperature. Notably for VOPyzPz-DIPP, this high-temperature limit extends down to low temperatures, indicating that low-energy phonons are essential to its relaxation. As discussed above, VOPyzPz-DIPP is indeed expected to have more of such low-energy modes than VOPc. Additionally, the peripheral groups of VOPyzPz-DIPP break the planar symmetry of the ligand, which according to our ligand-field model,[6,12,13] could loosen the selection rules and allow additional modes to couple more efficiently with spins. Thus, an abundance of low-energy phonons and additional coupling pathways would explain the T_1 behavior of VOPyzPz-DIPP.

Further experiments to measure the phonon spectrum are necessary to confirm these results. Due to their accessibility via Raman, IR, and THz spectroscopy, high-energy optical mode contributions to spin relaxation are currently best understood. For many molecular qubit candidates, including VOPc, specific optical modes couple strongest with spins and play the dominant role in spin relaxation. We demonstrated here that understanding the low-energy phonon behavior can also be important, particularly when studying the low-temperature behavior and structural dependencies of spin relaxation mechanisms. This contribution calls for experimental techniques such as inelastic neutron and X-ray scattering that can transfer momentum to the material and excite all phonon modes. To date, only two such studies have been published. They show how low-lying optical modes are critical for spin relaxation,[23] and that phonon modes themselves can be coupled, which transfers the strong spin-lattice coupling from optical to highly populated acoustic modes.[24]

9.5 Conclusions

Using pulse EPR techniques, we compared the spin-lattice relaxation behaviors of VOPyzPz-DIPP and VOPc. At 5 K, VOPyzPz-DIPP appears to have a slower T_1 than VOPc. Both follow a power law temperature dependence at low temperatures, but VOPyzPz-DIPP has an exponent that is 2.8 times larger than VOPc. This difference suggests that VOPyzPz-DIPP has more low-energy phonon modes that are available for spin-lattice relaxation, resulting in shorter spin-lattice relaxation beyond 10 K. In contrast to VOPc, where T_1 has two temperature regimes with distinct decay mechanisms, the T_1 behavior VOPyzPz-DIPP is governed by the same power law up to room temperature. A picture where a single local phonon mode dominates the spin-phonon coupling at elevated temperatures, therefore, cannot explain the T_1 behavior of VOPyzPz-DIPP. For VOPyzPz-DIPP, spin relaxation is likely the result of coupling with several acoustic and optical modes that may become available due to symmetry breaking, as well as additional phonon modes from the peripheral groups and structural disorder. This abundance of phonon modes available for spin-lattice coupling would also explain the differences in T_1 anisotropy for the two compounds (VOPyzPz-DIPP = 2.2 and VOPc = 6.0).

References

[1] Atzori, M.; Sessoli, R. The Second Quantum Revolution: Role and Challenges of Molecular Chemistry. *Journal of the American Chemical Society* **2019**, *141,* 11339–11352.

[2] DiVincenzo, D. P. The Physical Implementation of Quantum Computation. *Fortschritte der Physik* **2000**, *48,* 771–783.

[3] Atzori, M.; Tesi, L.; Morra, E.; Chiesa, M.; Sorace, L.; Sessoli, R. Room-Temperature Quantum Coherence and Rabi Oscillations in Vanadyl Phthalocyanine: Toward Multifunctional Molecular Spin Qubits. *Journal of the American Chemical Society* **2016**, *138,* 2154–2157.

[4] Follmer, A. H.; Ribson, R. D.; Oyala, P. H.; Chen, G. Y.; Hadt, R. G. Understanding Covalent versus Spin-Orbit Coupling Contributions to Temperature-Dependent Electron Spin Relaxation in Cupric and Vanadyl Phthalocyanines. *The Journal of Physical Chemistry A* **2020**, *124,* 9252–9260.

[5] Kazmierczak, N. P.; Hadt, R. G. Illuminating Ligand Field Contributions to Molecular Qubit Spin Relaxation via T_1 Anisotropy. *Journal of the American Chemical Society* **2022**, *144,* 20804–20814.

[6] Kazmierczak, N. P.; Mirzoyan, R.; Hadt, R. G. The Impact of Ligand Field Symmetry on Molecular Qubit Coherence. *Journal of the American Chemical Society* **2021**, *143,* 17305–17315.

[7] Warner, M.; Din, S.; Tupitsyn, I. S.; Morley, G. W.; Stoneham, A. M.; Gardener, J. A.; Wu, Z.; Fisher, A. J.; Heutz, S.; Kay, C. W. M.; Aeppli, G. Potential for Spin-Based Information Processing in a Thin-Film Molecular Semiconductor. *Nature* **2013**, *503,* 504–508.

[8] Bonizzoni, C.; Ghirri, A.; Atzori, M.; Sorace, L.; Sessoli, R.; Affronte, M. Coherent Coupling between Vanadyl Phthalocyanine Spin Ensemble and Microwave Photons: Towards Integration of Molecular Spin Qubits into Quantum Circuits. *Scientific Reports* **2017**, *7,* 13096.

[9] Cimatti, I.; Bondì, L.; Serrano, G.; Malavolti, L.; Cortigiani, B.; Velez-Fort, E.; Betto, D.; Ouerghi, A.; B. Brookes, N.; Loth, S.; Mannini, M.; Totti, F.; Sessoli, R. Vanadyl Phthalocyanines on Graphene/SiC(0001): Toward a Hybrid Architecture for Molecular Spin Qubits. *Nanoscale Horizons* **2019**, *4,* 1202–1210.

[10] Bader, K.; Winkler, M.; van Slageren, J. Tuning of Molecular Qubits: Very Long Coherence and Spin-Lattice Relaxation Times. *Chemical Communications* **2016**, *52,* 3623–3626.

[11] Zadrozny, J. M.; Niklas, J.; Poluektov, O. G.; Freedman, D. E. Multiple Quantum Coherences from Hyperfine Transitions in a Vanadium(IV) Complex. *Journal of the American Chemical Society* **2014**, *136,* 15841–15844.

[12] Mirzoyan, R.; Kazmierczak, N. P.; Hadt, R. G. Deconvolving Contributions to Decoherence in Molecular Electron Spin Qubits: A Dynamic Ligand Field Approach. *Chemistry – A European Journal* **2021**, *27,* 9482–9494.

[13] Mirzoyan, R.; Hadt, R. G. The Dynamic Ligand Field of a Molecular Qubit: Decoherence through Spin-Phonon Coupling. *Physical Chemistry Chemical Physics* **2020**, *22,* 11249–11265.

[14] Kazmierczak, N. P.; Lopez, N. E.; Luedecke, K. M.; Hadt, R. G. Determining the Key Vibrations for Spin Relaxation in Ruffled Cu(II) Porphyrins via Resonance Raman Spectroscopy. *Chemical Science* **2024**, *15,* 2380–2390.

[15] Marx, B.; Schrage, B. R.; Ziegler, C. J.; Nemykin, V. N. Synthesis, Spectroscopic, and Electronic Properties of New Tetrapyrazinoporphyrazines with Eight Peripheral 2,6-diisopropylphenol Groups. *Journal of Porphyrins and Phthalocyanines* **2023**, *27,* 363–372.

[16] Stoll, S.; Schweiger, A. EasySpin, a Comprehensive Software Package for Spectral Simulation and Analysis in EPR. *Journal of Magnetic Resonance* **2006**, *178,* 42–55.

[17] Eaton, S. S.; Eaton, G. R. Relaxation Mechanisms. In *eMagRes*; Wiley: 2016.

[18] Standley, K. J.; Vaughan, R. A. *Electron Spin Relaxation Phenomena in Solids;* Springer US: Boston, MA, 1969. DOI: 10.1007/978-1-4899-6539-4.

[19] Standley, K. J.; Wright, J. K. Spin-Lattice Relaxation in Two Organic Copper Complexes. *Proceedings of the Physical Society* **1964**, *83,* 361–367.

[20] Gu, L.; Wu, R. Origins of Slow Magnetic Relaxation in Single-Molecule Magnets. *Physical Review Letters* **2020**, *125,* 117203.

[21] Gu, L.; Wu, R. Origin of the Anomalously Low Raman Exponents in Single Molecule Magnets. *Physical Review B* **2021**, *103,* 014401.

[22] Shrivastava, K. N. Theory of Spin–Lattice Relaxation. *physica status solidi (b)* **1983**, *117,* 437–458.

[23] Garlatti, E.; Albino, A.; Chicco, S.; Nguyen, V. H. A.; Santanni, F.; Paolasini, L.; Mazzoli, C.; Caciuffo, R.; Totti, F.; Santini, P.; Sessoli, R.; Lunghi, A.; Carretta, S. The Critical Role of Ultra-Low-Energy Vibrations in the Relaxation Dynamics of Molecular Qubits. *Nature Communications* **2023**, *14,* 1653.

[24] Garlatti, E.; Tesi, L.; Lunghi, A.; Atzori, M.; Voneshen, D. J.; Santini, P.; Sanvito, S.; Guidi, T.; Sessoli, R.; Carretta, S. Unveiling Phonons in a Molecular Qubit with Four-Dimensional Inelastic Neutron Scattering and Density Functional Theory. *Nature Communications* **2020**, *11,* 1751.

Chapter 10

ULTRAFAST, ALL-OPTICAL COHERENCE OF MOLECULAR ELECTRON SPINS IN ROOM-TEMPERATURE AQUEOUS SOLUTION

- Adapted with permission from: Sutcliffe, E.; Kazmierczak, N. P.; Hadt, R. G. Ultrafast All-Optical Coherence of Molecular Electron Spins in Room-Temperature Water Solution. *Science* **2024**, *386*, 888–892. DOI: 10.1126/science.ads0512. © 2024 The American Association for the Advancement of Science.

10.1 Abstract

The tunability and spatial precision of paramagnetic molecules makes them attractive for quantum sensing. However, usual microwave-based detection methods have poor temporal and spatial resolution, and optical methods compatible with room-temperature solutions have remained elusive. Here, we utilized pump-probe polarization spectroscopy to initialize and track electron spin coherence in a molecule. Designed to efficiently couple spins to light, aqueous K_2IrCl_6 enabled detection of few-picosecond free induction decay at room temperature and micromolar concentrations. Viscosity was found to strongly vary decoherence lifetimes. This approach has improved the experimental time-resolution by up to five orders of magnitude, making it possible to observe molecular electron spin coherence in a system that only exhibits coherence below 25 K with traditional techniques.

10.2 Introduction

Molecular quantum bits (qubits) are highly tunable and spatially precise, making them desirable for quantum sensing applications.[1] By using molecules with unpaired electron spins, coherent superposition states may be generated between the Zeeman spin sublevels, enabling sensing through distinctly quantum degrees of freedom.[2] Yet to compete with existing techniques of biological imaging, spin-based quantum sensing must stand up to two key requirements. First, the spin system must display room-temperature coherence in the solution phase—the domain of dynamic biological processes. Second, the system should allow all-optical detection of the spin dynamics to enable precise microscopy. Anionic nitrogen vacancies in diamond (NV^-) satisfy both requirements, enabling impressive applications such as single-atom nuclear magnetic resonance (NMR),[3] mapping intracellular molecular dynamics,[4] strain sensing in nanoscale devices,[5] and imaging magnetic fields in live magnetotactic bacteria.[6] However, NV^- centers contain an intrinsic spatial constraint of several nanometers owing to the bulk of the lattice; they also have limited chemical tunability. Satisfying both sensing requirements in a molecular system would open a new realm of quantum sensing at the sub-nanometer scale.

Achieving simultaneous room-temperature coherence and all-optical addressability in a molecular qubit system provides significant challenges due to the intrinsic constraints of pulse electron paramagnetic resonance (EPR) and optically detected magnetic resonance (ODMR). These are the two leading spectroscopic techniques for measurements of the electron spin decoherence time of an initialized quantum state, referred to as the spin-spin relaxation time (T_2). Both pulse EPR and ODMR require electrical gating of microwave and optical pulses, precluding sub-nanosecond time resolution and thereby placing a significant constraint on which systems can be considered room-temperature coherent. In pulse EPR, short microwave pulses are applied on resonance with transitions between Zeeman-split M_S sublevels (Fig. 10.1A, left). A select few compounds show measurable T_2 at room temperature, including Cu(II) and V(IV)O compounds such as vanadyl phthalocyanine (VOPc).[7] However, the long wavelength of microwaves limits EPR imaging to a spatial resolution of hundreds of micrometers. ODMR protocols have been described for measuring T_1 all-optically,[8] though coherent state manipulation and measurement of T_2 still must use microwave pulses. Detection of an ODMR signal requires distinctive molecular design principles for spin-selective luminescence. Through mimicking the electronic structure and emission-based detection of the diamond NV^- center, S = 1 optically addressable qubits based on Cr(IV) have demonstrated optical spin addressability using ODMR[8] (Fig. 10.1A, center). Yet S = 1 qubit candidates based on Cr(IV), V(III), or Ni(II) have displayed deleteriously fast spin relaxation rates, with coherence undetectable by EPR above 60 K even in the best cases.[8–11] Coherence can still be initialized above 60 K, but the spins decohere faster than can be measured. Excited-state spin coherence at room temperature has been reported for organic radical systems using ODMR, but the excited state nature places further constraints on time resolution.[12–14] Thus, sub-nanosecond measurements of T_2 have the potential to unveil a new paradigm for molecular qubits displaying room-temperature coherence.

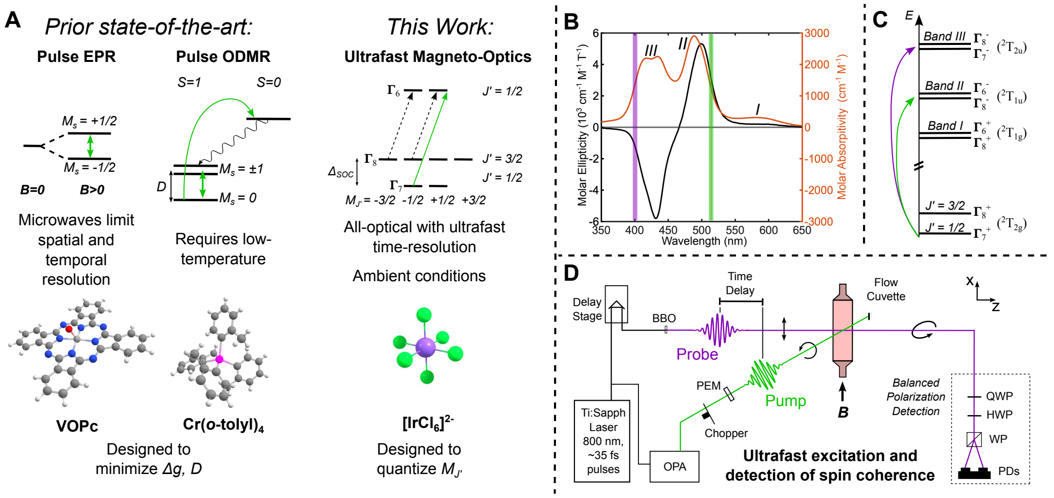

Figure 10.1: Methods for detecting spin coherence. (A) Methods and limitations of spectroscopic techniques for probing electron spin coherence, with characteristic molecules and molecular design criteria. (B) MCD and electronic absorption spectra of K_2IrCl_6 dissolved in H_2O with peaks labelled and pump/probe wavelengths highlighted. (C) Electronic structure of $[IrCl_6]^{2-}$. (D) Schematic of the setup used to measure ultrafast spin coherence. The angle between pump and probe pulses is exaggerated for clarity. Abbreviations, and the setup in full, are described in the Supplementary Materials.

Here, we demonstrated picosecond all-optical detection of electron spin coherence in a rationally-designed molecule. Central to our approach is the co-design of ultrafast magneto-optical instrumentation and molecular electronic structure. The decoherence rate could be measured robustly at room temperature in aqueous conditions and at low concentration. Proof-of-concept T_2 sensing of solvent viscosity is presented. Comparison to pulse EPR measurements showed that the magneto-optical instrumentation could access molecular spin coherence at orders-of-magnitude faster timescales and higher temperatures.

10.3 Design Criteria for All-Optical Molecular Qubits

The spatial and temporal limits of EPR have been successfully overcome in the semiconductor physics community through the use of ultrafast laser pulses.[15–17] At the Γ point of a cubic semiconductor, the sublevel scheme shown in Fig. 10.1A, right, is found.[18] Here, the spin of the electron couples to a threefold orbitally degenerate state (i.e., one with in-state orbital angular momentum, OAM) at the valence band edge, which splits the state into two levels by an amount, Δ_{SOC}, proportional to the magnitude of spin-orbit coupling (SOC). The split states, of symmetry Γ_7 and Γ_8, have different total effective angular momentum J', and when their sublevels are eigenstates of M'_J, circularly polarized light changes the spin state with complete efficiency.[19,20] Therefore, selective excitation of either $\Gamma_7 \rightarrow \Gamma_6$ or $\Gamma_8 \rightarrow \Gamma_6$ with circularly polarized light generates a net spin polarization. With a circularly polarized "pump" pulse to initialize the state, the spin coherence is subsequently detected through the change in optical polarization,[15–17] or even intensity,[19,21] of a weaker "probe" pulse. Application of a perpendicular magnetic field causes characteristic Larmor precession of the spin polarization. Such transient magneto-optic methods have temporal resolution of $< 10^{-13}$ s, broad spectral sensitivity[22–24] and can be utilized for microscopy with sub-micron spatial resolution.[25,26] Despite these clear advantages, whether this technique can be applied effectively to molecular qubits has been an open question.

Molecular systems present two key obstacles to efficient magneto-optical detection. First, unlike cubic semiconductor systems, J' is not a good quantum number in most paramagnetic molecules. In transition metal complexes, this effect arises from quenching of OAM via the ligand field.[27] When the sublevels are not quantized by M'_J, circularly polarized light instead has only a weak probability to alter the spin state through electric dipole transitions, relying on perturbative out-of-state SOC. Second, the individual J' states must be selectively addressable. Although direct-gap semiconductors have narrow excitonic transitions that make addressing only one J' state straightforward, most molecular systems possess much broader electronic transition linewidths. Both challenges may be solved by choosing a high symmetry transition metal complex with a threefold orbitally degenerate groundstate, which maximizes the OAM available to couple to the spin. Octahedral and tetrahedral complexes can produce such ground states according to the Tanabe-Sugano diagrams.[27] If the SOC is large enough such that $\Delta_{SOC} >> k_B T$, then the thermally populated ground states will have well-defined J', enabling selective addressability. Because M'_J is a good quantum number, circular polarization electric dipole selection rules will be exactly obeyed. Magnetic circular dichroism (MCD) arises from similar microscopic means,[28] so we expect that suitable candidates also exhibit large MCD signals at the relevant transitions. These criteria contrast with conventional wisdom for the development of molecular qubits exhibiting coherence at elevated temperatures, where one instead seeks to minimize OAM and in turn minimize the orbital contribution to the g value,[22] Δg, and the zero-field splitting,[29] D (Fig. 10.1A, bottom).

To the best of our knowledge, time-resolved magneto-optical measurements of this kind have so far only been applied to one molecular system: aqueous $CuSO_4$.[30] However, the electronic ground state of D_{4h} Cu(II) ions is orbitally nondegenerate, which does not satisfy the requirements for the efficient in-state SOC described above. Therefore, the initialization and readout rely on the much weaker perturbative mixing of excited states into the ground state through out-of-state SOC. Because of this fact, optical detection of decoherence required prohibitively high Cu(II) concentrations (~1 M) and pulse energies (~10 μJ per pulse). As a consequence, comparatively large nonlinear artifacts such as the optical Kerr effect (OKE) limited the temporal resolution to $\sim 10^{-10}$ s.

A system satisfying all of these criteria is K_2IrCl_6, an air- and water-stable S=½ complex. Its electronic absorption and MCD spectra exhibit three strong bands in the visible (Fig. 10.1B). Extensive prior spectroscopic characterization on this compound revealed the electronic structure shown in Fig. 10.1C.[31–33] Because the unpaired electron principally resides on the Ir(IV) center,[34,35] Δ_{SOC} is ~5000 cm^{-1},[36] giving the ground state Γ_7^+ symmetry and J' =½ at room temperature. The three bands seen in the spectra correspond to ligand-to-metal charge transfers. Because these result in the electron spin on the ligands, the excited state Δ_{SOC} is much smaller and, therefore, unresolvable, though this has minimal impact on spin initialization. The large MCD signal (Fig. 10.1B) for the parity-allowed bands II and III further suggests these are ideal candidates to use for initialization and readout.

10.4 Ultrafast Detection of Free Induction Decay

To measure electron decoherence, we used the setup shown in Fig. 10.1D, which is described fully in the Supplementary Materials. Spin polarization was initialized along z by a 512 nm, circularly-polarized pump pulse. An almost-collinear, 400 nm probe pulse recorded the spin polarization along z for a given time-delay as a change in Faraday ellipticity, detected using bridged photodiodes. The sample was flowed to minimize photodegradation and, using a room-temperature-bore superconducting magnet, a field of up to 5 T could be applied along x to induce Larmor precession. A photoelastic modulator (PEM) was used to circularly polarize the 1 μJ pump pulses. The source laser was triggered at 1.014 kHz off of the 50.176 kHz oscillation frequency of the PEM to ensure every consecutive pump pulse had orthogonal polarization;[37] right- and left-handed circularly polarized pump pulses initialized the spin polarization in opposing directions along z. The coherence here was

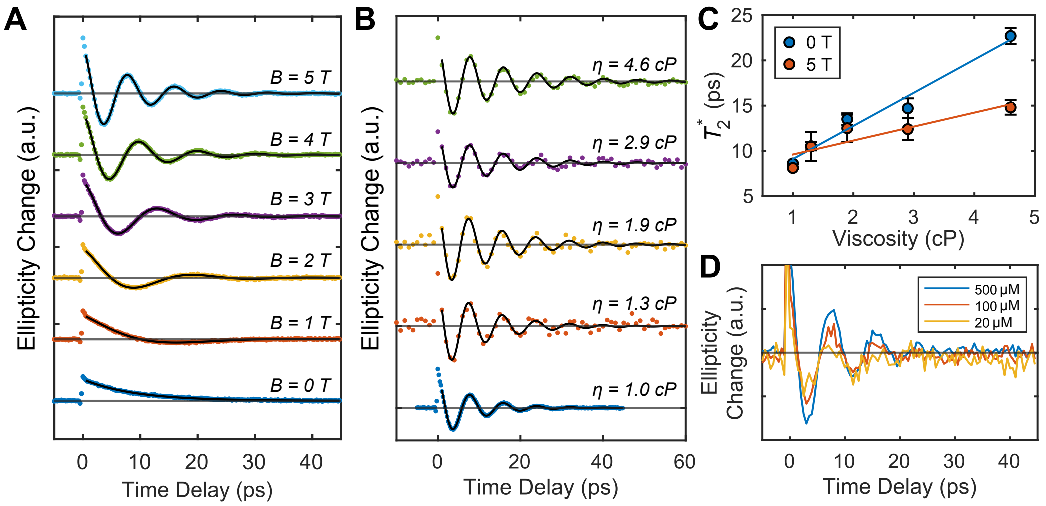

Figure 10.2: Ultrafast free induction decay at room temperature. (A) TRFE measurements on K_2IrCl_6 dissolved in H_2O at various field strengths with fits to Eq. (10.1) shown in black. (B) In water:glycerol mixtures to modify viscosity at 5 T with fits to Eq. (10.1) shown in black. (C) Viscosity dependence of T_2^* measured at 0 T and 5 T alongside 68% error bounds and corresponding linear fits. (D) Concentration sensitivity in H_2O at 5 T. OKE spike at time-zero omitted to best show free-induction decay.

generated between the $M'_J = \pm½$ sublevels of the Γ_7^+ ground state. Detection at the frequency of pump intensity and polarization modulation thus gave only the change in probe polarization that was pump-dependent and odd with respect to the initialized polarization. This setup had the effect of greatly reducing potential OKE artifacts and other photophysics unrelated to spin dynamics in solution phase measurements. Varying the time-delay between pump and probe yielded the time-resolved Faraday ellipticity, TRFE.

Characteristic damped oscillations of free induction decay were observed in the TRFE data for a 2 mM solution of K_2IrCl_6 in H_2O (Fig. 10.2A). This decay corresponded to the dephasing of electron spins; it also included any potential effect of field inhomogeneities on dephasing, so it was termed T_2^*, as is commonplace in NMR. The TRFE traces were fit to

$$\eta(t) = \eta_0 \exp\left(-\frac{t}{T_2^*}\right) \cos\left(\omega_L t + \phi\right) \tag{10.1}$$

where η_0, T_2^*, and ϕ were free parameters; the Larmor frequency, $\omega_L = g_{iso}\mu_B B/\hbar$, provided an isotropic g value, $g_{iso} = 1.74$, with magnetic field strengths, $B = 0$ –

5 T. These fits are shown as black lines in Fig. 10.2A and yielded an almost exact description of the data beyond 0.5 ps. These data unambiguously demonstrated the observation of ultrafast free induction decay of the molecular Ir(IV)-based electron spins. At 0 T in H_2O, T_2^* was 8.60 ps and spanned 9.27 to 8.14 ps across the range of field strengths (fig. S2, table S1).

Pumping band II and probing the higher energy band III reduced the potential impact of excited-state electronic relaxation on the observed T_2^*. Transient absorption spectroscopy was used to verify that T_2^* was not merely determined by excited-state electronic relaxation (figs. S8–11). K_2IrCl_6 in H_2O exhibited an excited-state lifetime of 17 ps at 0 T, almost double T_2^*. Additionally, in DMSO, the excited-state lifetime was 430 ps, yet T_2^* was 17.6 ps (figs. S3,9). Together with the good monoexponential fit, these data suggest the excited-state population played a minimal role in the measured T_2^*.

One further, albeit subtle, advantage of this technique over pulse EPR is that the applied magnetic field could be varied continuously across an arbitrarily large range and even eliminated without impacting our ability to measure T_2^*. This fact made studying the field dependence of T_2^* relatively straightforward, where we observed an overall decrease in T_2^* with $|B|$ (fig. S2), likely due to the inhomogeneous g values in the bulk system.[38] This behavior was mirrored across solvents, with T_2^* in DMSO exhibiting a much stronger field dependence than in H_2O (fig. S3). The phases of the oscillations showed a roughly B^3 dependence, likely due to the optomagnetic field of the pump pulse (Supplementary Text).

10.5 Sensing Viscosity with T_2^*

On the picosecond timescale at room temperature, dephasing is expected to involve molecular tumbling contributions.[39] To test this, 0 and 5 T TRFE traces were recorded for water:glycerol solutions (up to 40% glycerol), which systematically varied the viscosity. At 5 T, T_2^* increased significantly with increasing solution viscosity (Fig. 10.2B). An increasing trend in T_2^* vs. viscosity was observed for both the 0 T and 5 T cases (Fig. 10.2C). At 5 T, the trend was complicated by the oscillations and inhomogeneities in g value. However, for 0 T, T_2^* varied linearly with viscosity and more than doubled in magnitude (8.60 and 21.9 ps in neat H_2O and 3:2 water:glycerol, respectively). Because the molecular tumbling time is also proportional to viscosity,[40] such a trend was consistent with this dephasing mechanistic hypothesis. These observations suggest that complex immobilization in biological macromolecules should significantly prolong coherence times. Hyperfine coupling to solvent molecules could also contribute to dephasing along with molecular tumbling; indeed, dissolving the Ir(IV) complex in D_2O instead of H_2O increased T_2^* from 8.60 to 10.1 ps at 0 T (fig. S5 and table S1). Future studies of the temperature dependence of T_2^* might additionally elucidate spin-vibrational coupling contributions to decoherence.[41]

For quantum sensing applications, sensitive detection is vital, and the high sensitivity of EPR is a key reason for its widespread applicability. Oscillations at 5 T in H_2O could still be observed upon reducing the concentration 100-fold to 20 μM (and using 2 μJ pump pulses, Fig. 10.2D), a similar detection limit to EPR.[42]

10.6 Comparison with EPR

Pulse EPR currently constitutes the standard method for measuring electron spin coherence lifetimes. We compared the TRFE measurement to the information obtainable from pulse EPR on the same complex (Fig. 10.1). $[IrCl_6]^{2-}$ is an S=½ species with a broad, isotropic continuous wave (CW) EPR signal centered at g = 1.807 in a frozen solvent glass (Fig. 10.3A). The 0.07 discrepancy between the g values from CW-EPR and TRFE is likely due to the phase transition and wide temperature difference between the measurements. Q-band pulse EPR inversion recovery and Hahn-echo decay measurements were conducted to obtain T_1 and T_m, respectively. T_m denotes the phase-memory time when applying a single refocusing π pulse for echo detection, and constitutes a common approximation to T_2 measured by EPR. Strong echo signals leading to precise time constant determination were observed over a 5 - 15 K temperature range. However, the echo intensity at 20 K became weak owing to fast spin relaxation, leading to degraded signal-to-noise in the inversion recovery trace (Fig. 10.3B). The polarization inversion observed at short time was reduced by 50% relative to the 5 K measurement, indicating a substantial amount of the polarization relaxed during the spectrometer deadtime; this process constituted a ≥120 ns period after the refocusing pulse during which the spin echo could not be measured. Due to the deadtime constraint and the minimum pulse timing increment of 2 ns, we estimated the EPR limit of detection for T_1 and T_m to be on the order of 100 ns. T_1 and T_m could not be reliably ascertained by pulse EPR above 20 K.

The fitted T_1 values varied strongly as a function of temperature due to thermal population of vibrational modes that coupled to the spin (Fig. 10.3C). By contrast,

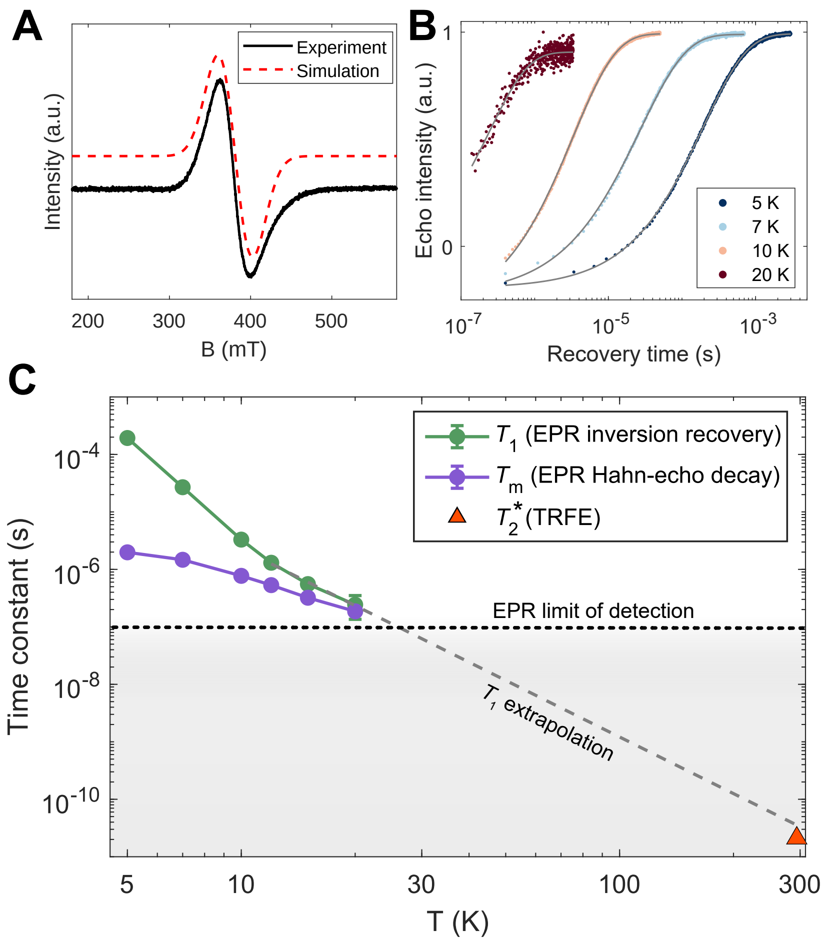

Figure 10.3: Comparison between EPR and TRFE capabilities. (A) X-band CW-EPR spectrum of 2 mM K_2IrCl_6 in a 3:2 water:glycerol glass at 15 K (ν = 9.637 GHz). Simulated trace with isotropic g = 1.807. (B) Q-band pulse EPR inversion recovery traces collected at the maximum microwave echo intensity (1318 mT, ν = 34.110 GHz). (C) Comparison between T_1/T_m from pulse EPR and the TRFE measurement; error bars are mostly smaller than data points. Extrapolation line produced from a linear fit to T_1 between 12 and 20 K.

T_m displays a weaker scaling with temperature below 10 K, which became stronger above 10 K as T_1 approached T_m. This difference arose because the maximum value of T_m (the transverse relaxation) was limited by T_1 (the longitudinal relaxation), as longitudinal recovery of equilibrium spin polarization necessarily removed magnetization from the transverse plane of the Bloch sphere. Thus, T_1 constituted the fundamental limitation on the observation of high-temperature spin coherence.[39] We extrapolated T_1 beyond the EPR limit of detection for comparison to the TRFE measurements. We found that T_2^* at room temperature and 1.3 T agreed well with the extrapolated prediction for T_1-limited-T_2 (Fig. 10.3C). This extrapolation should be taken loosely, as it cannot account for the change in relaxation dynamics induced by melting of the water:glycerol glass. However, it suggests overall consistency between the time constants measured by pulse EPR and those measured by TRFE.

In summary, the TRFE magneto-optical approach has detected a spin coherence lifetime that was four orders of magnitude smaller than the pulse EPR limit of detection (8 ps vs. ~100 ns). This result extended the temperature range of coherence detection by a factor of 15 for K_2IrCl_6, from 20 K to 294 K (Fig. 10.3C). These results demonstrated that TRFE has already accessed a new regime of ultrafast molecular spin dynamics.

10.7 Discussion

The present work has enabled room-temperature, all-optical quantum sensing by significantly improving the experimental time-resolution of molecular electron spin coherence measurements. The literature of microwave-addressable qubits has classified compounds as room-temperature coherent or not based on whether they possess spin echo lifetimes beyond the 100 ns limit of detection of pulse EPR, and ligand field design strategies have been described to enable this functionality.[43,44] Yet under the ~1 ps limit of detection of the TRFE measurement, molecules not formerly considered "room-temperature coherent" in pulse EPR can now become room-temperature coherent, as exemplified by K_2IrCl_6. The fast spin relaxation of K_2IrCl_6 can thus be tolerated in order to reap the benefits of J' quantization for polarized optical spectroscopy.

Furthermore, the TRFE scheme transforms "microwave-addressable qubits" into "optically-addressable qubits" by imparting an optical spin interface to molecules with an isolated doublet ground state ($J' = ½$). This feature eliminates the requirement to match the non-Kramers NV^- electronic structure for optical addressability. Freed from strict imitation, synthetic efforts in molecular quantum information science may now focus on different design criteria, including air-/water-/photo-stability, biological compatibility, and maximized ellipticity signal produced through in-state OAM. K_2IrCl_6 constitutes the first example following many of these criteria, but we anticipate that further synthetic efforts contain great potential to optimize TRFE molecular quantum sensor design. Additionally, the TRFE instrumentation is amenable to microscopy implementations with improved spatial precision over EPR imaging. The co-design of magneto-optical instrumentation and molecular sensors constitutes an exciting new path forward for quantum information science.

References

[1] Yu, C.-J.; von Kugelgen, S.; Laorenza, D. W.; Freedman, D. E. A Molecular Approach to Quantum Sensing. *ACS Central Science* **2021**, *7,* 712–723.

[2] Degen, C. L.; Reinhard, F.; Cappellaro, P. Quantum sensing. *Reviews of Modern Physics* **2017**, *89,* 035002.

[3] Abobeih, M. H.; Randall, J.; Bradley, C. E.; Bartling, H. P.; Bakker, M. A.; Degen, M. J.; Markham, M.; Twitchen, D. J.; Taminiau, T. H. Atomic-Scale Imaging of a 27-Nuclear-Spin Cluster Using a Quantum Sensor. *Nature* **2019**, *576,* 411–415.

[4] McGuinness, L. P.; Yan, Y.; Stacey, A.; Simpson, D. A.; Hall, L. T.; Maclaurin, D.; Prawer, S.; Mulvaney, P.; Wrachtrup, J.; Caruso, F.; Scholten, R. E.; Hollenberg, L. C. L. Quantum Measurement and Orientation Tracking of Fluorescent Nanodiamonds Inside Living Cells. *Nature Nanotechnology* **2011**, *6,* 358–363.

[5] Knauer, S.; Hadden, J. P.; Rarity, J. G. In-Situ Measurements of Fabrication Induced Strain in Diamond Photonic-Structures Using Intrinsic Colour Centres. *npj Quantum Information* **2020**, *6,* 1–6.

[6] Le Sage, D.; Arai, K.; Glenn, D. R.; DeVience, S. J.; Pham, L. M.; Rahn-Lee, L.; Lukin, M. D.; Yacoby, A.; Komeili, A.; Walsworth, R. L. Optical Magnetic Imaging of Living Cells. *Nature* **2013**, *496,* 486–489.

[7] Atzori, M.; Tesi, L.; Morra, E.; Chiesa, M.; Sorace, L.; Sessoli, R. Room-Temperature Quantum Coherence and Rabi Oscillations in Vanadyl Phthalocyanine: Toward Multifunctional Molecular Spin Qubits. *Journal of the American Chemical Society* **2016**, *138,* 2154–2157.

[8] Bayliss, S. L.; Laorenza, D. W.; Mintun, P. J.; Kovos, B. D.; Freedman, D. E.; Awschalom, D. D. Optically Addressable Molecular Spins for Quantum Information Processing. *Science* **2020**, *370,* 1309–1312.

[9] Fataftah, M. S.; Bayliss, S. L.; Laorenza, D. W.; Wang, X.; Phelan, B. T.; Wilson, C. B.; Mintun, P. J.; Kovos, B. D.; Wasielewski, M. R.; Han, S.; Sherwin, M. S.; Awschalom, D. D.; Freedman, D. E. Trigonal Bipyramidal V^{3+} Complex as an Optically Addressable Molecular Qubit Candidate. *Journal of the American Chemical Society* **2020**, *142,* 20400–20408.

[10] Wojnar, M. K.; Laorenza, D. W.; Schaller, R. D.; Freedman, D. E. Nickel(II) Metal Complexes as Optically Addressable Qubit Candidates. *Journal of the American Chemical Society* **2020**, *142,* 14826–14830.

[11] Kazmierczak, N. P.; Luedecke, K. M.; Gallmeier, E. T.; Hadt, R. G. T_1 Anisotropy Elucidates Spin Relaxation Mechanisms in an S = 1 Cr(IV) Optically Addressable Molecular Qubit. *The Journal of Physical Chemistry Letters* **2023**, *14,* 7658–7664.

[12] Gorgon, S. *et al.* Reversible Spin-Optical Interface in Luminescent Organic Radicals. *Nature* **2023**, *620,* 538–544.

[13] Mena, A.; Mann, S. K.; Cowley-Semple, A.; Bryan, E.; Heutz, S.; McCamey, D. R.; Attwood, M.; Bayliss, S. L. Room-Temperature Optically Detected Coherent Control of Molecular Spins. *arXiv:2402.07572 [physics, physics:quant-ph]* **2024**.

[14] Singh, H.; D'Souza, N.; Zhong, K.; Druga, E.; Oshiro, J.; Blankenship, B.; Reimer, J. A.; Breeze, J. D.; Ajoy, A. Room-Temperature Quantum Sensing with Photoexcited Triplet Electrons in Organic Crystals. *arXiv:2402.13898 [cond-mat, physics:physics, physics:quant-ph]* **2024**.

[15] Berezovsky, J.; Mikkelsen, M. H.; Stoltz, N. G.; Coldren, L. A.; Awschalom, D. D. Picosecond Coherent Optical Manipulation of a Single Electron Spin in a Quantum Dot. *Science* **2008**, *320,* 349–352.

[16] Gupta, J. A.; Knobel, R.; Samarth, N.; Awschalom, D. D. Ultrafast Manipulation of Electron Spin Coherence. *Science* **2001**, *292,* 2458–2461.

[17] Press, D.; Ladd, T. D.; Zhang, B.; Yamamoto, Y. Complete Quantum Control of a Single Quantum Dot Spin Using Ultrafast Optical Pulses. *Nature* **2008**, *456,* 218–221.

[18] Yu, P. Y.; Cardona, M. *Fundamentals of Semiconductors: Physics and Materials Properties;* Graduate Texts in Physics Springer Berlin Heidelberg: Berlin, Heidelberg, 2010. DOI: 10.1007/978-3-642-00710-1.

[19] Giovanni, D.; Ma, H.; Chua, J.; Grätzel, M.; Ramesh, R.; Mhaisalkar, S.; Mathews, N.; Sum, T. C. Highly Spin-Polarized Carrier Dynamics and Ultralarge Photoinduced Magnetization in $CH_3NH_3PbI_3$ Perovskite Thin Films. *Nano Letters* **2015**, *15,* 1553–1558.

[20] Scholes, G. D. Selection Rules for Probing Biexcitons and Electron Spin Transitions in Isotropic Quantum Dot Ensembles. *The Journal of Chemical Physics* **2004**, *121,* 10104–10110.

[21] Lin, X.; Han, Y.; Zhu, J.; Wu, K. Room-Temperature Coherent Optical Manipulation of Hole Spins in Solution-Grown Perovskite Quantum Dots. *Nature Nanotechnology* **2023**, *18,* 124–130.

[22] Kirilyuk, A.; Kimel, A. V.; Rasing, T. Ultrafast Optical Manipulation of Magnetic Order. *Reviews of Modern Physics* **2010**, *82,* 2731–2784.

[23] Sutcliffe, J.; Johansson, J. O. A Femtosecond Magnetic Circular Dichroism Spectrometer. *Review of Scientific Instruments* **2021**, *92,* 113001.

[24] Oppermann, M.; Bauer, B.; Rossi, T.; Zinna, F.; Helbing, J.; Lacour, J.; Chergui, M. Ultrafast Broadband Circular Dichroism in the Deep Ultraviolet. *Optica* **2019**, *6,* 56-60.

[25] Steinbach, F.; Schick, D.; von Korff Schmising, C.; Yao, K.; Borchert, M.; Engel, W. D.; Eisebitt, S. Wide-Field Magneto-Optical Microscope to Access Quantitative Magnetization Dynamics with Femtosecond Temporal and Sub-Micrometer Spatial Resolution. *Journal of Applied Physics* **2021**, *130,* 083905.

[26] Huang, D.; Lattery, D.; Wang, X. Materials Engineering Enabled by Time-Resolved Magneto-Optical Kerr Effect for Spintronic Applications. *ACS Applied Electronic Materials* **2021**, *3,* 119–127.

[27] Figgis, B. N.; Hitchman, M. A. *Ligand Field Theory and Its Applications;* Wiley-VCH: New York, 1st ed.; 1999.

[28] Piepho, S.; Schatz, P. *Group Theory in Spectroscopy With Applications to Magnetic Circular Dichroism;* John Wiley: New York, 1983.

[29] Fataftah, M. S.; Freedman, D. E. Progress Towards Creating Optically Addressable Molecular Qubits. *Chemical Communications* **2018**, *54,* 13773–13781.

[30] Furue, S.; Kohmoto, T.; Kunitomo, M.; Fukuda, Y. Optical Induction of Magnetization and Observation of Fast Spin Dynamics in Aqueous Solutions of Copper Ions. *Physics Letters A* **2005**, *345,* 415–422.

[31] Piepho, S. B.; Dickinson, J. R.; Spencer, J. A.; Schatz, P. N. High Resolution Magnetic Circular Dichroism Spectrum of Cs_2ZrCl_6:Ir^{4+}. *The Journal of Chemical Physics* **1972**, *57,* 982–990.

[32] Dickinson, J. R.; Piepho, S. B.; Spencer, J. A.; Schatz, P. N. High Resolution Magnetic Circular Dichroism and Absorption Spectra of Cs_2ZrBr_6:Ir^{4+}. *The Journal of Chemical Physics* **1972**, *56,* 2668–2677.

[33] Henning, G. N.; McCaffery, A. J.; Schatz, P. N.; Stephens, P. J. Magnetic Circular Dichroism of Charge Transfer Transitions: Low Spin d^5 Hexahalide Complexes. *The Journal of Chemical Physics* **1968**, *48,* 5656–5661.

[34] Bhaskaran, L.; Ponomaryov, A. N.; Wosnitza, J.; Khan, N.; Tsirlin, A. A.; Zhitomirsky, M. E.; Zvyagin, S. A. Antiferromagnetic Resonance in the Cubic Iridium Hexahalides $(NH_4)_2IrCl_6$ and K_2IrCl_6. *Physical Review B* **2021**, *104,* 184404.

[35] Owen, J.; Stevens, K. W. H. Paramagnetic Resonance and Covalent Bonding. *Nature* **1953**, *171,* 836–836.

[36] Keiderling, T. A.; Stephens, P. J.; Piepho, S. B.; Slater, J. L.; Schatz, P. N. Infrared Absorption and Magnetic Circular Dichroism of Cs_2ZrCl_6:Ir^{4+}. *Chemical Physics* **1975**, *11,* 343–348.

[37] Bonmarin, M.; Helbing, J. Polarization Control of Ultrashort Mid-IR Laser Pulses for Transient Vibrational Circular Dichroism Measurements. *Chirality* **2009**, *21,* E298–E306.

[38] Gupta, J. A.; Awschalom, D. D.; Efros, A. L.; Rodina, A. V. Spin Dynamics in Semiconductor Nanocrystals. *Physical Review B* **2002**, *66,* 125307.

[39] Stoll, S.; Goldfarb, D., Eds.; *EPR Spectroscopy: Fundamentals and Methods;* Wiley: Hoboken, N.J, 1st edition ed.; 2018.

[40] Huffman, J. L.; Poncelet, M.; Moore, W.; Eaton, S. S.; Eaton, G. R.; Driesschaert, B. Perchlorinated Triarylmethyl Radical 99% Enriched ^{1}3C at the Central Carbon as EPR Spin Probe Highly Sensitive to Molecular Tumbling. *The Journal of Physical Chemistry B* **2021**, *125,* 7380–7387.

[41] Mirzoyan, R.; Kazmierczak, N. P.; Hadt, R. G. Deconvolving Contributions to Decoherence in Molecular Electron Spin Qubits: A Dynamic Ligand Field Approach. *Chemistry – A European Journal* **2021**, *27,* 9482–9494.

[42] Möser, J.; Lips, K.; Tseytlin, M.; Eaton, G. R.; Eaton, S. S.; Schnegg, A. Using Rapid-Scan EPR to Improve the Detection Limit of Quantitative EPR by More than One Order of Magnitude. *Journal of Magnetic Resonance* **2017**, *281,* 17–25.

[43] Kazmierczak, N. P.; Mirzoyan, R.; Hadt, R. G. The Impact of Ligand Field Symmetry on Molecular Qubit Coherence. *Journal of the American Chemical Society* **2021**, *143,* 17305–17315.

[44] Kazmierczak, N. P.; Hadt, R. G. Illuminating Ligand Field Contributions to Molecular Qubit Spin Relaxation via T_1 Anisotropy. *Journal of the American Chemical Society* **2022**, *144,* 20804–20814.

Chapter 11

CONCLUSION

The contemporary surge of interest in molecular quantum information science has generated two key research directions regarding molecular spin dynamics, namely (1) mechanism and (2) applications. The mechanistic direction seeks to understand the fundamental processes controlling the lifetime of quantum superposition states in molecules. While the processes of spin-lattice relaxation and spin-spin decoherence have been studied since the first half of the 20th century, prior descriptions proved to be insufficiently precise to guide contemporary efforts. Through new synthesis, spectroscopy, and modern computational and *ab initio* theory, the 21st century has seen a significant expansion in our understanding of molecular spin dynamics mechanisms. This mechanistic work will enable progress on the second direction: designing molecular spin systems with practical applications. An isolated two-level spin system undergoing superposition decoherence constitutes only the very simplest of quantum systems, and harnessing the proposed power of molecular quantum information science will likely require larger-scale molecular quantum systems with entanglement and improved addressability.

This thesis principally describes contributions to the mechanistic direction. Three key questions have been addressed regarding the T_1 relaxation process. First, what physical interaction enables the energy transfer between spins and vibrational motions? This is referred to as the coupling mechanism, and we have seen that a variety of proposals have been put forward in the literature, each relating to different components and constructions of the molecular Hamiltonian. Second, do specific nuclear motions control spin relaxation, and if so, what are the salient characteristics of these nuclear motions? This is the question of whether spin relaxation possesses vibrational selectivity. Third, can guidelines be formulated to rationally control the spin relaxation rate in paramagnetic metal complexes? This is the question of chemical design principles.

Part 1 of this thesis (Chapters 1–4) has described the development of ligand field spin dynamics (LFSD) as a framework for answering these questions using the language and techniques of inorganic coordination chemistry. By deriving equations for spin-phonon coupling coefficients from ligand field theory (Chapter 1), LFSD has predicted that the ligand field excited state energies should exert a controlling effect on the rates of spin relaxation. This prediction has been experimentally verified via MCD spectroscopy (Chapter 4), providing an important contribution to the understanding of the coupling mechanism. The group theory approach for spin-phonon coupling selection rules has rationalized why complexes close to D_{4h} or C_{4v} point groups tend to possess the longest T_1 times (Chapter 2), owing to an increase in vibrational selectivity. Resonance Raman spectroscopy (Chapter 3) in conjunction with pulse EPR has shown that higher-energy molecular stretching vibrations are the ones selectively driving T_1 in these high-symmetry compounds, and not low-energy phonons as predicted by some previous models.

While this approach has shown significant success, in some cases it proved challenging to unambiguously verify LFSD versus competing spin relaxation theories using the available spectroscopic data. This issue particularly arises regarding the vibrational selectivity question, as no experimental technique yet exists for selecting a vibrational mode and directly measuring its contribution to T_1. Thus, the next direction in the thesis research sought to bolster the experimental evidence used to test spin relaxation theories.

Part 2 of this thesis (Chapters 5–7) has described a new spectroscopic observable, T_1 anisotropy, which probes vibrational contributions in a more direct way than previous pulse EPR procedures. The existence and direction of T_1 anisotropy (Chapter 5) falsified several spin Hamiltonian models for T_1, demonstrating that spin-orbit coupling and ligand field excited states must be explicitly considered in any plausible theory of the coupling mechanism. Subsequent theoretical models by Lunghi[1] and Shushkov[2] have both moved in this direction, and we are excited to see the progress of *ab initio* theory in reproducing the observed T_1 anisotropy values. T_1 anisotropy has been employed to detected unique vibrational contributions in $S = 1$ Cr(IV) optically-addressable qubits relative to $S = ½$ microwave-addressable qubits (Chapter 6), which may shed light on the origin of fast spin relaxation in the Cr(IV) systems. Variable-temperature profiling of T_1 anisotropy (Chapter 7) provides a powerful way to detect multiple vibrational contributions to relaxation and their associated energies, even when they are not visible in the temperature-dependent T_1 by standard pulse EPR methodology. The T_1 anisotropy concept has proven a fruitful approach for constraining theoretical coupling mechanisms.

Part 3 of this thesis (Chapters 8–10) describes the translation of LFSD and T_1 anisotropy insights to generate chemical design principles for spin dynamics. Through collaboration with the Agapie group, it has proven possible to synthesize a new macrocyclic ligand framework that simultaneously suppresses ligand field electronic structure contributions to the coupling mechanism and reduces vibrational population contributions to relaxation (Chapter 8). This has enabled elongation of T_1 to a new record for CuN_4 molecular complexes. These observations are in full agreement with LFSD predictions for both the coupling mechanism and vibrational selectivity. In collaboration with the Nemykin group, it has been shown that bulky disordered substituents can alter the nature of vibrational selectivity, leading to significant changes in the T_1 anisotropy (Chapter 9). Finally, a detailed consideration of ligand field electronic structure revealed a new way of generating and probing spin superpositions through time-resolved Faraday ellipticity (TRFE, Chapter 10). The design principles for a TRFE-addressable molecule (maximization of orbital angular momentum) are inverted to relative microwave-addressable molecules (minimization of orbital angular momentum), yet both mechanisms can be understood through the LFSD spin dynamics framework. Chapter 10 provides a direct connection to potential quantum sensing applications, to be discussed further below.

The majority of the conclusions in this thesis have gained widespread acceptance in the field. One key point of ongoing debate in the literature, however, relates to the vibrational selectivity question. Our work, on the basis of group theory using a $\partial g/\partial Q$ model as well as a spin-orbit wavefunction model, has pinpointed metal-ligand totally symmetric stretching modes as driving T_1 (Chapters 2 and 5). This conclusion is additionally supported by the correlations between local mode energies and totally symmetric vibrations in porphyrin systems (Chapter 3), as well as the success of M-L symmetric stretching modes in predicting T_1 trends for CuN_4 macrocycles (Chapter 8). However, there exist two *ab initio* spin relaxation theories that reach different conclusions, both with respect to our work and with respect to each other. First, Lunghi and coworkers have argued for the preeminence of ultra-low energy phonons and vibrations in driving T_1.[1] Their computed T_1 vs. temperature traces match experiment reasonably well for low symmetry compounds (C_{2v}/D_{2h} or lower) which display predominantly power law scaling. However, their calculations have not yet replicated experimental behavior for higher symmetry complexes (C_{4v} or D_{4h}) where strong local mode character is observed by EPR. We note that the systems studied by the most recent version of their theory have been restricted to the lower symmetry cases, while the systems used to develop our LFSD assignment are largely of the higher symmetry cases (e.g., copper and vanadyl phthalocyanine). It is possible that low-energy phonons are more important in C_{2v}/D_{2h} and when disordered substituents are introduced (Chapter 9), while molecular stretching vibrations become dominant in higher symmetry, ordered complexes. Correlation of *ab initio* and experimental results across a broader compound spectrum should clarify this point.

Separately, Shushkov has described a non-adiabatic theory of spin relaxation.[2] It agrees with the LFSD model that higher-energy molecular vibrations drive much of the T_1 behavior, as opposed to low energy phonons, and it agrees that symmetry-based vibrational selectivity for spin relaxation is present. However, it assigns these key higher-energy molecular vibrations to modes of different symmetries than the modes pinpointed in our work. The non-adiabatic mechanism proceeds through a spin-vibrational orbit interaction, which is produced from the mixing of degenerate normal modes. Thus, degenerate modes in D_{4h} and C_{4v}, such as e_g and e_u modes, are predicted to be dominant. It is more difficult to experimentally separate the effect of molecular e_u and a_{1g} modes from each other because they occupy similar positions in energy space, and thus could both in principle each lead to the observed local mode behavior via EPR. If both e_u and a_{1g} modes have similar trends in energy across different ligand frameworks, then the nonadiabatic assignments could potentially account for the vibrational energy trends discussed in Chapters 3 and 8. However, the apparent implication of the degenerate mode mechanism would be that complexes with a fourfold rotation axis should have faster spin relaxation than those without. This seems in tension with experimental results, as C_{4v} complexes such as vanadyl phthalocyanine are prized for their slow spin relaxation rates. We look forward to further benchmarking of the nonadiabatic theory across complexes of various symmetries to address this point.

It is possible that a shift will occur in molecular spin dynamics research. At the beginning of this work in 2020, the detailed mechanisms of slow spin relaxation were not widely understood. Now in 2025, it appears most key mechanistic considerations for $S = 1/2$ spin lifetimes have been brought to light, and a consensus resolution on the question of vibrational selectivity is in reach within a matter of years. Similar progress has been made in understanding the mechanisms of T_2 by Stoll, Galli, Freedman, Zadrozny, and others.[3–5] However, understanding superposition lifetimes in a two-level spin system is only the prelude for practical applications, including designer entanglement and addressability schemes. Now that many of the key design principles for prolonging T_1 and T_2 have been described, attention will likely shift to demonstrating quantum information processing tasks, such as molecular quantum sensing.

Two lines of development can be imagined. First, molecular quantum sensing protocols can be designed in the spirit of the notable successes using anionic nitrogen vacancy (NV^-) diamond centers. There is an impressive and growing body of literature on NV^- quantum sensing which uses the properties of an isolated spin system possessing coherence at room temperature. Molecular analogs are attractive for significantly enhanced spatial precision than NV^-, so developing molecules that can perform similar tasks is clearly an important goal. Freedman and Awschalom have developed Cr(IV) molecules active for optically-detected magnetic resonance (ODMR) in the same manner as NV^- centers.[6] However, a key challenge is fast spin relaxation in these systems limiting coherence below 60 K. Recently, strategies for producing ODMR activity in organic radicals have been developed by Yuen-Zhou and coworkers, including experimental realization by Wasielewski.[7–10] Alternative excited-state spin dynamics methods in organic molecules have been described by Friend,[11] and room-temperature coherent control in photoexcited pentacene has been described by Bayliss and Ajoy.[12,13] Given the reduced spin-orbit coupling of organic radicals, these approaches significantly reduce the spin relaxation rates, enabling room temperature operation. Chemical stability in biological media will become an increasingly important design consideration as room-temperature quantum sensing applications are pursued. Alternatively, quantum sensing protocols can be built using the TRFE detection scheme described in Chapter 10. While this concept is comparatively new, several significant advantages exist relative to ODMR, including ultrafast time resolution and a potentially wider scope of molecules that could display room-temperature spin coherence without the need for a high spin ground state and photoluminescence. We note that all these exciting directions can be pursued without the need for multiple entangled spin centers.

The second approach seeks to build molecules capable of multi-qubit gate operations and entanglement schemes. Wasielewski has built photogenerated spin-correlated radical pair systems capable of enacting quantum teleportation protocols via entanglement,[14] and there exist bimetallic metal complexes designed for the purpose of entanglement by Freedman, Sessoli, and others.[15,16] However, demonstrations of multi-qubit processing using molecular electron spins have been scarce. This is important because controlled entanglement is likely necessary to realize the full potential of molecular quantum sensing. Degen[17] has described three levels of experiments that can be classified as "quantum sensing," listed below:

1. Use of a quantum object to measure a physical quantity.
2. Use of quantum coherence (i.e., superposition states) to measure a physical quantity.
3. Use of quantum entanglement to improve the sensitivity or precision of a measurement, beyond what is possible classically.

The mechanistic understanding of T_1 and T_2 recently developed in the community will enable type-II quantum sensing. The examples of NV^- quantum sensing shows that type-II quantum sensors can already lead to very significant achievements, so the pursuit of type-II molecular quantum sensing is certainly worthy. However, much of the original excitement surrounding the quantum sensing concept stems from type-III sensing. Activity in this area has been limited by the lack of systems for producing and controlling molecular entanglement. Exploration of type-III molecular quantum sensing would prove an exciting future research frontier.

References

[1] Mariano, L. A.; Nguyen, V. H. A.; Petersen, J. B.; Björnsson, M.; Bendix, J.; Eaton, G. R.; Eaton, S. S.; Lunghi, A. The Role of Electronic Excited States in the Spin-Lattice Relaxation of Spin-1/2 Molecules. *Science Advances* **2025**, *11,* eadr0168.

[2] Shushkov, P. A Novel Non-Adiabatic Spin Relaxation Mechanism in Molecular Qubits. *The Journal of Chemical Physics* **2024**, *160,* 164105.

[3] Canarie, E. R.; Jahn, S. M.; Stoll, S. Quantitative Structure-Based Prediction of Electron Spin Decoherence in Organic Radicals. *The Journal of Physical Chemistry Letters* **2020**, *11,* 3396–3400.

[4] Bayliss, S. L.; Deb, P.; Laorenza, D. W.; Onizhuk, M.; Galli, G.; Freedman, D. E.; Awschalom, D. D. Enhancing Spin Coherence in Optically Addressable Molecular Qubits through Host-Matrix Control. *Physical Review X* **2022**, *12,* 031028.

[5] Jackson, C. E.; Ngendahimana, T.; Lin, C.-Y.; Eaton, G. R.; Eaton, S. S.; Zadrozny, J. M. Impact of Counter Ion Methyl Groups on Spin Relaxation in $[\mathrm{V(C_6H_4O_2)_3}]^{2-}$. *The Journal of Physical Chemistry C* **2022**, *126,* 7169–7176.

[6] Bayliss, S. L.; Laorenza, D. W.; Mintun, P. J.; Kovos, B. D.; Freedman, D. E.; Awschalom, D. D. Optically Addressable Molecular Spins for Quantum Information Processing. *Science* **2020**, *370,* 1309–1312.

[7] Poh, Y. R.; Morozov, D.; Kazmierczak, N. P.; Hadt, R. G.; Groenhof, G.; Yuen-Zhou, J. Alternant Hydrocarbon Diradicals as Optically Addressable Molecular Qubits. *Journal of the American Chemical Society* **2024**, *146,* 15549–15561.

[8] Poh, Y. R.; Chen, X.; Cheng, H.-P.; Yuen-Zhou, J. Electron Sextets as Optically Addressable Molecular Qubits: Triplet Carbenes. *ChemRxiv:10.26434/chemrxiv-2025-px2sj* **2025**.

[9] Poh, Y. R.; Yuen-Zhou, J. Enhancing the Optically Detected Magnetic Resonance Signal of Organic Molecular Qubits. *ACS Central Science* **2025**, *11,* 116–126.

[10] Kopp, S. M.; Nakamura, S.; Phelan, B. T.; Poh, Y. R.; Tyndall, S. B.; Brown, P. J.; Huang, Y.; Yuen-Zhou, J.; Krzyaniak, M. D.; Wasielewski, M. R. Luminescent Organic Triplet Diradicals as Optically Addressable Molecular Qubits. *Journal of the American Chemical Society* **2024**, *146,* 27935–27945.

[11] Gorgon, S. *et al.* Reversible Spin-Optical Interface in Luminescent Organic Radicals. *Nature* **2023**, *620,* 538–544.

[12] Mena, A.; Mann, S. K.; Cowley-Semple, A.; Bryan, E.; Heutz, S.; McCamey, D. R.; Attwood, M.; Bayliss, S. L. Room-Temperature Optically Detected Coherent Control of Molecular Spins. *Physical Review Letters* **2024**, *133,* 120801.

[13] Singh, H.; D'Souza, N.; Zhong, K.; Druga, E.; Oshiro, J.; Blankenship, B.; Montis, R.; Reimer, J. A.; Breeze, J. D.; Ajoy, A. Room-Temperature Quantum Sensing with Photoexcited Triplet Electrons in Organic Crystals. *Physical Review Research* **2025**, *7,* 013192.

[14] Rugg, B. K.; Krzyaniak, M. D.; Phelan, B. T.; Ratner, M. A.; Young, R. M.; Wasielewski, M. R. Photodriven Quantum Teleportation of an Electron Spin State in a Covalent Donor-Acceptor-Radical System. *Nature Chemistry* **2019**, *11,* 981–986.

[15] von Kugelgen, S.; Krzyaniak, M. D.; Gu, M.; Puggioni, D.; Rondinelli, J. M.; Wasielewski, M. R.; Freedman, D. E. Spectral Addressability in a Modular Two Qubit System. *Journal of the American Chemical Society* **2021**, *143,* 8069–8077.

[16] Ranieri, D.; Santanni, F.; Privitera, A.; Albino, A.; Salvadori, E.; Chiesa, M.; Totti, F.; Sorace, L.; Sessoli, R. An Exchange Coupled Meso-Meso Linked Vanadyl Porphyrin Dimer for Quantum Information Processing. *Chemical Science* **2023**, *14,* 61–69.

[17] Degen, C. L.; Reinhard, F.; Cappellaro, P. Quantum Sensing. *Reviews of Modern Physics* **2017**, *89,* 035002.

Appendix A

SUPPORTING INFORMATION FOR CHAPTER II: THE IMPACT OF LIGAND FIELD SYMMETRY ON MOLECULAR QUBIT COHERENCE

The Supporting Information is available free of charge at:
https://pubs.acs.org/doi/10.1021/jacs.1c04605. All Supporting Information PDF files have also been archived at the following DOI: 10.22002/qvk8g-3f293. Detailed description of computational approach; validation of the T_1 model; tabulation of vibrational modes and spin-phonon coupling coefficients; group theory tables; example input files; and molecular coordinates.

Appendix B

SUPPORTING INFORMATION FOR CHAPTER III: DETERMINING THE KEY VIBRATIONS FOR SPIN RELAXATION IN RUFFLED COPPER(II) PORPHYRINS VIA RESONANCE RAMAN SPECTROSCOPY

The Supporting Information is available free of charge at: https://pubs.rsc.org/en/content/articlelanding/2024/sc/d3sc05774g. All Supporting Information PDF files have also been archived at the following DOI: 10.22002/qvk8g-3f293. Crystallographic information can be found in the Cambridge Crystallographic Data Centre (CCDC), deposition number 2303071.

Appendix C

SUPPORTING INFORMATION FOR CHAPTER IV: A SPECTROCHEMICAL SERIES FOR ELECTRON SPIN RELAXATION

The Supporting Information is available free of charge at:
https://pubs.acs.org/doi/10.1021/jacs.4c16571. All Supporting Information PDF files have also been archived at the following DOI: 10.22002/qvk8g-3f293. Synthesis and characterization methods, powder X-ray diffraction, X-ray crystallography, UV-vis spectroscopy, MCD methods, MCD analysis, EPR methods, and computational methods. Deposition Number 2383406 contains the supplementary crystallographic data for this paper. These data can be obtained free of charge via the joint Cambridge Crystallographic Data Centre (CCDC) and Fachinformationszentrum Karlsruhe Access Structures service.

Appendix D

SUPPORTING INFORMATION FOR CHAPTER V: ILLUMINATING LIGAND FIELD CONTRIBUTIONS TO MOLECULAR QUBIT SPIN RELAXATION VIA T_1 ANISOTROPY

The Supporting Information is available free of charge at:
https://pubs.acs.org/doi/10.1021/jacs.2c08729. All Supporting Information PDF files have also been archived at the following DOI: 10.22002/qvk8g-3f293. Synthesis and sample preparation, experimental methods, fitting of EPR spectra, additional T_1 anisotropy experiments, quantification of T_1 anisotropy, ligand field theory derivation of T_1 anisotropy, computational methods, analysis of excited state energies, spin-phonon coupling coefficients, xyz coordinates used for computations, example TDDFT input file, and example Matlab script for fitting T_1 anisotropy.

Appendix E

SUPPORTING INFORMATION FOR CHAPTER VI: T_1 ANISOTROPY ELUCIDATES SPIN RELAXATION MECHANISMS IN AN S = 1 CHROMIUM(IV) OPTICALLY ADDRESSABLE MOLECULAR QUBIT

The Supporting Information is available free of charge at:
https://pubs.acs.org/doi/10.1021/acs.jpclett.3c01964. All Supporting Information PDF files have also been archived at the following DOI: 10.22002/qvk8g-3f293. Experimental methods, temperature-dependent EPR fitting, T_1 anisotropy fitting, and theoretical derivation of T_1 anisotropy functional forms.

Appendix F

SUPPORTING INFORMATION FOR CHAPTER VII: SPECTROSCOPIC SIGNATURES OF PHONON CHARACTER IN MOLECULAR ELECTRON SPIN RELAXATION

The Supporting Information is available free of charge at: https://pubs.acs.org/doi/10.1021/acscentsci.4c01177. All Supporting Information PDF files have also been archived at the following DOI: 10.22002/qvk8g-3f293. Sample preparation, pulse EPR methods, temperature dependent T_1 and T_m curves for Cu(acac)$_2$, comparison of T_1 for differing pulse sequences, T_1 local mode fitting, influence of saturation recovery pulse sequence parameters on T_1 anisotropy, influence of paramagnetic concentration on T_1 anisotropy, factor analysis methods, single-crystal pulse EPR methods, computational methods, tabulation of T_1 anisotropy data, example Matlab code for VTVH-T_1 factor analysis, supplementary references.

Appendix G

SUPPORTING INFORMATION FOR CHAPTER VIII: SLOW ELECTRON SPIN RELAXATION AT AMBIENT TEMPERATURES WITH COPPER COORDINATED BY A RIGID MACROCYCLIC LIGAND

The Supporting Information is available free of charge at: https://pubs.acs.org/doi/10.1021/jacs.5c00803. All Supporting Information PDF files have also been archived at the following DOI: 10.22002/qvk8g-3f293. Experimental details, synthesis and characterization of compounds, crystallographic characterization, continuous wave and pulsed electron paramagnetic resonance data, computational work, nuclear magnetic resonance data, and UV–vis data. Deposition Numbers 2414749–2414753 contain the supplementary crystallographic data for this paper. These data can be obtained free of charge via the joint Cambridge Crystallographic Data Centre (CCDC) and Fachinformationszentrum Karlsruhe Access Structures service.

Appendix H

SUPPORTING INFORMATION FOR CHAPTER IX: QUANTIFYING THE EFFECTS OF PERIPHERAL SUBSTITUENTS ON THE SPIN-LATTICE RELAXATION OF A VANADYL MOLECULAR QUANTUM BIT

The Supporting Information is available free of charge at: http://www.worldscientific.com/doi/suppl/10.1142/S1088424624500329. All Supporting Information PDF files have also been archived at the following DOI: 10.22002/qvk8g-3f293. Crystallographic data have been deposited at the Cambridge Crystallographic Data Centre (CCDC) under the numbers CCDC-2208789. Copies can be obtained on request, free of charge, via https://www.ccdc.cam.ac.uk/structures/ or from the Cambridge Crystallographic Data Centre, 12 Union Road, Cambridge CB2 1EZ, UK (fax: +44 1223-336-033 or email: deposit@ccdc.cam.ac.uk).

Appendix I

SUPPORTING INFORMATION FOR CHAPTER X: ULTRAFAST, ALL-OPTICAL COHERENCE OF MOLECULAR ELECTRON SPINS IN ROOM-TEMPERATURE AQUEOUS SOLUTION

The Supporting Information is available free of charge at:
science.org/doi/10.1126/science.ads0512. All Supporting Information PDF files have also been archived at the following DOI: 10.22002/qvk8g-3f293. Materials and Methods, Supplementary Text, Figures S1 to S16, Tables S1 to S3, References (47-49).

INDEX

B

bibliography
  by chapter, 1, 57, 78, 102, 130, 144, 165, 179, 195, 209

F

figures, 1, 4, 5, 7, 8, 12, 17, 19, 33, 35, 38, 41, 43, 46, 48, 50, 57, 60, 61, 64, 66, 69, 70, 78, 81, 83, 86, 87, 92, 94, 102, 105, 107, 108, 110, 113, 119, 122, 130, 133, 134, 136, 137, 144, 148, 149, 153, 156, 165, 167, 169, 171, 173, 182, 185, 188, 189, 197, 200, 203

T

tables, 15, 40, 63, 71, 109, 111, 122, 174